# A Proposal to NOAO for the BigBOSS Experiment at Kitt Peak National Observatory

October 1, 2010

D. Schlegel[a], et al.



[a] Lawrence Berkeley National Laboratory

## EXECUTIVE SUMMARY

We propose a DOE-NSF Stage IV ground-based dark energy experiment called BigBOSS to study baryon acoustic oscillations (BAO) and the growth of structure with a wide-area galaxy and quasar redshift survey. This proposal is submitted in response to the Call issued by NOAO on November 18, 2009 for major new instrumentation and a high-impact science program for the 4-m Mayall telescope at Kitt Peak. We will build and deploy a robotically-actuated, fiber-fed spectrograph capable of taking 5000 simultaneous spectra over a wavelength range from 340 nm to 1060 nm, with a resolution $R = \lambda/\Delta\lambda = 3000 - 4800$. The focal plane is located at prime focus, where a new optical corrector will provide an impressive 3 degree diameter field of view. The BigBOSS proposal also includes delivery of a spectroscopic pipeline and data management system to reduce and archive all data for public access. BigBOSS builds upon the SDSS-III/BOSS project, re-using many aspects of the BOSS instrument and computing pipeline designs.

The BigBOSS Key Science project is a 14,000 square degree survey that will be carried out using 500 nights over five years. Using data from imaging surveys that are already underway, we will select spectroscopic targets that trace the underlying dark matter distribution. In particular, we will measure the redshifts of bright [OII] emission line galaxies (ELGs) up to a redshift $z = 1.7$ and luminous red galaxies (LRGs) up to $z = 0.9$, extending the BOSS LRG survey in both redshift and survey area. In total, over 20 million galaxy redshifts will be obtained to measure the BAO feature, trace the matter power spectrum at smaller scales, and detect redshift space distortions. Additional constraints on early dark energy and on the curvature of the universe will be obtained with measurements of the Ly-$\alpha$ forest in the spectra of over 600,000 $2.2 < z < 3.5$ quasars.

The BigBOSS Mayall survey will provide a significant advance in our understanding of the expansion history of the universe and dark energy. Using the BAO measurement from galaxies alone, BigBOSS will more than double the BAO figure of merit obtained prior to its operation and achieve an accuracy on the BAO standard ruler of 0.4% for $0.5 < z < 1.0$ and 0.6% for $1.0 < z < 1.7$. Exploiting redshift space distortions will increase the power of BigBOSS substantially, and using the full power spectrum will boost this further.

BigBOSS will also enable an unprecedented multi-object spectroscopic capability for the U.S. community through an existing NOAO facility. Approximately 1000 fibers will be available to the community during the BigBOSS survey for synchronous observing programs. A rich variety of scientific goals will also be advanced through use of the legacy data from the BigBOSS survey and through PI-led programs using the BigBOSS instrument for dedicated spectroscopic surveys.

BigBOSS is complementary to the imaging surveys that are underway or planned for this decade. The BigBOSS survey will cover much of the PanSTARRS-1 and PTF survey areas in the Northern hemisphere, and will also have substantial overlap with the DES and LSST survey areas, which are primarily in the Southern hemisphere but have equatorial and northern ecliptic regions. The overlap with DES and LSST in particular will provide spectra for photometric redshift training useful for the weak lensing and galaxy cluster measurements and will enable a host of other scientific goals. A potential follow-on project (subject to an invitation from NOAO) would move the BigBOSS focal plane, optics and spectrographs down to the Mayall's twin in the southern hemisphere, the Blanco telescope at CTIO after completion of the DES program. An additional 10,000 square degree BAO survey could be carried out from the Blanco, for a total survey area of 24,000 square degrees. From CTIO, the BigBOSS instrument would then have concurrent access to the same sky that LSST will be mapping, and the prospects for synergistic programs are enormous.

The scope of the BigBOSS project is comparable to that undertaken by DES, and we foresee a similar partnership between NSF/NOAO and DOE/OHEP. Details of this partnership will be determined with input from DOE, NSF, and the NOAO user community. Our conceptual plan is that construction would be managed by Lawrence Berkeley National Laboratory, while installation and operation would be managed by NOAO/Kitt Peak. Survey observing support and science operations will be managed jointly. Construction of the instrument is estimated to take four years beginning in 2012, for first light in 2016.

# Contents

# 1 Introduction

## 1.1 BigBOSS in Context

On November 18, 2009, NOAO announced an opportunity to "pursue a large science program with the Mayall 4-meter telescope on Kitt Peak and to develop a major observing capability" for the National Observatory[1]. In particular, the Call encouraged proposals which would enable (and pursue) "large, high-impact science programs and [improve] the capabilities [within] the U.S. System of ground-based optical and near-IR telescopes". In response to this call, we, the BigBOSS Team, propose to develop, in collaboration with NOAO, a highly multiplexed, wide-field fiber-fed spectrograph for the prime focus of the Mayall 4m Telescope. The BigBOSS spectrograph focal plane has 5000 robotically actuated fibers covering a 3° diameter field of view. The fibers feed 10 identical spectrographs, each covering the wavelength range from 340 to 1060 nm with a resolution $R = \lambda/\Delta\lambda = 3000-4800$. This instrument will enable a Key Project addressing fundamental questions in cosmology, and will provide the NOAO community with a significant new observational resource.

With the discovery that the bulk of gravitating matter in the universe is in a "dark" form [Zwicky, 1933; Rubin, Ford & Thonnard, 1980], and the even more startling discovery that the universal expansion is *accelerating* [Riess et al., 1998; Perlmutter et al., 1999], perhaps driven by a new form of energy with negative pressure, we have had to come to terms with the fact that 96% of the energy density of the universe is contained in some hitherto undetected (and unsuspected!) form. Over the last decade, there has been a growing realization that understanding these new components of the universe (i.e., the dark matter and dark energy) requires fundamentally new physics. Numerous ideas have been advanced to explain the acceleration and predict its redshift evolution (e.g., Frieman, Turner & Huterer 2008). However, despite intense efforts over the last decade since its discovery, there is still no consensus as to the nature of dark energy. Our understanding is still limited by our lack of data, specifically by our limited knowledge of the expansion rate (and the countering effects of gravity as traced by the growth of structure) as a function of redshift, and the field looks to astronomical observations for guidance.

It is therefore hardly surprising that numerous recent community-based reviews have recommended that a major undertaking of the astronomy and

[1]See "Announcement of Opportunity for Large Science Programs Providing Observing Capabilities for the Mayall 4m Telescope", http://www.noao.edu/kpno/largescience.html

physics communities be focused on constraining the equation of state of dark energy, or more generally the accurate measure of the Universe's expansion history. These reviews include *Connecting Quarks to the Cosmos* (Committee on the Physics of the Universe 2003); the Report of the Dark Energy Task Force (Albrecht et al. 2006); the Report of the High Energy and Particle Astrophysics (HEPAP) Particle Astrophysics Scientific Assessment Group (PASAG; Ritz et al. 2009); *New Worlds, New Horizons in Astronomy & Astrophysics*, and the Report of the Committee for a Decadal Survey of Astronomy and Astrophysics (Blandford et al. 2010, http://www.nap.edu/catalog/12951.html).

BigBOSS is sufficiently ambitious that great discoveries are possible. BigBOSS will obtain observational constraints that will bear on three of the four "science frontier" questions identified by the Decadal Survey: Why is the universe accelerating? What is dark matter? What are the properties of neutrinos? Indeed, the BigBOSS project was recommended for immediate R&D support by the PASAG report. The second highest priority from the Astro2010 Decadal Survey was the creation of a funding line within the NSF to support a "Mid-Scale Innovations" program, and used BigBOSS as a "compelling" example for support. This choice was the result of the Decadal Survey's Program Prioritization panels reviewing 29 mid-scale projects and recommending BigBOSS "very highly".

## 1.2 The BigBOSS Cosmology Program

BigBOSS on the 4m Mayall Telescope at the Kitt Peak National Observatory will enable (1) a cosmological investigation of unprecedented scale and scientific value; and (2) a unique capability for NOAO's user community. It will provide astronomers with the ability to spectroscopically target very large, statistically significant samples of astronomical objects with relative ease, thus enabling astrophysical investigations of unprecedented scale and areal coverage.

The legacy of the Mayall and Blanco Telescopes at NOAO includes fundamental advances in cosmological exploration, namely the discovery of dark matter, the pioneering use of supernovae as standard candles, and the resulting unexpected discovery of the cosmological acceleration. As mentioned, this last discovery, in particular, has revolutionized cosmology and focused efforts on characterizing the acceleration and understanding the "dark energy" that is driving it.

BigBOSS will equip the Mayall telescope for the next phase in this endeavor of cosmological discovery to measure the geometry of the universe

and characterize its accelerating expansion with unprecedented accuracy. As described in more detail in the following chapters, our team will use BigBOSS for 500 nights spread over 5 years to undertake a redshift survey of $\approx 20$ million galaxies up to a redshift $z = 1.7$ over 14,000 deg$^2$ to directly measure the baryon acoustic oscillation scale. BigBOSS will measure the Hubble parameter and angular diameter distance to sub-percent accuracies. As a quantitative measure, BigBOSS galaxy BAO results will more than double the DETF figure of merit relative to all Stage III galaxy BAO results combined, increasing it from 42 to 92, using only Planck data as a prior in both cases. Adding analysis of redshift space distortions could increase this to more than 200. If the full power spectrum can be employed as far as $k = 0.2h\,\mathrm{Mpc}^{-1}$, this would raise the figure of merit to more than 500. Additional information will come from the analysis of the Lyman-alpha forest in the spectra of 600,000 QSOs in the redshift range $2.2 < z < 3.5$. Exactly how far these analyses can be pushed beyond the basic BAO analysis is a very active area of research and not yet known.

The redshift survey used to measure the baryon acoustic scale will be used to attack other problems in cosmology. These include constraints (or measurements!) of the neutrino mass, constraints on inflationary models, and tests of modified gravity. These will also be used for pohtometric redshift calibration of DES and LSST. BigBOSS will follow the model of the Sloan Digital Sky Survey and make publicly available both its reduced and calibrated survey data and high order data products, since these will enable a host of studies related to galaxy evolution and large scale structure.

## 1.3 BigBOSS and the NOAO Community

BigBOSS will have a major impact on the NOAO community's ability to successfully undertake large spectroscopic surveys of high astrophysical impact. Beyond its impact on cosmology, BigBOSS is an instrument of remarkable astrophysical grasp and fills an important hole in the U.S. System. Wide-field multi-object spectroscopy to enable spectroscopic surveys has been called out as a desired capability on 4-m class telescopes by various reports, including "The Ground-Based O/IR National Observatory: A Roadmap to 2020", the report of the Future of NOAO Committee; "Renewing Small Telescopes for Astronomical Research" (ReSTAR); "Report of the First Workshop on the Ground-Based O/IR System" (2000).

BigBOSS provides a timely addition of multi-object spectroscopic capability to the U.S. System. BigBOSS will provide the much-needed spectroscopic follow-up for imaging surveys, with a 3-degree field of view that com-

parable to PanSTARRS (3 deg), Dark Energy Survey (2.2 deg) and LSST (3.5 deg). With its ability to obtain nearly 5000 spectra over a 3° diameter field with a single observation, BigBOSS will also enable the U.S. astronomical community to undertake revolutionary studies of astronomical objects. Such studies include: surveying the kinematics and chemical properties of stars in the Milky Way to understand our Galaxy's structure, dynamical and chemical history; mapping the evolution of large scale structure in the galaxy distribution over the last 8 billion years; extending studies of galaxy evolution of the scope undertaken by the Sloan Digital Sky Survey to higher redshift; carrying out large scale surveys for identifying and studying rare populations (e.g., high redshift QSOs, bright lensed galaxies, low metallicity stars, very cool white dwarfs); probing the structure of the interstellar and intergalactic media; and many, many more.

BigBOSS will be a facility instrument for the Mayall telescope with NOAO community access. The tools for planning observations and reducing the data will are deliverables with the instrument, allowing NOAO users to plan and execute their observations. BigBOSS will therefore benefit the community in three basic ways: (1) the data from the BigBOSS survey proposed herein will be made available publicly to the astronomical community through an archive; (2) fibers will be made available to the community during the regular BigBOSS survey for targets of opportunity or community-proposed science targets; (3) the instrument and observing system will be made available for use by the community through NOAO's proposal process. This brings many of the benefits of the SDSS-I, SDSS-II and SDSS-III more directly to the NOAO community, albeit on a grander scale.

## 1.4 The BigBOSS Team

LBNL will take on the role of leading and managing the project. The structure of our collaboration will be based on the successful models followed by the Dark Energy Survey and the Sloan Digital Sky Survey, and will have clearly defined roles for member institutions and individuals. Our team includes groups with extensive experience and proven track records in the construction of wide-field optics and astronomical instruments, particularly those used for multi-object spectroscopy; the development and use of high-resistivity CCDs in astronomy; the construction and operation of fiber positioners; and in the organization, management, and execution of large collaborative projects. It includes (a growing number of) team members from U.S. universities and a range of talented international collaborators.

As we secure funding and grow the team, we will welcome involvement

from other committed Universities and individuals. To this end, if our proposal is successful, we will work with NOAO with the goal of engaging other members of the U.S. community in the design and execution of this project.

## 1.5 Summary of Cost, Schedule and Funding

Many of the institutions and individuals listed as collaborators on this proposal have already committed significant resources toward the science plan, survey plan, and instrument R&D presented in this document. Continued R&D, constuction, operation and science proposals will be submitted to the Department of Energy, the National Science Foundation, and other U.S. and international funding agencies. NOAO acceptance of this proposal is a prerequesite for these future funding requests.

The schedule presented in §**??** is predicated on succcessful funding, a 2012 start and culminates in first light in 2016.

# 2 Key Science Project

## 2.1 BigBOSS and the Investigation of Dark Energy

We now know that our rather complete understanding of the fundamental interactions of matter is limited to 4% of the energy composition of the universe. Some 23% is composed of dark matter, presumably yet-to-be-discovered elementary particles and the remaining 73% is not matter at all. That 73% – the dark energy –might be due to a uniform and unchanging energy density described by a cosmological constant, albeit with a value miniscule by comparison with what would be expected on dimensional grounds, or alternatively it might be variable in time and space. Either would cause a dramatic change in our picture of the universe as a whole. The third alternative is equally dramatic: a failure of General Relativity.

Among the four primary techniques for studying dark energy identified by the Dark Energy Task Force [Albrecht et al., 2006], measurement of baryon acoustic oscillations was singled out as having the fewest astrophysical uncertainties. BAO uses only the redshift and angular locations of galaxies; the brightness and shapes of the galaxies are irrelevant. What is measured is the two-point correlation function for the distance between galaxies. We know that there is an enhancement at a co-moving distance of about 100 $h^{-1}$ Mpc as a relict of waves that propagated in the electron-photon-baryon plasma until it turned into neutral atoms at a redshift of about 1000.

Measuring the apparent size of this 150-Mpc meter-stick at various redshifts yields measurements of the Hubble parameter $H(z)$ and the angular-diameter distance, $d_A(z)$. From these it is straightforward to constrain tightly the dark energy density $\Omega_{DE}$ and the dark energy equation of state $w(z) = p(z)/\rho(z)$, the ratio of its pressure to its energy density. In particular, this would enable us to rule out a cosmological constant as the source of the accelerating expansion if $w$ is sufficiently different from $-1$.

A first measurement of BAO was achieved in 2005 [Eisenstein et al., 2005], using the spectroscopic survey of SDSS. A sample of about 47,000 luminous red galaxies (LRGs) in the range $0.16 < z < 0.47$ showed a peak in the two-point correlation function with about 3-$\sigma$ significance. Another SSDS observation was made using photometric-$z$ measurements with a much larger sample, 600,000 galaxies. Using photo-$z$'s degrades the measurements, especially that of $H(z)$, and thus requires many more galaxies. The SDSS Data Release 7 result Percival et al. [2010] uses nearly 900k galaxies to obtain measurements of $[d_A^2/H]^{1/3}$ with a precision of about 3%.

The next step in BAO measurement is the BOSS experiment [Schlegel, White, and Eisenstein, 2009], currently in progress. It is part of the SDSS-III program and will collect spectra of 1.5 million LRGs out to $z = 0.7$. In addition, BOSS will use QSOs as sources to detect the distribution of neutral hydrogen along the line of sight. These Ly-$\alpha$ forest measurements will supplement the LRG measurements and extend the range of $z$ that can be studied.

DETF established a nomenclature for dark energy experiments, which has been adopted generally. Stage I dark energy experiments are those that were completed at the time of the DETF report, May 2006. Stage II experiments were those underway at the time of the DETF report. Stage III were near-term, medium cost experiments, while Stage IV were major experiments like JDEM and LSST.

BOSS is a Stage III experiment. We propose here a Stage IV measurement of baryon acoustic oscillations, with an increase in statistics of a factor of 15 over BOSS and an extension as well in the $z$ range covered.

BigBOSS will measure much more than the BAO signal. The three-dimensional galaxy power spectrum, that is the Fourier transform of the two-correlation function, encodes information about the initial source of fluctuations and the expansion history, consituents, and structure of the universe. While the remarkable measurements of the cosmic microwave background by COBE, WMAP, and now Planck, give a two-dimensional snapshot of the universe at the moment of recombination of electrons and nuclei to form atoms, the tomographic measurements of the three-dimensional power spectrum provide a motion picture of the evolution of universe.

DETF provided a single figure of merit, which can be used to compare the capability of various combinations of experiments to probe dark energy. Using the simple parameterization

$$w(a) = w_0 + (1 - a)w_a, \tag{2.1}$$

a figure of merit can be defined as the reciprocal of the area of an error ellipse in the $w_0 - w_a$ plane. A conventional normalization takes for the figure of merit the square root of the determinant the $2 \times 2$ Fisher matrix for $w_0$ and $w_a$. The Figure of Merit Scientific Working Group [[Albrecht et al., 2009]] defined a more complex collection of measures. We shall content ourselves with the DETF figure of merit. FoMSWG also introduced a figure of merit, $1/\sigma(\gamma)^2$, to describe the test of General Relativity.

As we show below, BigBOSS will dramatically increase our understanding of cosmology and of dark energy in particular. At a minimum, the galaxy

measurement of BAO should approximately double the figure of merit available from Stage III experiments. But the potential from additional BigBOSS measurements is very much greater. Redshift space distortions provide additional information on the basic cosmological parameters and could double the figure of merit on top of the increase from BAO. Exactly how far this can take us will depend on the range in $k$ that can be used without encountering problems of non-linearity and galaxy bias. Exploitation of the full power spectrum provides independent information, that could double the figure of merit once more, or even exceed that. Detailed calculations are provided in subsequent sections.

BigBOSS will have an impact on cosmology beyond even the issue of dark energy. By measuring the power spectrum across a range of $z$, it will obtain measurements and limits on the primordial power spectrum that can be compared with the predictions of inflationary theory. Similarly, it will search for non-Gaussianity. BigBOSS will also address a fundamental question of particle physics, the absolute scale of neutrino masses, a quantity extremely hard to measure in nuclear or particle physics experiments.

Altogether, BigBOSS will provide a remarkably broad program in fundamental science for a relatively modest investment.

## 2.2 Overview of BigBOSS BAO Survey

The BigBOSS instrument features 5000 robotically actuated fibers located at the Mayall prime focus, feeding ten three-arm spectrographs. This new instrument will enable a massively parallel wide-field spectroscopic survey using 500 nights over five years at the Mayall telescope, and will also provide the NOAO community with a powerful new capability to carry out large-scale spectroscopic observations. A summary of the BigBOSS instrument is given in Table 2.1; more details can be found in Chapter 5.

The BigBOSS key science project is a wide-area survey designed to map the large-scale structure of the universe over the redshift range $0.2 < z < 1.7$ using emission-line galaxies (ELGs) and luminous red galaxies (LRGs). ELG redshifts are determined through detection of the [OII] doublet at a restframe wavelength of $3727\mathring{A}$, while LRG redshifts are determined using the 4000 $\mathring{A}$ Balmer break feature. LRGs are more highly biased tracers of the dark matter halos and thus better suited for measuring the BAO feature, while the less strongly biased ELGs can be detected to higher redshifts and are better suited for measuring the early growth of structure and redshift space distortions. The use of two different galaxy populations with overlapping redshift distributions provides an intrinsic systematic check.

Table 2.1: BigBOSS instrument overview.

| Parameter | Value | units |
|---|---|---|
| Configuration | Prime Focus | |
| Focal plane diameter | 0.95 | m |
| Linear field of view diameter | 3 | degrees |
| Slew & settle time (3 deg move) | $< 1$ | minute |
| Number of fibers | 5000 | |
| Fiber center-to-center spacing | 12 | mm |
| Fiber actuator throw diameter | 15 | mm |
| Fiber diameter | 120 | $\mu m$ |
| Fiber cable length | 30 | m |
| Wavelength coverage | 340 - 1060 | nm |
| Resolution | 3000 - 4800 | $\lambda/\Delta\lambda$ |
| Re-positioning speed | $< 1$ | minute |
| Re-positioning accuracy | $< 5$ | $\mu m$ |

In addition, quasars (QSOs) at high redshift ($2.2 < z < 3.5$) will be used as backlights to probe large-scale structure detected via the Ly-$\alpha$ absorption spectra, a technique that is currently being pioneered by the BOSS experiment. Each QSO provides many measurements of the matter distribution along its path, so the small fraction of fibers allocated to QSOs still provides a well-sampled map of large scale structure at very early times, constraining models of early dark energy and providing strong constraints on curvature.

The BigBOSS targets are selected from photometric imaging surveys that are currently in progress and are expected to be completed and available in time for BigBOSS, such as the Palomar Transient Factory (PTF), PanSTARRS-I and WISE. As described in detail in Chapter 4, ELG and LRG targets are defined by selection algorithms based on colors and magnitudes. LRG targets are chosen to complement the ongoing 10,000 sq-deg BOSS survey with an additional 4,000 square degrees and with galaxies at higher redshift. The first year of the survey will target a higher density of QSO targets (250 per square degree) covering the redshift range from $z = 0$ to $z = 3.5$. The QSO spectra collected during the first year will be analyzed, and a subset of QSO targets (denoted "Ly-$\alpha$ QSOs") will be selected at a target density of about 50 per square degree with high purity in the redshift range $2.2 < z < 3.5$.

In this proposal we present a baseline survey as a demonstration of the

scientific reach that will be possible with BigBOSS. While it has been worked out with sufficient detail to provide a credible demonstration of the strong scientific potential of BigBOSS, we fully expect it to be improved as planning continues. The full justification of this baseline survey feasibility, informed by exposure time calculations, completeness estimates, and weather simulations, can be found in Chapter 6.

We expect that further optimization of survey parameters will be possible. The optimization of the BigBOSS survey strategy is a complex task, which folds together the projected instrument sensitivity, the available targets that can be selected from photometric survey data, the allocation of fibers to various categories of objects for different exposure times, projections of expected weather, airmass and seeing conditions, and tradeoffs between survey depth, breadth and completeness. Thus, we have not yet settled on a fully optimized survey strategy. In particular, a number of improvements in efficiency can be anticipated. For example, the robotically actuated targeting is intrinsically flexible, and it will even be possible to modify the survey strategy as it progresses, in response to initial results and new information from other experiments.

For the baseline BigBOSS survey we assume 500 nights of observing at the Mayall telescope, distributed uniformly over five years, excluding the monsoon months. The average observing time per night during this period is 9.5 hours, defined to include the period when the sun is at least 18° below the horizon (astronomical twilight). Based on weather and seeing records at the Mayall we project that 62% of this time will be useful for astronomical observations, for a total of 2945 hours.

The basic requirements of a large-scale structure survey are simple to express (although of course we have verified them with full parameter-constraint estimates on the survey baseline and variants upon it). Generally speaking, the most powerful survey is the one that covers the largest area, with the constraint that the co-moving target density be greater than about $1 \times 10^{-4}(h/Mpc)^3$. The lower limit on the density results from our desire to use reconstruction to partially correct for the erasure of structure due to non-linearity, as described by [Eisenstein et al., 2007]. A survey planning tool (originally developed for WFMOS) has been used to optimize the observing plan over the nominal footprint, taking into account airmass, seeing, extinction and sky brightness. The details are described in Chapter 6; the essential result is that BigBOSS can cover 14,000 square degrees in five years with the galaxy and QSO densities described in Table 2.2.

Table 2.2: BigBOSS survey overview.

| Parameter | Value | units |
|---|---|---|
| Survey area | 14,000 | sq. degrees |
| Focal plane area | 7 | sq. degrees |
| Fibers per exposure | 5000 | |
| Fiber density | 714 | per sq. degree |
| Exposures in survey | 10,000 | |
| Mean # of observations | 5 | per area |
| Max. target density | 3570 | per sq. degree |
| Number of nights | 500 | |
| Fraction clear | 0.62 | |
| Useful observing | 2945 | hours |
| Ave. time per pointing | 88 | minutes |
| Overhead per exposure | 1 | minute |
| Ave. exposure per tile | 16.6 | minutes |
| ELG min. [OII] flux | $0.9 \times 10^{-16}$ | ergs/s/cm$^2$ |
| ELG exposures per target | 1 | |
| ELG mean exposure time | 16.6 | minutes |
| ELG fiber allocation | 0.53 | |
| ELG target density | 2335 | per sq. degree |
| ELG fiber completeness | 0.80 | |
| ELG target selection efficiency | 0.65 | |
| ELG redshift measurement efficiency | 0.9 | |
| ELG redshifts | 1092 | per sq. degree |
| Total ELGs | 15,302,200 | |
| LRG exposures per target | 2 | |
| LRG mean exposure time | 33.2 | minutes |
| LRG fiber allocation | 0.16 | |
| LRG target density | 356 | per sq degree |
| LRG fiber completeness | 0.80 | |
| LRG target selection efficiency | 0.90 | |
| LRG redshift measurement efficiency | 0.95 | |
| LRG redshifts | 244 | per sq. degree |
| Total LRGs | 3,409,000 | |
| Total Galaxies | 18,711,200 | |
| QSO exposures per target | 5 | |
| QSO mean exposure time | 83 | minutes |
| Ly-$\alpha$ QSO fiber allocation | 0.07 | |
| Ly-$\alpha$ QSO target density | 63 | per sq. degree |
| Ly-$\alpha$ QSO fiber completeness | 0.80 | |
| Ly-$\alpha$ QSO redshift measurement efficiency | 0.9 | |
| Ly-$\alpha$ QSOs | 45 | per sq. degree |
| Total Ly-$\alpha$ QSOs | 630,000 | |

The BigBOSS survey described in Table 2.2 is composed of a densely packed set of 10,000 spectroscopic observations over 14,000 $\deg^2$, or about 0.7 observations per $\deg^{-2}$. Since the focal plane available in each observation is about 7 $\deg^{-2}$, the observations are highly overlapping. In particular, on average each area of sky is covered by five independent observations ("Mean # of observations").

This configuration, combined with the flexibility of the fiber actuator system, allows BigBOSS some capability to balance exposure times and target number densities. Thus, we can take single exposures for the ELGs, using the overlapping observations to accumulate a large number density. Simultaneously, since we cover the same piece of sky multiple times, we can take double exposures for LRGs and five exposures for QSOs, since those target sets have lower number-densities.

In particular, the ELGs have a mean exposure time of 16.6 minutes, for each object in a single observation. This exposure time allows us to detect a single line from the prominent [OII] doublet in an ELG spectrum at $8\sigma$ for a minimum detectable line flux of $0.9 \times 10^{-16}$ergs/s/cm$^2$. This threshold is conservative and our galaxy counts do not include the slightly fainter ELGs that will be detected at lower significance. LRGs are each observed twice, for a total exposure time of 33.2 minutes, and QSOs are each observed five times, for a total exposure time of 88 minutes. Approximately 2% of all fibers are reserved for calibration targets such as standard stars and sky background. For more details on the BigBOSS exposure time calculator, see Appendix A, which describes the instrumental throughput, the expected seeing (median 1.1 arcsec), and the effects of extinction and sky glow due to the atmosphere at a median airmass of 1.3.

To estimate the total number of objects that will be surveyed we must take into account several sources of inefficiency, which we list in Table 2.2. First, we find that in the proposed configuration and proposed target densities we achieve about 80% fiber completeness (the percentage of all potential targets that actually have their full set of exposures completed). Second, some fraction of the selected objects will either (1) not have bright enough spectral features required to attain a redshift, (2) lie outside our redshift range of interest, or (3) are the incorrect type of object. We detail these effects in Chapter 4 and encapsulate these effects into an overall "target selection efficiency". We expect this factor to be most important for ELGs and QSOs where the efficiency critically depends on photometric selection techniques. Third, some fraction of otherwise properly selected objects will have non-detectable or low quality redshifts from pipeline software ("redshift measurement efficiency"). This effect is largest for the ELGs, where

some fraction of the targets inevitably will have [OII] [OII] doublets that are lost due to bright sky emission lines. However, these last two sources of inefficiency are much less important for LRGs, which we expect to target and detect highly reliably.

Also listed in Table 2.2 is the fraction of available fibers used for each target class ("fiber allocation"). Additionally, we reserve 2% of the fibers for sky and calibration. Note that in this baseline survey, a total of about 80% of the fibers are utilized in each exposure, leaving a substantial number of unused fibers. These fibers — 10 million distributed across the entire 14,000 deg$^2$ survey — will be made available for ancillary science targets as described in more detail in Chapter 3.

This survey will yield the galaxy density distribution in $z$ displayed in Table 2.3 and the QSO density distribution shown in Table 2.4.

Table 2.3: Anticipated galaxy density per unit redshift per square degree and per unit comoving volume.

| $z$ | $dn/dz_{LRG}$ (sq. deg.)$^{-1}$ | $dn/dz_{ELG}$ (sq. deg.)$^{-1}$ | $dn/dV_{LRG}$ ($10^{-4}h^3$Mpc$^{-3}$) | $dn/dV_{ELG}$ ($10^{-4}h^3$Mpc$^{-3}$) |
|---|---|---|---|---|
| 0.15 | 47. | 248. | 2.777 | 14.629 |
| 0.25 | 118. | 148. | 2.777 | 3.497 |
| 0.35 | 210. | 70. | 2.777 | 0.925 |
| 0.45 | 315. | 121. | 2.777 | 1.066 |
| 0.55 | 426. | 430. | 2.777 | 2.799 |
| 0.65 | 443. | 888. | 2.284 | 4.576 |
| 0.75 | 534. | 1360. | 2.284 | 5.821 |
| 0.85 | 541. | 1712. | 1.997 | 6.316 |
| 0.95 | 435. | 1654. | 1.423 | 5.407 |
| 1.05 | 289. | 1285. | 0.856 | 3.804 |
| 1.15 | 105. | 941. | 0.286 | 2.569 |
| 1.25 | 0. | 681. | 0.000 | 1.737 |
| 1.35 | 0. | 583. | 0.000 | 1.406 |
| 1.45 | 0. | 631. | 0.000 | 1.453 |
| 1.55 | 0. | 592. | 0.000 | 1.313 |
| 1.65 | 0. | 424. | 0.000 | 0.911 |

We summarize this BigBOSS overview section by guiding the reader to in-depth presentations of the individual features of our proposed program. The remaining sections of Chapter 2 derive the cosmological constraints

Table 2.4: QSO density per unit redshift and per square degree. BOSS QSO distribution rescaled to BigBOSS target density.

| | | | | | | |
|---|---|---|---|---|---|---|
| $z_{med}$ | 1.85 | 1.95 | 2.05 | 2.15 | 2.25 | 2.35 |
| $dn/dz_{QSO}$ | 5.51 | 7.54 | 12.0 | 39.6 | 74.1 | 68.7 |
| $z_{med}$ | 2.45 | 2.55 | 2.65 | 2.75 | 2.85 | 2.95 |
| $dn/dz_{QSO}$ | 54.7 | 43.7 | 34.1 | 25.0 | 22.3 | 20.0 |
| $z_{med}$ | 3.05 | 3.15 | 3.25 | 3.35 | 3.45 | 3.55 |
| $dn/dz_{QSO}$ | 19.1 | 16.2 | 13.7 | 8.52 | 4.55 | 3.62 |

that BigBOSS can reasonably be expected to deliver, based on the instrument summary shown in Table 2.1 and survey yields anticipated in Table 2.2 above. In Chapter 3, we present some aspects of the science that the BigBOSS capabilities will deliver to the community. Target selection is a central requirement of BigBOSS and we describe our plans for developing target lists in Chapter 4. The BigBOSS instrument, including the telescope corrector, the focal plane, the spectrograph, the sensors, and the data system are described in Chapter 5. In Chapter 6 we explain our survey operations plan. Data management is described in Chapter 7, including deliverable data products to the community. Project management for construction and for operations are detailed in Chapter 8. Costs are presented in Chapter 9. An Appendix describes the Exposure Time Calculator (ETC) on which our target exposure times are based.

## 2.3 Primary Cosmological Constraints from BigBOSS

### 2.3.1 Galaxy BAO measurements

Initial fluctuations in the matter density provided sources for "acoustic" waves that propagated in the photon-electron-baryon plasma of the early universe. See, for example, Eisenstein & Hu [1998]. Before the wave terminates at the time of recombination, it travels a comoving distance $s$, which can be computed quite precisely from the cosmological parameters and which is approximately 100 $h^{-1}$ Mpc. An excess of matter is left both at the source of the wave and at the surface of the sphere of radius $s$. The sources are randomly but the pattern of separation at a distance $s$ is visible in the two-point correlation function $\xi(r)$.

The distance $s$ provides a meter stick. Viewed transversely, the 150 Mpc meter stick subtends an angle $\theta$ such that

$$s = (1+z)d_A(z)\theta \tag{2.2}$$

where $d_A(z)$ is the angular-diameter distance to an object at redshift $z$. Viewed along the line of sight, a peak in the two-point correlation function will be present when $\Delta z$ is such that

$$(1+z)[d_A(z+\Delta z) - d_A(z)] \approx \frac{\Delta z}{H(z)} \approx s \tag{2.3}$$

The observation of the peak in the two-point correlation function thus provides a means of measuring both $H(z)$ and $d_A(z)$.

In practice, it is, of course, galaxies, not dark matter, that are observed and one supposes that the fluctuations in the galaxy density and the fluctuations in the matter density are proportional:

$$\delta_g(x) = b\delta_m(x), \tag{2.4}$$

where of course this relation can hold only when we average over sufficiently large domains. The bias $b$ will depend on the type of galaxy observed and on the redshift $z$.

Predictions for the effectiveness of BAO measurements in determining cosmological parameters use the Fisher matrix methodology. See, for example Seo & Eisenstein [2007]. The effect of finite statistics on the measured power spectrum – shot-noise – are incorporated via the prescription of Feldman, Kaiser & Peacock [1994], which introduces a factor

$$\left[\frac{\overline{n}P(k)}{1+\overline{n}P(k)}\right]^2. \tag{2.5}$$

We have used the code of Seo and Eisenstein [Seo & Eisenstein, 2007] in our calculations. The integral over $k$-space must not include the non-linear regime and this is taken into account by including the suppression factor [Eisenstein, Seo & White, 2007]

$$\exp\left(-\frac{1}{2}k_\perp^2\Sigma_\perp^2 - \frac{1}{2}k_\parallel^2\Sigma_\parallel^2\right). \tag{2.6}$$

The parameters $\Sigma_\perp$ and $\Sigma_\parallel$ are given by

$$\Sigma_\perp = \Sigma_0 D(z), \tag{2.7}$$
$$\Sigma_\parallel = \Sigma_\perp(1+f), \tag{2.8}$$

where $D(z)$ is the growth function, normalized to $(1+z)^{-1}$ for large $z$ and where $f = d\ln D/d\ln a$.

The scale for the suppression of the non-linear regime is set by

$$\Sigma_0 = 12.4h^{-1}\,\mathrm{Mpc} \times (\sigma_8/0.9)\ . \tag{2.9}$$

The non-linear effects can by partially undone by the process of "reconstruction," [Eisenstein et al., 2007]. We have assumed a maximum reconstruction factor of 0.5 by reducing $\Sigma_\perp$ and $\Sigma_\parallel$ according to

$$\Sigma_0 \to \Sigma_0\left[1 - 0.5\left(\frac{\overline{n}P(k)}{1+\overline{n}P(k)}\right)^2\right]. \tag{2.10}$$

Our calculations are based on the expected numbers of galaxies BigBOSS will obtain as described in Sec.2.2 and Sec.4. These numbers are displayed in Table 2.3.

For the galaxy distributions in Table 2.3 we have taken the bias of the LRGs to be 1.7 and that of the ELGs to be 0.76 at $z = 0$. We have also assumed that the growth of structure in the galaxy-galaxy power spectrum is exactly canceled by the $z$ dependence of the bias, i.e.

$$P_g(z,k) = b_g(0)^2 P_g(0,k). \tag{2.11}$$

For the power spectrum, we use the parameterization given in the code of Seo & Eisenstein [2007] We assume a negligible redshift error for BigBOSS, and rms 0.001 $(1+z)$ error for JDEM.

We follow FoMSWG in taking the values of the parameters of the fiducial cosmology to be the ΛCDM model of WMAP5 displayed in Table 2.5.

Table 2.5: Values of the cosmological used in calculations. Here $k_\star = 0.05$ Mpc$^{-1}$. Using $\omega_M + \omega_B + \omega_{\rm rad} + \omega_k = h^2$ , the derived value of $h$ is 0.719, which implies a Hubble constant of $H_0 = 71.9$ kms$^{-1}$Mpc$^{-1}$ . Our choices also imply $\sigma_8 = 0.791$.

| | |
|---|---|
| $n_S$ | 0.963 |
| $\omega_M$ | 0.13263 |
| $\omega_B$ | 0.02273 |
| $\omega_k$ | 0 |
| $\omega_{\rm DE}$ | 0.3843 |
| $\ln \Delta^2_\zeta(k_\star) \equiv \ln A_s$ | $-19.9628$ |

Table 2.6: Predicted fractional uncertainties for BigBOSS in $D$ and $H$ in bins of $z$ for 14k square degrees with the distribution given in Table 2.3.

| $z$ | $\sigma(d_A/s)/(d_A/s)$ | $\sigma(Hs)/Hs$ |
|---|---|---|
| 0.05 | 0.0625 | 0.1183 |
| 0.15 | 0.0293 | 0.0519 |
| 0.25 | 0.0213 | 0.0367 |
| 0.35 | 0.0168 | 0.0290 |
| 0.45 | 0.0134 | 0.0231 |
| 0.55 | 0.0108 | 0.0185 |
| 0.65 | 0.0094 | 0.0160 |
| 0.75 | 0.0082 | 0.0140 |
| 0.85 | 0.0076 | 0.0128 |
| 0.95 | 0.0077 | 0.0127 |
| 1.05 | 0.0087 | 0.0136 |
| 1.15 | 0.0117 | 0.0170 |
| 1.25 | 0.0182 | 0.0245 |
| 1.35 | 0.0205 | 0.0272 |
| 1.45 | 0.0194 | 0.0257 |
| 1.55 | 0.0204 | 0.0269 |
| 1.65 | 0.0265 | 0.0340 |
| $< 0.5$ | 0.0089 | 0.0153 |
| $0.5 - 1.0$ | 0.0038 | 0.0064 |
| $> 1.0$ | 0.0056 | 0.0080 |

Table 2.7: Figures of merit achieved with and without BigBOSS (14k square degrees). The Stage III BAO includes BOSS, HETDEX, and WiggleZ.

| + | Stage III BAO | BigBOSS galaxy BAO + StageIII BAO |
|---|---|---|
| Planck | 42 | 92 |
| Planck + Stage III weak lensing + Stage III supernovae | 92 | 173 |

We work with bins of $\Delta z = 0.1$ and in each bin we determine the expected fractional uncertainty in $d_A(z)$ and $H(z)$. The results are shown in Table 2.6.

From the uncertainties in $d_A$ and $H$ we can derive uncertainties in $w_0$ and $w_a$ and thus the DETF figure of merit. The results are shown in Table 2.7 and Fig. 2.1.

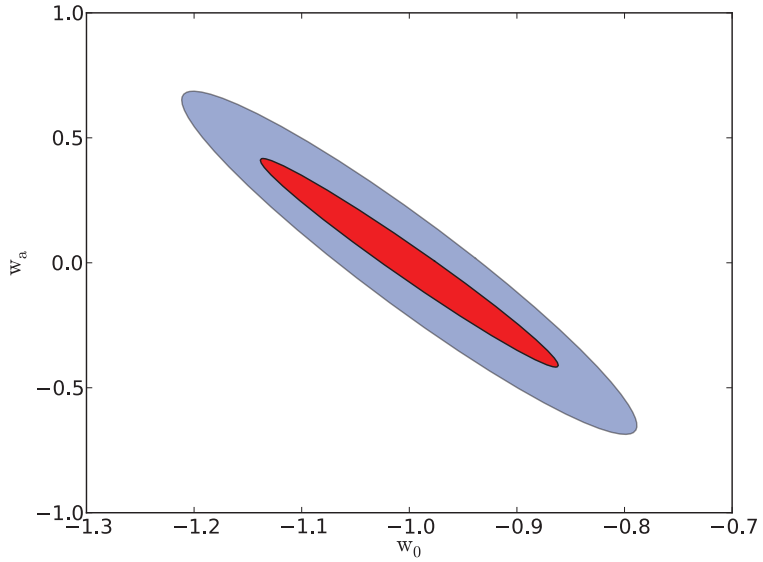


Figure 2.1: Contours at $\Delta\chi^2 = 1$ in the $w_0$-$w_a$ plane. Inner (red) ellipse uses BigBOSS BAO together with Planck. The outer ellipse uses only Planck, BOSS, WiggleZ, and HETDEX.

### 2.3.2 Broad-band power spectrum from galaxies and QSOs

Considerable cosmological information resides in the broadband power spectrum apart from the acoustic oscillation features. The low-$k$ slope measures the primordial perturbations power law index, carrying information on inflation; the turnover depends on the redshift of matter-radiation equality, constraining the matter density and extra relativistic degrees of freedom such as additional neutrino species; the higher-$k$ tail provides leverage on the primordial power index tilt and running, neutrino masses, and dark matter properties.

The evolution of the amplitude with redshift is driven by the growth factor $D(z)$, depending on dark energy properties, the matter density, and spatial curvature, as well as the gravitational framework and non-Gaussianities. Elements of galaxy formation such as bias also enter: this adds a source of uncertainty but also a rich opportunity to probe structure formation and astrophysics.

With a finite volume, the modes labeled by $\mathbf{k}$ are discrete and the fluctuations in a single mode are a large as the power $P$ itself. To this must be added the shot-noise, $1/n$, which is a consequence of making the discrete measurements of galaxies, where $n$ is the density of observed galaxies. A good measurement can be obtained only by averaging over many modes in a large volume $V$:

$$\sigma_{P(k)} = \frac{1}{\sqrt{N}} P(k)(1 + \frac{1}{nP}); \qquad N = V \frac{d^3k}{2(2\pi)^3}, \tag{2.12}$$

where the extra $(1/2)$ is the result of $\delta(x)$ being real. For an interval in redshift space $\Delta z$ and sky coverage $\Omega$, a shell in $k$-space of thickness $\Delta k$ will have a statistical uncertainty for the power given by

$$\sigma_{P(k)} = [\Omega D_{co}(z)^2 \Delta z / H(z)]^{-1/2} [k^2 \Delta k / (4\pi^2)]^{-1/2} P(k)(1 + \frac{1}{nP}) \tag{2.13}$$

For example, at $z = 1$ and $k = h\mathrm{Mpc}^{-1}$, a 14,000 square degree survey has a statistical precision, ignoring the the shot-noise factor, of 0.3% for intervals of $\Delta z = 0.4$ and $\Delta k = 0.01\, h\, \mathrm{Mpc}^{-1}$.

The power spectrum grows as a function of time as gravity amplifies the mass perturbations. In the linear regime, the fluctuations $\delta(x)$ are proportional to the growth function $D(z)$.

Setting aside redshift space distortion discussed below, the galaxy-galaxy power spectrum at $z$ is related to the mass-mass power spectrum today by

$$P_{gg}(k, z) = b(z)^2 [D(z)/D(z = 0)]^2 \sigma_8^2 P_{mm}(k), \tag{2.14}$$

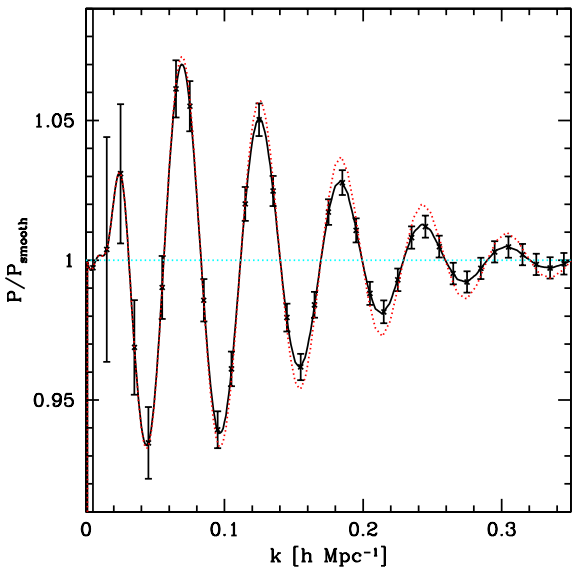


Figure 2.2: Simulated data showing the power spectrum for a bin $0.5 < z < 0.9$, with $\Delta k = 0.01h$ Mpc$^{-1}$. Solid black line is non-linearly degraded post-reconstruction, red dotted is linear.

where we have chosen to display explicitly the normalization of the matter-matter power spectrum as $\sigma_8^2$.

Using Eq.(2.13) Fig. 2.2 shows what power spectrum measurements from the BigBOSS survey described in Sec.2.2 will look like. The expected uncertainties in the power spectrum as a function of $k$ for various bands in $z$ are shown in Fig. 2.3

Constraints on cosmological parameters from including the broadband power are much more incisive than those restricted to just the acoustic features. Modeling issues for nonlinearities are common to both and can be treated by marginalization over nuisance parameters [Schulz & White, 2006; Padmanabhan & White, 2009; Cresswell & Percival, 2009]. Scale-dependent galaxy bias can similarly be included via the halo model or a low order polynomial or Padé approximant in $k$ [Schulz & White, 2006; Padmanabhan & White, 2009; Cresswell & Percival, 2009; White, 2005]. Constraints on the amplitude of bias come from imaging data, higher order correlation functions, or cross-correlation with weak lensing data; generally biases are most covariant with the mass amplitude $\sigma_8$ rather than any of the dark energy cosmology parameters.

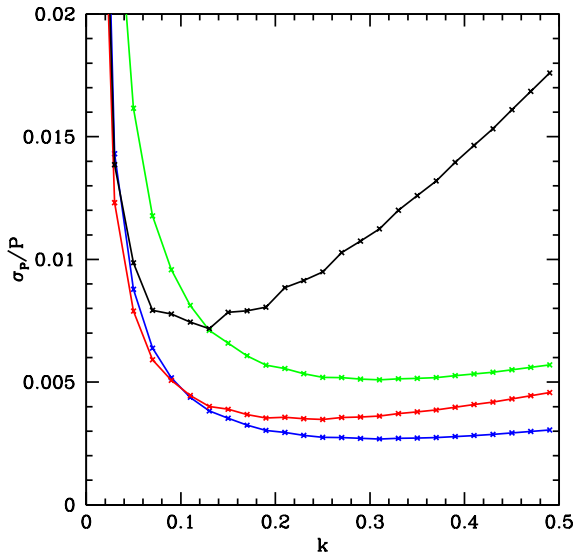


Figure 2.3: Expected uncertainties in the broadband power for bins of 0.2 $h^1$ Mpc delta k = 0.02 (indicated by points). $z < 0.5$ - green, $0.5 < z < 0.9$ - blue, $0.9 < z < 1.3$ - red, $z > 1.3$ - black.

Global fits over the cosmology parameters including neutrino masses and time varying dark energy were carried out by Stril, Cahn, & Linder [2010] for realizations similar to the BigBOSS survey design, but without including QSOs. Because one neutrino mass-squared splitting is about $25 \times 10^{-4}$ $\mathrm{eV}^2$, we know at least one neutrino has a mass of at least 0.05 eV or so. If neutrinos have inverted hierarchy, the minimum sum of the neutrino masses is twice this (since the other splitting is considerably smaller). For the 14k square degree survey, and combining information from BigBOSS's QSO+galaxies and forecasts for the Planck satellite, the obtained $1-\sigma$ limits on the sum of neutrino masses are $\sigma(\Sigma(m_\nu)) = 0.024$eV (integrating in k-space up to $k_{\rm max}(\mathrm{galaxies}) = 0.1h/\mathrm{Mpc}$ and $k_{\rm max}(\mathrm{Lyman}-\alpha) = 5h/\mathrm{Mpc}$). Thus BigBOSS will start approaching the region which is close to the guaranteed detection and could have a significant impact on our understanding of the masses and hierarchy of the neutrinos. Note that we have used a conservative upper limit of integration of information for the galaxies ($0.1h/\mathrm{Mpc}$) and that increasing this limit quickly brings the experiment into the regime of guaranteed detection. Therefore, with improved understanding of galaxy bias, its scale dependence and stochasticity, the BigBOSS can become a very powerful probe of neutrino physics.

Further optimization in the sculpting of the galaxy number density distribution, use of two galaxy populations of different biases [McDonald & Seljak, 2009], and inclusion of the Ly-$\alpha$ data can further improve the science reach and reduce the effect of systematic uncertainties. With Ly-$\alpha$ data we will achieve strong constraints on the primordial perturbation sector as well, with the combination of BigBOSS and CMB data imposing tight bounds on the scalar tilt and running, narrowing possible inflation models for the origin of cosmic structure.

As a growth probe, the broadband power spectrum contains a rich array of information and acts as the main cross-check on weak gravitational lensing conclusions. Many of the systematics in the two methods are independent, so comparing the two results delivers a valuable check on their accuracy. These two methods are in the linear and quasilinear density regimes, avoiding many of the complications due to nonlinear gravitational evolution and hydrodynamics. Thus the broad band power spectrum not only complements the use of the acoustic features as a geometric probe, but complements other growth probes.

### 2.3.3 Redshift space distortions

Under the standard assumption of isotropy, $\xi$ is a function only of the magnitude of $\mathbf{r}$, not its direction and correspondingly the power spectrum depends solely on the magnitude of $\mathbf{k}$. In fact, the redshift is not directly a function of the distance to the galaxy, but rather its velocity and thus depends on the peculiar velocity as well as the Hubble flow. The peculiar velocity has a random component, but in addition a component that is the response to the gravitational field of the non-uniform distribution $\delta$ itself. The magnitude of this portion of the peculiar velocity must be proportion to the rate of growth of the perturbation, $\dot{D}$, and in particular to

$$f = d\ln D/d\ln a. \tag{2.15}$$

As first shown by Kaiser [1987], a plane-wave disturbance with wave-vector $\mathbf{k}$ will appear enhanced by a factor $1 + (f/b)\mu^2$ where $\mu = \cos\theta$ and $\theta$ is the angle between $\mathbf{k}$ and the line-of-sight.

It is possible to show that, to a very good approximation, $f$ can be written as

$$f = \Omega_m(a)^\gamma, \tag{2.16}$$

where $\Omega_m(a)$ is the fraction of the energy density at scale factor $a$ that is due to matter and $\gamma$ is a constant, the gravitational growth index. If General Relativity holds, $\gamma$ is very near 6/11, with only a slight dependence on the equation of state of dark energy. In alternatives to General Relativity, $\gamma$ can differ from this value by as much as $0.1 - 0.2$.

The power spectrum depends on two factors of $\delta$ and thus the power spectrum as observed from redshift measurements is modified from its isotropic form to

$$P_{RSD}(\mathbf{k}) = (1 + \beta\mu^2)^2 P(k), \tag{2.17}$$

where $\beta = f/b$.

Observations to date have already demonstrated the feasibility of tracing the amplitude of the distortion field in the two point clustering statistics and have already led to preliminary estimates of $f(a)$ at various redshifts, although not yet at a useful level of precision [Guzzo et al., 2008]. For example, using Eq. (2.16) current constraints on the growth index $\gamma$ have an accuracy of about 40%, which is still far from the precision required to reject at least the two modified gravity models most discussed in literature i.e. DGP and $f(R)$ models. Nonetheless, it has been shown that large (nearly all-sky) and deep ($0 < z < 2$) galaxy redshift surveys will constrain the amplitude of the distortion field to the precision needed to discriminate

distinctive departures from general relativity on cosmological length scales [White et al., 2009; McDonald & Seljak, 2009; Guzzo et al., 2008].

BigBOSS, covering an order of magnitude larger volume than present-day surveys, will bring uncertainties on $f(a)$ down to few percent in the whole redshift window $0.5 < z < 1.6$. This accuracy will result in unprecedented constraints on both cosmological and gravitational parameters. See Fig. 2.4.

Two major sources of systematics might bias redshift distortions estimators and prevent BigBOSS estimates from being effectively "data-limited" i.e. from exploiting the whole information contained in the data. Orbital motions of galaxies within virialized structures scatter galaxy redshifts along the line-of-sight creating 'Fingers of God' and thereby erasing spatial information on small scales. This non-linear, small-velocity effect can be phenomenologically modeled and disentangled from the aspect of interest, i.e. linear bulk motions. A common procedure assumes that non-linear random velocities can be treated as an independent nuisance parameter, which can be marginalized. A more complete modeling of the distortion pattern seems required if we are to reach the forecasted level of precision (see, for example, Scoccimarro [2004]). Also galaxy biasing, especially if it manifests with non-linear and/or scale-dependent features, must be efficiently subtracted in order not to contaminate cosmological interpretation. The possibilities currently explored range from combining different probes to define bias-independent estimators [Song & Percival, 2009; Zhang et al., 2007], to exploiting independent biasing estimates extracted from higher than two-point clustering statistics [Verde et al., 2002; Marinoni et al., 2005].

### 2.3.4 Ly-$\alpha$ forest BAO and dark energy constraints

The Ly-$\alpha$ forest is a forest of absorption lines in the spectra of distant quasars blue-ward of the Ly-$\alpha$ emission line (at 1215.6Å rest-frame wavelength). The absorption is caused by the neutral hydrogen along the line of sight to the quasar in question. Since the neutral hydrogen traces cosmological density fields, Ly-$\alpha$ forest has been proposed as a method to infer the statistical properties of the Universe at the high redshift and thus constrain cosmology.

Since the atmosphere becomes increasingly opaque at wavelengths blue-ward of 3500Å, the ground observations of the Ly-$\alpha$ forest are limited to the quasars at redshifts greater than $z \sim 1.8$. In principle there is no upper limit to the redshift of the quasars used, but the decreasing number and luminosity of quasars set the natural upper limit to the redshifts around $z \sim 3.5$. Moreover, in each quasar, the readily available forest lies between

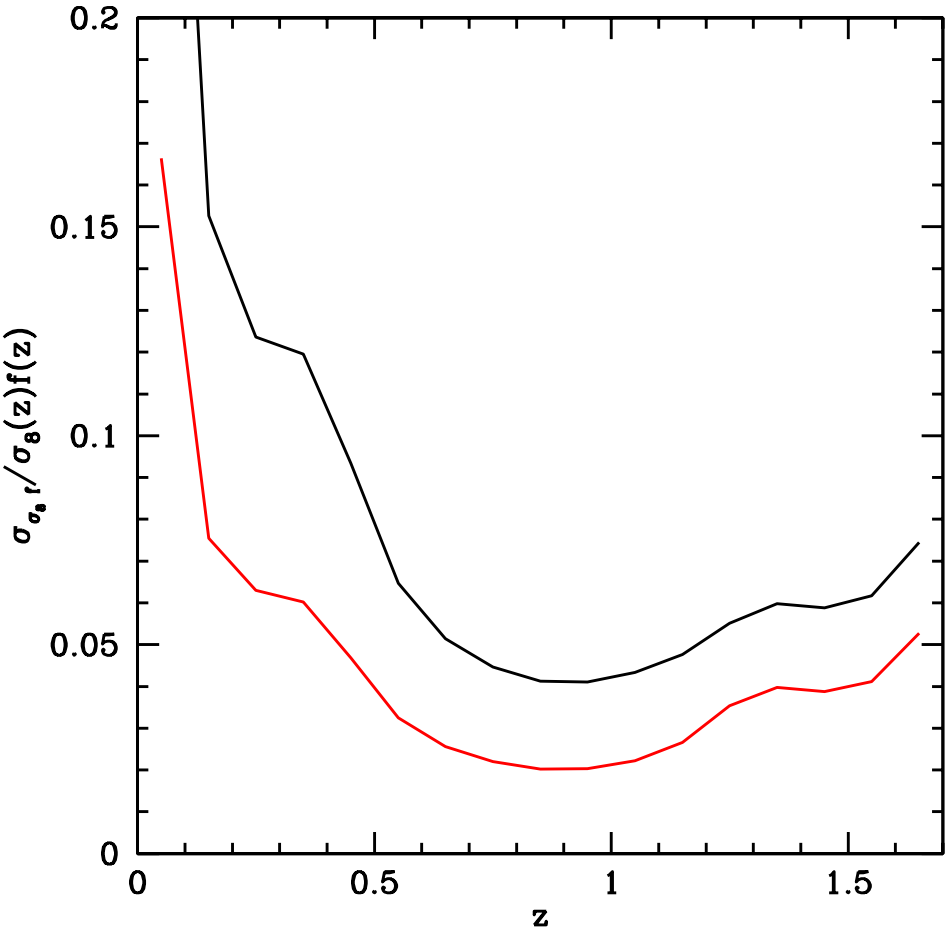


Figure 2.4: Constraints on $\sim \sigma_8(z)f(z)$ (amplitude of the power times growth rate), for $k_{\rm max} = 0.1$ or 0.2 $h$Mpc$^{-1}$ (upper and lower lines, respectively).

the rest frame Ly-$\alpha$ and Ly-$\beta$ emissions, where absorption is dominated by the Ly-$\alpha$ absorption. Therefore, a sample of quasars can be used to measure the density fields in the redshift range between $z \sim 1.9$ and $z \sim 3.4$. Ly-$\alpha$ is a unique probe of cosmology at those redshifts, since obtaining a dense enough sample of galaxies at those redshifts is observationally prohibitively expensive, while there is not enough neutral hydrogen for the proposed future experiments to measure the cosmic fields through the neutral-hydrogen 21-cm line.

To calculate the amount of neutral hydrogen, photoionization equilibrium is usually assumed. In this approximation, the number of recombinations of protons and electrons is balanced by the number of ionizations due to surrounding photo-ionization field. Since recombination is a two-body process and since ionization fraction is nearly unity, one would naively assume that the number density of neutral hydrogen atoms is proportional to the square of the density of ionized hydrogen. In practice, the exponent is closer to 1.8 because the gas in the denser environment is also hotter and the recombination coefficient has a non-negligible temperature dependence. The flux measured in the forest is therefore approximately given by

$$f(\lambda) = C(\lambda)e^{-\tau(z)} = C(\lambda)e^{A(1+\delta)^{\beta}}, \tag{2.18}$$

where $f$ is the flux measured by the spectrograph, $C$ is the unabsorbed quasar continuum, $A \sim 0.1$ and $\beta \sim 1.8$ are constants and we will use $\tau$ to denote optical depth throughout. This approach is usually referred to as the fluctuating Gunn-Peterson (FGPA) approximation.

The idea of measuring BAO through Ly-$\alpha$ forest was first proposed by Martin White in 2003. McDonald and Eisenstein have performed calculations that indicate that the BOSS experiment should be able to see the BAO through Ly-$\alpha$ forest and measure the angular diameter distance to $z = 2.5$ with an accuracy of 1.5%. In Slosar et al, cosmological simulations have been populated with neutral hydrogen gas according to FGPA approximation and the ability of BOSS to measure BAO through Ly-$\alpha$ forest has been confirmed. This work has been further extended with even larger simulations in White et al. [2009].

We must stress that BAO has never been seen before in the Ly-$\alpha$ forest and that the method still remains speculative in that regard. However, there are several reasons to be optimistic about the ability to have potential systematic effects under control. The most important tool that we have is the knowledge that the only signal that corresponds to real three-dimensional fluctuations in the optical depth to the Ly-$\alpha$ transition will

in fact correlate across different quasars. Other effects, such as continuum fluctuations, will be a source of noise, but these will average out in the cross-correlated pairs. Moreover, any systematic that could correlate across quasars in the rest-frame will correlate equally for nearby as well widely separated quasars. Therefore, any correlations between fluxes in nearby quasars above that present in widely separated quasars is unlikely to come from sources other than the real fluctuations in the optical depth. An important caveat is that fluctuations in the optical depth can also be associated with non-gravitational processes. For example, if the photoionization field fluctuates due to large-scale fluctuations in quasar number density, the optical depth field would follow. Such processes can introduce large-scale fluctuations. However, these effects are unlikely to produce a sharp feature that could be mistaken for the BAO peak. The smooth contributions to the two-point function can be modelled and marginalized over using techniques that are very similar to those employed by galaxy surveys.

### 2.3.5 Combined Constraints on Dark Energy

The Fisher matrix that represents the information about the cosmological parameters is obtained by adding together the Fisher matrices for all the $z$-bins and for all techniques considered. The results are shown in Table 2.8. BAO results from galaxies (gB) and QSOs (lB) are displayed separately. Redshift space distortions (R) contribute because $f = d\ln D/d\ln a$ depends on $H(a)$ and thus on the cosmological parameters of interest. The value of the redshift space distortion measurements depends on the maximum $k$ that can be used without non-linearity killing the measurement. The results for $\mathrm{R}_{.1,.2,.3}$ use $k < 0.1, 0.2, 0.3\,h\,\mathrm{Mpc}^{-1}$. The results indicated by $\mathrm{A}_{0.1,0.2,0.3}$ use the amplitude of the full broadband spectrum, not just the angular dependence. Table 2.7 shows that using BAO from galaxies alone, BigBOSS will approximately double the DETF FoM. Table 2.8 shows that the potential for BigBOSS is very much greater when less tested techniques like BAO from QSOs, the redshift space distortions, and the broadband spectrum are used.

Table 2.8: Anticipated BigBOSS figures of merit when various combinations of measures are used to determine the parameters$w_0$ and $w_a$ of the dark energy equation of state. [P]: Planck; [gB]: galaxy BAO; lB: Ly-$\alpha$ BAO; $[R_{k_{\rm max}}]$: redshift space distortion, for $k < k_{\rm max}$; $[A_{k_{\rm max}}]$: all galaxy information for $k < k_{\rm max}$. In all cases we use "propagator limited" galaxy information, i.e., signal power is suppressed by Seo & Eisenstein-like Gaussian damping factors (after reconstruction). The coverage is 14k square degrees with $dn/dz$ as predicted for BigBOSS in Table 2.3.

| Input | DETF Figure of Merit |
|---|---|
| P+gB | 92 |
| P+gB+lB | 114 |
| P+gB+$R_{.1}$ | 218 |
| P+gB+$R_{.2}$ | 309 |
| P+gB+$R_{.3}$ | 359 |
| P+gB+$R_{.1}$+lB | 250 |
| P+gB+$R_{.2}$+lB | 342 |
| P+gB+$R_{.3}$+lB | 391 |
| P+$A_{.1}$ | 234 |
| P+$A_{.2}$ | 555 |
| P+$A_{.3}$ | 759 |
| P+$A_{.1}$+lB | 258 |
| P+$A_{.2}$+lB | 581 |
| P+$A_{.3}$+lB | 788 |

## 2.4 Other Cosmological Constraints from BigBOSS Measurements

### 2.4.1 Galaxy-lensing cross-correlation

BigBOSS is not an imaging survey and so cannot be defined as a weak lensing survey in traditional sense. Weak lensing can be done using magnification bias of the spectroscopic galaxies [Hildebrandt, van Waerbeke & Erben, 2009], but this is not expected to be competitive against imaging surveys that are expected to be available at the time BigBOSS is operating. Magnification bias will however provide a complementary approach with complementary systematics, which may prove to be useful.

A more powerful approach is to combine BigBOSS with an imaging survey. One can argue that combining a redshift galaxy survey with a weak lensing survey provides the ultimate survey of large scale structure in the universe. In the following we will assume we have a deep photometric survey overlapping with BigBOSS area. LSST is the prime example.

As is well known a galaxy survey cannot directly measure the growth of structure in the universe (if the redshift space distortions are not included in the analysis; we will ignore these for now and revisit it later). This is because galaxies are a biased tracer of the dark matter and this bias is not known *a priori*. A weak lensing survey is not subject to this bias uncertainty since it measures total matter directly. Hence in a weak lensing survey we can measure the growth of structure. However, weak lensing surveys provide us with a two-dimensional information, since the signal is projected along the line of sight. This can be improved by weak lensing tomography [Hu, 1999], but even in that case a redshift survey will always give much more information than a weak lensing survey, since it measures the information effectively in three dimensions (apart from complications due to the redshift space distortions). Thus both a weak lensing survey and a galaxy redshift survey have some advantages and some disadvantages.

A weak-lensing survey combined with BigBOSS will allow the determination of bias and from that reconstruction of three-dimensional dark matter field. As mentioned in other sections, BigBOSS should also be able to measure redshift space distortions and thus determine the bias with another method. However, the two methods of measuring the bias, weak lensing and redshift space distortions, are not equivalent, since they measure different quantities: while weak lensing measures the total mass distribution, redshift space distortions measure the velocity density correlations, which can be reduced to a logarithmic growth of the structure $f = d\ln D/d\ln a$.

We can combine these methods, galaxy clustering, weak lensing and redshift space distortions, to derive a quantity that does not depend on either the galaxy bias nor on amplitude of clustering. Such a quantity, denoted $E_g$, is extremely sensitive to the modifications in gravity sector [Zhang et al., 2007]. It has already been used to eliminate a specific alternative to dark matter called TeVeS [Reyes et al., 2010]. With BigBOSS combined with LSST one should be able to reduce the errors by an order of magnitude and this will provide a very detailed probe of gravity on cosmological scales.

### 2.4.2 Constraints on inflation models

The inflationary paradigm is to date the best contender for the origin of the fluctuations of primordial density, which seeded the large scale structure we observe today. In its simplest formulation it predicts perturbations in the initial distribution that are very nearly scale independent and gaussian-distributed about the mean.

Arguments of symmetry together with predictions for nearly scale invariance fluctuations lead us to parametrize the primordial spectrum as a function of $k$ through the spectral index or tilt

$$n_{\rm S}(k) = \frac{d\ln P}{d\ln k}. \tag{2.19}$$

If we take $k_0$ as a reference scale, the primordial power spectrum can be expanded as

$$P(k) = P(k_0)(k/k_0)^{n_{\rm S}(k_0)+\frac{1}{2}\alpha\ln(k/k_0)} \tag{2.20}$$

where $\alpha = dn_{\rm S}/d\ln k$ at $k_0$. If there is no "running" of the spectral index, the primordial power spectrum is a pure power law.

The Harrison-Zel'dovich primoridal spectrum has $n_{\rm S} = 1$, while inflation predicts slight deviations from unity. Ruling out $n_{\rm S} = 1$ at a significant level of confidence would strengthen the case for inflation. The WMAP7 result is $0.963 \pm 0.014$ [Komatsu et al., 2010]. The current limits on running of the spectral index, obtained by the WMAP team, are $-0.061 < dn_{\rm S}/d\ln k < 0.017$ (95% CL) .

The Ly-$\alpha$ forest, because it is in the regime of linearity for a wide range of $k$, is an excellent complementary probe of $n_s$ and $\alpha$.

In Table. 2.9 we present forecasts on inflationary observables obtained with Fisher-matrix formalism applied to the power spectrum obtained from the power spectrum using BigBOSS quasars plus galaxies, and combined with Planck priors and existing higher resolution QSO spectra. We consider a 14k square degrees survey, targeting quasars between $2 < z < 5$

Table 2.9: Constraints on inflationary observables obtained for a 14k square degree survey using BigBOSS QSOs galaxies in combination with Planck satellite priors. (Integration in $k$-space up to $k_{\rm max}({\rm galaxies}) = 0.1h/{\rm Mpc}$ and $k_{\rm max}({\rm Ly}-\alpha) = 5h/{\rm Mpc}$).

| | $n_{\rm S}$ | $\alpha_s$ | $T/S$ |
|---|---|---|---|
| fiducial | 0.963 | 0.00 | 0.00 |
| $\sigma$-BigBOSS | 0.0019 | 0.00064 | 0.080 |
| $\sigma$-CMBPol | 0.0016 | 0.0036 | $\sim 10^{-4}$ |

with observed wavelength range 3700 Å$< \lambda <$ 4500 Å. We marginalize over intergalactic medium nuisance parameters, the mean absorption level $\langle F \rangle$, and $T_0$ and $\gamma$ in the temperature-density relation. The maximum k considered is $k_{\rm max} = 0.01h/{\rm Mpc}$ for galaxies, and $k_{\rm max} = 5h/{\rm Mpc}$ for Ly-$\alpha$ . For both CMB surveys, Planck and CMBPol we have taken residual foregrounds after map-cleaning $\sim 10\%$. In Fig.2.5 we present projected constraints on the $n_{\rm S} - \alpha$ plane, Fisher matrix ellipse contours for the same experimental realization.

These are impressive results. In standard slow-rolling inflationary models, the running of the spectral index is of the order $O((1-n_s)^2) \sim 1 \times 10^{-3}$ if $n_s \sim 0.96$. This means that BigBOSS will start to approach the region of guaranteed detection in minimal inflationary models. Detection of running of spectral index would be a confirmation of inflationary *prediction* and thus considerably strengthen the observational evidence for inflation.

*Testing Non-Gaussianity*

Power spectrum, or a two-point correlation function, has traditionally been the statistic of choice in cosmological observations. This is because many of the theories predict that the initial seeds are nearly gaussian distributed. Thus in the linear regime, expected to be valid on the largest scales in LSS and on almost all scales in CMB, one expects the fluctuations to be nearly gaussian and all the information is contained in their two-point function statistic. In the non-linear regime non-gaussianity develops and higher order correlations become non-vanishing, created by the nonlinear gravitational evolution.

Primordial non-gaussianity, determined by the higher order correlations present in the linear regime, is complementary to the information contained in the power spectrum, since it probes aspects of physics during inflation that cannot be probed otherwise. For example, while a single field slow-roll infla-

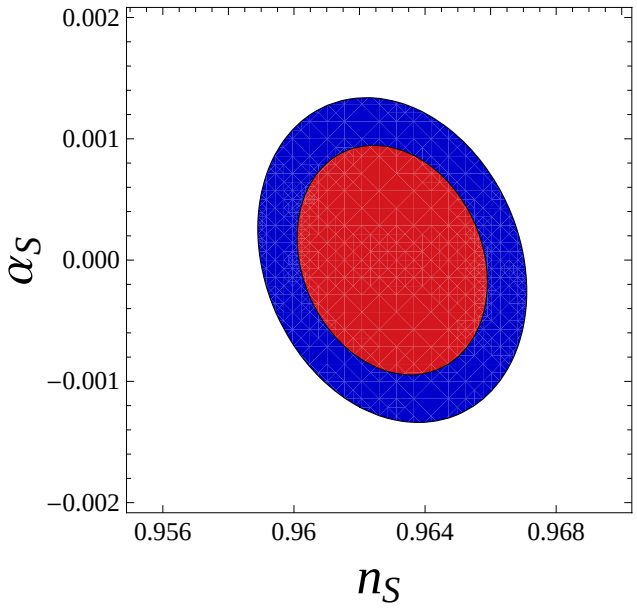


Figure 2.5: $1-\sigma$ and $2-\sigma$ constraints in the $n_{\rm S}-\alpha$ plane obtained with broadband power information from BigBOSS's QSO + galaxies combined with Planck satellite forecasts. (Integration in $k$-space until $k_{\rm max}(galaxies) = 0.1h/{\rm Mpc}$ and $k_{\rm max}({\rm Ly}-\alpha) = 5h/{\rm Mpc}$)

tion with canonical kinetic energy and adiabatic vacuum predicts very small amount of non-gaussianity, violation of any of these conditions may lead to large non-gaussianity. Many of these models predict the non-gaussianity of local type, $\Phi = \phi + f_{nl}\phi^2$, where $\Phi$ is the gravitational potential in the matter era and $\phi$ is the corresponding primordial gaussian case. Alternatives to inflation based on bounce also tend to predict large non-gaussianity of this type. A detection of primordial non-gaussianity would rule out the simplest model of inflation. Conversely, a non-detection at a level of $f_{nl} < 1$ would rule out many of its alternatives.

Until recently, the most powerful method to place limits on $f_{nl}$ was based on the bispectrum of cosmic microwave background (CMB), with the latest WMAP constraint giving one-sigma error of around 20 on $f_{nl}$ [Senatore, Smith & Zaldarriaga, 2010]. With a better angular resolution one can sample more modes and the error should be improved to about 5 with the higher angular resolution Planck satellite [Cooray, Sarkar & Serra, 2008].

An alternative approach using clustering of biased tracers of structure on very large scales has recently been proposed [Dalal et al., 2008]. It was shown

that the non-gaussianity leads to a unique scale dependence of the large-scale bias, one that increases strongly towards the large scales, and whose amplitude scales with the bias of the tracer relative to the dark matter. One can therefore place the limits on $f_{nl}$ by comparing the scale dependence of the power spectrum of the biased tracer to the one expected in cosmological models under the assumption of a scale independent bias. A first application of this method has been presented using the large-scale clustering of quasar and luminous red galaxies (LRG) galaxy data from the Sloan Digital Sky Survey (SDSS) [Slosar et al., 2008]. The result, a non-detection with one sigma error of about 25, is comparable to the latest CMB constraints from WMAP, suggesting this is a competitive method compared to the bispectrum from CMB and should be pursued further.

Based on the size and volume of the BigBOSS survey one could in principle expect to reduce the current errors by a factor of 5-10 [McDonald, 2008]. However, to achieve this the galaxies measured in BigBOSS must have sufficiently large bias, since only for biased tracers is the non-gaussian scale-dependent clustering is revealed. The current projections suggest the galaxies will have bias of around 2 at $1 < z < 2$, suggesting this may be possible. In this case the expected one-sigma error in $f_{nl}$ is about 5. One way to further improve the errors is by combining two tracers of LSS, one with a high bias and one with a low bias: in this case it may possible to cancel sampling variance, which is the dominant source of error on large scales [Seljak, 2009], but due to low number density this will have to include an additional tracer of structure, potentially combining with the LSST and DES data.

More detailed studies of halo mass distribution of BOSS galaxies, combined with numerical simulations of non-gaussian models [Desjacques, Seljak & Iliev, 2009], are needed to provide a better answer to the question what the ultimate reach of BigBOSS for non-gaussianity studies is, but it seems likely that the limits will be at least comparable to the best limits from CMB and possibly much better than that.

### 2.4.3 Modified Gravity

While BAO measure the change in geometric scales with cosmic expansion history, the power spectrum as a whole probes the growth history of structure in the universe. The power spectrum amplitude depends on the growth factor $D(z)^2$ and redshift space distortions are sensitive to the growth rate $f(z)$. Thus both $D(z)$ and $dD/d\ln a$ can be measured. Within the framework of general relativity, this essentially repeats the information in the

expansion history and distance measurements; that is, there is a one-to-one correspondence between expansion and growth.

This implies that measuring both expansion and growth, through the BAO scale and the overall power spectrum, enables a test of Einstein gravity. One model independent parameterization of the growth deviation from general relativity is the gravitational growth index $\gamma$ [Linder, 2005; Linder & Cahn, 2007; Linder, 2008]. This characterizes the growth rate as

$$f(z) = \Omega_m(z)^\gamma \,. \tag{2.21}$$

Note that at high redshift, as matter domination tightens, $\Omega_m(z)$ is close to unity and the uncertainty on $\gamma$ increases. Thus this test of gravity is essentially a low redshift test (although not so low that nonlinearities cloud interpretation). This is further strengthened by growth being a continuing process, so small differences in the rate are amplified as growth persists into the late universe. Stril, Cahn, & Linder [2010] found that an experiment similar BigBOSS as proposed here is capable of determining $\gamma$ to within 0.04 (7%), simultaneously with fitting the expansion history, neutrino mass, and other cosmological parameters.

However, most extensions to gravity modify the physics in time- and scale-dependent ways, so another approach to exploring gravity uses combinations of the potentials $\psi$ and $\phi$ entering the metric. One can think of these as characterizing the gravity connecting the Newtonian potential and the density field, i.e. $\nabla^2\phi = 4\pi G a^2 \delta\rho_m$, and the gravity connecting the potential and the velocity field, $\nabla\psi = -\dot{v}$. In general relativity these are the same: $\psi = \phi$, but they can differ in many other theories of gravity. The two connecting relationships most closely tied to observations are given by

$$-k^2(\phi+\psi) = 8\pi G_N a^2 \bar{\rho}_m \Delta_m \times \mathcal{G} \tag{2.22}$$

$$-k^2\psi = 8\pi G_N a^2 \bar{\rho}_m \Delta_m \times \mathcal{V} \,, \tag{2.23}$$

where $\bar{\rho}_m\Delta_m$ is the gauge invariant matter density perturbation and $G_N$ is Newton's constant. In general relativity, the time- and scale-dependent functions $\mathcal{G}$ and $\mathcal{V}$ are identically unity. While the cosmic microwave background and to a large extent weak gravitational lensing are sensitive to $\mathcal{G}$, strong growth probes such as the galaxy power spectrum can constrain $\mathcal{V}$, thus breaking the degeneracy between the metric ingredients. Seeing the two parameters separately is a critical step toward identifying the class of modification to gravity.

Gravity beyond general relativity tends to give scale dependent effects, and indeed this is a major clue to distinguishing gravitational modifications

from galaxy bias properties. A wide field survey that provides accurate growth measurements over a wide range of scales gives an important lever arm in wavenumber $k$. BigBOSS covers the key redshift range for growth of $z \approx 0.7-1.4$ and covers up to 14,000 deg$^2$. The detailed spectroscopy delivers information on the velocity field, providing measurements of the growth rate $dD/d\ln a$ in addition to the growth factor $D(a) = (\delta\rho/\rho)_a/(\delta\rho/\rho)_{\rm init}$.

Daniel & Linder [2010] demonstrate that the BigBOSS science design makes it a major experiment for testing gravity. Figure 2.6 reveals that BigBOSS can determine each gravity function and is an important complement to next generation Planck CMB and high redshift supernovae distance measurements. Even allowing for both time (redshift) and scale (wave mode) dependence, BigBOSS delivers results a factor of 10-100 times better than current constraints.

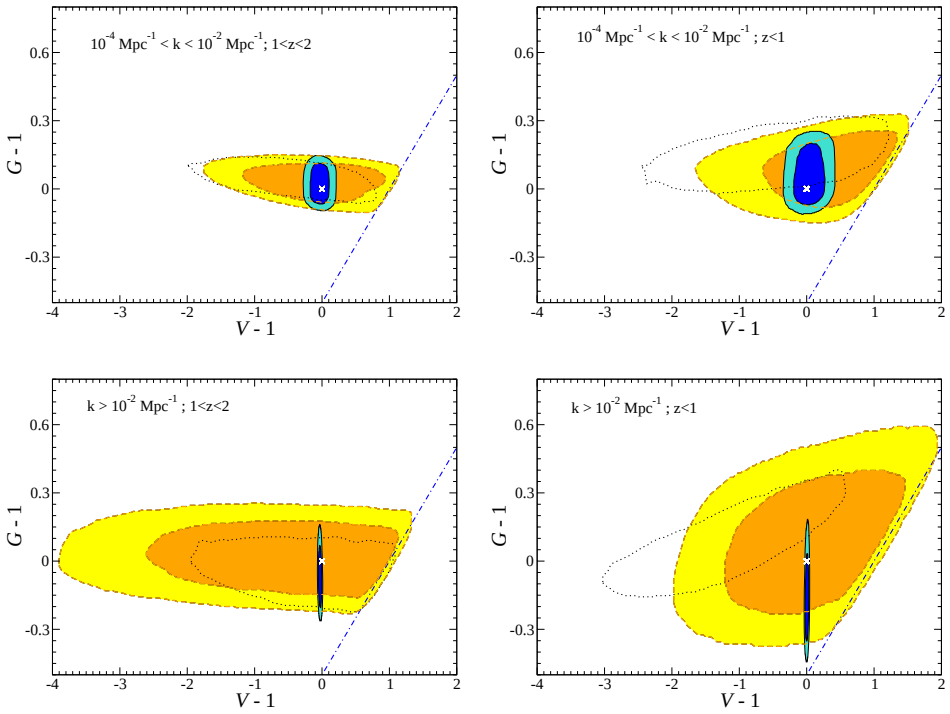


Figure 2.6: 68% and 95% cl constraints on $\mathcal{V}-1$ and $\mathcal{G}-1$ are plotted for the two redshift and two wavenumber bins using mock future BigBOSS, Planck, and supernova data (solid blue contours; dashed yellow contours show the degradation without BigBOSS). The dotted contours recreate the 95% CL current data contours, including galaxy and weak lensing information. The anticipated improvement in constraints is a factor of 10-100 in area. The x's denote the fiducial GR values. From Daniel & Linder [2010]

# 3 Community Science with BigBOSS

## 3.1 Overview

The primary motivation for the BigBOSS survey and multi-object spectrograph is to measure and constrain cosmological parameters, in order to understand the nature of "dark energy". However, the data collected will enable a multitude of astrophysical science beyond this core cosmology survey. In this section, we explore some of the many possible scientific investigations that will be enabled by BigBOSS beyond the realm of BAO.

These BigBOSS "community science" programs can be divided into three categories. First, the legacy spectroscopic database from the core BigBOSS survey will enable multiple projects, especially in the domain of extragalactic astronomy and galaxy evolution. Second, as described elsewhere in this proposal, roughly 20% of the 5,000 BigBOSS spectrograph fibers will be unallocated to cosmology targets in any given tiling. Hence these fibers furnish an opportunity to schedule "synchronous observing" programs in parallel with the BigBOSS BAO survey. Finally, the BigBOSS instrument will be available for dedicated use by PI-led programs in non-BigBOSS survey time and in the years beyond the BigBOSS mission.

It is important to note that the topics covered in this chapter are *by no means* an exhaustive list of the possible applications of BigBOSS data and hardware. The BigBOSS project collaboration is committed to the full integration of input from the astronomical community into our survey planning and operations, so as to maximize the joint scientific return between BAO cosmology and broader astronomical science. To this end, we will engage the community by way of a BigBOSS science planning workshop, as described in Section 3.9.

The breakdown of this chapter is as follows. Section 3.2 describes numerous galaxy-evolution science projects that the BigBOSS core survey will enable, as well as additional scientific applications to be found in a subset of "calibration fields" that will be observed repeatedly over the course of the survey. In Section 3.3 we describe applications of BigBOSS survey data to the science of active galactic nuclei (AGN), quasars, and the intergalactic medium (IGM). In Section 3.4 we discuss the scientific synergies between the BigBOSS legacy database and concurrent large-scale imaging survey programs. We propose the mode of "syncronous observing" in Section 3.5, and indicate possible applications to the systematic spectroscopic follow-up of transient sources in Section 3.6. Section 3.7 outlines two possible large science programs that could be conducted with the BigBOSS instrument in

a principal-investigator (PI) led mode of operation. Section 3.8 describes the support and deliverables that we will provide to members of the astronomical community who wish to make use of BigBOSS data and observing modes. Finally, Section 3.9 presents the rationale for a "community science workshop" that we propose to convene in advance of BigBOSS commissioning.

## 3.2 Galaxy Evolution

The spectroscopic legacy data from the BigBOSS survey will be particularly powerful for a wide range of galaxy-evolution studies. In this section, we list a subset of the possible community-science projects in this area. We also describe in Section 3.2.1 a set of BigBOSS survey calibration fields that will enable further galaxy-evolution science projects beyond the scope of the baseline survey parameters.

**The Evolution of Massive Galaxies: Star Formation, Merging, and AGN** The evolution in the number density, luminosity, and stellar mass of $L > L_\star$ galaxies provides a very strong constraint on galaxy evolution models [De Lucia & Blaizot, 2007] as merging and star formation result in different shape evolutions of the luminosity function at the bright end [Bower et al., 2006; Croton et al., 2006]. To accurately measure the luminosity function (LF) and its evolution significantly above $L_\star$ requires a survey with a large volume and with precise redshifts. Volume is needed as the most massive objects are rare and current studies suffer greatly from Poisson uncertainties. At the same time precise redshifts are necessary as redshift errors - and their corresponding error in luminosity - can significantly distort the shape and normalization of the exponential tail of the LF [Marchesini et al., 2007]. Current studies using medium band filters can achieve the desired redshift accuracy but they require prohibitively large time allocations to obtain the photometric data over very large areas [van Dokkum et al., 2009]. The total BigBOSS survey area will contain roughly 880,000 galaxies with $M > 3 \times 10^{11} M_\odot$ at $z < 1.0$. Compared to current spectroscopic samples [e.g., Brown et al., 2007; Faber et al., 2007], this will yield orders of magnitude better measurements of the LRG LF and will extend to higher redshifts than BOSS, where the evolution in the massive galaxy population is expected to become more rapid. BigBOSS will also characterize the ELF luminosity function to fainter magnitudes than for LRGs. Taken together these LFs will constrain the evolutionary channels by which ELGs merge and form LRGs.

BigBOSS will also deliver the best measurement of evolution in the [OII] luminosity function from redshift $z = 1.5$ to $z = 0.7$, where the color-selection for emission line galaxies is most effective. [OII] may be taken as a proxy for star-formation rate [e.g., Kewley, Geller & Jansen, 2004]. A statistical correction for the significant extinction can be determined using the Balmer decrement calculated from higher order Balmer lines. This will allow the measurement of a statistical [OII] extinction as a function of [OII] luminosity, stellar mass, and broad-band SED shape. We expect to detect H$\beta$ with similar significance to [OII] for all of our ELGs and so should be able to adequately calibrate the [OII]-SFR relation for our sample. For lower-luminosity emitters the higher order Balmer lines will be statistically detected by stacking the spectra as a function of [OII] and H$\beta$ luminosity, stellar mass, and SED shape.

BigBOSS will provide an extremely precise measurement of the evolution of average AGN activity from $z = 1.3$ to the present. AGN identification will in general, be from the presence of [OII] lines with no accompanying Balmer emission [Yan et al., 2006; Montero-Dorta et al., 2009], though AGN will also be identified via the detection of high ionization lines such as [NeV], large [OIII]/H$\beta$ ratios for lower-$z$ objects, or indeed even low-ionization line, e.g. MgII, which are only seen in emission for AGN. By correlating AGN activity with other galaxy properties, e.g. stellar mass, this measurement will further quantify the role of AGN in suppression of star formation. These studies are specifically enabled by the large wavelength range and high throughput of BigBOSS.

**Strong Lensing and Galaxy Structure** The SDSS has led to the discovery of the largest single sample of confirmed strong galaxy-galaxy gravitational lens galaxies [Bolton et al., 2006, 2008a] through the detection of two redshifts in single spectra. This sample of lenses has provided a measurement of the mass-density structure of elliptical galaxies and its dependence on galaxy mass [Koopmans et al., 2006; Bolton et al., 2008b]. Scaling from the known incidence of strong gravitational lenses identified by SDSS, the BigBOSS spectroscopic database should provide 10,000–20,000 new lenses through this discovery channel. With this large number of lenses it will be possible to "stack" the lenses in bins of redshift and halo mass. This will open a unique path to measure the mass-dependent redshift evolution in the halo morphology. In addition, the large number of spectra to be obtained by BigBOSS makes it likely that several multiple-redshift lenses will be found such as the double Einstein ring system [Gavazzi et al., 2008], with additional applications to precise galaxy-structure measurement and

cosmography.

**A Blind Spectroscopic Survey** A fraction of the BigBOSS survey fibers, partially overlapping with the sample of fibers allocated to the measurement of the night sky foreground, can be devoted to a blindly pointed spectrum sample. This program will constitute the largest ever blind spectroscopic survey (very roughly one square degree) and will provide a fundamentally different census of the universe than that which is provided by photometrically targeted surveys, including discovery of extremely high equivalent-width emission line galaxies. By virtue of these spectra being distributed uniformly throughout the BigBOSS area, this survey will be unaffected by the cosmic variance that plagues narrower field blind spectroscopic surveys. The large wavelength coverage of BigBOSS will furthermore permit identification of multiple significant emission lines across a wide range of redshifts (from low-redshift H$\alpha$ to high-redshift Ly$\alpha$ - see Fig. 3.1), in contrast to longslit-based programs that concentrate on small wavelength (and hence redshift) windows [e.g., Martin & Sawicki, 2004].

**Stacked Spectra as a Function of Photometric Properties** Although the individual galaxy spectra from the core BigBOSS survey will be of relatively low signal-to-noise ratio, the vast number of such spectra will permit the creation of extremely high SNR stacked spectra [e.g., Eisenstein et al., 2003; Schiavon et al., 2006; Cimatti et al., 2008] as a function of redshift, color, and luminosity. These high SNR stacks will enable the measurement of precision abundances, low-level emission lines, and detailed SFHs for much of the sample. With the combination of BigBOSS resolution and wavelength coverage, this library of stacked spectra will be a definitive resource for the study of physical galaxy properties and their evolution.

**Galaxy Clusters** Over the course of its operations, BigBOSS will be able to obtain spectroscopic redshifts for the brightest cluster galaxies of a large number of photometrically selected galaxy cluster candidates, such as the $\sim 20,000$ clusters expected to be delivered by the Red-Sequence Cluster Survey 2 [RCS-2; Yee et al., 2007]] or the many thousands of clusters expected to be yielded by future Sunyaev-Zeldovich (SZ) surveys and by the Planck satellite [e.g., Chamballu et al., 2010]. The SZ cluster programs are especially promising as cosmology probes as they directly probe the presence of an intra-cluster medium and are not dependent on virialization or galaxy properties within the cluster. For these surveys, however, no redshift estimate is available from the SZ determination itself. The main survey will

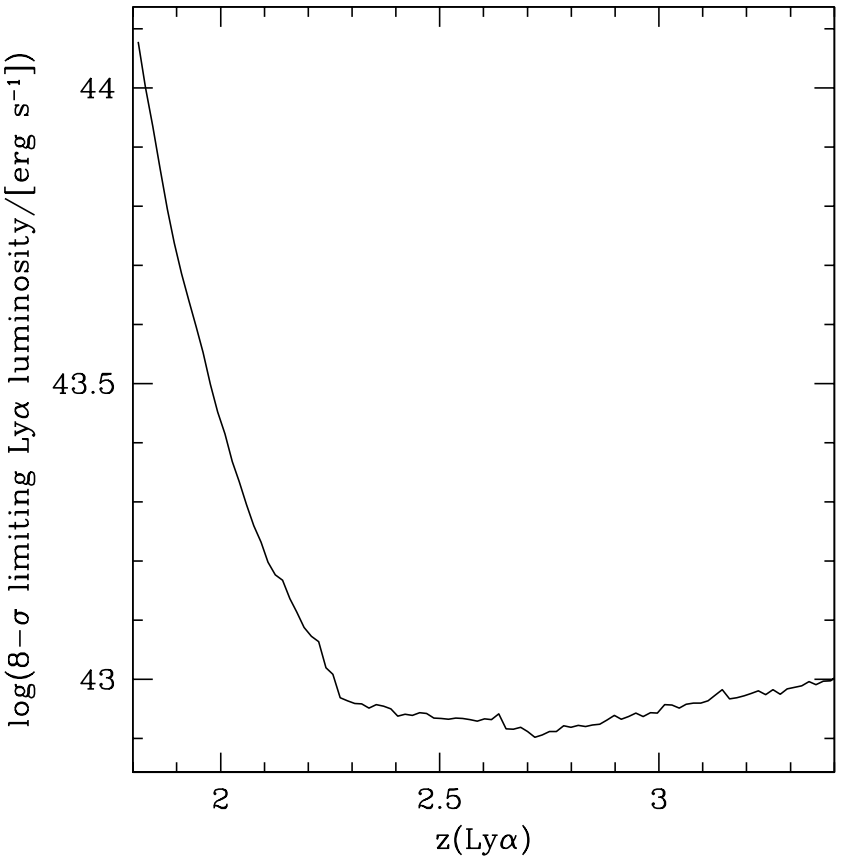


Figure 3.1: The expected 8-$\sigma$ detection limit for Ly$\alpha$ luminosity as a function of redshift. The large wavelength range of the BigBOSS spectrograph results in a large redshift range with a roughly constant line sensitivity.

likely target the Brightest Cluster Galaxy (BCG) in many of these clusters at $z < 0.7$ providing critical redshift information that will enable the cluster surveys to maximize the leverage of their samples.

**The Brightest High-z Galaxies: Giants and Lensed Normal Galaxies** The large area of the BigBOSS instrument and survey will permit spectroscopy of rare, bright color-selected Lyman-break galaxy (LBG) candidates, to be confirmed via the Lyman-alpha emission line at redshifts $z \sim 3-5$. The small handful of known extremely bright LBGs have mostly been discovered either serendipitously [e.g., Yee et al., 1996], or by systematic searches that have resulted in 10s of objects [e.g., Kubo et al., 2009]; BigBOSS offers the possibility of systematically identifying several hundred such objects across the sky. Many of these will be strongly lensed by intervening galaxies, groups, and clusters and therefore will have substantially lower luminosities that have been amplified by gravitational lensing. There are only a handful of such objects currently known, which hampers the detailed studies of the physical conditions in the "normal" star-forming population at $z > 1.5$. Deeper follow-up ground-based spectroscopy of these objects will then permit high SNR survey-scale studies of the IGM and star-formation in young galaxies at high redshifts [e.g., Pettini et al., 2000] at the highest, and more normal masses and SFRs. From space, JWST will yield access to deep MIR spectroscopy for these rare objects, giving a direct view on the dust content and ionization sources in these distant galaxies [e.g., Papovich et al., 2009].

### 3.2.1 Science with Calibration Fields

In order to properly characterize the BigBOSS survey performance and accurately measure the sampling and completeness functions, we will define 4 to 6 calibration fields, at least two of which can be targeted at any time of the year. These fields will be targeted at least once during each BigBOSS run, and over the period of the survey will build up a total area of ≈30-40 deg$^2$ which is densely sampled with deep spectroscopy. By carefully choosing the calibration fields to lie in regions which have wide-area multi-wavelength and archival spectroscopic coverage (e.g.: selected PS1 calibration fields; overlapping with M31; the best studied portions of the Sagittarius stream; the 9 deg$^2$ NDWFS Boötes field; the 2 deg$^2$ COSMOS field; the SXDF and UDS fields etc.), these fields will be invaluable for many ancillary science programs (e.g., galaxy evolution, Galactic structure, etc.) and will have high legacy value. Thanks to repeat visits these calibration fields will cover a to-

tal area of ≈30-40 deg$^2$, with a much higher spatial sampling, and with the possibility of hitting targets multiple times to increase the effective survey depth. In addition to providing an excellent means of calibrating the survey performance, the calibration fields will enable galaxy-evolution science that is not achievable with the main survey, some of which we describe here.

**A Deep, Magnitude-Limited Sub-Survey** The calibration fields will be used to construct a magnitude-limited sample of galaxies that goes significantly deeper than the main survey. It is well known that color selection techniques, such as those used in the main cosmology survey miss important elements of the galaxy population (e.g. [Franx et al., 2003]). A magnitude-limited survey will therefore be very important for more general galaxy evolution studies by quantifying the biases associated with the color-selection of the main survey.

In addition, this sample will be extremely valuable for measuring the evolution of the galaxy luminosity function to fainter luminosities, for correlating SFR with physical galaxy properties well below $L_\star$, and for calibrating the spectroscopic redshift distribution of the faint blue galaxy population used in weak gravitational lensing surveys. Precise knowledge of this distribution is essential for all applications of weak lensing to astrophysics and cosmology [e.g., van Waerbeke et al., 2006]]. The full BigBOSS survey will suppress the systematics of cosmic variance in this measurement to a greater extent than any other survey, while the deeper calibration-field component will push further down the luminosity function. We note that all BigBOSS faint-galaxy redshift distributions can be boot-strapped to the distributions of even fainter galaxies using the spatial cross-correlation calibration technique of Newman [2008].

**Multiple-Member Galaxy-Cluster Redshifts** The main BigBOSS survey will obtain many thousands of brightest-cluster-galaxy redshifts, as described above. However, depending on the tiling strategies, it will be hard for the main survey to sample more than $\sim 1$ galaxy per square arcminute, which implies that it will be very difficult to get more than a couple of redshifts for each cluster. In contrast, the higher spatial sampling of the deeper calibration survey has the potential of getting many more redshifts per cluster. In addition to providing secure spectroscopic confirmation of the clusters, this will also allow dynamical masses to be calculated, thanks to the 70km/s resolution of the spectrographs. Scaling from the number of clusters in the IRAC shallow survey [Eisenhardt et al., 2008] we expect that the calibration fields contain $\sim 1000 - 1200$ galaxy clusters at $z < 1$ and

$\sim 450 - 550$ at $z > 1$. A well-characterized set of clusters over such a wide redshift range will enable studies of the large-scale regions around galaxy clusters, the trend in galaxy populations surrounding these intersections of the cosmic web, and a useful calibration for cluster mass measurements.

**Correlation of Galaxy Properties with Environment** The local environment in which galaxies reside is known to be one of the key controlling factors for their formation, properties, and evolution [e.g., Dressler, 1980; Blanton et al., 2005; Cooper et al., 2006]. Using the more highly sampled data from the calibration fields, the BigBOSS project will permit extremely detailed studies of the empirical correlations between galaxy properties (color, luminosity, stellar mass) and environments [e.g., Cooper et al., 2008]. Even in the smaller calibration-field subset of the BigBOSS survey, we will attain sufficient numbers to split galaxies into multiple bins in redshift, stellar mass, and environmental density simultaneously. The data on the individual $z < 0.5$ objects will be extremely good, even with the short exposure times.

A recent particularly promising approach has been to decompose galaxies into central and satellite galaxies based on their luminosities and clustering [e.g., Yang et al., 2007]. This approach has yielded new insights as it appears that central and satellite galaxies have different properties at a fixed stellar and halo mass. Understanding this apparent dichotomy is key to understanding the physical role of environment in galaxy evolution. Locally this has been most successfully attempted with SDSS [e.g. Pasquali et al., 2009] taking advantage of the extensive spectroscopic coverage, but the redshift evolution in the central vs. satellite population has not been explored due to the lack of sufficiently fine sampling over a large area. The deeper magnitude-limited portion of the survey would have a higher spatial sampling and would enable group and satellite catalogs to be constructed at redshifts $z < 1$ opening up a new avenue for environmental studies beyond the local universe.

## 3.3 AGN, Quasars and IGM Science

We now turn our thoughts towards the AGN and Quasar population and describe the prospects generated by the BigBOSS survey and instrument, for the detailed study of the global active galaxy population, as well that of individual systems. We also note the exciting possibility of generating a large dataset of Damped Lyman-$\alpha$ (DLA) and Broad Absorption Line (BAL) objects, that will provide key insights into the topology and feed-

back mechanisms of the IGM and cosmic web at high redshifts.

**Global Quasar Census**

With the advent and completion of two major quasar surveys, the 2dF QSO Redshift survey [2QZ; Croom et al., 2004] and the SDSS Quasar Survey [Schneider et al., 2010], the number of *spectroscopically confirmed* quasars stands a little over $10^5$ objects. With these samples in hand, great strides have been made in measuring the global properties of the quasar population, and its evolution with redshift.

In particular, we now have good handles on the the bright end of the optical quasar luminosity function at all redshifts to $z \sim 6$ [Richards et al., 2006], and have the first evidence for optical AGN downsizing, at $z \lesssim 2.5$ [Croom et al., 2009]. The evolution of the clustering of the brightest optically selected quasars is also now reasonably measured at redshifts $z \leq 2.2$ [Croom et al., 2005; Ross et al., 2009] and $z > 3.5$ [Shen et al., 2007], though simply due to the relatively rare nature of the high-$z$ quasars, the $z > 3.5$ measurements are hampered by low-number statistics, even in the final SDSS dataset. Clustering measurements give a handle on the mass of the host dark matter haloes that the observed quasar population inhabit, with current measurements suggesting this mass to be $M_{\rm DMH} \sim 2 \times 10^{12} h^{-1} M_{\odot}$, at all redshifts. Also key is the combination of QLF and clustering measurement, which, when combined, are able to give estimates of quasar lifetimes, $t_q$ [e.g. Martini & Weinberg, 2001; Haiman & Hui, 2001; Shen, 2009; Shankar et al., 2010]. The measured value of $t_q$, and how it depends on e.g. the host halo mass, environment and the duty cycle of the central engine Supermassive black hole (SMBH), is currently still a relatively poorly constrained parameter, and one that is a key discriminator in the suites of semi-analytic and N-body models [e.g. Booth & Schaye, 2009; Bonoli et al., 2009].

Due to the evolution of the QLF and the flux-limited nature of most quasar samples, there is a strong correlation between redshift and luminosity in current quasar samples, making it difficult to isolate luminosity dependence of clustering from redshift dependence, the so-called "Luminosity-redshift" ($L - z$) degeneracy. This affect is especially acute at redshifts $z \sim 3$, at the height of "Quasar Epoch".

Furthermore, once selection effects are taken into account, and the sample is divided into redshift, luminosity, or another physical parameter [Shen et al., 2009], even these 100,000 strong quasar datasets can only comprise a few thousand objects in each bin of interest, leading to a low S/N measurement, e.g. when pair-counting at small-scales in clustering measurements

[e.g., Myers et al., 2007; Ross et al., 2009]. The dataset from the currently on-going SDSS-III:BOSS Quasar Survey will begin to address some of these issues, but only at redshifts with $2.2 < z < 3.5$ and only for objects $18.0 \leq i \lesssim 21.5$. Although BOSS observes quasars fainter than $i = 21.5$, the relatively low completeness for these objects will most likely lead to them not being used in any global statistical analysis.

BigBOSS, however, has the capacity to completely revolutionize the measurements of global quasar properties such as the QLF and clustering, in turn actually testing and ruling out sets of models. With the efficient low, $z < 2.2$, QSO target selection discussed later on in Section 4, the ability to have e.g. a $10^6$ dataset of spectroscopcially confirmed luminous AGN, over all redshifts, up to $z \sim 6$, is in hand. This is best demonstrated by studying Figure 3.2, where the $L - z$ plane is comprehensively filled, with the dynamic range at any given redshift now $\gtrsim 5$ magnitudes. Indeed, BigBOSS has the ability to readily sample luminous AGN with $\log M_{BH} \approx 6$ at $z < 0.7$, and will be able to highly compliment the ELG sample at higher redshifts.

**Dual Supermassive Black Holes in BigBOSS**

A wealth of observations have shown that galaxy mergers are common and that nearly all galaxies host a central supermassive black hole (SMBH); consequently, some galaxies must host two SMBHs as the result of recent mergers. These are known as **"dual SMBHs"** for the first $\sim 100$ Myr after the merger when they are at separations $\gtrsim 1$ kpc [Begelman, Blandford & Rees, 1980; Milosavljević & Merritt, 2001]. These dual-SMBH systems are an important testing ground for theories of galaxy formation and evolution. For example, simulations predict that quasar feedback in mergers can have extreme effects on star formation [Springel, Di Matteo & Hernquist, 2005] and that the core-cusp division in nuclear stellar distributions may be caused by the scouring effects of dual SMBHs [Milosavljević et al., 2002; Lauer et al., 2007]]. A statistical study of dual SMBHs and their host galaxies would thus have important implications for theories of galaxy formation and SMBH growth. It could also place interesting constraints on the source population of future gravitational-wave experiments such as *LISA*.

However, identifying dual SMBHs has so far been difficult. They are observationally identifiable when sufficient gas accretes onto them to power dual active galactic nuclei (AGN), and a handful of dual AGN have been spatially resolved in radio, infrared, optical, and/or X-ray images of nearby galaxies [Komossa et al., 2003; Rodriguez et al., 2006; Bianchi et al., 2008]. A

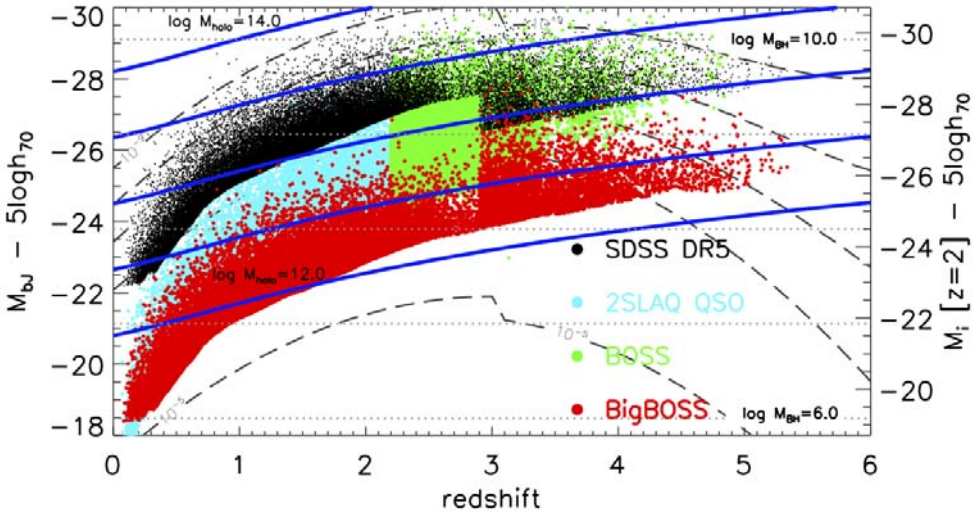


Figure 3.2: The Quasar $L-z$ plane for recent quasar surveys, including the SDSS (black points), 2SLAQ QSO (cyan), BOSS (green), and the projected BigBOSS data (red). The projected BigBOSS data come from assuming a significantly fainter sample than SDSS (see Section 4 for fuller details on quasar target selection), but it should be noted that the selection function present in the SDSS data, e.g. at $z \sim 2.7$, will not be present in the BigBOSS data. Note also that there are 105,000 objects in the SDSS DR7 catalog, but only $\approx 9,000$ faint, $g \leq 21.85$ low-redshift QSOs in hand from the 2SLAQ Survey [Croom et al., 2009]. Dashed lines indicate the evolution of the host halo space density, as inferred from the observed quasar luminosity function. Horizontal dotted lines show the corresponding black hole mass, while the solid lines are halo virial predictions. This figure is kindly modified from the original form in [Croton, 2009], where the reader is referred to for further details.

new approach is needed to advance from anecdotal discoveries of individual systems to a systematic survey of dual SMBHs.

A promising new approach to building such a statistical sample is to select dual AGN candidates as galaxies with double-peaked narrow AGN emission lines in their optical spectra, as identified using standard line-ratio diagnostics [Baldwin, Phillips, & Terlevich, 1981; Kewley et al., 2006], In contrast to the case of double-peaked *broad* lines from AGN accretion disks [Eracleous et al., 1997], double-peaked *narrow* lines can arise from two accreting SMBHs at separations $\gtrsim 1$ kpc, each with its own narrow-line region (NLR). Spatially resolved detections of the two NLRs are necessary to distinguish this situation from other sources of double-peaked emission, such as outflows within a single NLR. This approach was pioneered in the DEEP2 Galaxy Redshift Survey, in which slitmask spectroscopy allows emission lines to be resolved in both position and velocity space. Two such dual AGN were identified in DEEP2, at redshifts $z = 0.6$ and $z = 0.7$ [Gerke et al., 2007; Comerford et al., 2009]. More recently 271 galaxies, at $0.1 < z < 0.6$, with double-peaked narrow AGN emission lines have been identified in the Sloan Digital Sky Survey (SDSS) as dual AGN candidates [Smith et al., 2010; Wang et al., 2009; Liu et al., 2010].

However, the extreme rarity of double-peaked AGN demands a larger survey for statistical studies, and with BigBOSS such a survey of dual SMBHs across a large redshift range is finally possible. **BigBOSS spectroscopy has the potential to yield $\gtrsim 20,000$ dual SMBH candidates at redshifts $0 < z < 2$ and with line-of-sight velocity differences of $\gtrsim 100$ km s$^{-1}$ between the SMBHs.** Follow-up slit spectroscopy of these candidates could confirm $\gtrsim 10,000$ dual SMBHs in BigBOSS, which would vastly increase the number of known dual SMBHs as well as extend the known dual SMBH population to $z > 1$ for the first time; combined, this would enable significant advances in the observational understanding of galaxy formation and SMBH growth as a function of redshift.

**Identifying Dual SMBH Candidates in BigBOSS:** Dual SMBH candidates will be selected from the 20 million BigBOSS spectra in two steps. First, emission line flux ratios can be used to diagnose which galaxies host AGN, as high [O III] $\lambda$5007/H$\beta$ and high [N II] $\lambda$6583/H$\alpha$ signifies AGN activity [Baldwin, Phillips, & Terlevich, 1981; Kewley et al., 2006]. Assuming that $\sim 10\%$ of galaxies power AGN [e.g., Montero-Dorta et al., 2009], there will be roughly 2 million active galaxies in BigBOSS. Next, dual AGN candidates can be chosen as the active galaxies with double-peaked AGN emission lines. Assuming that the fraction of SDSS active galaxies with

double-peaked AGN emission lines ($\sim$ 1%) is similar for BigBOSS, there will be roughly 20,000 double-peaked AGN in BigBOSS. In reality this number is likely a lower limit, as the improved spectral resolution of BigBOSS ($R \sim 2300$ – 6100) compared to SDSS ($R \sim 1800$) enables detections of dual AGN with smaller velocity differences. For instance, at $z = 0.5$ BigBOSS spectra resolve double-peaked [O III] $\lambda$5007 emission lines with velocity differences as small as 50 – 130 km s$^{-1}$, whereas for an analogous system SDSS spectra cannot resolve velocity differences less than 170 km s$^{-1}$.

**Confirming Dual SMBHs in BigBOSS:** Since BigBOSS fiber spectra carry no spatial information, follow-up observations of the spatial structure of the AGN emission are necessary to determine which double-peaked AGN are in fact produced by dual AGN and not other sources such as AGN outflows. The follow-up observations will be the same as those pursued for the double-peaked AGN in SDSS, where long slit spectroscopy at Lick, MMT, Keck, and Gemini observatories have shown that at least half have the two distinct, compact emission components characteristic of dual AGN [Figure 3.3 in Comerford et al., 2010]. Assuming a similar rate for BigBOSS, follow-up longslit spectroscopy could yield $\gtrsim 10,000$ dual SMBHs in BigBOSS; the exact number could well be limited by the amount of follow-up telescope time obtained.

**Absorption Systems, Black Hole Winds and the Cosmic Web**

With the advent of the SDSS, much progress has been made studying the abudance and nature of heavy column damped Lyman-$\alpha$ (DLA) systems, with $N_{\rm HI} > 10^{20.3}$ cm$^{-2}$, (e.g. Wolfe, Gawiser, Prochask, ARA&A, 2005; Prochaska & Wolfe, 2009) and how these systems relate to the universal distribution of H I gas, and the complex interaction between the IGM and galactic star formation. Also, catalogs, some with base timelines of decades or more, (Gibson et al. 2009; Allen et al. 2010) are now in hand that study the Broad Absorption Lines (BALs) viewed in the spectra of quasars. These BALs are extreme events, instrinsic to the quasar, and traditionally associated with winds originating from the central accretion disk.

A survey such as BigBOSS, as opposed to SDSS, or even SDSS-III:BOSS, is required to make progress here, as the fraction of DLAs and BALs is typically $\sim$ 5% and $\sim 10 - 15$ of the total, $z > 2.2$ quasar population, respectively. A first natural step would be a monitoring campaign for the BALs, which would involved reobserving, at trivial fiber cost, all known BAL quasars. With the goal of observing over 600,000 high-$z$ quasar sight-lines

over a substantial fraction of the Northern sky, gives the possibilites for not only mapping out the interlinked cosmic web in unprecedented detail, but also the statistics needed to see how AGN feedback and winds then impact on the IGM.

## 3.4 Synergies between BigBOSS, DES and LSST

As a massive spectroscopic survey, BigBOSS will provide a unique and important complement to the direct-imaging science projects currently being planned with the Dark Energy Camera (DECam) on the 4m Blanco Telescope, as well as to future imaging surveys with the Large Synoptic Survey Telescope (LSST). Although both DECam and LSST will be located in the Southern hemisphere, their planned surveys will include significant overlap with the baseline BigBOSS survey footprint. The LSST survey footprint (see figure 2.1 in the LSST Science Book, LSST Science Collaboration 2009) extends to a declination limit of a minimum of $+3^\circ$ across the entire sky, with an additional northern extension to $\approx+30^\circ$ (their so-called "northern Ecliptic region") at right ascensions between RA = 60 and $120^\circ$ (4-8$^h$). The Dark Energy Survey will cover an equatorial strip from $-50^\circ$ to $+55^\circ$ ($-3.3^h$ to $+3.7^h$, overlapping with SDSS Stripe 82), and an additional region between RA = $30^\circ$ and $55^\circ$ ($2^h$ and $3.7^h$) which lies north of DEC=$-15^\circ$ (Jim Annis, personal communication). The BigBOSS spectroscopy within these regions will provide important complementary data for these surveys. For example, the spectroscopy will help with: the calibration of the photometric redshifts for the weak lensing and cluster finding programs; measuring redshifts for the dominant galaxies in the cluster candidates; spectroscopic classification of variable objects (e.g., SN host galaxies, AGN typing, stellar typing, spectroscopic binaries, etc.); dwarf/giant separation for Galactic structure studies; reddening measurements from stellar extinction; AGN classification and redshifts for determining demographics, luminosity functions, evolution, etc.; redshifts of lenses and lensing galaxies in strong gravitational lenses; metal line tomography of the intergalactic medium along the lines of sight to bright QSOs; and so on. In addition, BigBOSS spectroscopy will also complement ongoing imaging surveys undertaken in the northern hemisphere (e.g., PanSTARRS, PTF, etc.) and future space-based all-sky surveys.

## 3.5 Synchronous Observing Programs

The baseline BigBOSS survey, as described in Chapters 2 and 6, will be able able to place approximately 80% of its fibers on the ELG, LRG and QSO

targets that reach the survey goals in redshift coverage and exposure time. While work is continuing on optimizing the BigBOSS survey strategy, the baseline survey demonstrates that some fraction of the fibers in any tiling, 500-1000 fibers or about 100 per square degree, will be un-filled by targets from the main BigBOSS survey. We propose that these fibers be made available to other science programs proposed by the astronomical community at large, to be executed synchronously with the BigBOSS survey.

The opportunity to submit target objects to such synchronous programs that use the un-allocated fraction of BigBOSS fibers would provide the astronomical community with a completely unique resource: access to a five year observing program that will cover 14,000 square degrees and can reach S/N 10 $\text{Å}^{-1}$ at 4000 Å for a point source $g$ magnitude of 19.5 [2]. This is a capability uniquely well matched to programs with targets that are sparsely distributed over the sky, or that require a spectroscopic search for rare but scientifically valuable objects. An example of the first type of program is a search for stars in the distant halo of the Milky Way. Luminous red giant stars at distances greater than 50 kpc from the Galactic center are only a few per square degree, and can be reliably selected from multicolor photometry [Morrison et al., 2001; Majewski et al., 2003; Yanny et al., 2009]. These rare stars are one of the few kinematic tracers available at large Galactocentric distance to measure the total mass of the Galaxy and its dark matter halo [e.g. Battaglia et al., 2005]. An example of the second type of program is a spectroscopic search of color- or objective prism selected candidates for the most metal-poor, chemically primitive stars in the Galaxy [Beers et al., 1985; Christlieb et al., 2001].

To implement these synchronous observing programs led by the community, we propose that NOAO solicit proposals and evaluate them for scientific and technical merit through its regular time allocation process. The successful investigators would then submit target lists to the BigBOSS team for each year's observing. After the location of the BigBOSS pointings are determined based on the optimal tiling of the survey targets, the same code that assigns the BigBOSS fibers would then assign the unused fibers to objects from the synchronous program target lists. With the pointing center already established, the only remaining freedom in placing the unused fibers is the 181 arcsec diameter of the patrol region of the actuators. These programs would be subject to the same bright magnitude cutoff as the BigBOSS targets in order to prevent excessive scattered light from contaminating neighboring fibers, and would be observed in units of the standard

[2] as calculated using the BigBOSS ETC

BigBOSS 16.6 minute exposures.

The most straightforward kind of synchronous program to implement would be those that can submit large lists of targets all at the same priority, expecting to obtain spectra for only the fraction of the input catalog that can be allocated to the unfilled fibers. A useful analogy is an Hubble Space Telescope Snapshot Survey program, where successful proposers submit a list of un-prioritized targets and a fraction of those targets are observed as scheduling of the other approved programs allows. Examples of these programs would include surveys of the Galactic halo and thick disk populations, blue horizontal branch stars, surveys of white dwarf candidates to identify unusual or rare sub-samples, AGN surveys, etc.

In contrast, synchronous programs that have very few targets per pointing, such as the Milky Way halo red giants described above, would have to be included at high priority in the BigBOSS survey tiling optimization. Programs of this kind have the potential to create samples of many thousands of objects for targets as sparse as one per square degree, making it possible to characterize the populations of very rare and poorly understood classes of objects that are currently limited by the rate at which samples can be collected using single-object spectroscopy. Other examples of these programs include observations of extreme metal poor stars, rare (e.g., very cool or magnetic) white dwarfs, field brown dwarf candidates (e.g., from the WISE survey), very high-redshift QSO candidates, occasional interesting targets of opportunity.

While a small fraction of fibers allocated to such sparse synchronous programs would probably not impact the BigBOSS survey efficiency, assigning all of the leftover fibers probably would. In order to pursue this option, the BigBOSS team would have to do detailed tiling simulations to determine a threshold for additional constraints from the synchronous programs. The multi-year duration of the BigBOSS survey is an advantage here, as this more complicated but potentially very productive variant on the synchronous programs could be implemented in the second and later years of the survey, after the BigBOSS team has a season's experience with the tiling and fiber allocation.

We discuss here two of many possible investigations matched to the unique and new discovery space that would be made available through synchronous programs carried out over 14,000 square degrees of the BigBOSS survey. Blue horizontal branch stars in the halo of the Milky Way are, along with the halo giants described above, important probes of the stellar density profile and total mass of the galaxy because their distances can be determined accurately ($\sim$10%, [Clewley et al., 2004]) out to 50 kpc for $r =$

19.5. Candidates can be selected photometrically, but require spectroscopic confirmation at sufficient S/N to separate then from the less luminous field blue straggler population. Using efficient color cuts that select BHB candidates based on their hot effective temperatures and large Balmer jumps, the density of candidates is a few per square degree. As an example, SDSS had an "ancillary science" program for unused fibers analogous to the synchronous BigBOSS programs discussed here. BHB candidates were one of the SDSS ancillary programs, and over the 8032 square degrees of the survey 14,366 BHB candidates were allocated fibers, about 8 per 7 square degree SDSS field[3] This SDSS sample was used in [Xue et al., 2008] to make one of the best available determinations of the mass the Galaxy. The SEGUE project, a survey of Mily Way stars using the SDSS survey telescopes and spectrographs [Yanny et al., 2009] targeted BHB candidates at high priority, and allocated a fiber to all candidates in all of its 200 pointings. The final number of BHB candidate spectra in the same color-selection region as used for the SDSS ancillary program is 2930, a density not much larger than that from the SDSS BHB sample despite the fact that SEGUE had access to all 640 fibers in the SDSS field. For the BHBs, and for other similar sparse classes of targets, the survey area is the primary limitation on the size of the sample. Another class of objects observed as part of the SDSS ancillary science and is a good model for a BigBOSS synchronous program is the white dwarf catalog of [Eisenstein et al., 2006]. This sample doubles the number of spectroscopically confirmed white dwarfs. This catalog has been used for statistical studies of white dwarf stellar physics as well as the star formation history and age of the Galactic stellar populations [Harris et al., 2006]. In addition, rare classes of these objects like the "ultracool" white dwarfs that can be used to determine ages for the oldest stars in the Galactic disk and halo [Gates et al., 2004; Kilic et al., 2006], magnetic [Schmidt et al., 2003] and pulsating [Mukadam et al., 2004] white dwarfs, and white dwarf plus M-star binary systems [Silvestri et al., 2006]. These last can be further searched with time-resolved spectroscopy for compact, post common-envelope binaries in order to better understand the formation mechanism of these systems which are the precursors of cataclysmic variables X-ray binaries and possibly SN Ia.

[3]The large range accessible to each fiber on the SDSS plug plates resulted in a large fraction of the BHB candidates allocated to fibers; such a sparse target list would have to be included in the BigBOSS tiling to have a similar efficiency, as discussed above.

## 3.6 BigBOSS and the Transient Sky

The BigBOSS survey has the potential to spectroscopically characterize the transient sky, if its mapping footprint on the sky is preceded by an imaging survey with a time-domain/transient-detection component. The likely imaging data that would be used for targeting this mode would be drawn from the Palomar Transient Factory and/or the PanSTARRS surveys; a small fraction of BigBOSS fibers could be assigned to targets selected due to their variability in these imaging surveys. The bulk of these objects are likely to be AGN or variable stars. Nevertheless, by targeting essentially all the variable targets above some relatively bright magnitude and variability amplitude, BigBOSS can provide a near-complete census of the transient sky and thus holds the potential to discover and physically characterize some hitherto unknown variable class of objects.

## 3.7 The BigBOSS Instrument and P.I. Programs

### 3.7.1 Case Study: M31

The BigBOSS spectrograph on the Mayall telescope is well matched to perform a wide-field spectroscopic survey of our nearest massive neighbor, the Andromeda Galaxy (M31). The M31 survey described below demonstrates the unique capabilities of the BigBOSS spectrograph for high impact ancillary science. The proposed survey is expected to execute outside the main BAO science survey, yet compliments the main survey observing schedule: M31 is observable in Fall semester when the Galactic plane partly obscures the extragalactic sky.

In LCDM galaxy formation, galaxies form through the accretion and merging of smaller systems. Since galaxy relaxation times are longer than the age of the universe, their past accretion histories are currently encoded as substructure in the phase space distribution of stars. Mapping the photometric, kinematic and chemical distribution of stars in a given galaxy can thus reveal its accretion history and serve as a critical test of galaxy formation theory.

A wealth of substructure in the form of tidal streams and faint dwarf galaxy satellites has been discovered in recent photometric surveys of nearby massive spiral galaxies (e.g., MW: [Belokurov et al., 2006]; M31: [Ferguson et al., 2002]; nearby spiral galaxies: [Martinez-Delgado et al., 2010]). Much of this work is focused the Milky Way and M31 galaxies, where it possible to resolve individual stars and thus reach extremely low surface brightness levels. The limiting surface brightness for resolved star studies is set not

only by the photometric depth, but can also be improved by minimizing the contamination of foreground/background sources in the sample. For example, using a spectroscopically selected sample of resolved stars, the surface brightness profile of M31 has been measured down to $\mu_V = 35$ mag sq arcsec [Guhathakurta et al., 2005]. A spectroscopic survey for substructure based on individual stars is motivated by two goals. First, spectroscopy provides an extra phase space dimension (two spatial and one velocity) in which to search for structure in 6D phase space. A second, and equally important, motivation for spectroscopy is to better removing foreground/background objects based on velocity and chemistry, thus pushing the search for substructure to significantly fainter surface brightness limits than possible with photometry alone.

There are compelling advantages to studying the galactic structure of M31. It is sufficiently nearby that individual red giant branch stars are easily resolved and have an apparent magnitude of $r \sim 21$ at the mean distance of M31, providing many thousands of stellar spectroscopic targets per square degree. It is sufficiently far away that surveying a large portion of the M31 halo requires covering a few hundred square degrees, as compared to the full sky coverage needed to understand the Milky Way. An on-going photometric survey of M31, the Pandas survey, has discovered many new tidal streams and dwarf galaxies, and provides an good catalog for spectroscopic target selection. Existing spectroscopic coverage of M31 is limited is deep pencil beams through the M31 disk and halo. These data have provided and tantalizing look at the kinematic and chemical structure of M31. A full mapping of the kinematics and abundances of the M31 halo would be a tremendous step forward compared to these pencil beam surveys through the halo that currently exist.

The BigBOSS spectrograph is uniquely positioned to perform a wide-field spectroscopic survey of M31. The number of M31 stars accessible to spectroscopy with the BigBOSS+Mayall telescope is between 1000-5000 M31 RGB stars per square degree for projected radii 50 kpc and beyond in M31. This is well matched to the number of BigBOSS fibers. With a few hundred pointings at reasonable exposure times, the BigBOSS instrument could map the resolved stellar population of M31 to impressive depth and completeness, with a spectral resolution delivering precise radial velocities and substantial chemical-composition sensitivity.

### 3.7.2 Case Study: "Galactic Archaeology"

The history of star formation, chemical enrichment, hierarchical galaxy mass assembly, and dynamical evolution can be resolved in greater detail in our own Milky Way than in any other galaxy. The fossil record of this history is encoded in the detailed phase-space distribution and chemical composition of Galactic stars. The BigBOSS instrument offers the potential to map radial velocities and elemental abundances for a larger number of stars over a larger volume of our galaxy than any other survey.

Surveys such as the SDSS SEGUE project have revealed a wealth of kinematic substructures within the stellar populations of our Galaxy. The forthcoming APOGEE survey of the SDSS-III project promises to deliver a comparably detailed picture of the structure of Galactic distributions of multiple elemental abundance ratios, ushering in a new age of "near-field cosmology" in the confrontation with detailed quantitative predictions of the ΛCDM model of galaxy formation and evolution. With its sensitivity, multiplex capability, field-of-view, and spectral resolution, the BigBOSS instrument could provide the next generational step in this area of research if used for a dedicated survey of Galactic stellar populations.

A Milky-Way stellar spectroscopic survey with the BigBOSS instrument is particularly compelling in the context of GAIA ESA cornerstone mission. GAIA, which is set to launch in 2012 and to begin public data releases in 2014, will measure parallaxes and proper motions for $10^9$ stars, along with radial velocities for $10^8$ stars. The radial velocity precision to be achieved by the GAIA spectrometers does not match the astrometric precision of the mission (in terms of line-of-sight versus transverse physical velocities), and hence there will be a great need for large-scale spectroscopic follow-up in order to complement GAIA astrometry and deliver the highest possible sensitivity to phase-space substructures in the Milky Way. BigBOSS could provide these accurate RVs for GAIA stars in the magnitude range $17 < V < 20$, complemented by chemical abundance measurements for stars with $V < 14$.

## 3.8 Community Support and Deliverables

As illustrated by the SDSS, the community value of large spectroscopic survey programs is immeasurably enhanced by the timely distribution of high-level data products and corresponding documentation. The details of the data products that we will release to the community, and the infrastructure with which this distribution will be carried out, are given in Section 7.5 of

this proposal. In brief, we will distribute target lists, targeting photometry, survey window functions, reduced spectra, and derived spectroscopic parameters including redshifts and object classifications. The primary means of distribution will be via an online database interface, in the manner developed for the SDSS. All survey data will be released to the public at semi-regular intervals, the dates of which will be determined and advertised at the outset of the survey. Details of the survey data as distributed to the public will be posted to a website that will be available for public viewing simultaneously with the public data releases.

Community targets submitted for synchronous observation as described above will be calibrated and extracted to the 1D spectrum level by the main BigBOSS survey pipeline. These spectra will be made available to synchronous proposers with relatively short turn-around, and distributed via password-protected web or FTP directories. (We anticipate that during the hardware and software commissioning phase, there will be a somewhat longer delay in providing reduced synchronous-program data, during which we will verify the correct operation of our observing modes, pipeline analysis, and distribution system.)

In order to support the dedicated use of the BigBOSS spectrograph for PI-led programs, we will deliver a functioning suite of targeting and observation-planning software to NOAO. We will also release all of our spectral data-analysis software under an open-source license, and will consult with PI users in order to maximize their scientific return from their data. Since we anticipate that PI programs may operate in different regimes and have different scientific data-analysis requirements, it is anticipated that PI-led programs will contribute some software-development effort as necessary to meet their specific program goals, to the extent that they differ from the analysis requirements of the core BigBOSS survey.

## 3.9 Community Science Workshop

In order to maximize the broader impact of the BigBOSS survey and instrument within the astronomical community, we propose to hold a BigBOSS community science workshop in advance of the start of survey operations. The purpose of this workshop would be three-fold. First, the workshop will convey the details of BigBOSS to a wide professional audience, and allow for extensive back-and-forth discussion between interested astronomers and the BigBOSS project team. Second, the workshop will provide an opportunity for interested researchers to meet and form collaboration networks based upon common interests in BigBOSS data and capabilities. Third, the work-

shop will give our team the best possible overview of the range of interest in BigBOSS and the supplementary and PI proposals that are likely to be forthcoming, thereby allowing us to optimally strategize for commissioning, operations, and data reduction. We tentatively propose that this workshop be held in fall 2011 or spring 2012, with ample advance notice and publicity.

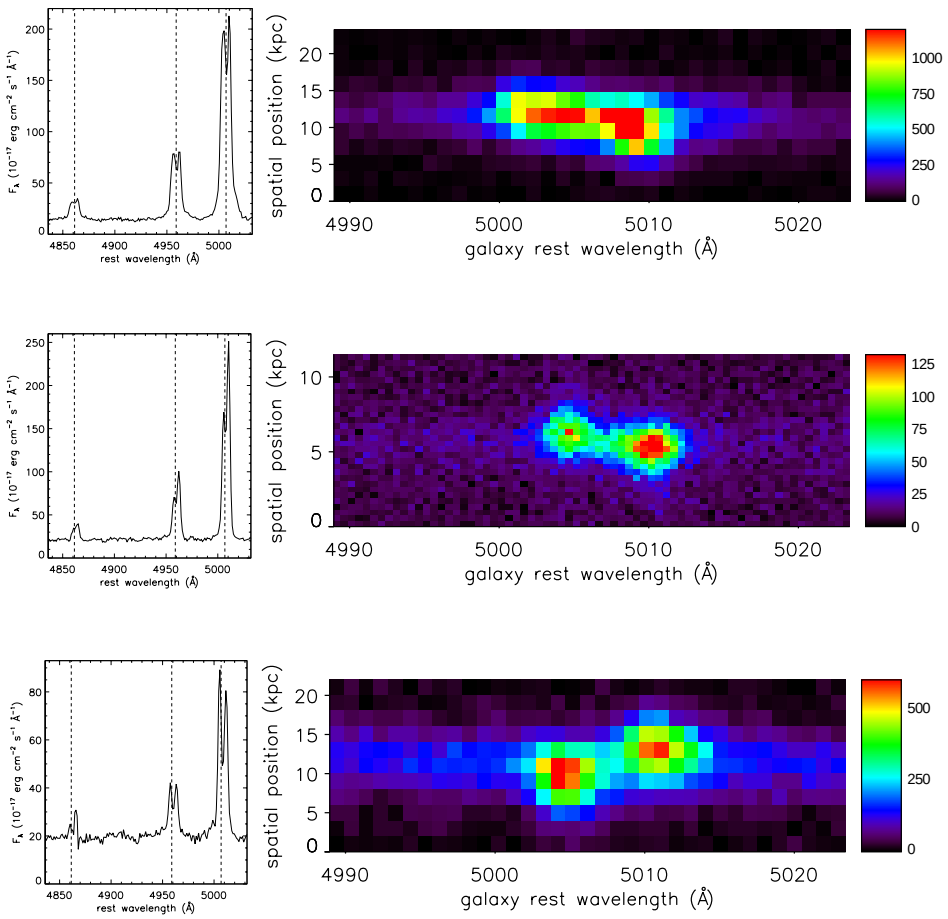


Figure 3.3: Spectra of three example double-peaked AGN in SDSS. Each objects's double-peaked AGN emission lines at H$\beta$, [O III] $\lambda$4959 and [O III] $\lambda$5007 (where the dashed vertical lines show the expected wavelengths) are visible in a portion of the SDSS spectrum (left), and the spatial separation between each object's two emission components in [O III] $\lambda$5007 is shown in a portion of the two-dimensional spectrum (right). The two-dimensional spectra were obtained with Lick (top, bottom) and with the MMT (middle), and the two compact emission components separated by $\sim$1 kpc suggest that these objects are dual AGN. Similar follow-up observations of double-peaked AGN in BigBOSS could vastly increase the sample of known dual AGN.

# 4 Target Selection

## 4.1 Summary of Targeting Requirements

The primary science goal for the BigBOSS survey is to measure with high precision the baryon acoustic feature imprinted on the large scale structure of the universe, as well as distortions of galaxy clustering due to redshift-space effects. The survey will achieve this science goal through spectroscopic observations of three distinct classes of extragalactic sources over the redshift range $0 < z < 3.5$: luminous red galaxies (LRGs), star-forming emission line galaxies (ELGs), and quasi-stellar objects (QSOs). Each of these categories will require a different set of selection techniques to provide sufficiently large samples of spectroscopic targets from available photometric data. Further, to ensure high efficiency, the methods used must select objects with spectral features that will produce a reliable redshift or Ly-$\alpha$ forest measurement within the BigBOSS wavelength range. The requirements for each of the BigBOSS targets is summarized in Table 4.1.

Table 4.1: Summary of the minimum galaxy sample requirements for BigBOSS primary science

| Target | Feature | Redshift | Min. Vol. Density $(h/\mathrm{Mpc})^{-3}$ | Areal Density (obj/deg$^2$) |
|---|---|---|---|---|
| LRG | 4000Å break | $0.6< z <1.0$ | $3 \times 10^{-4}$ | 350 |
| ELG | [OII] emission | $0.7< z <1.7$ | $1 \times 10^{-4}$ | 2300 |
| QSO | Ly-$\alpha$ forest | $2.2< z <3.5$ | $1 \times 10^{-5}$ | 50 |

The lowest redshift sample of BigBOSS targets will be composed of LRGs. These luminous, massive galaxies ceased star formation more than a billion years before the time of observation, and therefore have evolved, red composite spectral energy distributions (SEDs). The BOSS survey is targeting these objects to $z < 0.6$ using SDSS *gri* colors and measuring spectroscopic redshifts using the prominent 4000Å break continuum feature. Since BigBOSS will need to extend to $z < 1.0$ and therefore other selection techniques are required. In particular, we will select LRGs using the prominent 1.6$\mu$m (restframe) "bump". This feature corresponds to the peak of LRG SEDs and provides a strong correlation between optical/near-infrared (NIR) color and redshift at $z < 1$. We will therefore use 3.4$\mu$m photometry from the space-based Wide-Field Infrared Survey Explorer (WISE) to efficiently select LRGs in the redshift range of $0.6 < z < 1.0$.

The majority of the spectroscopic redshift measurements for BigBOSS

will come from emission-line galaxies at redshifts $0.7 < z < 1.7$. These galaxies possess high star formation rates, and therefore exhibit strong line emission from ionized HII regions around massive stars, as well as blue composite SEDs. One of the strongest features of HII region spectra is the [OII] 3727 Å doublet, which consists of a pair of emission lines separated in wavelength by 2.8Å. The spacing of this doublet provides a unique signature, allowing for definitive line identification and secure redshift measurements even if it is the only feature observed. This has made it a key tool for measuring redshifts in several smaller-area spectroscopic surveys (such as DEEP2 and WiggleZ); as a result, the properties of strongly line-emitting galaxies have been well studied. The goal of the BigBOSS ELG target selection will be to provide a large sample of ELGs with sufficient [OII] line flux to obtain a redshift detection and measurement out to $z < 1.7$. We will use forthcoming large-area *gri*-band optical photometric datasets to select these targets.

The highest-redshift target sample will consist of QSOs. We will be able to measure large-scale structure using the foreground neutral-hydrogen absorption systems which make up the Ly-$\alpha$ forest at $2.2 < z < 3.5$. Unfortunately, QSOs have SEDs and magnitudes very similar to blue stars, which generally leads to inefficient and incomplete targeting for spectroscopic samples. BOSS selects quasars with a combination of techniques that depend critically on SDSS $u$-band measurements, providing 40 targets / sq. deg with a 50% success rate of finding a QSO at an appropriate redshift for Ly-$\alpha$ absorption studies. BigBOSS will achieve twice the BOSS target density by using variability information from time-series photometric surveys and allocating a portion of the BigBOSS survey to QSO target identification. BigBOSS will therefore provide redshifts for QSOs over a wide redshift range ($z < 3.5$) and only expose longer on the confirmed $z > 2.2$ quasars to measure the Ly-$\alpha$ forest.

For the purposes of the following targeting discussion, we define a few terms which we will use to describe the effectiveness of our selection techniques.

- *completeness*: The fraction of objects selected out of all the available objects of the desired class (e.g., the fraction of all $0.6 < z < 1$ LRGs with $r < 22.5$ that are selected by our targeting techniques)

- *redshift window efficiency*: The fraction of selected objects which lie within the detectable wavelength range and are of the correct object type.

- *spectral flux efficiency*: The fraction of selected objects that contain a spectral flux appropriate for redshift measurement. For LRGs and QSOs, this term encapsulates the accuracy of the photometric magnitude limit relative to the spectral continuum. For the ELG selection, this term encapsulates how the [OII] line flux is loosely correlated with the magnitude limit of the sample.

- *target selection efficiency*: As defined in §2.2, this is the product of the redshift window efficiency and spectral flux efficiency.

These measures are separate from considerations of what fraction of objects selected as targets are actually placed on fibers (discussed in §6.1) or which yield redshifts from pipeline software.

In this chapter, we will show that the combination of time-series photometry in forthcoming wide-area surveys and simple color selections can achieve the target density requirements of Table 4.1. We also provide expected redshift distributions of the targeted samples from the presented target selections. Chapter 5 details the design of the BigBOSS instrument, which informs a spectral simulator presented in Appendix A. This detailed spectral simulator aids in the design of the targeting strategy (such as magnitude limits), calculates exposure times, and estimates redshift measurement efficiencies. Given the expected target densities and exposure times, the overall survey strategy is developed in Chapter 6. Included in the survey strategy is an optimized method to tile the sky that maximizes the area of detected target redshifts and minimizes the overall time for the survey. Chapter 6 also outlines a strategy for fiber allocation and calculates the total usage of available fiber exposure times. The main results of these chapters are summarized in Table 2.2 and are used to calculate the DETF Figure of Merit in Table 2.8.

## 4.2 Photometric Surveys

Selecting extragalactic sources for BigBOSS will require the use of imaging data for targeting. Therefore, the success of the survey is predicated on the availability of photometry over the entire BigBOSS footprint to sufficient depth to achieve our target number density requirements (after taking selection efficiency into account). Large area surveys with more than 10,000 $\deg^2$ of extragalactic sky coverage are rare in the Northern Hemisphere. However, there are several ongoing surveys that will deliver multiband photometry in the BigBOSS footprint within the next few years. These forthcoming datasets will serve as the backbone for BigBOSS target selection.

We describe these surveys in more detail below.

### 4.2.1 SDSS

The Sloan Digital Sky Survey [Abazajian et al., 2009] has served as an excellent photometric data source for wide-field studies. SDSS includes multiband (*ugriz*) photometry which can efficiently separate a wide variety of stellar and extragalactic sources using their optical spectral energy distributions (SEDs). The $5\sigma$ magnitude depths for the SDSS *ugriz* bands are 22.0, 22.2, 22.2, 21.3, and 20.5, respectively. The BOSS survey is designed to take advantage of this photometry, targeting both LRGs and Ly-$\alpha$ QSOs selected using SDSS imaging. SDSS covers a 10,000 deg$^2$ footprint with contiguous coverage over the North Galactic Cap and partial coverage of the South Galactic Cap.

The main SDSS photometric sample will largely not be deep enough to be useful for spectroscopic targeting in BigBOSS. However, we can use the well characterized properties of SDSS spectrophotometry to help calibrate the spectroscopic properties of BigBOSS. For example, the relative spectral calibration of SDSS F-stars can readily be used by BigBOSS to calibrate relative throughputs and to monitor variable sky transmission. Further, the results of the BOSS QSO survey and variability studies in the deeper Stripe 82 will inform the BigBOSS QSO target selection and reduce the number of stellar contaminants in our quasar survey. SDSS photometry and spectroscopy will provide a well-tested data source to calibrate with and compare samples against throughout the BigBOSS survey.

### 4.2.2 PanSTARRS

The PanSTARRS $3\pi$ survey [Pan-STARRS website, 2010] is a transient-sensitive survey designed to observe 30,000 deg$^2$ of sky over 12 epochs in each of the five *grizy* survey filters. The multiband photometry generated from the co-added exposures will reach depths that exceed that of SDSS and will serve as a source database for BigBOSS target selection. PanSTARRS has been designed to be a staged experiment, with additional telescopes scheduled to come online in the next decade. However, only the first of those telescopes (PS1) is currently taking survey data and will accomplish 360 seconds of total exposure time in three years of operation. Upon completion of this survey, we expect that the PanSTARRS co-added data will be released for public consumption and use for spectroscopic followup. Additional targeting information could also come from PS1 time-domain photometry, but

the public availability of the time variability information is uncertain at this time. Therefore, the BigBOSS targeting strategy does not depend on the availability of time-domain photometry from PS1.

### 4.2.3 Palomar Transient Factory

The Palomar Transient Factory (PTF) [Law et al., 2009] is a photometric survey designed to find transients over 12,000 deg$^2$ in the Northern Hemisphere. PTF is using the 1.2m Oschin Telescope at Palomar Observatory with the CFH12K camera to conduct this survey. Thus far, PTF has focused on obtaining Mould $R$ band photometry with a nominal 5 day cadence and 60 seconds of exposure time, as well as shallower coverage in the $g$'-band. Four years of survey operations will yield a total of four hours' exposure time in $R$ over the entire survey footprint. We project that the $R$-band depth of the final co-added data will be $\sim 0.5$ magnitudes fainter than PS1 and therefore more valuable to our target selection. In addition, since LBNL is a partner in the PTF collaboration, BigBOSS will have guaranteed access to time variability information from the PTF survey.

### 4.2.4 Ground-based Photometric Error Model

Our strawman plan for BigBOSS ELG target selection will focus on the co-added $gi$ bands from the PS1 survey and the co-added $R$ band from PTF. Since neither PS1 nor PTF have completed their surveys, we must model the photometric errors that match the depths expected from each survey. The error model can then be applied to synthetic magnitudes generated from galaxy SED templates convolved with the PTF and PS1 filter bands to reasonably represent the photometric quality of the surveys. The photometric signal to noise ratio for various telescope parameters is modeled with the

Table 4.2: Assumed PTF and PS1 parameters for the photometric error model in Eq. 4.1.

| Survey | band | $m_{site}$ | t (s) | $\omega$ (arcsec) | m ($5\sigma$) |
|---|---|---|---|---|---|
| PS1 | g | 22.85 | 360 | 1.3 | 23.4 |
| PTF | r | 21.55 | 10800 | 2.0 | 23.5 |
| PS1 | i | 22.05 | 360 | 1.0 | 22.7 |

equation

$$S/N = 10^{(-0.4m+0.4m_{site})} \times \left(\frac{t}{\pi\omega^2}\right)^{1/2}, \tag{4.1}$$

where $m$ is the source magnitude, $m_{site}$ is the site-dependent sensitivity, $t$ is the total exposure time, and $\omega$ is the FWHM of the source in arcseconds. Each filter band an independent value of $m_{site}$ which is solved for from the survey-reported $5\sigma$ depth shown in Table 4.2 . Figure 4.1 shows the photometric error versus source magnitude for the $gi$ bands from PS1 and $R$ band from PTF. For these estimates, we use a mean galaxy half light radius of 0.3" to represent the extended ELG galaxy objects observed at high redshift.

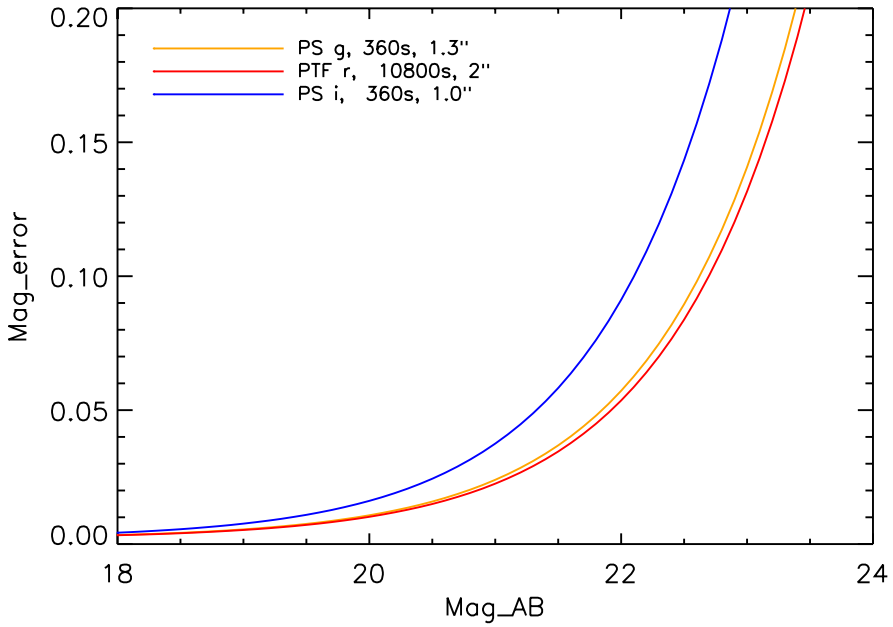


Figure 4.1: Assumed magnitude errors for the Palomar Transient Factory and PanSTARRS $3\pi$ survey.

### 4.2.5 WISE

Ground-based photometry will not always be optimal for selecting all targets of interest. In such cases, we can additionally make use of space-based surveys, which can obtain deep imaging at infrared wavelengths much more

efficiently. The experiment of greatest utility for BigBOSS is the WISE (Wide-field Infrared Survey Explorer) satellite, which is conducting an all-sky survey at wavelengths of 3.4, 4.6, 12 and 22$\mu m$ [Wright et al., 2010]. In the course of its 10-month mission (to be completed in 2010), 99.99% of the sky will be imaged at least 8 times, while regions near the ecliptic poles will be observed more than 100 times.

The key WISE channel for BigBOSS is 3.4$\mu m$, which will go the deepest for galaxy populations of interest, with 5$\sigma$ limit estimated to be somewhat better than the WISE goal of 120$\mu$Jy in the least-covered areas (we will use 100$\mu$Jy / 18.9 mag AB as an estimate of the actual limit in this proposal in the most conservative case), and reaching the confusion noise limit of 63 $\mu$Jy (19.4 mag AB) in the deepest regions (E. Wright, priv. comm.). The final WISE public data release is scheduled to occur in March 2012, providing ample time for optimizing BigBOSS target selection.

### 4.2.6 Other Imaging Surveys

For reference, we list below other wide field imaging surveys which, if available and well documented by the time of the BigBOSS survey, could be used to help define our targets.

**A. U-band Surveys**

The South Galactic Cap U-band Sky Survey [SCUSS website, 2010] is a joint project amongst the Chinese Academy of Sciences, its National Astronomical Observatories unit, and Steward Observatory, with observations planned to begin in September 2010. Using a mosaic of four 4K×4K CCDs covering a one square degree field, the survey plans to observe a 3,700 square degree field within the South Galactic cap using the 90-inch (2.3m) Bok telescope at Kitt Peak (belonging to Steward Observatory). Given the expected survey exposure time of 5 minutes per field, the limiting magnitude reached is estimated to be about 23 mag (5$\sigma$). A complimentary survey to SCUSS could also be performed in the Northern Hemisphere. A collaboration of French and Canadian astronomers have proposed a $u$-band CFHT Survey which would cover a minimum of 5,000 square degrees in the Northern extragalactic sky. A pilot survey, which should start in 2011, will observe the ∼800 sq. degree region covered by the CFHT Red Cluster Sequence-2 (RCS2) survey with MegaCam. Upon completion of this pilot survey, the CFHT $u$-band survey could then continue to partially cover the SDSS and PS1 footprint. The exposure times are expected to be about 10 minutes per field and the limiting magnitude will reach roughly $u \sim 24$ (5$\sigma$).

**B. DES**

The Dark Energy Survey (DES) [Abbott et al., 2005] will use a new wide-field camera for the 4-meter Blanco telescope at CTIO, the Dark Energy Camera (DECam), to probe dark energy via a wide-area photometric survey (as well as a smaller-area survey focused on detecting type Ia supernovae; as the latter will only cover $\sim$ 40 square degrees, it is of little relevance for BigBOSS). The camera is scheduled to be installed in 2011. In total, DES will cover 5000 square degrees, primarily in the Southern sky, over the course of 525 nights of observations over five years. The survey will deliver *griz* imaging is expected to deliver $5\sigma$ (point source, 0.9" seeing) limiting magnitudes of $g = 26.1$, $r = 25.6$, $i = 25.8$, $z = 25.4$, considerably deeper than BigBOSS requirements. The DES footprint is expected to have $\sim 500$ deg$^2$ overlap with the BigBOSS footprint, primarily in the equatorial SDSS Stripe 82 region.

**C. LSST**

The proposed Large Synoptic Survey Telescope (LSST) [Ivezic et al., 2008] will conduct a deep, 6-band (*ugrizy*) photometric survey covering over 20,000 square degrees (primarily in the Southern sky) focused principally on studies of dark energy. By combining a large field of view camera (observing 9.6 square degrees at a time) with a large-aperture (8.4-meter diameter) telescope, LSST is designed to rapidly survey the sky to deep depths. This will enable studies of faint transients and asteroids as well as yielding extremely deep coadded images by combining roughly 1000 observations of each area of sky over 10 years. For the main survey, a single visit to each field will yield $5\sigma$ magnitude limits of $u = 23.9$, $g = 25.0$, $r = 24.7$, $i = 24.0$, $z = 23.3$, and $y = 22.1$; coadded depths will reach 26.3/27.5/27.7/27.0/26.2/24.9. Each patch of sky will be visited about 1000 times in ten years with a camera that covers 9.6 square degree field of view. The main survey will also extend well into the Northern Hemisphere (Dec$< +33$ for 2.2 airmass limit) to cover the entire Ecliptic plane. Therefore, we expect that there will be significant overlap between the BigBOSS footprint and LSST, perhaps as large as 6,000 deg$^2$. Once LSST starts survey operations in 2018, inclusion of their photometry from the first year of operations could rapidly improve target selection for BigBOSS in the overlapping area.

## 4.3 Luminous Red Galaxies

### 4.3.1 Target Properties

The largest volume surveys of large-scale structure to date have targeted the highest mass galaxies in the $z < 1$ universe, a population commonly known as luminous red galaxies (LRGs) [Eisenstein et al., 2001]. These objects are luminous and red in the restframe optical bands due to their high stellar mass and lack of ongoing star formation. They are commonly found in massive galaxy clusters today, and therefore they exhibit strong clustering and a relatively high large scale structure bias ([Eisenstein et al., 2005], [Ho et al., 2009], [Kazin et al., 2010]). Because of their strong 4000Å breaks and the correlation between their apparent magnitudes and luminosity distance, LRGs at $z < 0.6$ can be selected efficiently and their redshifts estimated based on SDSS-depth photometry [Padmanabhan et al., 2007], while the strong absorption features around the break allow redshifts to be identified definitively in spectra of modest signal-to-noise. They have therefore formed the cornerstone of the BOSS spectroscopic redshift survey.

Surveying LRGs at higher redshifts is beneficial for studying cosmology as their strong biasing to the underlying dark matter halos leads to a greater power spectrum amplitude, aiding BAO measurements. However, LRGs are increasingly difficult to select at higher redshifts as the 4000Å break passes into the $i$ band (at $z \sim 0.75$) and imaging at longer wavelengths (e.g. $z, J, H$, or $K$-band) is required to estimate LRG redshifts. At sufficiently high redshifts, an additional difficulty is that LRGs will be less common simply due to galaxy evolution. At these early times before their star formation has ceased, they will have bluer restframe SEDs, lower stellar masses, and weaker absorption breaks than local LRGs ([Faber et al., 2007], [Brown et al., 2007]). Only a small subset of the massive red galaxy population was in place as early as $z \sim 2$ ([Daddi et al., 2005], [López-Corredoira, 2010]).

At $z < 0.55$, the BOSS LRG sample selection yields a number density above $3 \times 10^{-4}$ galaxies per $h^{-3}$ Mpc$^3$, sufficient to achieve the BigBOSS science goals. Therefore, at lower redshifts, we will either use existing BOSS spectroscopic samples or apply the BOSS target selection in regions not yet covered. The BOSS selection will yield 119 LRGs per deg$^2$. At higher redshifts, however, we require different selection techniques with NIR imaging from space. The remainder of this section will focus on the strategy we will use in this domain.

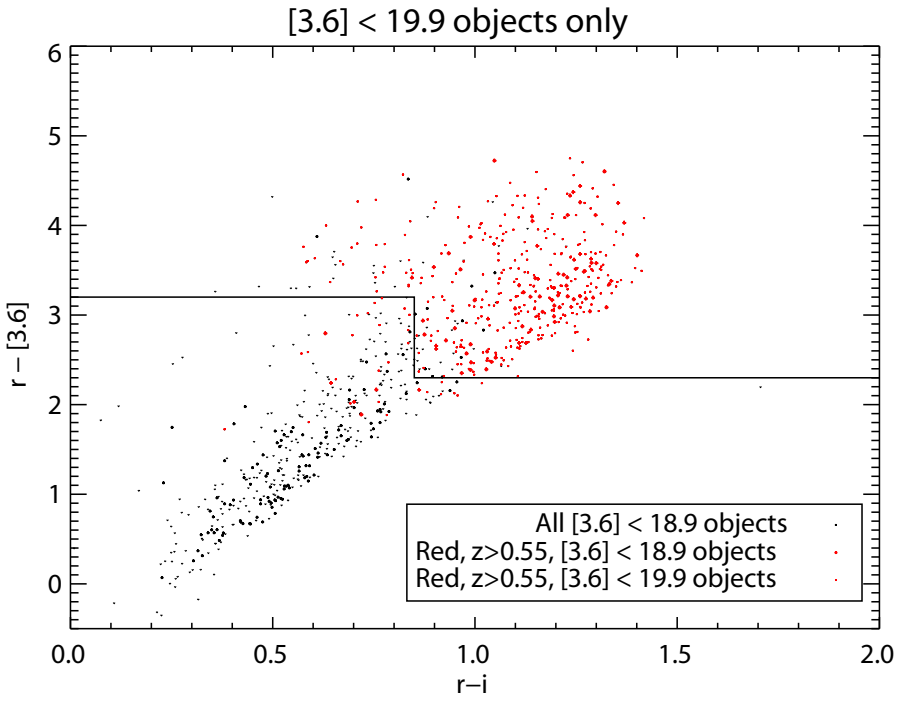


Figure 4.2: An optical/near-infrared color-color diagram for galaxies observed by the CFHT Legacy Survey, *Spitzer* IRAC, and the DEEP2 Galaxy Redshift Survey. In this and below figures, $r$ indicates CFHT LS $r$-band magnitude, $i$ indicates CFHT LS $i$, and [3.6] indicates IRAC 3.6$\mu$m AB magnitude. Galaxies with LRG-like SEDs at $z > 0.55$ are indicated by red points; those with [3.4$\mu$m] magnitudes below 18.9 are indicated by larger symbols.

### 4.3.2 Selection Technique

The spectral energy distributions of cool stars exhibit a local maximum at a wavelength of roughly 1.6$\mu$m, corresponding to a local minimum in the opacity of $H^-$ ions [John, 1988]. This feature, commonly referred to as the "1.6$\mu$m bump" dominates the near-infrared spectra of stellar populations with ages above $\sim$ 10 Myr, and represents the global peak in $f_\nu$ for populations older than $\sim$ 500 Myr [Sawicki, 2002]. Since they possess few young stars, luminous red galaxies at $z \sim 0.5 - 1$ will therefore exhibit relatively large near-infrared to optical flux ratios at wavelengths of $\sim 2 - 4\mu$m. The lowest-wavelength channel in WISE, centered at 3.4$\mu$m, is nearly optimal

for selecting these objects as it overlaps the bump at redshift $z \sim 1$. The infrared-to-optical flux ratio of LRGs rises monotonically with redshift as $z$ approaches 1, then will decline beyond $z \sim 1.1$. As a consequence of both the increased rarity of LRGs and the greater luminosity distance, LRGs at $z > 1$ are uncommon at the magnitudes BigBOSS will survey. A simple cut in $r$ - [3.4$\mu$m] color should therefore select LRGs effectively while adding in information from more optical bands can help in rejecting non-LRGs.

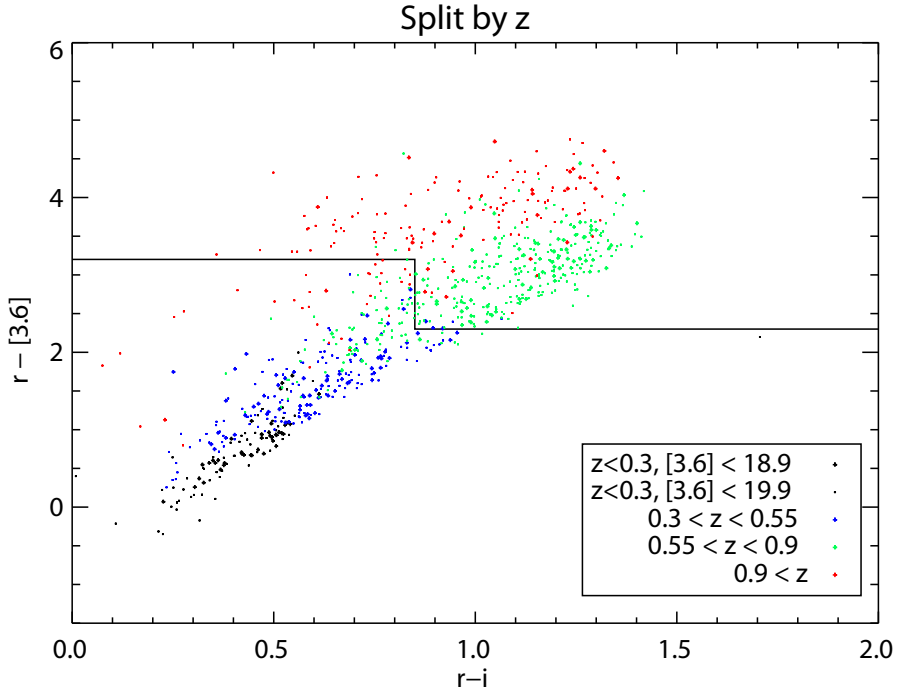


Figure 4.3: As Figure 4.2, with objects color-coded according to their redshift and symbol sizes determined by [3.4$\mu$m] magnitude.

To test selection techniques, we have employed publicly-released data from the AEGIS survey [Davis et al., 2007], which incorporates pan-chromatic imaging and spectroscopy from the DEEP2 Galaxy Redshift Survey [Davis et al., 2003]. In particular, we use optical catalogs derived from CFHT Legacy Survey data [Gwyn, 2008], NIR imaging catalogs from *Spitzer* IRAC [Barmby et al., 2008], and redshifts and restframe colors from DEEP2. All magnitudes used are on the AB system. In our tests, we use IRAC 3.6$\mu$m magnitudes as a proxy for WISE 3.4$\mu$m photometry; actual BigBOSS target selection will be optimized using WISE itself. At $z < 1.25$, 3.6$\mu$m lies on

the long-wavelength side of the bump, so the measured IRAC flux should be lower than 3.4$\mu$m flux for a given galaxy; as a consequence, estimates of [3.4$\mu$m] $< 18.9$ or $< 19.4$ sample sizes from this analysis will be conservative. As seen in Figures 4.2, 4.3, and 4.4, galaxies with red restframe colors (restframe $U - B > 0.9$) at redshift $z > 0.55$ are almost entirely confined to a limited region in an optical/near-infrared color-color plot. A strawman LRG selection criterion is shown by the solid lines in this figure.

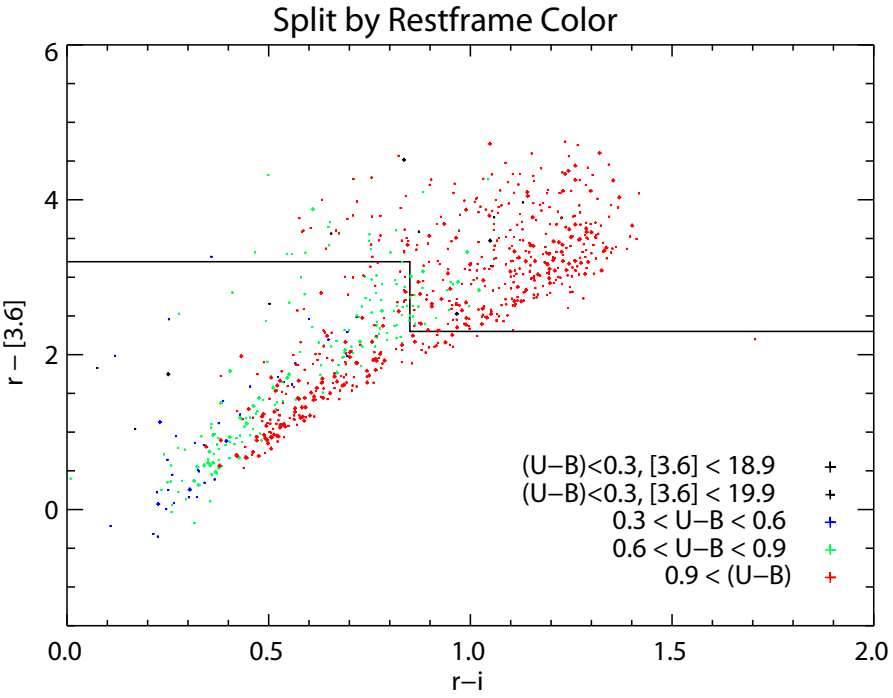


Figure 4.4: As Figure 4.2, with objects color-coded according to their restframe $U - B$ color. Objects with $U - B > 0.9$ generally have spectral energy distributions similar to LRGs.

Since the 1.6$\mu$m bump is present in all but the youngest stellar populations, a pure cut in infrared-to-optical ratio (or equivalently $r - [3.4\mu\text{m}]$ color) is effective at selecting objects in the target redshift range, but roughly 15% of the selected objects will be bluer than LRGs. By making the selection cut dependent on an optical color (both $g - r$ and $r - i$ have been tested and prove to be equally effective), these blue interlopers can be partially rejected; even a crudely optimized box (as shown in Figs. 4.2 – 4.4) improves the LRG redshift window efficiency to 90%.

### 4.3.3 Sample Properties

There are 420 objects per square degree within the depicted selection box with [3.6$\mu$m] magnitude $< 18.9$ (a conservative limit), or 1120 with [3.6$\mu$m] $< 19.4$; we adopt these as two fiducial scenarios for BigBOSS LRG samples. As these target densities are based on a single, 0.4 square degree region within the Extended Groth Strip, these source densities are subject to sample (or "cosmic") variance as well as Poisson uncertainty; they are uncertain at the 10-15% level as a result.

We can use DEEP2 redshifts to estimate the redshift distributions we will obtain from our $z > 0.55$ LRG target selection, though given the limited area covered by DEEP2, CFHT LS, and IRAC, both sample/cosmic variance and Poisson variance are large within small $0.1\Delta z$ bins. We consider two scenarios: a shallow sample selected to have [3.6$\mu$m] magnitude $< 18.9$ and $i < 21.5$; and a deeper sample with [3.6] $< 19.4$ and $i < 22$, yielding 380 or 670 targets per square degree, respectively. In Figure 4.5, we plot the redshift distributions of the resulting samples, along with the overall redshift distribution of all galaxies in our LRG selection box and the number density goal of $3 \times 10^{-4}$ objects per $h^{-3}$ Mpc$^3$. Both of these samples are larger than the LRG population assumed in Section 2.2. However, as seen in the figure, we have more than enough targets at $z < 0.8$ and will downsample at those redshifts accordingly. The apparent magnitude of LRGs is strongly correlated with their redshift as they are on the exponential tail of the luminosity function, allowing us to sculpt the LRG redshift distribution efficiently.

Our spectral flux efficiency for $z > 0.55$ LRGs will primarily be a function of optical magnitude, as this will determine the signal-to-noise we achieve in the spectrum of a given galaxy. We therefore will only target WISE-selected LRGs down an $r$ or $i$ magnitude limit. Figure 4.6 shows the effect changing this limiting magnitude will have on the surface density of selected targets, assuming either a [3.6] $< 18.9$ or [3.6] $< 19.4$ sample. We find that a limiting magnitude of $r \sim 22.5$ or $i \sim 21.5$ should produce a volume density sufficient for the BigBOSS LRG sample. Given the photometric survey magnitude limits of PTF and PS1, we expect that the optical spectral flux will be highly accurate at these limits ($\sim 0.05\%$ magnitude error), and therefore the overall target selection efficiency will be dominated by the LRG redshift window efficiency at 90%.

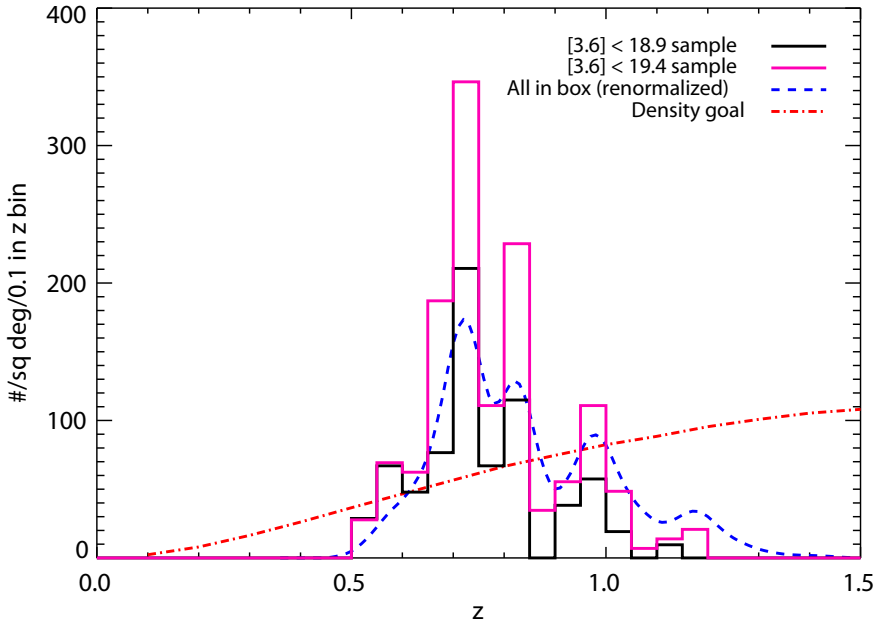


Figure 4.5: Redshift distributions for $z > 0.55$ LRG samples, estimated using data from DEEP2, CFHT LS, and *Spitzer* IRAC. Due to the small area covered and LRG sample sizes, both sample/cosmic variance and Poisson variance are large within small $0.1\Delta z$ bins. Distributions for two possible scenarios are plotted: a shallow sample selected to have [3.6$\mu$m] magnitude $< 18.9$ and $i < 21.5$ (solid black histogram); and a deeper sample with [3.6] $< 19.4$ and $i < 22$ (dot-dashed purple histogram). We also plot the redshift distribution of all galaxies in the LRG selection box (blue dashed line), renormalized to match the average number of galaxies per square degree from the other two samples. The dot-dashed red curve corresponds to the LRG number density goal of $3 \times 10^{-4}$ objects per $h^{-3}$ Mpc$^3$; this goal is easily achievable to $z = 0.8$, and we are within 30% of the goal to $z = 1$.

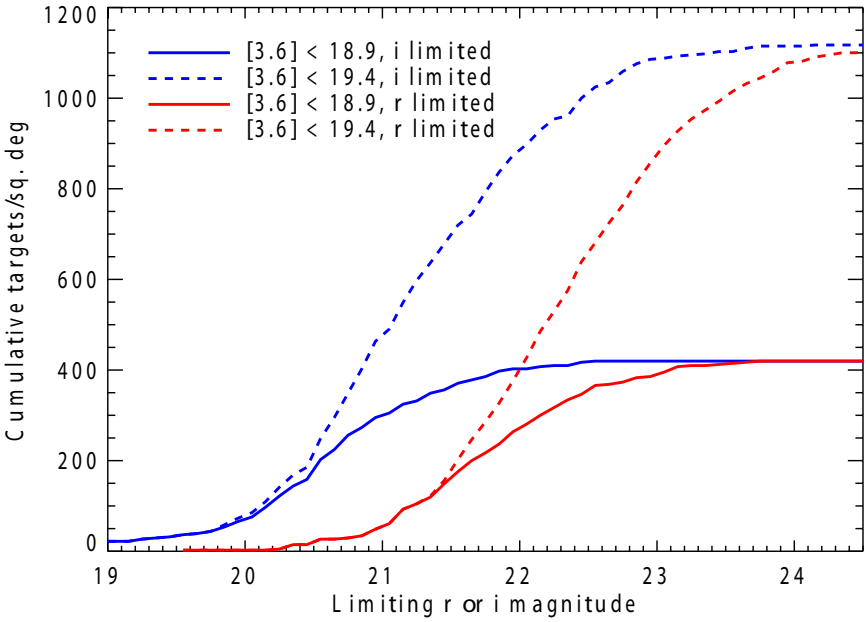


Figure 4.6: Surface densities of $z > 0.55$ LRGs as a function of limiting $r$ and $i$-band magnitude. We consider samples to two possible WISE depths, a conservative depth of $[3.6] < 18.9$ and the extended mission depth $[3.6] < 19.4$. Target LRG sample sizes are readily achievable so long as satisfactory signal-to-noise is obtained down to $r \sim 22.5$ or $i \sim 21.5$.

## 4.4 Emission Line Galaxies

### 4.4.1 Target Properties

The largest sample of galaxies that will be selected by BigBOSS are emission line galaxies. These galaxies are typically the brightest late-type spirals. The composite rest-frame colors of these galaxies are typically bluer than those of evolved galaxies such as LRGs, due to their active star formation in the recent past; however, as they can exhibit a wide range of internal dust properties, their colors can be significantly dependent on inclination effects. In the local universe, ELGs (defined using a constant emission line luminosity threshold) are much less numerous than at high redshifts ($z > 1$); this predominantly reflects the fact that the overall star formation rate of the Universe was $\sim 10\times$ higher at that time [Hopkins & Beacom, 2006]. The correlation of emission lines to star-formation is established well enough to measure the star-formation rate (SFR) to $z \sim 2$, around the peak of

the cosmic SFR [Kennicutt, 1998; Moustakas, Kennicut & Tremonti, 2006; Hopkins & Beacom, 2006].

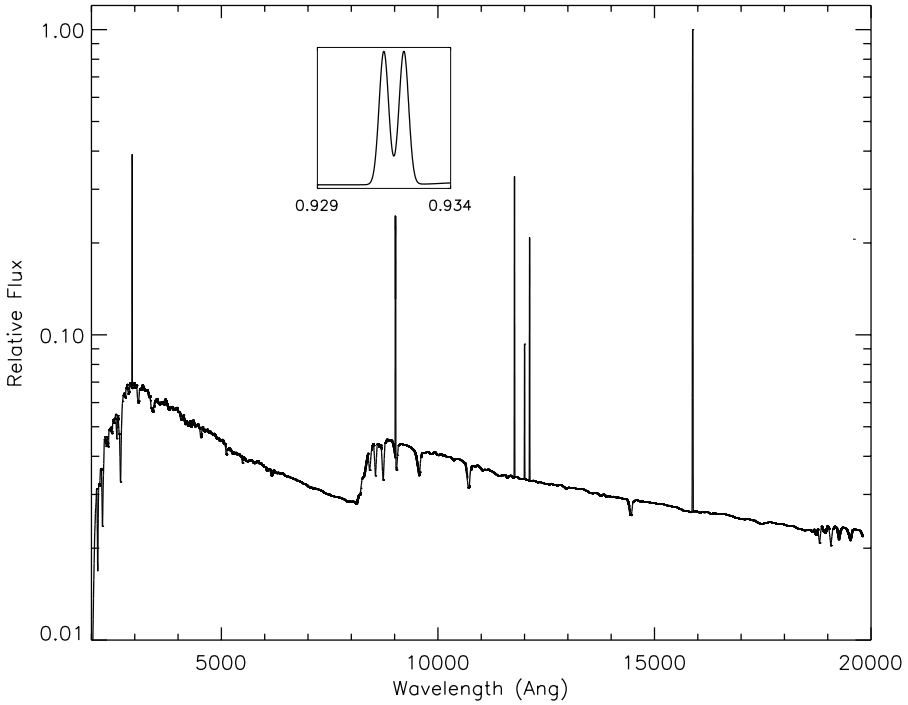


Figure 4.7: A template emission line galaxy spectrum at $z = 1.4$ sampled at a constant 0.76Å per pixel interval, similar to the resolution provided by the BigBOSS visible and red spectrographs. The inset figure shows that the [OII] doublet is resolved at this sampling frequency and is split almost evenly between the line components, as is generally observed.

In regions where star formation has recently occurred, short-lived, blue massive stars will provide large numbers of energetic photons into the local interstellar medium, resulting in ionized HII regions. As ions and electrons in these regions recombine, a variety of emission lines will result; the most luminous lines in the optical are members of the Hydrogen Balmer series or are emitted by oxygen ions. The total rate of ionizations and recombinations from a galaxy will be proportional to the total number of massive stars; hence, emission line fluxes provide a useful diagnostic of a galaxy's star formation rate.

Figure 4.7 shows an example synthetic $z = 1.4$ emission line galaxy spectrum constructed from a star-forming template SED [Bruzual & Char-

lot, 2003] with emission line fluxes calibrated to match zCOSMOS observations at lower redshifts (see Section 4.4.2 for details). The strongest of the emission lines are typically the H$\alpha$ line at 6563Å rest-frame and the forbidden [OII] doublet transitions at 3727Å. Additional strong lines include H$\beta$ $\lambda$4861 and the [OIII] $\lambda 4959 + 5007$ doublet. Of all the emission lines, the [OII] doublet will be most useful for probing the redshifts required by BigBOSS ($z < 2$) without requiring observations beyond 11000Å, where the near-IR sky background increases rapidly. An additional benefit to [OII] is that it is a doublet closely spaced in wavelength (3Å), providing a unique signature. Each component line contributes roughly one half of the total line flux, since electron densities typically range from 100-1,000 $e^-$ $cm^{-3}$ for star-forming galaxies [Pradhan et al., 2006; Kewley & Ellison, 2008].

The doublet nature of [OII] 3727Å emission provides a unique signature for line identification if observations have sufficiently high resolution; if both components are robustly identified, a secure redshift results, in contrast to single-line redshifts which can correspond to a number of possibilities in the absence of other detected features. The DEEP2 experiment [Davis et al., 2003] recognized the unique features of the [OII] emission line and used it (as well as the 4000Å break prominent in older stellar populations) to conduct a redshift survey focusing on the regime $0.7 < z < 1.4$. To date, the survey has resulted in 33,000 confirmed redshifts, most of them obtained via the [OII] doublet, measured in four different survey fields totaling $\sim$3 $deg^2$. Experience from DEEP2 shows that the resolution required to nominally split the [OII] doublet (220 km/s FWHM) is sufficient to produce two recognizably separate line features for the bulk of emission line galaxies, providing high confidence in the line identification[Weiner et al., 2005]. Only a small fraction of galaxies contain sufficiently high rotational velocities to blend the doublet, and those massive galaxies typically exhibit continuum absorption features from the Balmer series or Ca H & K. Further, [OIII] and H$\beta$ emission lines will be detectable at wavelengths below 11,000Å to $z \sim 1$, providing additional certainty to redshifts when the lines have sufficient flux to be detected. The success of the DEEP2 experiment in identifying and measuring emission-line redshifts serves an excellent test of strategies for BigBOSS.

### 4.4.2 [OII] Luminosity Function

With large [OII] datasets as DEEP2, it is possible to measure the number density of objects as a function of both [OII] luminosity and redshift. Since surveys of line luminosities are generally limited in completeness at either

the faintest or brightest luminosities due to choice of survey characteristics, it is important to include multiple samples that cover a wide range of luminosities. Figure 4.8 shows a compilation of the [OII] luminosity functions produced from multiple emission line datasets at a mean redshift of $z \sim 1.2$, including the DEEP2 Galaxy Redshift Survey [Zhu, Moustakas & Blanton, 2009] and narrow-band filter observations of the Subaru Deep Field [Ly et al., 2007; Takahashi et al., 2007] and the COSMOS field [Takahashi et al., 2007]. We find that the composite [OII] luminosity function is best represented by an Abell function (rather than a Schecter function) to match the power law behavior measured by DEEP2 at the bright end of the luminosity function. We parameterize the luminosity function according to

$$\frac{dN}{dLog(10)} = \frac{ln(10)}{ln(\sqrt{2})} \frac{N_b^2 L_b^2}{L_b^2 + L^2}, \tag{4.2}$$

where $N_b$ and $L_b$ characterize the luminosity function behavior as a function of redshift with

$$Log(N_b) = -3.5 + 2.0(x - x^2), \tag{4.3}$$

$$Log(L_b) = 40.95 + 3.0(x - x^2), \tag{4.4}$$

$$x = Log(1 + z). \tag{4.5}$$

The result of this model function is displayed in Figure 4.8 for $z \sim 1.2$. Another interesting feature is that for a fixed space density, the [OII] luminosity is greater at higher redshifts; this is a result of the $\sim 10\times$ larger mean star formation rates in blue galaxies of all types at $z \sim 1$ compared to today. To project line fluxes for redshifts at$z > 1.4$, we adopt a conservative scenario in which the star-formation rate remains constant from $1.4 < z < 2$ (roughly 1Gyr of cosmic time) and no more evolution occurs in of the [OII] line luminosity (J. Moustakas, priv. comm.).

To formulate the ELG selection criteria for BigBOSS, we use fit galaxy templates and photometric redshifts from the COSMOS survey [Ilbert et al., 2009] and generate synthetic magnitudes using the *Le Phare* photometric redshift software. The COSMOS templates incorporate emission lines calibrated based on [OII] fluxes from VVDS spectroscopic measurements [Le Févre et al., 2005]. For $z > 1.4$, the [OII] fluxes are calibrated by the M(UV)-[OII] relation [Kennicutt, 1998]. This calibration of the [OII] flux with redshift is accurate to 0.2 dex, and this scatter is maintained in the catalog for those objects where the calibration is implemented.

As a check of the COSMOS [OII] flux calibration, we plot the luminosity function measured from the catalog in Figure 4.8. We find that the luminosity function is in good agreement with our model Abell function. The

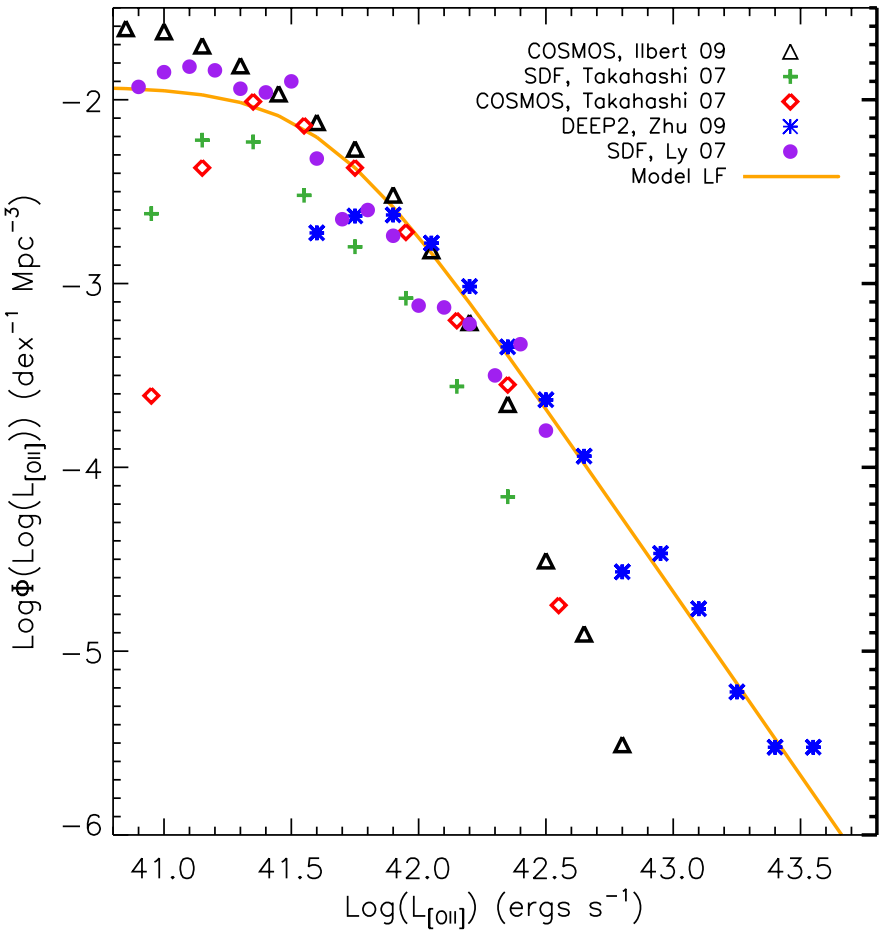


Figure 4.8: The [OII] luminosity function measured from photometric and spectroscopic surveys near $z$ 1.2. The luminosity function from DEEP2 spectroscopic measurements behaves as a power law on the bright end and shows good agreement with previous work in the Subaru Deep Field (SDF) and COSMOS field [Ly et al., 2007; Takahashi et al., 2007; Ilbert et al., 2009]. Note that each survey has incompleteness at both the bright and faint ends but the model luminosity function tracks the best sampled data in a given regime.

COSMOS LF includes more objects than DEEP2 at low luminosities largely because it is based on a photometric-redshift sample (with [OII] emission assigned according to the heuristics described above), and hence includes objects fainter than the DEEP2 limit of $R = 24.1$. However, the DEEP2 LF, which has been based upon spectroscopic redshifts, appears to better track the observed LF from the deepest narrow-band imaging (SDF) at higher line luminosities. It appears that the methods used to assign [OII] fluxes to objects with photometric redshifts from COSMOS may break down at the highest luminosities, possibly due to the VVDS calibrators consisting predominantly of redder galaxies lying at $z < 1$ (due to the $i = 22.5$ magnitude limit applied and lack of secure redshifts at higher $z$ – an illustration of the disadvantages of low-resolution [$R \sim 200$] observations when [OII] is the only feature observed).

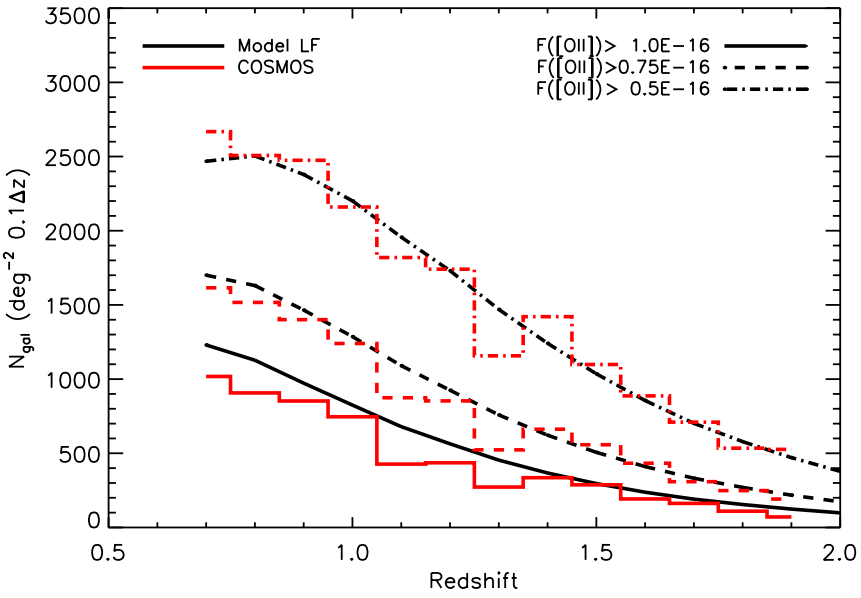


Figure 4.9: Comparison of redshift distributions at three limiting [OII] line fluxes as predicted from COSMOS photometric redshift and restframe spectrum fits calibrated with VVDS [OII] line flux data [Ilbert et al., 2009] and from the model [OII] luminosity function depicted in Fig. 4.8. The agreement is extremely good save at the highest fluxes, for which we would expect the COSMOS estimates to be low based on the previous figure.

By integrating the model luminosity function above a given flux limit, we can construct redshift distributions representative of the ELGs available for targeting by BigBOSS (Figure 4.9). As an additional check on the COSMOS catalog and our model LF, we also plot the redshift distribution resulting from applying the same cuts to the COSMOS sample. We find that the two methods predict similar redshift distributions over a range of [OII] flux limits near the minimum detectable line flux for BigBOSS. This result is reasonable since the bulk of the sample comes from objects in the range where the LFs are in good agreement, having $L_{[OII]} \sim 10^{41.5} - 10^{42.5}$ (ergs $s^{-1}$). The agreement between the model luminosity function and COSMOS predictions increases our confidence that the number density of bright [OII] emitters is well measured up to $z < 1.4$ and conservatively estimated for $1.4 < z < 2$.

**Linear Bias** The linear clustering bias of bright emission line galaxies relative to their dark matter halos is a matter of current study, but several sources have made relevant measurements. DEEP2 looked at the bias as a function of restframe color at a median redshift of z=0.9 ([Coil et al., 2008], hereafter C08). They found that the blue galaxies, those with the strongest star-formation and [OII] emission line measurement, had an absolute linear bias of $b = 1.28 \pm 0.04$ over a scale length of $1 - 10h^1$ Mpc at $z = 0.9$. C08 found that this clustering strength is consistent with similar ELG bias measurements from other samples [Marinoni et al., 2005] and that the absolute linear bias at $z \sim 1$ is greater than that in the nearby universe.

Other studies have looked at the clustering as a function of [OII] luminosity to investigate whether there is any correlation between halo mass and line brightness. Using Subaru X-ray Deep Field and semi-analytic models of the relationship between baryonic gas mass and dark matter halos, Sumiyoshi et. al. (2009) estimated the linear bias for various UV-calibrated [OII] flux limits over three redshift bins between $0.5 < z < 1.7$. They found that the bias was largely insensitive to their [OII] flux estimates except for the very brightest objects ($F_{[OII]} > 1 \times 10^{-15}$ ergs/s/cm$^2$) but the overall bias increased with redshift. For our initial BigBOSS projections, we assume that the bias increases with redshift to preserve a constant clustering amplitude; this assumption provides a rough fit to measured galaxy correlation function amplitudes for massive star-forming objects at redshifts from $z \sim 0$ (SDSS) to $z \sim 4$ (Steidel). Based on the clustering of $z \sim 1$ samples, we adopt the model $b = 0.76/g(z)$ where $g(z)$ is the cosmological growth function normalized by a factor of $1/(1 + z)$.

### 4.4.3 Selection Technique

The vast majority of spectroscopic targets for BigBOSS will be ELGs, and therefore the survey efficiency will largely depend on the the efficient selection of ELG targets from photometric data. Given that DEEP2 efficiently selects ELGs with $z > 0.7$ using broadband optical photometry, we expect that BigBOSS can use similar methods to select objects in a similar redshift range with a high confidence in success. We will therefore first describe the methods applied for DEEP2, and then discuss how they may be adapted for BigBOSS.

Figure 4.10 shows the expected CWW and Kinney-Calzetti tracks [Coleman, Wu & Weedman, 1980; Calzetti et al., 1994] over the redshift range $0 < z < 2$ in CFH12K Mould $BRI$ photometry for a range of galaxy spectral energy distributions (SEDs). As can be seen from this figure, galaxies of all types have $BRI$ colors that rapidly become redder in $R - I$ as the 4000Å break transitions into the $R$-band at $z \sim 0.7$; this effect is strongest for red galaxies and weakest for starbursts. This allows an efficient division between $z < 0.7$ and $z > 0.7$ objects; the dot-dashed line in the figure shows the color selection actually used by DEEP2, which was optimized for completeness at $z > 0.75$ using redshifts of objects in the Extended Groth Strip (where no color preselection is applied). Star-forming galaxies with $z > 0.75$ – roughly equivalent to our emission-line sample – occupy a region in color space below and to the right of the dashed line. The DEEP2 selection had a target completeness of 97% for galaxies at $z > 0.75$ and a targeting efficiency (i.e., fraction of the selected sample which has $z > 0.75$) of 85%. The total selection efficiency for the DEEP2 sample was therefore $\sim 82\%$.

Due to the depth limits of available photometric surveys (see Section 4.2) and differing survey goals, BigBOSS will likely use a shallower imaging dataset than DEEP2 with a smaller color selection box to maximize the probability of obtaining [OII] detections. To simulate the expected photometry, we have generated synthetic magnitudes from the COSMOS fit galaxy templates for the photometric redshift sample described in 4.4.2 in both the Sloan $griz$ bands (PS1) and the Mould $GR$ bands (PTF). We also add random magnitude errors onto the synthetic magnitudes based upon the models described in Section 4.2.4.

Figure 4.11 shows the location of objects in the $gri$ color plane using the COSMOS synthetic photometry and the expected PTF and PS1 photometry to $r_{AB} < 23.4$. The figure also color codes galaxies which have [OII] flux above $9 \times 10^{-17}$ ergs/s/cm$^2$ in three redshift bins: $0.7 < z < 1.2$, $1.2 < z < 1.6$, and $1.6 < z < 2.0$ (refer to Appendix A for a calculation of the

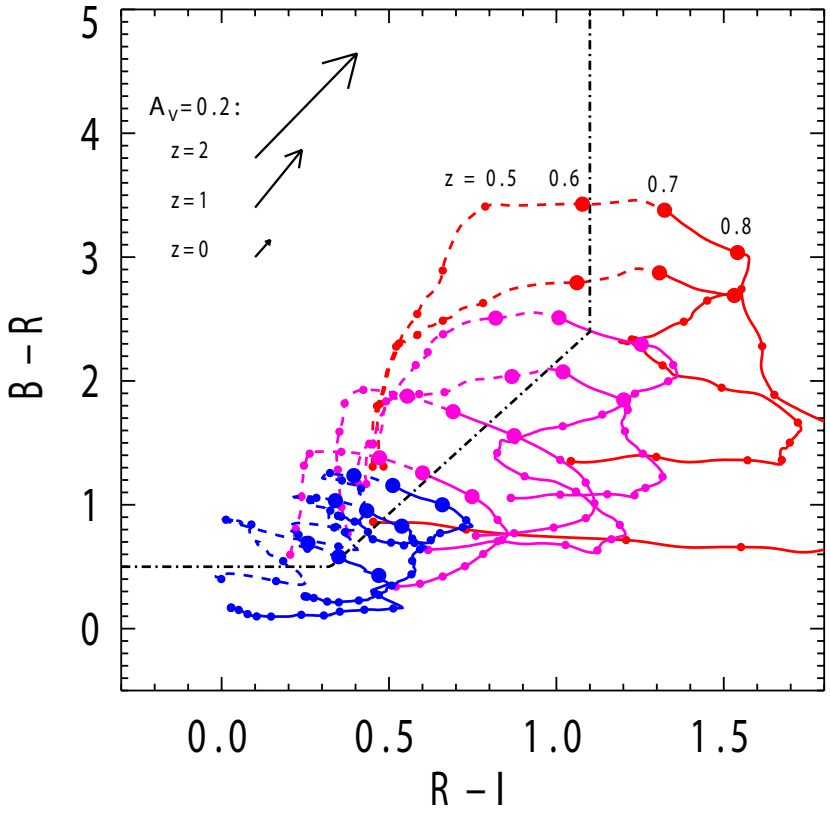


Figure 4.10: BRI color-magnitude diagram illustrating the target selection techniques applied for the DEEP2 Galaxy Redshift Survey utilizing CFH12K photometry. The colored tracks are the trajectories of objects with CWW and Kinney-Calzetti [Coleman, Wu & Weedman, 1980; Calzetti et al., 1994] template spectra through this color space over the redshift range $0 < z < 2$. Red lines correspond to early-type templates and blue to late-type starbursts; dots indicate intervals of 0.1 in $z$. The black line (dot-dashed) shows the DEEP2 color selection applied, which has been optimized using observed redshifts in the Extended Groth Strip (where no color cut is applied) to select $z > 0.75$ objects below and to the right of this line.

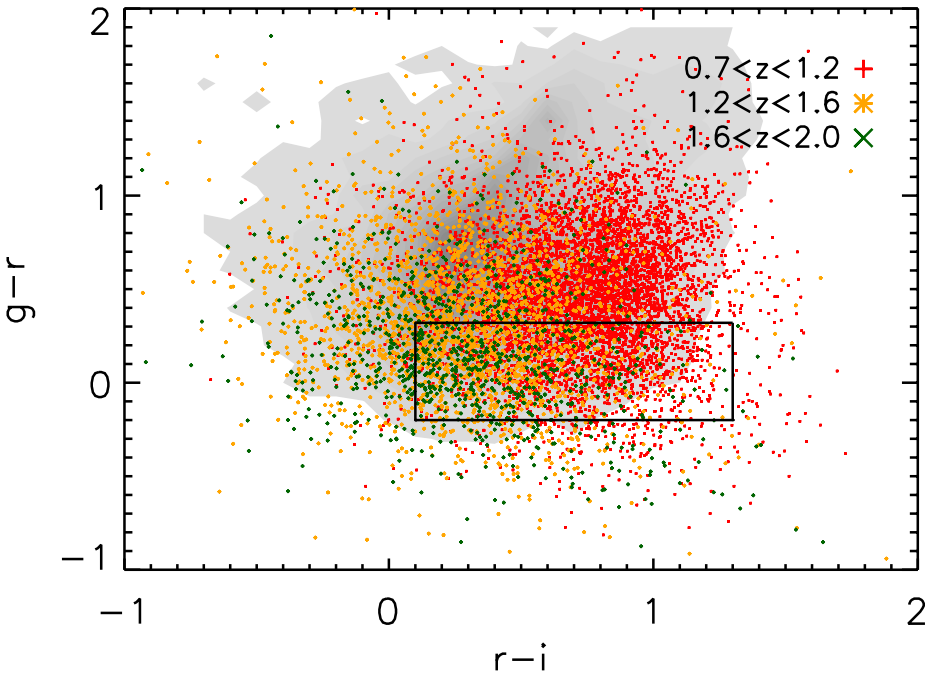


Figure 4.11: Emission line galaxy color selection using synthetic photometry for the 1.3 deg$^2$ COSMOS sample described in §4.4.2, applying PTF $r$ and PS1$gi$ magnitude errors estimated as described in §ss4:photsurveys . The gray contours indicate all galaxies with $r < 23.4$ and the data points indicate those galaxies which have an [OII] flux greater than $9\times10^{-17}$ ergs/s/cm$^2$ (see Appendix A). The black box indicates a simple color cut that would select the brightest [OII] emission line galaxies with $z > 0.7$ with high efficiency.

expected BigBOSS [OII] line flux limit). As was also seen for the DEEP2 BRI selection, low-redshift star-forming galaxies have bluer $(r - i)$ colors than $z \sim 1$ objects, but the SEDs migrate towards bluer colors as redshift increases. We also show an illustrative color selection box which we will use to predict BigBOSS sample properties in the next section. This selection is not unique; one can choose a variety of other selections that will generally modify the target densities at $z \sim 1$ as opposed to higher or lower redshifts.

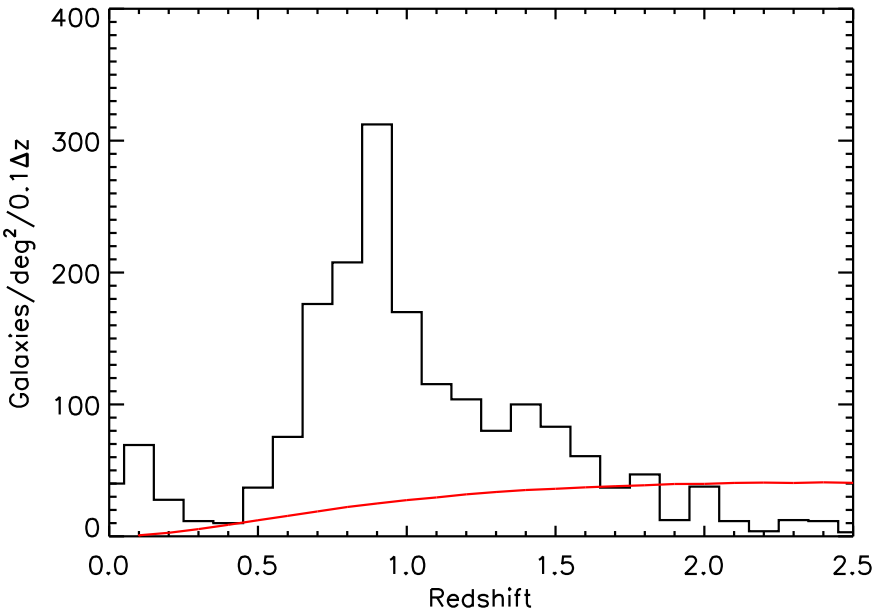


Figure 4.12: The predicted redshift distribution of objects found in the ELG color selection box in Figure 4.11, based on COSMOS photometric redshifts and synthetic photometry. The red line represents a constant volume number density corresponding to the target goal of $n = 1 \times 10^{-4}$ $(h/\mathrm{Mpc})^{-3}$.

### 4.4.4 Sample Properties

Figure 4.12 shows the redshift distribution (based on COSMOS photometric redshifts) for objects located in the simple selection box shown in Figure 4.11. The selection produces a distribution of ELGs with a redshift range of $z > 0.7$ where the number density of targets exceeds the BigBOSS requirements (Section 4.1) to a redshift of $z = 1.7$. Our initial optimization studies have shown that the FoM is optimized best when the greatest volume of the Universe can be sampled with the greatest efficiency and number density in the allotted survey time, in line with previously published results [Parkinson et. al., 2010]. The particular shape of the redshift distribution is a second order effect in optimizing the dark energy FoM.

Based on the redshift distribution shown in Figure 4.12, we estimate a redshift window efficiency of 70% at selecting [OII] ELGs in the BigBOSS from $0.7 < z < 1.7$. A full 92% of the objects reside at $z < 1.7$, where BigBOSS will have sensitivity to [OII] and other prominent emission lines (e.g.,

H$\alpha$, H$\beta$, and [OIII]). The redshift window efficiency is therefore dominated by the high redshift tail of the distribution and can be improved by reducing the magnitude limit of the selection (at the expense of overall target density), by including additional color information, or by pushing the selection box redder in $r - i$.

In Figure 4.13, we plot the total surface density of ELGs that have $F_{[OII]} > 9 \times 10^{-17}$ ergs/s/cm$^2$ within the *gri* color selection box as a function of $r$-band magnitude limit. In order to use the focal plane fibers with $> 80\%$ efficiency, we project that the ELG target density should be $\sim 20\%$ higher than the fiber density (cf. §6), or about 2300 ELGs / deg$^2$. We see that the ELG selection provides this target density for an $r$-band limit of $r < 23.4$. Figure 4.13 also shows the color-selected fraction of objects that will have [OII] line fluxes above various limits as a function of the limiting $r$ magnitude. We find that the fraction of objects lying in the selection box that have $F_{[OII]} > 9 \times 10^{-17}$ ergs/s/cm$^2$ is roughly 70%; this will be our expected spectral flux efficiency. It should be noted that objects with [OII] fluxes below this limit may well yield redshift measurements, but they will have a lower signal-to-noise. Higher values of spectral flux efficiency could be obtained by lowering the magnitude limit of the selection, resulting loss in the total number density of selected targets unless the color selection box is revised.

In Table 2.2, we record the total ELG target selection efficiency as the product of the ELG spectral flux efficiency (70%) and the fraction of selected objects in our detection window of $z < 1.7$ (92%). The total ELG target selection efficiency is therefore 65%. The final rate of redshift success (the product of fiber completeness, targeting efficiency, and redshift efficiency) for the BigBOSS ELG target selection presented here is estimated to be $\sim 40\%$; this is the number of potential ELG targets which will be actually placed on a fiber, will yield a redshift, and will turn out to be in the desired redshift range. Although this may seem low, it matches the DEEP2 selection efficiency almost exactly (as DEEP2 had a targeting efficiency of 82%, was able to observe 70% of potential targets, and yielded redshifts for 70% of objects observed). It is therefore not unusual for a color-selected survey of the $z \sim 1$ universe.

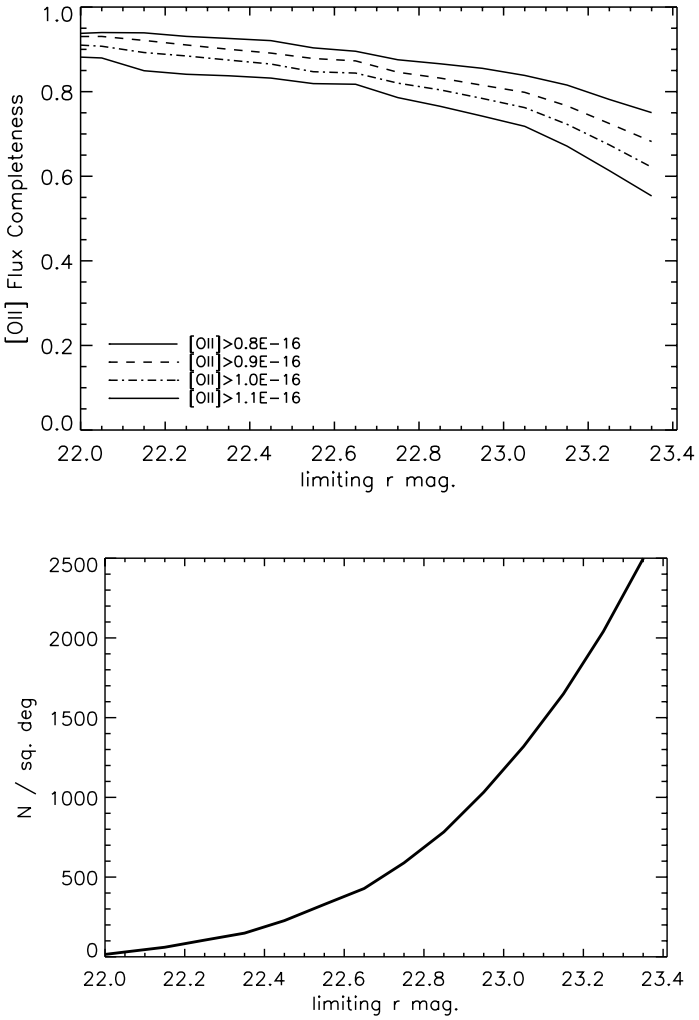


Figure 4.13: *top:* Cumulative ELG target density as a function of $r$-band magnitude limit after applying the [OII] flux limit of $9 \times 10^{-17}$ ergs/s/cm$^2$. The BigBOSS survey requires $\sim 2300$ total ELG targets per square degree to efficiently use the focal plane fibers. *bottom:* The fraction of color-selected objects in Figure 4.11 having [OII] flux above a certain value, as a function of limiting $r$ magnitude. The overall spectral flux efficiency for our expected $9 \times 10^{-17}$ ergs/s/cm$^2$ flux limit (see Appendix A), assuming an $r$-band limit of $r < 23.4$, is therefore $\sim 70\%$.

## 4.5 Quasi Stellar Objects

### 4.5.1 Target Properties

Quasi stellar objects (QSOs) are extremely luminous extragalactic sources associated with active galactic nuclei (AGN). QSOs are related to gravitational accreation onto supermassive black holes within these active galaxies, and unobscured type 1 quasars are produced from the beaming of synchrotron radiation along the polar axis of the black hole. As such, the morphology for the brightest of these objects are viewed by the observer to be point-like rather than the typical extended source nature of galactic emission. Further, the SEDs have unique "hard" spectra in the X-ray wavelength regime, bright Ly-$\alpha$ emission in the rest-frame UV, and the power law behavior of $F_\nu \propto \nu^{-\alpha}$ in the mid-infrared bands [Stern et al., 2005]. While the specific physical processes that lead to the formation of QSOs is a ongoing topic of study, current data show that quasar luminosities are correlated with their spheroidal mass and that galaxy mergers contribute to growth of both the dark matter halos and the central massive black hole [Hopkins et al., 2006]. QSOs are therefore correlated with galaxy clusters with massive dark matter halos at high redshift [Croom et al., 2005; Ross et al., 2009] and the number density of quasars increases at earlier times when galaxy merger rate was greater, peaking at $z \approx 2 - 2.5$ [Richards et al., 2009].

Although broad-line quasar spectra have particular features that separate them from typical star-forming galaxy SEDs, the point-like morphology, apparent magnitudes, and exponential frequency dependence give unobscured (type 1) quasars photometric characteristics that mimic faint blue stars in optical wavelengths. Figure 4.15 shows QSOs overlap the stellar locus for several Sloan *ugriz* color-color planes. The greatest separation from the stellar locus comes from *ugr* colors where the "UV excess" in $u-g$ produces bluer colors than that of most stars. However, the UV excess is less strong for $z > 2$ quasars where the Ly-$\alpha$ forest dampens the hard QSO spectrum. While sophisticated neural-network algorithms have been developed to utilize all available SDSS color information to produce quasar photometric redshifts [Yeche et al., 2010], the current photometric selection used by BOSS to target Ly-$\alpha$ QSOs from $2.2 > z > 3.5$ still has a 50% targeting efficiency. The BOSS selection produces 20 QSOs / deg$^2$ down to the SDSS photometric limit of $g < 22.1$.

To increase the number of Ly-$\alpha$ forest sightlines over those measured in BOSS, the BigBOSS target selection goal is to deliver a highly-complete Ly-

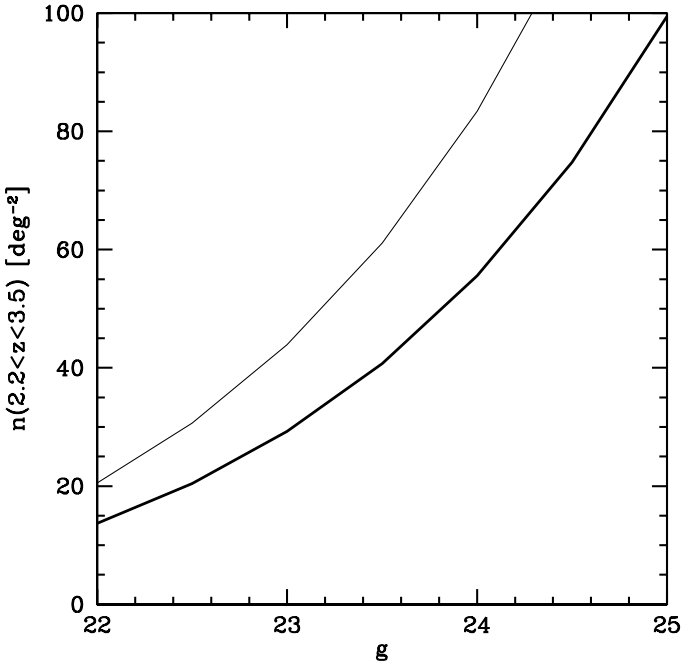


Figure 4.14: Surface density of quasars, per sq. deg., integrated over the range $2.2 < z < 3.5$, for the J06 luminosity function (thin line), or 2/3 of that (thick line) for a 66% complete sample.

$\alpha$ QSO sample. This selection goal presents multiple photometric targeting challenges. First, there is a larger uncertainty in the faint end of the underlying QSO luminosity function. Figure 4.14 shows the integrated surface density for $2.2 < z < 3.5$ QSOs from the Jiang et al. (2006, hereafter J06) luminosity function. At $g = 23$, a *complete* sample would give 45 QSOs / deg$^2$ in this redshift range whereas the LSST luminosity function [Hopkins et al., 2007b; Abell et al., 2009] predicts 85 QSOs / deg$^2$, nearly a factor of two higher in target density. Incomplete QSO samples must go to even fainter magnitude limits to increase the target surface density. An additional challenge is that the multiband photometric data used in the selection must be deeper than that of SDSS but cover a similar area on the sky. While the PTF and PS1 co-added survey data will fulfill this requirement, neither of the surveys will acquire deep $u$-band photometry that provides a useful selection for $z > 2$ QSOs.

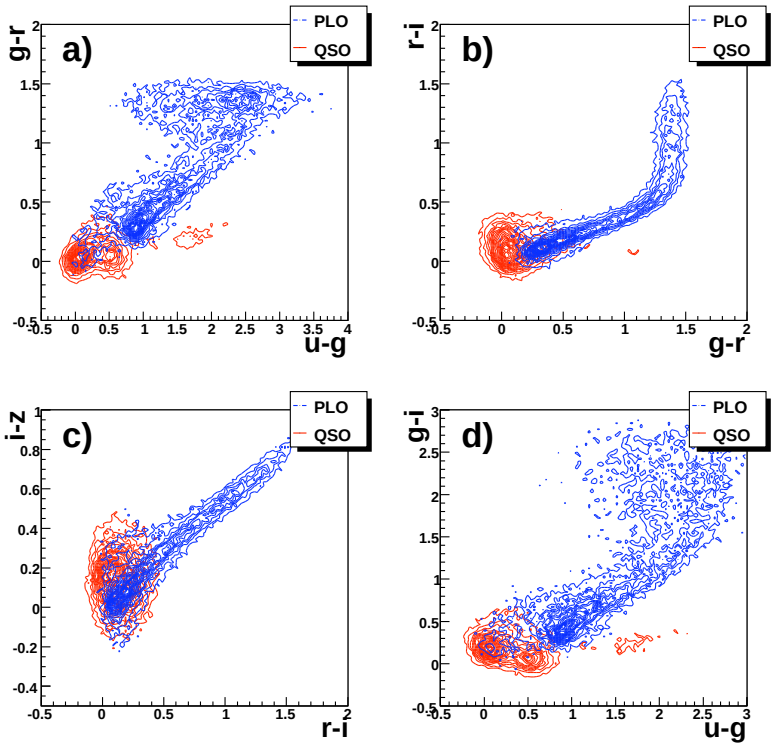


Figure 4.15: The *ugriz* colors of SDSS objects photometrically classified as stellar point-like objects (PLO) and those spectroscopically classified as QSOs (see Yeche et al., (2009)). For the BOSS Ly-$\alpha$ QSO selection, a neural-network algorithm uses available SDSS colors and spectroscopic templates to select the objects most likely to be QSOs with $z > 2.2$.

### 4.5.2 Selection Technique

Since standard, efficient selection techniques will likely not be possible without the availability of deeper $u$-band photometry, BigBOSS will employ a selection strategy based on QSO variability. Because quasars have a central massive black hole with ongoing accretion, the luminosity of the quasar can have episodic variation on timescales of months to years. This variability is intrinsically different from stellar sources when comparing them through their structure function, a measure of the the amplitude of the variability as a function time delay between two observations. Selecting quasars by their structure function has been successfully tested in the QUEST survey [Rengstorf et al., 2004; Bauer et al., 2009]. Further, the technique has

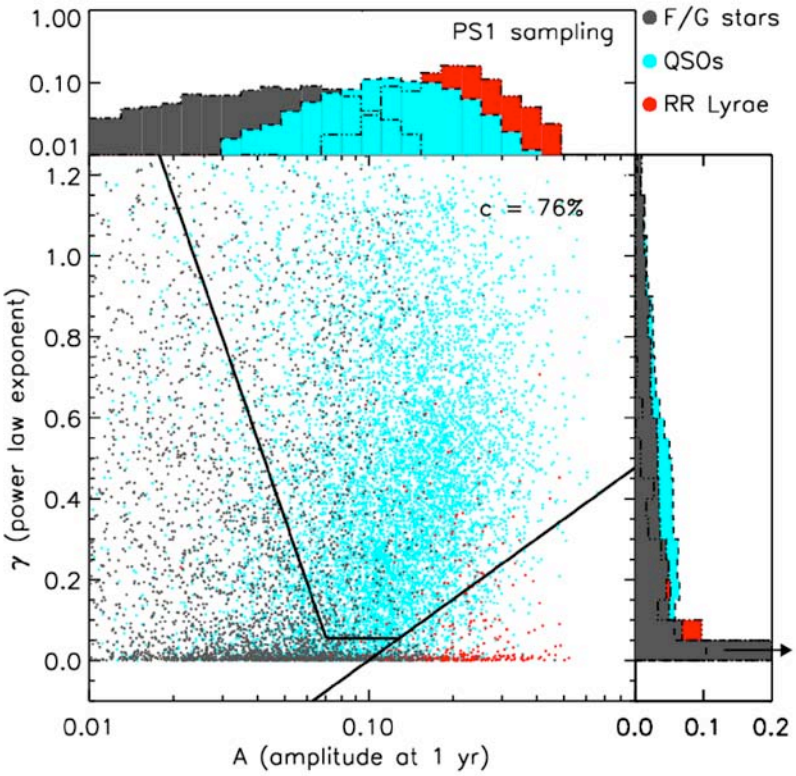


Figure 4.16: The QSO variability structure function selection from S10. The data came from 15,000 known objects in SDSS Stripe 82 and were down-sampled to 6 epochs in *griz* bands expected from PS1 $3\pi$ survey. The gray points are for F/G stars, the red points are RR Lyrae stars, and the aqua points are confirmed QSOs.

recently been modified to include a power-law behavior and observer rest-frame time lag information, removing the *a prior* measurement of quasar redshift ([Schmidt et al., 2010] hereafter S10). The structure function in parameterized in terms of $A$, the mean amplitude of the variation on a one year time scale and $\gamma$, the logarithmic slope of the variation on this time scale. Figure 4.16 shows the QSO structure function selection from S10 as derived from SDSS Stripe 82 with spectroscopically confirmed objects. The data in the figure have been down-sampled to co-add of 6 epochs in the *griz* bands to mimic the data expected to come from the PS1 survey. S10 found good separation in the selection from typical stellar contaminants such as F/G stars and RR Lyrae variable stars, delivering a total sample completeness of 75% on known QSOs.

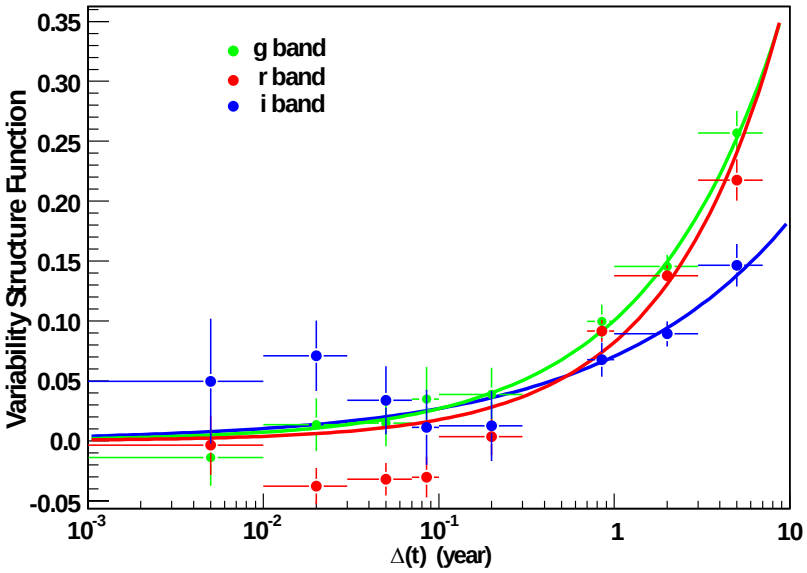


Figure 4.17: The three-band structure function created from SDSS Stripe 82 data for $z > 2.2$ QSOs.

A similar variability selection can be be found by looking at the structure function in each of the *gri* colors. Figure 4.17 shows the structure function from Stripe 82 *gri* co-added data, reaching limits similar to that of the PS1 survey. The three-band selection uses a loose selection of $(g-r) < 0.9$ down to $i_{AB} < 23.5$ to select all blue point-like sources (stars and QSOs). In this case, the amplitude $A$ of the structure function in each band is allowed to be independently fit while the amplitude variation $\gamma$ is simultaneously fit

from all bands. The three-band structure function information is then fed to a Neural Network (NN) to select QSO from stars [Palanque-Delabrouille et al., 2010]. This method is currently tested in BOSS with SDSS Stripe 82 and will produce results soon.

### 4.5.3 Sample Properties

The combination of the wide color cut that includes the stellar locus plus variability information from multiple bands allows us to select a QSO sample with a high degree of completeness. Figure 4.18 shows the number of QSO targets that we should expect from the BigBOSS QSO selection as a function of the completeness of the sample relative to the underlying QSO luminosity function. We find that we should expect 180 targets / deg$^2$ at the 80% completeness level and 250 targets / deg$^2$ at the 90% completeness level for QSOs with $z > 2.2$. Further, Figure 4.19 shows the trend of achieving 80% and 90% completeness as a function of QSO redshift is generally flat with only a small $< 10\%$ degradation at the highest redshifts where the faint objects begin to drop out of the targeted sample.

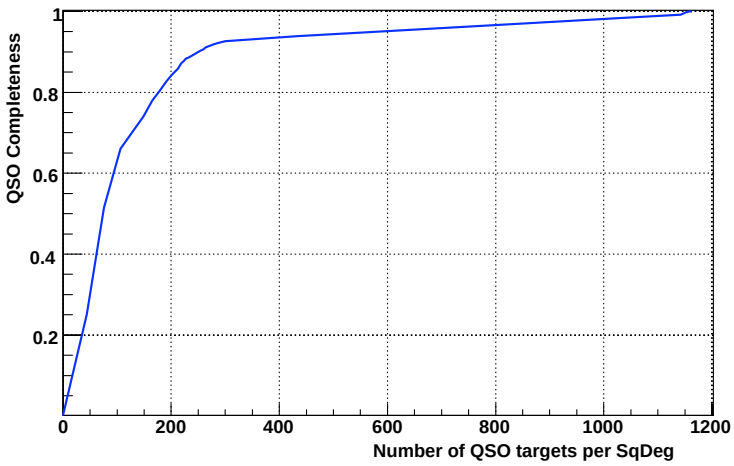


Figure 4.18: The achieved $z > 2.2$ QSO completeness for increasing target density using the color-variability QSO selection. A 80% completeness is achieved at 180 targets / deg$^2$ and 90% completeness is achieved at 250 targets / deg$^2$.

Assuming an average of the J06 and LSST QSO luminosity functions and the above completeness, we expect to produce $\sim 60$ Ly-$\alpha$ QSO targets

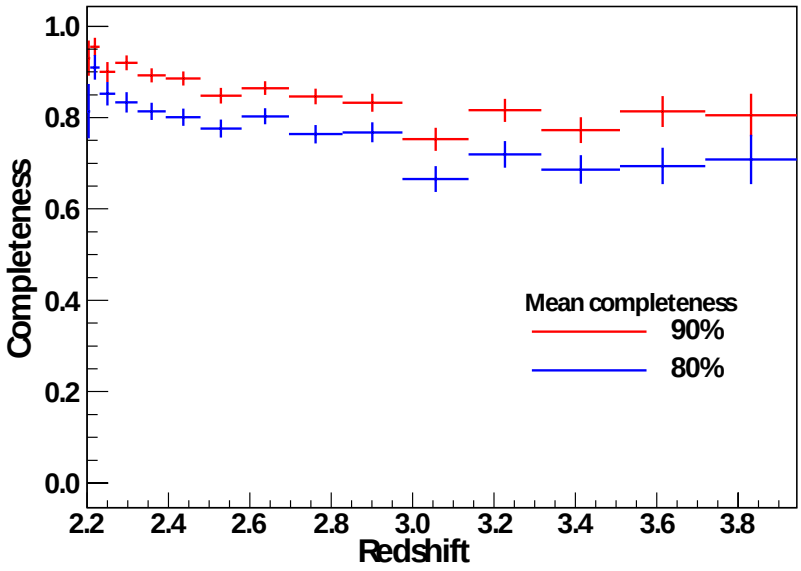


Figure 4.19: The QSO completeness as a function of redshift using the QSO color-variability selection.

/ deg$^2$ to$g < 23$ in the BigBOSS QSO sample. We estimate the redshift distribution of this sample by using the confirmed QSO redshifts from the BOSS survey and rescaling the distribution to the expected total areal density. The BigBOSS QSO redshift distribution is recorded in Table 2.4 and shown in Figure 4.20 after accounting for fiber completeness and redshift success rates. While the redshift distribution for BigBOSS may differ from BOSS because the selection criteria are different, we expect that the BOSS selection is *more* restrictive given the heavy dependence on shallow $u$-band photometry. Figure 4.20 should therefore be considered a conservative estimate for BigBOSS Ly-$\alpha$ quasars, particularly in the tail of the distribution.

An interesting side effect to this selection is that the targeted objects will have similar intrinsic variability to Ly-$\alpha$ QSOs. We expect that the largest population of selected objects that are not Ly-$\alpha$ quasars will be faint horizontal branch stars where the time-domain photometric sampling will produce spurious targets with similar characteristics in color and variability. Further, it is likely that there will be a significant fraction of $z < 2$ QSOs targeted in this color-variability scheme. The extent to which we will sample both Ly-$\alpha$ QSOs and $z < 2$ QSOs using the color-variability technique is currently under study using BOSS ancillary target runs and will produce

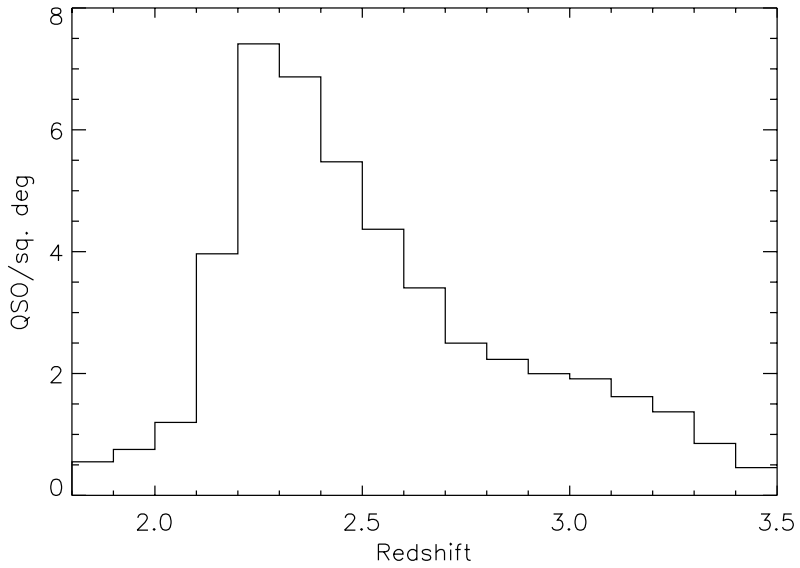


Figure 4.20: The BigBOSS redshift distribution for Ly-$\alpha$ QSOs. This sample is taken from the confirmed BOSS quasar distribution and rescaled to the BigBOSS target areal density (60 deg$^{-2}$), taking into account fiber completeness and measurement success rates (see Table 2.2).

results in the early Winter of 2010.

Because the QSO targeting technique produces a large areal density of targets ($\sim$ 250 deg$^{-2}$) to achieve a highly-complete QSO sample, the survey operations of BigBOSS will need to mitigate the 25% target selection efficiency for Ly-$\alpha$ QSOs and prevent spending exorbitant amounts of survey time on objects that are not Ly-$\alpha$ QSOs. BigBOSS will increase the overall efficiency of survey exposure times by sampling the entire target distribution in the first tiling pass within the survey (see Section 6 for details). The spectra produced from the first tiling will provide sufficient redshift information to cull the target distribution to only the $z > 2.2$ QSOs. Therefore, additional exposures can be assigned to only the confirmed Ly-$\alpha$ QSO sample.

### 4.5.4 Low-redshift QSO sample

Since the wide color cut of $(g - r) < 0.9$ aims to achieve a highly-complete QSO sample without the use of $u$-band dropouts, we can also expect to

sample a large portion of the entire QSO population over a wide redshift range. In particular, the $z < 2$ QSO sample can be cross-correlated with information from the WISE mid-IR bands. The constraints from WISE can either be used to veto these QSOs from the BigBOSS survey or they can help select a wider sample of the total QSO population for ancillary science. To determine the constraints provided by WISE photometry on $z < 2$ QSO target selection, we used data from the Spitzer observations of the Böotes Field of the NOAO Deep Wide Field Survey, the so-called Spitzer Deep Wide-Field Survey (hereafter SDWFS; [Ashby et al., 2009]). SDWFS reaches 80% completeness limits of 18.2, 18.1, 16.8 and 16.1 Vega mag in the [3.6], [4.5], [5.8] and [8.0] bands respectively over an area of over 9 deg$^2$, and is essentially complete at the depths corresponding to the WISE $5\sigma$ point source limits.

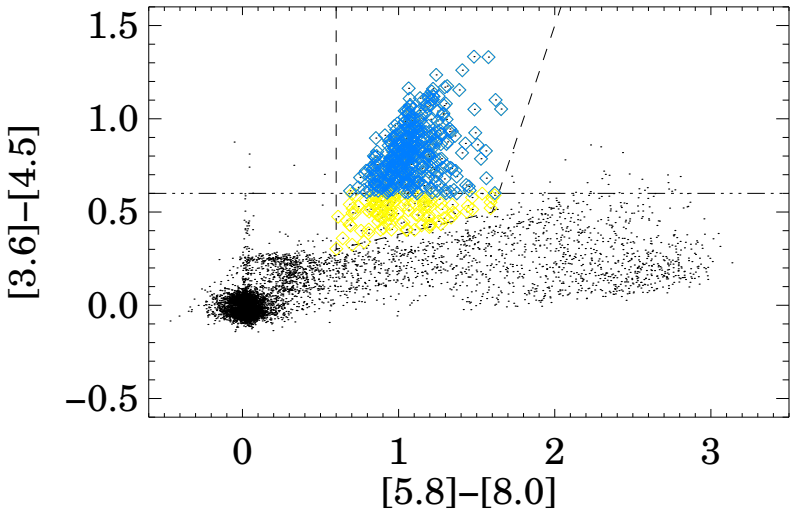


Figure 4.21: The IRAC color-color diagram for the SDWFS sources [Ashby et al., 2009] with flux densities satisfying the WISE $5\sigma$ point source limits in the [3.6] and [4.5] bands (i.e., the "SDWFS/WISE sample). Note the bulk of the AGN are easily selected using a single color criterion of [3.6]-[4.5]≥0.6.

The IRAC 4-band color-color diagram of these SDWFS/WISE sources is shown in Figure 4.21. The dashed lines show the "AGN wedge as dened by [Stern et al., 2005]. While WISE does not have the benet of the [5.8] and [8.0] bands, one could construct a similar 4-color diagram using the 4 WISE bands, but this would restrict the samples to the sources that are detected in all four bands. Instead, a simple 2-color selection of [3.6]-[4.5]≥0.6 results in

selecting the bulk of the sources in the "AGN wedge. Applying this selection to the sample in Figure 4.21 results in 407 sources, which corresponds to a surface density of 50 deg$^{-2}$. Of these sources, 91% lie within the AGN wedge and 98% have $I_{Vega} < 22$. The main contaminants are likely to be very low-redshift star-forming galaxies with strong PAH emission and a few high-redshift obscured galaxies. The former could be easily excluded using a star-galaxy separation either based on a ground-based optical imaging survey.

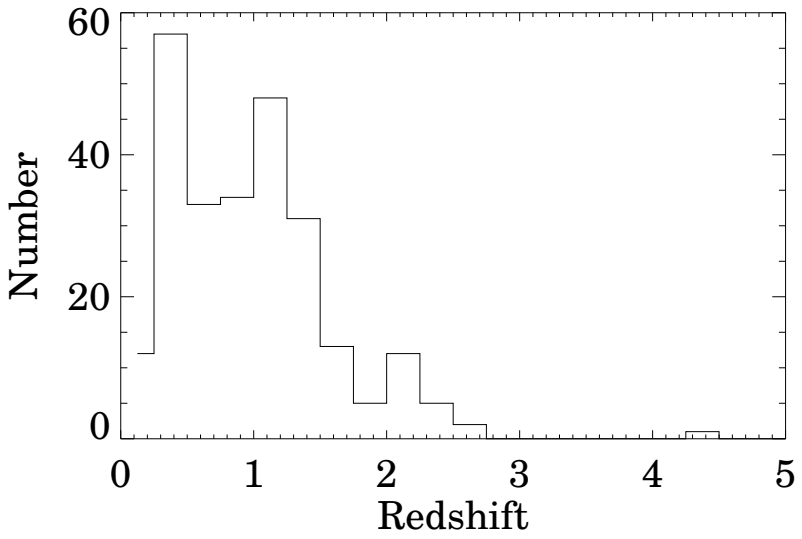


Figure 4.22: Redshift distribution of the SDWFS/WISE sample of sources obtained from the AGES [Kochanek et al., 2004] and other spectroscopic campaigns. 46% of the sources lie at redshifts z≥1.

Approximately 62% of the objects in the SDWFS/WISE sample have spectroscopic redshifts from the AGN and Galaxy Evolution Survey (AGES; Kochanek et al. (2010), in preparation; see also [Kochanek et al., 2004]) and other spectroscopic campaigns using the W. M. Keck Observatory telescopes. The redshift histogram in Figure 4.22 shows that 46% of the broad-line QSOs with redshift information have $z \geq 1$ and only 7% have $z \geq 2.0$. We find that the magnitude distributions of sources with and without spectroscopic redshifts is roughly similar and hence we can justify deriving estimates regarding the redshift distribution by simple scaling.

# 5 The BigBOSS Instrument

## 5.1 Overview

The BigBOSS instrument is composed of a set of telescope prime focus corrector optics, a massively multiplexed, roboticized optical fiber focal plane, and a suite of medium resolution spectrographs, all coordinated by a real time control and data acquisition system. The conceptual design achieves a wide field instrument on the Mayall 4-m telescope at KPNO.

Before delving in the instrumentation in more detail, we describe how some of the key parameters were derived, such as field of view, number of fibers, fiber size and positioning accuracy, spectrograph partitioning, integration time and the like.

In Section 2, the use of galaxy [O II] doublet(3727Å and 3729Å) emission lines to measure the redshift of Luminous Red Galaxies ($0.2 < z < 1$) and Emission Line Galaxies ($0.7 < z < 1.7$) and the Ly-$\alpha$ (1215Å) forest for Quasi-Stellar Objects($2 < z < 3.5$). These determine the instrument wavelength span requirement to be 340–1060 nm.

To accomplish the 14,000 deg$^2$ survey area in 500 nights with exposures to the required depth requires a large field of view. Feasible designs with a 3° linear FOV were demonstrated in earlier NOAO work and expanded on by work done for BigBOSS. The existing Mayall prime focus is replaced with a six element corrector illuminating the focal plane with a f/4.5 telecentric beam that is well matched to the optical fibers acceptance angle. This large FOV can be accomplished within a total optical blur budget of 28 $\mu$m RMS.

With existing fiber optic actuators, the focal plane can accommodate 5000 fibers on a 12 mm pitch. The fiber tips can be placed with 5 $\mu$m rms accuracy. When combined with the telescope blur and site seeing of 1 arcsec RMS, the convolved 105 $\mu$m FWHM image of a galaxy fits in the 120 $\mu$m fiber we have chosen. The modestly tight fit is to minimize inclusion of extraneous sky background.

Galaxy light collected in the fibers is delivered to the spectrograph system. To achieve resolutions of 3000–4000 to resolve the [O II] doublet lines while keeping the spectrographs optical element small and optimized for high throughput, the system is divided into ten identical spectrographs each with three bandpass-optimized arms. Each spectrograph records 500 fibers and each arm is instrumented with 4k×4k CCD.

The BigBOSS exposure time calculator described in Appendix A is used to determine the exposure time required to reach the minimum SN requirements of 2 and 6 for the [O II] doublet lines 3727Å and 3729Å for an Emis-

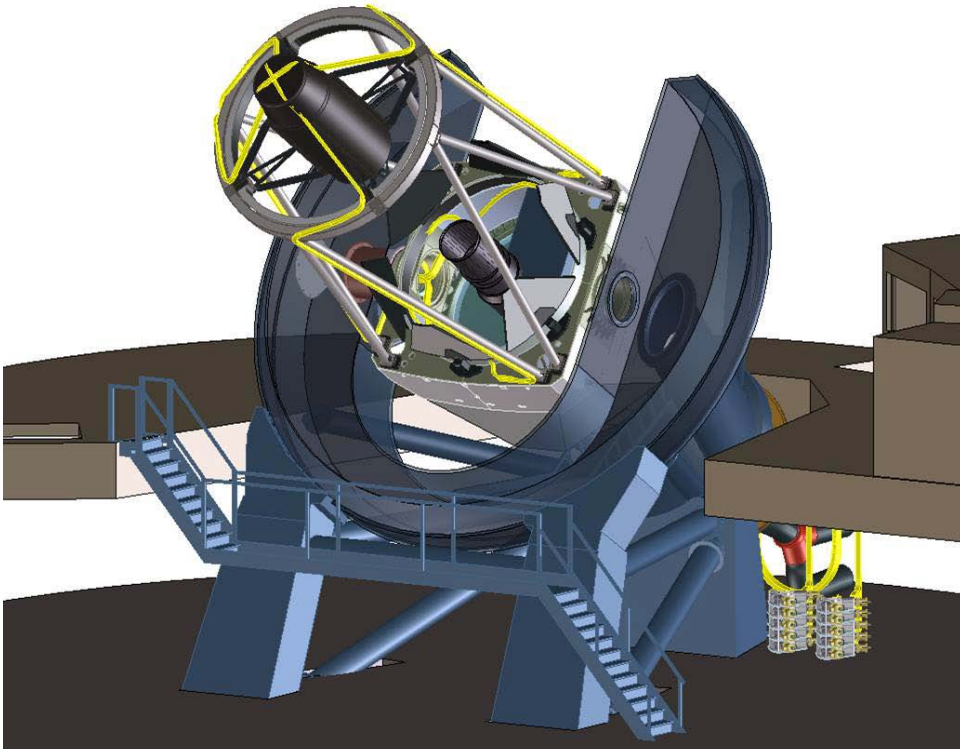

Figure 5.1: BigBOSS instrument installed at the Mayall 4-m telescope. A new corrector lens assembly and robotic positioner fiber optic focal plane are at mounted at the prime focus. The yellow trace is a fiber routing path from the focal plane to the spectrograph room incorporating fiber spooling locations to accommodate the inclination and declinaton motions of the telescope. The two stack-of-five spectrograph arrays are adjacent to the telescope base at the end of the fiber runs.

sion Line Galaxy with a luminosity of $0.9\times10^{-}16$ ergs/cm$^2$/s. Including known detector characteristics (readnoise, dark current, and quantum efficiency), effective telescope aperture, mirror refection, fiber coupling and transmission losses, and spectrograph throughput, we determine that 15 minute exposures are required. We set a goal of one minute deadtime between exposures to read the spectrograph detectors, reconfigure the fibers and repoint the telescope.

Table 5.1 summarize the instrument parameters we have just described and the foldout shows in detail the interplay of the systems.

Table 5.1: Instrument Parameters.

| | |
|---|---|
| **Telescope** | |
| 3° linear FOV | |
| 3.8 m diameter aperture, f/4.5 | |
| 1.8 m linear obscuration | |
| Focal length 17.1 m | |
| Wavelength response 340–1060 nm | |
| Blur <28 $\mu$m RMS (0.35 arcsec) | |
| Focal surface | |
| 4000 mm convex sphere | |
| 950 mm diameter | |
| **Fiber System** | |
| 5000 robotic fibers | |
| Fiber diameter 1.45 arcsec (120 $\mu$m) | |
| Fiber spacing 145 arcsec (12 mm) | |
| **Spectrographs** | |
| Bandpasses | |
| Blue: | 340–540 nm |
| Visible: | 500–800 nm |
| Red: | 760–1060 nm |
| Resolution | |
| Blue: | 3000 |
| Visible: | 2960 |
| Red: | 4140 |
| **Cameras** | |
| 4k×4k pixels per channel | |
| 3 pixel minimum sampling | |
| Pixel size | |
| Spatial: | 0.75 arcsec |
| Blue: | 0.488 |
| Visible: | 0.732 |
| Red: | 0.732 |
| QE (400–1000 nm) | >80% |
| Read noise | <2.5 e |
| Dark current | <0.03 e/s/pixel |
| Pixel rate | 100 kpixel/sec/port |
| **Instrument cycle time (parallelizable)** | |
| CCD readout | 40 s |
| Fiber positioning | 60 s |
| Telescope slew and guide lock | <60 s |

# KITT PEAK 4-m (Mayall) TELESCOPE

- Parameters: http://www-kpno.kpno.noao.edu/kpno-misc/mayall_params.html

**FACILITY MODIFICATIONS:**
- Primary mirror edge sensing
- Thermal control to 3 deg w/ glycol
- Cooling pipes
- Paint M1 support structure diffuse black

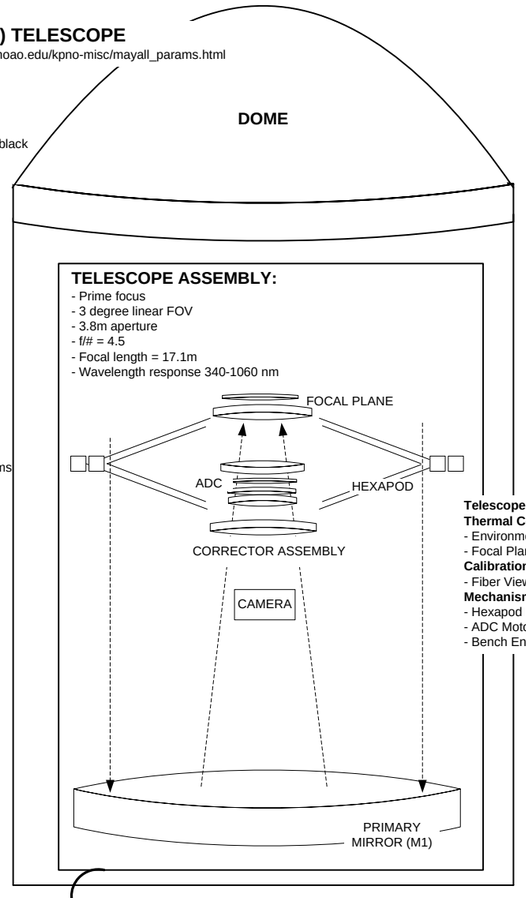


**FOCAL PLANE and FIBERS:**
- 4m radius of curvature (convex)
- 950mm diameter
- 5000 broad spectrum fibers
- Provides 1.45 arcsec dia on sky

**CORRECTOR ASSEMBLY:**
- 4 lens corrector
- 4 plate ADC
- Hexapod motor controlled

**ADC:**
- 2 opposite-rotating Risley prisms
- LLF1 or N-PSK3 material
- 1 degree tolerance on rotation

**Hexapod (PI or ADS-Int.):**
- 5 to 10 um step size
- +/-2mm despace
- +/-1mm lateral
- 1 deg tilt

**FIBER VIEW CAMERA:**
- Measures fiber location
- Views illuminated fiber tips
- Kodak 50Mpix CCD
- Canon f/2.8 Lens
- 71mm aperture
- 25 demagnification
- Uses existing M2 mounting IF

**OBSCURATION (not shown):**
- 1.8m obscuration
- Required for stray light

**PRIMARY MIRROR (M1):**
- Existing 4m mirror
- F/number = f/4.5
- Concave, hyperbolic

**FIBER RUN (5000 Fibers, sub-bundle units):**
- 30-40m fiber run from Focal Plane to Spectrographs
- Low OH fused silica (340-1060nm)
- Core 120 um diameter
- Provides maximum attenuation of 30% @ 340nm
- Fiber testing

## FTS CONTROL ROOM

- 10x Spectrograph bench-mounted in FTS control room
- Floor has cooling pipes
- Vibration-isolated
- Thermally controlled to +/-1 degree
- (Remote control room in Tucson)

**Telescope Thermal Control:**
- Environmental Monitors
- Focal Plane Thermal Control

**Calibration Control**
- Fiber View Lamps

**Mechanism Control:**
- Hexapod Motor Control
- ADC Motor Control
- Bench Environment Monitors

## FOCAL PLANE ASSEMBLY:

- 950mm diameter curved focal surface
- 5000 fibers on hex grid
- 1.45 arcsec fiber diameter
- 170 arcsec fiber spacing

**FIBER POSITIONERS:**
- 12 mm pitch
- Each fiber individually actuated
- Position accuracy = 100um
- Position precision = 5um
- Reconfiguration time < 45 seconds

**MOTORS:**
- TBD motors
- 1 rotational axis motor
- 1 translation axis motor

**GUIDERS and FOCUS MODULES:**
- 4 Guiders
- 4 Stepped focus detectors
- 1 wavefront sensor

**FP STRUCTURE:**
- Al structure (TBD)
- Air cooled

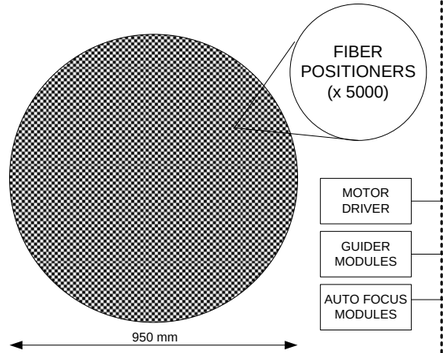


## DATA ACQUISITION

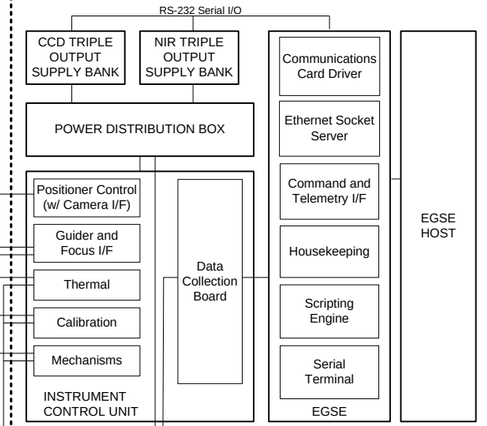


**EGSE HOST:**
- User control and data analysis platform
- Actively control ICU
- Scripting
- Graphical User Interface (GUI)
- Data Archive
- Post Processing

Databases:
- Telescope pointing list
- Positioner pointing lists
- Position measurements
- Environment conditions
- Detector config parameters

Communications:
- Telescope Operations
- Pipeline data system
- Target scheduling
- Operations console

**Spectrograph Thermal Control:**
- Cryostat Thermal Control
- Cryostat Vacuum Control
- Bench Environment Monitors

**Calibration Control:**
- Fiber Slit Array Lamps

**Mechanism Control:**
- Shutters

Detector Control, Data Power

## SPECTROGRAPHS:

- 2 blocks of 5 spectrographs
- 3-arm spectrograph (Red, Visible, Blue Channels)
- Covers simultaneous wavelength range of 340-1060nm

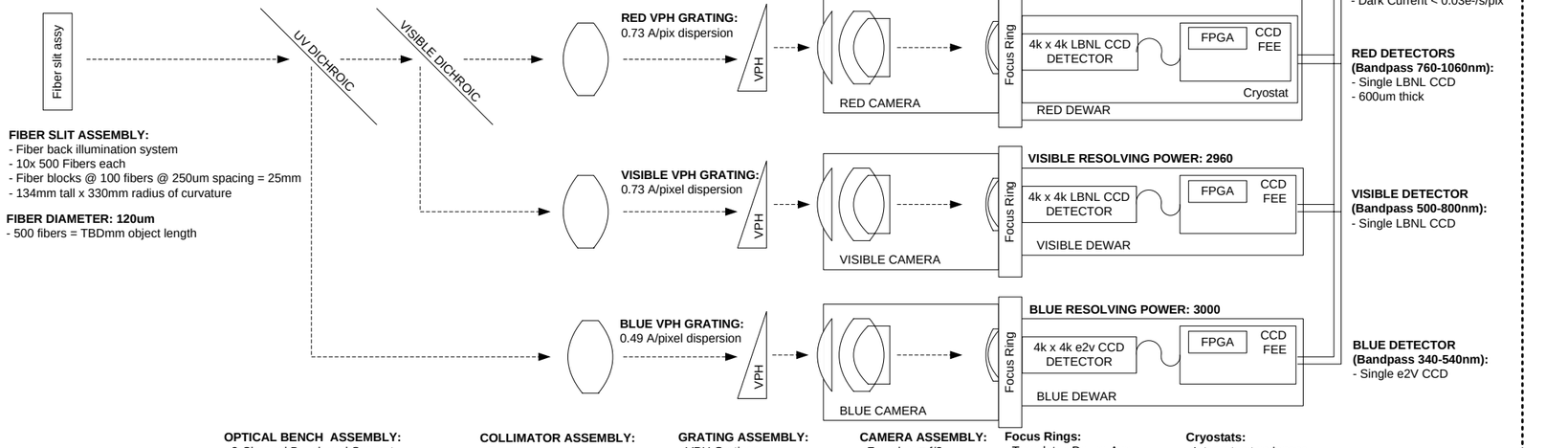


**FIBER SLIT ASSEMBLY:**
- Fiber back illumination system
- 10x 500 Fibers each
- Fiber blocks @ 100 fibers @ 250um spacing = 25mm
- 134mm tall x 330mm radius of curvature

**FIBER DIAMETER: 120um**
- 500 fibers = TBDmm object length

**OPTICAL BENCH ASSEMBLY:**
- 3-Channel Bench and Support
- Dichroic and Fiber IF Assembly
- Silica Substrate Dichroics

**COLLIMATOR ASSEMBLY:**
- Fnumber = f/4
- <82.5mm Pupil Size

**GRATING ASSEMBLY:**
- VPH Gratings

**CAMERA ASSEMBLY:**
- Fnumber = f/2
- Includes shutters

**Focus Rings:**
- Translates Dewar Assy
- Tilt, tip, focus adjustment

**Cryostats:**
- Integrates two lenses
- Positions CCD to +/-15 microns
- Cools CCDs to 170K
- Regulation to +/- 0.1K

**Detector Characteristics**
- 4096 x 4096 pixels
- 0.75 arcsec pixel size (15um)
- Detector QE > 80%
- Read noise < 2.5e-
- Dark Current < 0.03e-/s/pix

**RED DETECTORS (Bandpass 760-1060nm):**
- Single LBNL CCD
- 600um thick

**VISIBLE DETECTOR (Bandpass 500-800nm):**
- Single LBNL CCD

**BLUE DETECTOR (Bandpass 340-540nm):**
- Single e2V CCD

## 5.2 Telescope Optics

### 5.2.1 Design

BigBoss employs a prime focus corrector to provide a telecentric, seeing-limited field to an array of automated fiber positioners. Basic design requirements are listed in Table 5.2.

Table 5.2: Telescope Requirements.

| Requirement | Value | Description |
|---|---|---|
| Compatibility | N/A | Use existing telescope mount and M1 of Mayall and Blanco 4-m telescopes. Include mount for existing f/8 M2. |
| *f/#* | 4.5 | 3.8 m aperture, 17.1 m focal length |
| Geometric blur | $< 0.8$ arcsec FWHM | RMS across field |
| Zenith Angle | 0–60° | Will require atmospheric dispersion corrector (ADC) to meet blur requirements |
| Field of View | 3° | Full field of view |
| Wavelength Range | 340–1060 nm | Simultaneous correction required across entire band |

Cassegrain and prime focus options were explored. Prime focus was selected for its superior stray light performance, increased throughput due to simplified baffling and smaller central obscuration, and lower cost. The corrector includes four corrector elements, and a pair of ADC elements (each

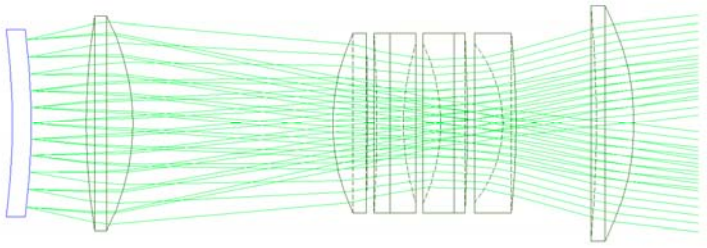

Figure 5.2: BigBoss prime focus corrector consists of four corrector elements and two ADC prism doublets.

consisting of two powered prisms). Materials and design of the corrector and ADC were selected for manufacturing feasibility. All elements of the corrector are long-lead items, and initial contacts have been made with raw material suppliers and lens manufacturers. Corning can supply the large fused silica pieces, and N-BK7 and LLF1 are current production glasses at Schott.

Figure 5.2 shows the optical layout of the BigBoss prime focus corrector and ADC. The four singlet corrector elements are fused silica, each with one aspheric and one spherical surface. Element C1 is the largest lens, 1.25 m fused silica. Lens elements were sized to have more than 15 mm of radius beyond the clear aperture to allow for polishing fixturing and mounting. The ADC consists of two wedged doublets, with spherical external surfaces, and a flat, cemented wedge interface. ADC elements are made of LLF1 and N-BK7, and all are within the current production capability of Schott. A minimum 300 mm gap exists between Element 4 and the central fiber positioner (focal surface).

Figure 5.3 shows the ideal rms geometric blur performance (no manufacturing, alignment or seeing errors) of the BigBoss corrector mounted on the Mayall telescope. For reference, the required FWHM geometric blur of 0.8 arcsec corresponds to a blur RMS of 28 $\mu$m, so realistic manufacturing margins exist.

### 5.2.2 Focal Surface

The focal surface is a convex sphere of 4000 mm radius of curvature and has a diameter of 950 mm. This is the surface that the optical fiber tips must placed on to 10 $\mu$m accuracy.

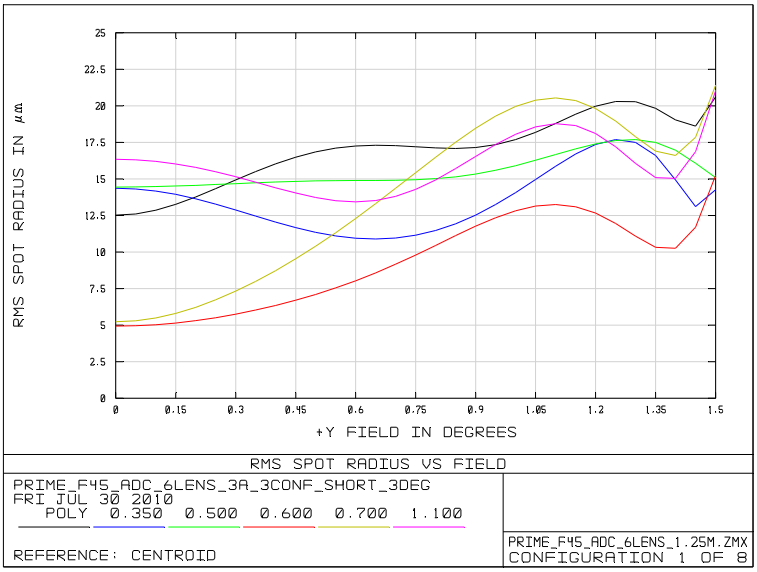


Figure 5.3: Ideal geometric blur performance of BigBoss corrector on Mayall 4-m telescope. The required 0.8 as FWHM corresponds to a geometric blur radius of 28 $\mu$m.

### 5.2.3 Tolerancing

The Mayall telescope is seeing-limited with an atmospheric FWHM of 0.9 arcsec, or 72 $\mu$m FWHM. For the 17.1 m focal length of BigBoss, this corresponds to an RMS radius of 32 $\mu$m. Peak geometric blur (multispectral) of the perfect telescope across the 3° FOV is 18.3 $\mu$m, or 43 $\mu$m FWHM. With manufacturing, alignment and thermal drift, the telescope geometric blur is 28 $\mu$m RMS, or 66 $\mu$m FWHM. The overall peak budget for seeing, residual phase error, manufacturing, alignment error and thermal drift is 100 $\mu$m FWHM, or 1.2 arcsec. This is a worst-case number, and performance of the telescope is better over the majority of the field.

Tolerances for the telescope are broken down into three major categories: compensated manufacturing errors, compensated misalignment, and uncompensated errors. Manufacturing errors such as lens radius of curvature and thickness may be compensated to a certain degree by varying the spacing of the lens elements during assembly and alignment. Table 5.3 shows compensated manufacturing tolerances on the individual optical elements.

Residual alignment errors and thermal drift in the assembled corrector are compensated by a motion of the entire corrector barrel and focal

Table 5.3: Compensated Manufacturing Tolerances. $V$ is vertex lateral error ($\mu$m), $T$ is thickness error ($\mu$m), $W$ is wedge ($\mu$m at edge), $R1$ is surface 1 radius error ($\mu$m sag), $K1$ is surface 1 conic (%), $R2$ is surface 2 radius ($\mu$m sag), $K2$ is surface 2 conic (%), and $n$ is index of refraction (ppm).

| | *V* | *T* | *W* | *R1* | *K1* | *R2* | *K* | *n* |
|---|---|---|---|---|---|---|---|---|
| C1 | 100 | 1000 | 10 | 20 | | 20 | | 5 |
| C2 | 100 | 250 | 10 | 40 | | 50 | 0.01 | 5 |
| ADC1-1 | 100 | 50 | 10 | 100 | | Flat | | 5 |
| ADC1-2 | 100 | 50 | 10 | Flat | | 50 | | 5 |
| ADC2-1 | 100 | 50 | 10 | 100 | | Flat | | 5 |
| ADC2-2 | 100 | 50 | 10 | Flat | | 20 | | 5 |
| C3 | 250 | 250 | 15 | 100 | | 15 | 0.1 | 5 |
| C4 | 100 | 1000 | 50 | 50 | 1 | 50 | | |
| Focal Plane | | | | 10000 | | | | |

plane via motorized hexapod. Residual errors after these compensations are primarily higher-order aberrations, and are budgeted as compensated tolerances in Table 5.4.

Table 5.4: Compensated Alignment Tolerances.

| | Lateral Error ($\mu$m) | Despace Error from previous surface ($\mu$m) | Tilt Errors ($\mu$m at edge) |
|---|---|---|---|
| C1 | 10 | Compensator | 10 |
| C2 | 10 | 10 | 7 |
| ADC1 | 20 | 100 | 15 |
| ADC2 | 30 | 100 | 15 |
| C3 | 50 | 100 | 9 |
| C4 | 75 | 100 | 20 |
| Focal Plane | 400 | 100 | 15 |

The current operations plan involves characterization of the telescope for gravity sag as a function of elevation, and thermal drift of telescope focus. These are compensated continuously by motion of the hexapod. Other manufacturing errors may not be compensated (between observations) by motion of the hexapod, for example, corrector glass inhomogeneities. Such effects are currently being quantified, but the optical performance of the corrector (geometric blur) has more allowance than other existing and planned

(e.g., DES) designs.

### 5.2.4 Optical Mounts

Corrector and ADC elements have coefficients of thermal expansion between 0.5 and 8.1 ppm/°C. The largest element is corrector element C1 (1.25 m in diameter). Operational temperatures range from -10° to 30°. Although larger transmissive elements have been built, detailed design and careful attention will be necessary during the design, fabrication and test phases in order to achieve the science goals of BigBoss.

Overall responsibility for mounting and aligning the large glass elements of the corrector lies with University College London (UCL), who is also responsible for the similar corrector barrel assembly for DES. Requirements and goals for the optical mounts are listed in Table 5.5.

Table 5.5: Glass mount design guidelines

| Item | Tolerance |
|---|---|
| No metal on glass interfaces | Reduce surface contact stress on substrate |
| RTV athermalized glass mounts | Near zero-stress at glass/metal interface, metal ring slightly higher CTE than glass. |
| Flexure link from metal lens mount (low expansion) to barrel | Maintain alignment while allowing compliance between lens barrel and lens mount. |
| Modular, pinned construction, barrel assembled in sections | Ability to disassemble corrector to access individual lenses. |

Glass elements of the corrector are brittle, and must first be attached to an athermalized ring of work-hardened material. Invar (a low-expansion Ni/Fe alloy) has a CTE slightly higher than that of fused silica ($1.2\times10^{-6}$/°C versus $0.55\times10^{-6}$/°C), and precise thickness RTV pads around the perimeter of the silica lens allow an assembly of fused silica, RTV and a surrounding invar cell to expand and contract with minimal stress. Once mounted in the cell, standard fastener construction can be used to mount the lens cell via the metal ring. Figure 5.4a shows a cross-section of a similar mount designed by UCL for the DES project. Titanium cell rings ($9.2\times10^{-6}$/°C) are used with RTV to similarly athermalize the higher expansion N-BK7 and LLF1 lenses ($6.2\times10^{-6}$/°C and $7.1\times10^{-6}$/°C, respectively). A circular array of flexure blades allows for thermal expansion between the lens cell and the

corrector barrel. This heritage design is currently being implemented by UCL on the DES project (see Figure 5.4b).

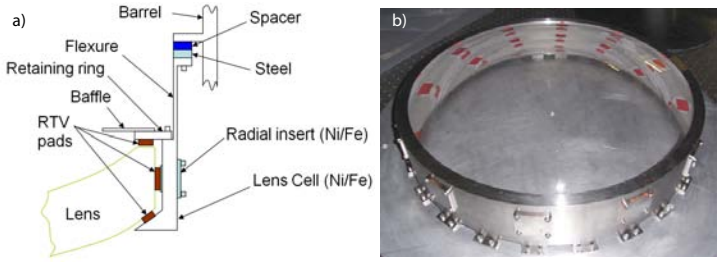


Figure 5.4: Schematic of athermalized, flexure-mounted lens cell design (left) and 550 mm prototype lens and lens cell at UCL (right).

### 5.2.5 Coatings

The preferred coating technology for the BigBoss lenses is either a hard (and durable) coating of $MgF_2$, or a tuned Sol-Gel coating. While Sol-Gel can be tuned to some degree for the bandpass of the telescope, it is not as durable as $MgF_2$. Cost, risk, performance and alignment constraints on the various coating technologies will be investigated during the fabrication of the corrector lenses, and a final decision is not necessary at this time. The likely configuration for the coatings is a hybrid $MgF_2$ undercoat with a tuned Sol-Gel overcoat (demonstrated performance of <0.5% loss over the visible band). At least two vendors (REOSC and SESO) are capable of coating the optics, including the 1.25 m diameter C1 element. It is expected that improved capability will be available subsequent to lens polishing.

### 5.2.6 Stray Light and Ghosting

A major benefit, and reason for selecting the prime focus option over Cassegrain, is the simplified stray light baffling. A wide-field Cassegrain design appropriate for BigBoss would require a 50% linear obscuration, with carefully designed M1 and M2 baffles in order to block direct sneak paths to the detector. With a prime focus design, out-of-field rays miss the focal plane entirely. The main sources of stray light (first order stray light paths) are surfaces illuminated by sky light, and directly visible to the focal plane. Chief among these surfaces are the structure surrounding M1, which will be painted with durable diffuse and specular black stray light coatings (Aeroglaze Z302, Z306

and Ebanol). Other first order stray light paths include particulate contamination on M1 and the surfaces of the correctors.

The BigBoss corrector was designed and analyzed to ensure internal reflections within the corrector do not contribute significantly to stray light at the focal surface. The main causes of reflections are typically reflections off concave surfaces (facing the focal surface), and are most significant for elements in close proximity to the focal surface. Figure 5.5 shows a ghost stray light path from the C4 corrector element, which has been reduced by ensuring the radius of curvature of the first optical surface is smaller than its separation from the focal plane. As shown, the focus of the ghost is located off the focal surface, and only a diffuse reflected return, off two surfaces with >0.98% transmission surfaces contributes to the stray light at the focal plane. Additional point source transmittance analysis with realistic contamination and surface roughness is currently underway with the existing stray light model of the telescope and corrector.

Reflections between the focal plane array and nearby corrector surfaces are a typical source of stray light in an imaging wide-field corrector system. Because the fiber positioners can be made rough, and painted black, this source of stray light may be virtually eliminated on a robotic fiber array.

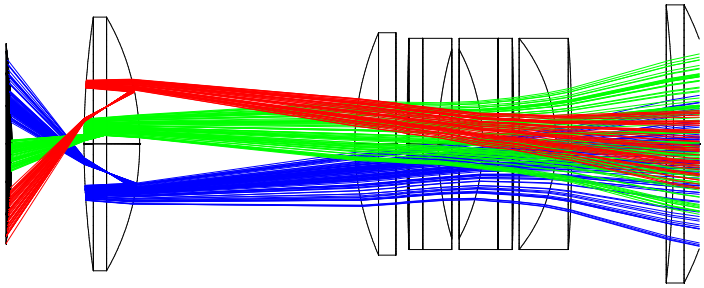

Figure 5.5: Reflections off corrector lens surfaces could contribute ghost background noise. Elements are designed to reduce bright ghost irradiance on the focal plane to acceptable levels.

### 5.2.7 Atmospheric Dispersion Corrector

Chromatic aberration must be sufficiently small to place incoming light between 0.34–1.060 nm within the geometric blur allocation. Because observations will be between $0 - 60^{\circ}$ from zenith, an atmospheric dispersion corrector will be necessary. The ADC elements are 0.9 m in diameter and

made of Schott LLF1 and N-BK7. Wedge angles within the two elements are roughly 0.3°. Figure 5.6a shows the PSF across a 3° FOV at an angle 60° from zenith with the ADC rotated to correct for atmospheric dispersion. Figure 5.6b is for the uncorrected case. Rotational tolerance requirements for the ADC are greater than 1°, and the ADC rotator is consequently not a high-precision mechanism.

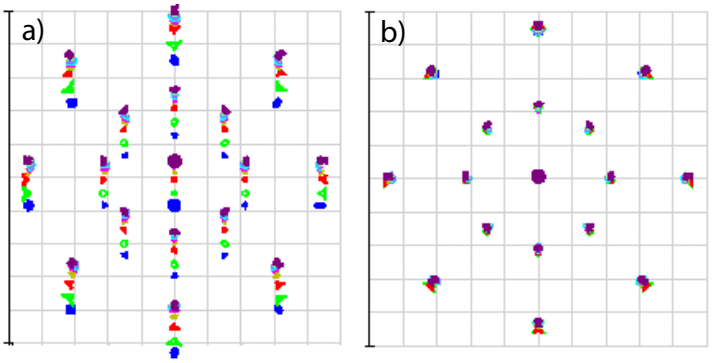


Figure 5.6: Geometric raytrace shows effects of atmospheric dispersion on telescope point spread function. a) A heavily chromatically aberrated view of the sky 60° from zenith. This chromatic aberration is removed by rotating the ADC prisms 85° as shown in b). The dispersion being compensated here is 3 arcsec.

### 5.2.8 Hexapod Adjustment Mechanism

Compensations for gravity sag, temperature change and composites dryout are affected by a six-degree-of-freedom hexapod mechanism. The focal plane and corrector elements are positioned relative to one-another during alignment, and moved as a unit by the hexapod. Requirements for the hexapod are as listed in Table 5.6.

### 5.2.9 Fiber View Camera

During the course of the survey, before any given exposure, after the mechanism to arrange the position of the 5000 fibers has completed its task the Fiber View Camera will take a picture of the fibers on the fiber plane to check the correctness of all of the fiber positions, and if needed allow the correction of any misplaced fibers. The camera will be located on the axis of the telescope at a distance of 1 m below corrector element C1, as shown

Table 5.6: Hexapod Mechanism Requirements

| Motion Requirement | Value | Comments |
|---|---|---|
| Despace | ±2 mm | Focus direction |
| Lateral | ±1 mm | Lateral translation |
| Tilt | TBD | Tilt of corrector, pitch and yaw directions |
| Step size | 5 $\mu$m | Also called actuator granularity |

on Figure 5.7. The camera will be supported in this position by thin spider legs from the ring supporting the first element of the corrector optics. In this position the lens of the fiber view camera will be 5 m from the fiber plane. To get an image of the 950 mm diameter fiber plane on a 40 mm CCD will require the camera to have a demagnification of about 25. This can be accomplished with a 200 mm focal length lens. The fibers will be back-illuminated at the spectrograph end by a 10 mW LED.

One complication with this arrangement is that the camera will have to take the picture of the fiber plane through the corrector optics. This introduces some distortions in the images. A detailed study of the image shapes, using the BEAM4 ray tracing program, shows that these distortions are at an acceptable level. A set of fixed and surveyed reference fibers will be mounted in the focal plane and imaged simultaneously with the movable fibers. These can be used to deconvolve any distortion and any motion of the camera with respect to the focal plane due to gravity sag.

**Design Considerations.** The performance requirements for the fiber view camera are summarized in Table 5.7. We note further that since we plan to illuminate the fibers with a monochromatic LED, the CCD of choice should be monochromatic. The plan is then to build a custom camera body (see Figure 5.8) and use a commercially available CCD, the Kodak KAF-50100, and a commercially available lens, the Canon EF 200 mm f/2.8 L II USM. There also exists commercially available clocking and readout electronics for this Kodak CCD that we plan to use.

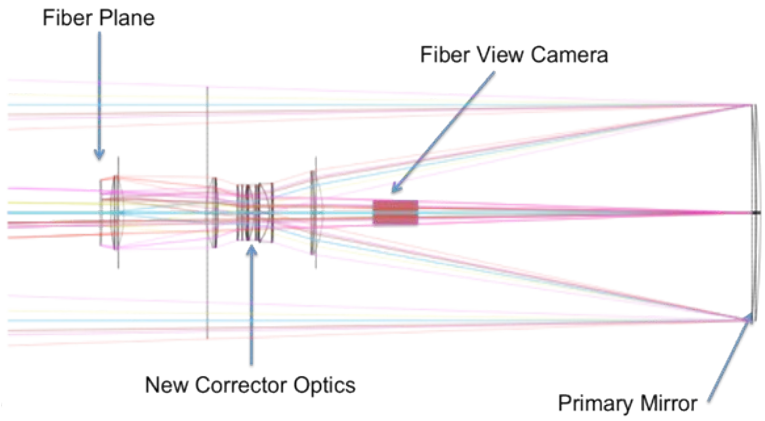


Figure 5.7: The Mayall Telescope showing the placement of the corrector optics and the fiber view camera

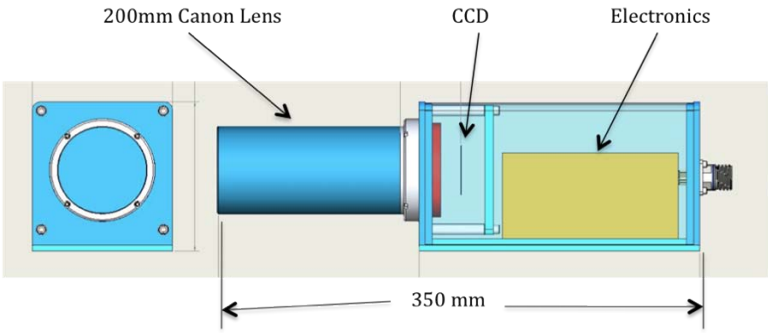


Figure 5.8: Schematic of the Fiber View Camera

**Fiber Illumination.** We plan to illuminate each fiber at their end in the spectrometer with a monochromatic 10 mW LED. We estimate that each fiber will emit $2\times10^9$ photons/sec into a 30° cone at the focal surface. The solid angle of the fiber view camera lens will capture $3\times10^5$ photons/sec/fiber image. With 25% quantum efficiency this gives 75,000 electrons/sec/fiber image on the CCD.

**Dark Current and Read Noise.** It is desirable to run the camera at room temperature. The dark current in this Kodak CCD is advertised as 15 e/pixel/sec at 25°C and the read noise is 12.5 e at a 10 MHz read out rate. Both of these are quite negligible compared to the high fluxes expected from the fibers.

**Fiber Position Precision.** With a demagnification of 25 the 120 $\mu$m diameter fiber will have a 5 $\mu$m diameter image on the CCD. Including the optical distortions we still expect image sizes well under 10 $\mu$m, not a match to the 6 $\mu$m CCD pixels. We plan to defocus the lens slightly to produce large enough images to allow interpolations to much better than the pixel size. A Monte Carlo calculation was performed to determine the optimal image size. For the discussion here we will assume a 25 $\mu$m diameter image with significant flux spread over 16 pixels. With a one second exposure we expect 75,000 electrons per image. With such large signal to noise, we expect to centroid the fiber position to $\sim$0.1 $\mu$m. Systematic effects can double this to 0.2 $\mu$m. With the factor of 25 demagnification this translates to a 5 $\mu$m measurement error on the fiber plane.

**Occupancy and Ability to Resolve Close by Fibers.** With 16 pixels in a fiber image, the 5000 fibers will occupy 80,000 pixels. Compared to the $50\times10^6$ pixels on the CCD, this gives an acceptable occupancy of $\sim2\times10^{-3}$. The fiber positioning mechanism sets the closest separation between any two fibers to be 3 mm. With the factor of 25 demagnification this means 120 $\mu$m or a 20 pixel separation on the CCD, so that overlap of the images will not be a problem. We have developed code to carry out a simultaneous fit to two images when two images are close together so that the tails of one image under the other and vice versa are correctly taken into account.

**Modelling and Scene Calibration.** The fiber position measurement precision quoted in Table 5.7 is based on the assumption that given the high statistics we can measure the position of the centroid of the image on the CCD to 3% of the pixel size. A Monte Carlo simulation will be useful to determine the optimum image size on the CCD for the best precision. In addition to the statistical error there will be systematic effects that limit the precision, such as variations in pixel size and response, lens distortions, etc. Before installation of the camera on the telescope a measurement and calibration of the precision in a test set up is anticipated.

## 5.3 Focal Plane

The BigBOSS Focal Plane system is being studied by the Instituto de Astrofísica de Andalucía (IAA-CSIC, Granada, Spain). The IAA-CSIC, in collaboration with the company AVS is working on its conceptual design. The Focal Plane parameters depend heavily on the support structure (Corrector barrel) and on the final design of the Fiber Positioners (actuators).

Table 5.7: Fiber View Camera Requirements

| Feature | Req. | Goal |
|---|---|---|
| Centroid Precision on Focal Plane | $\leq$15 $\mu$m | $\sim$5 $\mu$m |
| Absolute Position Calibration | $\leq$15 $\mu$m | $\sim$5 $\mu$m |
| Nearest Neighbor Distance | 3 mm | 1.5 mm |
| Exposure Time | $\leq$2 sec | $\sim$1 sec |
| Readout Time | $\leq$2 sec | $\sim$1 sec |
| Thermal Stability | $\leq\pm$1°C | 1°C |
| Mounting (Vibration) | $\leq$15 $\mu$m/sec | 5 $\mu$m/sec |
| Scattered Light | None | None |

The focal surface is as a convex spherical cap with 4000 mm radius of curvature and 950 mm in diameter. The focal plate is foreseen to be an aluminum plate $\sim$100 mm thick. Its primary purpose is to support the fiber positioners such that the fibers patrol area form tangents to the focal surface.

### 5.3.1 Interfaces

The focal plane will be supported by a structure attached to the back of the corrector barrel. Due to the distance to the corrector (about 200 mm), the focal plate cannot be directly attached to the corrector barrel and some structure in between (adapter) will be necessary. This will need to provide manual adjustment for initial focusing.

The focal plane supports several systems, most importantly being the 5000 fiber positioners as already mentioned. These insert from the back of the focal plane to facilitate replacement. Insertion depth, tilt and rotation angle are precisely controlled, tolerances allocated from an overall focus depth budget. There is an array of fixed fibers that can be back illuminated to serve as fiducials for a fiber view camera. Guiding and focus sensors also reside on the focal plane.

The focal plane is electrically connected with the power supplies for the fibers positioners, positioners wireless control system, electronics for guiding and focusing sensors, fiber view camera lamps, and environment monitors. Electromagnetic interference, both received and transmitted, will need careful study.

The amount of fibers and cables coming from the prime focus makes its handling an important and difficult task. These must be routed from the focal plane to telescope support cage while minimizing obscuration of the primary mirror. Careful packing within the footprint of the primary

optics support vanes coming from the telescope Serrurier truss will need be designed.

### 5.3.2 The Focal Plate Adapter

A structure is needed in order to attach the focal plate to the corrector barrel. A simple structure made of two circular flanges linked by a number of trusses should be able to cope with the flexures and sag. A few reference pins will be used to obtain mounting repeatability. Interface of the adapter will be the corrector barrel on one side, and the focal plate edge on the other side. The adapter requirements are shown in Table 5.8.

Table 5.8: Focal Plate Adapter Requirements.

| | |
|---|---|
| Outer diameter | $\sim$950 mm |
| Positioning error (XY) | $< 100$ $\mu$m (absolute) |
| Wedge error (between interfaces) | $< 0.25$ mrad |

### 5.3.3 The Focal Plate

The Focal Plate will be a solid piece of metal, probably aluminium, with multiple drills for actuator housing. The plate does not need to have a spherical shape, but the holes hosting the actuators must have their axes converging to the focal surface center and the plate must support the actuators so that their tips lie on the spherical focal surface. An example of suitable shape is shown in Figure 5.9. The edge of the plate must match the adapter flange which attaches to the corrector barrel. A few reference pins will be used to obtain a repeatable positioning onto the flange. Because the holes hosting the actuators do not follow any regular pattern (see Fiber Positioner Topology section), they will have to be machined from the model coordinates via a 5-axes machine tool. Care must be taken with the thermal expansion of such a large metal plate (aluminium might not be ideal to this respect), which could easily overcome the actuators required positioning precision. It could be necessary to set up a thermally controlled environment around the plate and the actuators, which could be obtained by enclosing the back of the focal plane with a vacuumed box, the other side of the focal plane being enclosed by the corrector last lens. In general, during the focal plane AIV, it will be necessary to characterize all the reference positions of the actuators via the Fiber View camera (with fiber back-illumination), which makes it much easier to fulfill the positioning precision over such a

large array of actuators. The requirements for the Focal Plate are shown in Table 5.9.

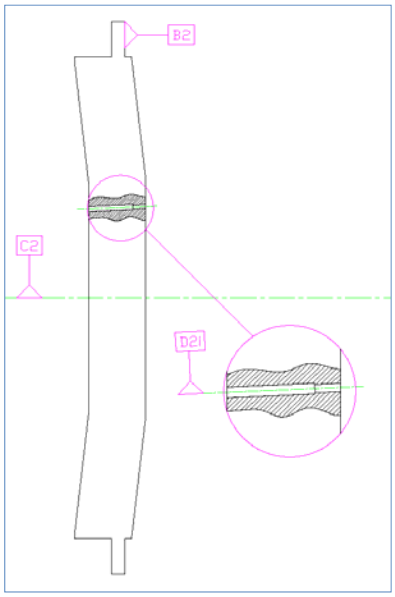


Figure 5.9: Focal plate cross section, where only one actuator housing is shown as an example. B2 is the interface with the adapter, while C2 is the plate axis and D2 is one sample actuator axis.

Table 5.9: Focal Plate Requirements. See also Figure 5.9.

| | |
|---|---|
| Number of actuators | 5,549 |
| Outer diameter | 950 mm |
| Positioning error | $< 100$ $\mu$m (absolute) |
| Perpendicularity error (B2-C2) | $< 0.4$ mrad |
| Actuator housing tilt error (C2-D2) | $< 2$ mrad |
| Focal Plate Thickness | 100 mm |
| Tot Max allowed weight | 700 Kg |

### 5.3.4 Fiber Positioners

A key enabling element for an efficient survey is a robotically manipulated fiber positioning array. The ability to reposition the fiber array on a timescale of ∼1 min greatly improves on-sky operational efficiency when compared to manual fiber placement methods. Requirements for the fiber positioner system are shown in Table 5.10.

Table 5.10: Fiber Positioner System Requirements.

| | |
|---|---|
| Number of actuators | 5,000 |
| Actuator pitch | 12 mm center to center |
| Patrol radius | 12 mm/$\sqrt{(3)}$=7 mm (filled survey) |
| Defocus over patrol disk | $< 10$ $\mu$m including spherical departure |
| Positioning accuracy | $< 100$ $\mu$m (absolute) |
| Positioning precision (over 200 $\mu$m distance) | $< 5$ $\mu$m (absolute) |
| Power | $< 0.4$ W peak during actuation, $< 5$ mW while waiting for command |
| Fiber termination | 1.25×10 mm ferrule, replaceable without disassembly of actuator |
| Stray light treatment | Diffuse black paint on upper surfaces of fiber positioner. |

The fiber positioners selected for BigBoss will be assembled by USTC (China) who have experience designing and manufacturing the actuators for the LAMOST project. Multiple variants of the LAMOST actuator redesigned for BigBoss are currently under test at USTC, including a 10 mm diameter (12 mm pitch) actuator, as well as a 12 mm and 15 mm diameter variants. The 12 mm diameter version (see Figure 5.10) has a measured repeatability (precision) better than 5 $\mu$m. Key changes to the LAMOST design included installation of smaller diameter motors with co-linear axes, and a redesign to the gear system. The LBNL/USTC team is currently working to achieve a 10 mm diameter (12 mm pitch) actuator designs. The Instituto de Astrofísica de Andalucía (IAA-CSIC, Granada, Spain) in collaboration with the company AVS is also working on a parallel design for the BigBOSS 10 mm diameter actuator. The IAA-CSIC/AVS already got extensive experience with the design and construction of a high precision fiber positioner prototype for the 10 m Gran Telescopio Canarias. They are also now designing the BigBOSS focal plate.

The choice of power and command signaling architecture for the robotic

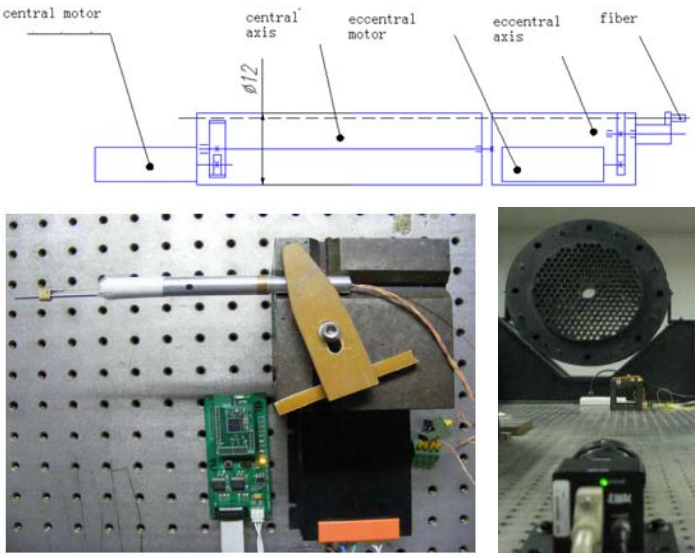


Figure 5.10: 12 mm diameter actuator under test at USTC

actuators is driven by packaging constraints. LAMOST experience showed that fiber, power and command line routing space is at a premium on a high-density robotic focal plane array. LAMOST opted to implement a hybrid wire/wireless scheme, in which only power lines and fibers were connected to each actuator and commanding was implemented by a ZIGBEE 2.4 GHz wireless link. With even greater fiber density, BigBoss has baselined ZIGBEE wireless communication. Five transmitters will each communicate with 1,000 actuators. The thermal cover on the aft end of the corrector will serve as a faraday cage to contain RF transmission from the ZIGBEE array. Although ZIGBEE commanding is currently baselined, power-line commanding is also under consideration.

Figure 5.11 shows the baseline actuator control board as implemented by USTC, and the overall architecture. In order to reduce the size of the board relative to that of LAMOST, a smaller microcontroller (without integral ZIGBEE) was selected. The power converter of the LAMOST board was made unnecessary by selecting a motor driver, microcontroller and ZIGBEE IC that operate at the same voltage. Each group of 250 actuators will be powered by one dedicated 250 W power supply.

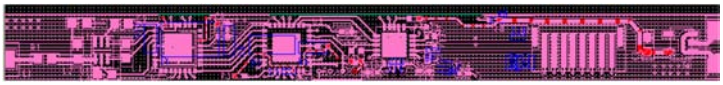

Figure 5.11: BigBoss wireless actuator control board is 7 mm wide, with 4-layers. This USTC design is simplified relative to that of LAMOST.

### 5.3.5 Fiber Positioner Topology

Each fiber must be positionable over a disc (patrol area) in order to gather the light of a targeted galaxy. The disc is necessarily flat because of the positioner characteristics, while the focal surface is convex spherical, with a radius of curvature of 4000 mm and a diameter of 950 mm. Two questions arise.

**First, what is the best position of the disc with respect to the spherical focal surface?** Placing the disc tangent to the sphere is not ideal because the borders of the disc would be affected by defocusing. The same is true if the circumference of the disc is embedded in the spherical surface; in this case the center of the disc would suffer the defocusing. The best position must be somewhere between these two extreme positions, and we assume it to be that position for which the defocus is the same at the center and at the border of the patrol disc (other positions could be used, with little practical difference). Figure 5.12) illustrates the trades. For a 4000 mm radius of curvature, and 6.93 mm patrol radius, and imposing $W = S$, we have the same defocus at the center and at the border of the patrol disc. The best position is found with the patrol disc 2.5 $\mu$m away from being tangent to the focal surface, a small number. It also tells us that the defocus at the center and border of the patrol disc is also 2.5 $\mu$m.

**Second, is it possible to distribute the actuators uniformly over the spherical surface?** Here, "uniformly" means that the distances between the centers of one patrol disc and its six neighbors (hexagonal pattern is assumed) is the same all over the focal plane. A sphere can not be tessellated with uniform size hexagons. The task is to find a distribution as uniform as possible over a sphere, and, ideally, a distribution which can be easily transferred to a drilling machine for fabrication. The process adopted here is to stretch a flat, uniform distribution of hexagons onto a sphere. Figure 5.13 shows two possible types of deformations that can be used. The bipolar mapping follows a opposite process to that of mapping a portion of

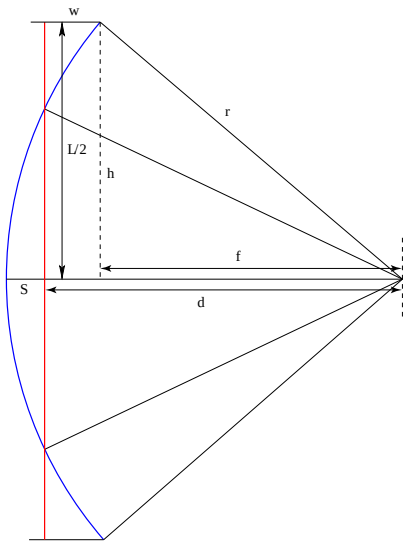


Figure 5.12: Cross section of a patrol disc (the vertical line) when intersecting the focal surface (curved line). $L/2$ is the patrol radius and $r$ is the focal surface radius of curvature. $S$ and $W$ are the deviations in and out of the focal plane.

the Earth onto a plane map—the regions close to the poles (at the top of the figure) have a greater density than those close to the center. The multipolar mapping yields a different distribution, which gives a rotation-invariant pattern about the center, thus a slightly more uniform distribution. Other distributions could be used (for example an orthogonal projection, or a central projection centered at the curvature center), but it is found that the multipolar mapping gives the best results.

For the spherical focal surface of 950 mm diameter and 4000 mm radius of curvature with a 12 mm center-to-center between actuators (5549 actuators), the multipolar mapping has a center-to-center difference of 26 $\mu$m; the orthogonal projection yields 78 $\mu$m, the bipolar mapping yields 79 $\mu$m and the central projection 153 $\mu$m. Thanks to the large radius of curvature and relatively small diameter of the focal surface, the differences are of the order of tens of microns, but they cannot be neglected and will make the machining of the focal plane challenging. We note that the anti-collision software algorithm for moving the actuators also must take into account the varying safe distances across the focal plane.

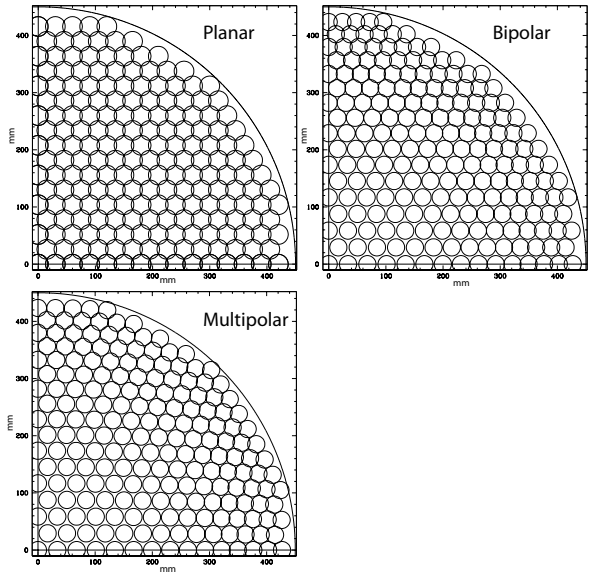


Figure 5.13: Distribution of patrol discs over a flat disc (top left), over a spherical cap with the bipolar mapping (top right) and with the multipolar mapping (bottom left). The radius of curvature of the spherical cap is greatly reduced here (600 mm) in order to exaggerate the deformations. The patrol discs cannot be nested properly in the case of the spherical cap, thus their size is arbitrary. The picture is meant to just give the idea so only one quarter of the focal plane is shown, the rest being symmetric.

### 5.3.6 Guide Sensors

The Mayall telescope control is expected to point the telescope to within ∼3 arcseconds of the desired observation field. The BigBoss star guidance system (SGS) is required to assist in telescope pointing at levels below 10 mas and ensure each of the optical fibers is located to within 15 $\mu$m of the desired target on the sky. Trade studies between two star guider designs are in progress. Regardless of the final design, the system must contain at least two viewing fields with radius of 30 arcsec. This will allow the SGS to determine the current pointing of the telescope once the Mayall control has finished slewing to a new location. By comparing an observed star field to a star catalog (NOMAD, for example) the current telescope pointing can be determined.

The system must also be large enough to ensure that several guide stars are available for tracking. The resolution of the star centroids must be better

than several microns. The difference between observed and desired telescope pointing are then sent back to the telescope control system for adjustment. Finally, the fibers can be arranged relative to the observed pointing direction. The telescope is then updated periodically with correction requests for telescope pointing from the tracked star locations.

The two designs being considered have both been used in other systems. The first and more common design incorporates imaging sensors within the focal plane. A baseline design would be four optical CCDs located in each focal plane quadrant. Despite the added complexity of optical sensors on the focal plane, it provides a relatively stable location between fiber positioners centers and the guider. Figure 5.14 shows an example of this layout on the LAMOST telescope.

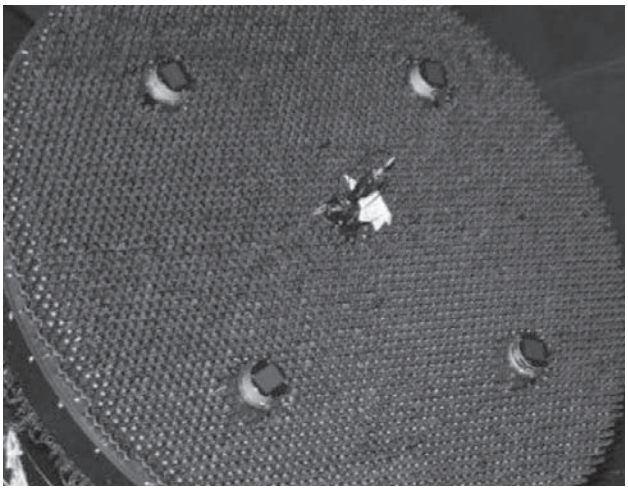

Figure 5.14: Photograph of the LAMOST focal plane with star guiders.

A second design is similar to that deployed in SDSS-III (Figure 5.15). All star guidance would be obtained via imaging optical fibers that are fixed in the focal plane. The fibers would transport star field images to remote cameras. At least two of the imaging fibers would need to be at least 30 arcseconds in diameter in order to acquire the current pointing direction. This design offers focal plane simplicity but has additional light losses in the fibers.

In either design, at least 240 arcmin$^2$ of sky would need to be covered by the fixed imaging fibers or the guider sensors. This area ensures that enough guide stars would always be available in a magnitude range both sufficiently bright for detection and within the dynamic range of the sensor. Star cata-

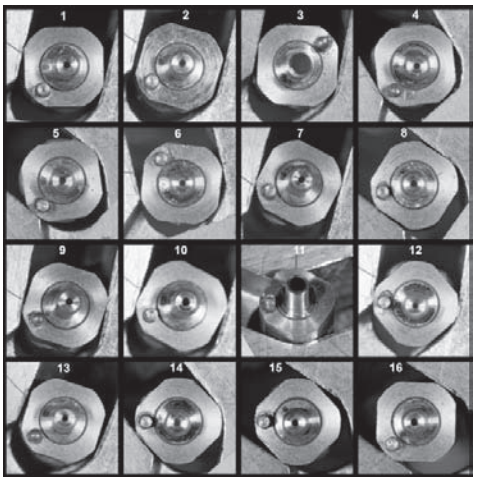


Figure 5.15: Photograph of the BOSS guider fibers. Two are large field fibers for star acquisition.

logs indicate that there are ∼0.14 stars per arcmin$^2$ in the magnitude range $15 < g < 17$ or 0.07 stars per arcmin$^2$ in the magnitude range $14 < g < 16$.

### 5.3.7 Focus Sensors

Two separate instruments will be deployed to monitor the telescope focus. First, a Shack Hartman sensor will be installed in the center of the field of view. This is a well known technology and will provide wavefront errors.

Second, a focus sensor comprised ∼11 steps of viewing above and below focus in the focal plane. The defocus steps are provided by varying thicknesses of glass above the imaging sensor. Nominal steps are 0, ±50, ±100, 250, 500 and 100 $\mu$m. Stars imaged above and below focus will form an annular shaped pattern. Analysis of these many donut shapes will provide corrections needed in focus.

The sensor technology used in this focus sensor will mirror that of the fine guidance star sensors. The first option is a single imaging sensor (CCD) in the center of the field of view. The other option is several imaging fibers each positioned at varying positions above or below focus. Focus information derived from the sensors will drive the six-axis corrector barrel hexapod to perform a focus adjustment at an update period yet to be determined.

The focus sensors will image stars above, below and in focus. The current focus and alignment of the telescopes can be determined from the coefffi-

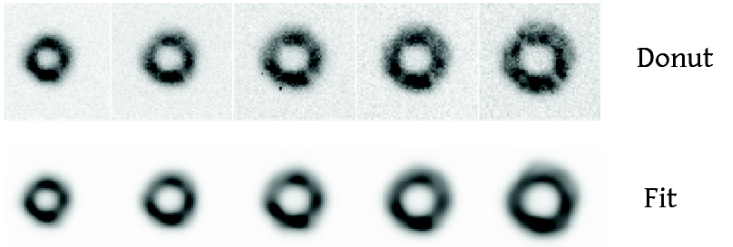


Figure 5.16: Star images taken at the Blanco telescope and the associated Zernike expansions.

Table 5.11

| | |
|---|---|
| $Z_4$ | Defocus |
| $Z_5$ | Astigmatism x |
| $Z_6$ | Astigmatism y |
| $Z_7$ | Coma x |
| $Z_8$ | Coma y |
| $Z_9$ | Trefoil x |
| $Z_{10}$ | Trefoil y |
| $Z_{11}$ | Spherical Abberation |

cients of a Zernike expansion of these images (Eq. 5.1). Table 5.11 shows the optical meaning of several Zernike terms. The in focus star images provide seeing information that assists in the above and below focus image calculations. Figure 5.16 shows an example taken with the Mosaic 2 camera at the Blanco telescope.

$$W(u,v) = \sum_{i=4}^{i=37} c_i Z_i(\rho,\theta) \tag{5.1}$$

In BigBOSS, donut images will be captured and processed with a frequency of around one minute. After a 15 minute data integration, many measurements of focus and alignment (changes) will be available. The hexapod can then apply any needed corrections to the optical system during the data readout period.

### 5.3.8 Fiber View Camera Fiducials.

As described in the fiber view camera section, a set of fixed fibers in the focal plane are used as fiducials. The number and deployment await detailed stud-

ies from the development of the view camera fiber position reconstruction code. At the moment, it is thought that these fibers would be illuminated by lamps in the focal plane region, saving routing them off the telescope structure.

### 5.3.9 Thermal Control

Source light is collected at the prime focus by 5,000 robotically controlled actuators. Each actuator has a peak power of 0.4 W while actuating, and an idle (waiting for Zigbee command) power of roughy 2 mW. On average, each repositioning of the array is estimated to dissipate 150,000 joules, which could raise the temperature of the focal plane assembly by roughly 1°C. This temperature increase is not negligible, and would be expected to degrade telescope seeing unacceptably. We are trying to better estimate these numbers.

Other potential heat sources are guider and focus sensor electronics, lamps for fiber view camera ZIGBEE base stations.

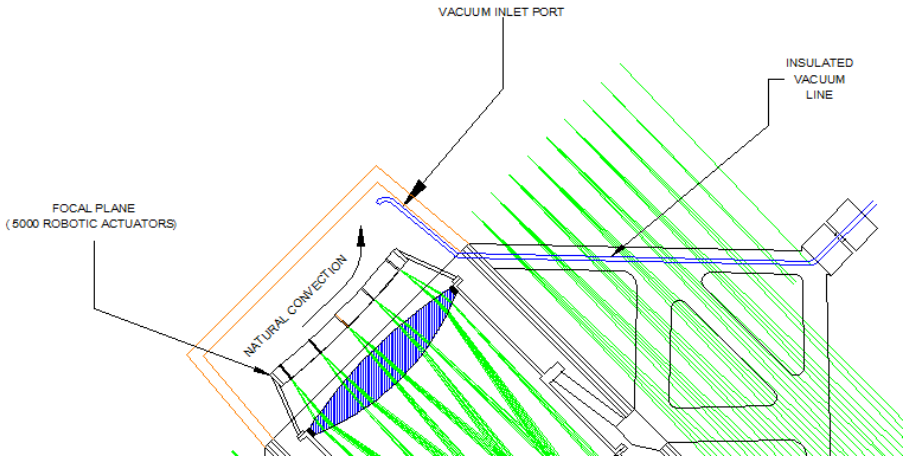


Figure 5.17: Heat generated by the fiber positioners is capped, and vacuumed away by an insulated suction line.

The cooling approach adopted on BigBoss employs an insulated cap behind the focal plane, and an insulated vacuum to draw away warm air from the focal plane. Figure 5.17 shows the nested corrector mount on the radial spider vanes. The corrector moves within a barrel assembly capped at the top by an insulated cover. Heat generated in the focal plane region

is removed by natural convection (gravitational pumping) and contained by the cover. An insulated vacuum line located at the top corner of the cover removes warm air directly from the top of the corrector, and removes it from the dome (where it is released into the atmosphere downwind of the telescope). Ambient air is drawn into the corrector barrel through the gap between the corrector and outer barrel. Flow of air into a vacuum port is essentially irrotational (potential) flow, and does not generate vorticity and turbulence, as would an air outlet line.

Forced air cooling was rejected due to due to its consequences for seeing, and glycol loops were rejected due to risk to the primary mirror.

## 5.4 Fibers

### 5.4.1 Overview

The fiber system consists of a close-packed focal-plane array of 5000 computer-actuated input fibers ends to collect target flux, a fiber run to transport flux to the spectrographs, approximately 40 m distance, and the output end of the fibers, arranged in 10 sets of curved linear arcs of 500 fibers each that feed a bank of 10 spectrographs. The planar-faced fiber input ends are to be placed with 10 $\mu$m accuracy within the patrol radius of each fiber actuator. Each fiber input end can be non-destructively removed and replaced from its actuator assembly with precise axial location. The fiber run uses guides, trays, and spools to reach from the focal plane to the spectrograph room. To facilitate installation and maintenance, the fiber system concept includes an intermediate fiber-to-fiber connector within the fiber run. The output ends are modularized into sub-slit blocks of 100 fibers. The fiber system and its requirements are summarized in Table 5.12. Key performance and technology issues are discussed in detail thereafter, with important contributions by the IAA-CSIC/Durham University collaboration, thanks to the Durham University experience with the FMOS and others fibre systems (thanks to G. Murray and J. Allington-Smith).

### 5.4.2 Technology and Performance

Fiber throughput is science critical as light loss requires longer exposure times with a lower survey rate, limiting to the rate of sky coverage. Fiber throughput is effected by the fiber glass bulk transmission and losses at the fiber ends due to polishing imperfections and surface reflection. Low-OH silica fibers such as Polymicro FBP or CeramOptec Optran (Figures 5.18 and 5.19) are well matched to the desired pass band and have a minimum

Table 5.12: Fiber Requirements and Specifications.

| |
|---|
| **Fibers** |
| 5000 each |
| Low OH fused silica (340–1060 nm) |
| Core 120 $\mu$m diameter |
| Cladding and jacketing combined outside diameter $< 240$ $\mu$m |
| Fiber performance robust to repeated actuator flexing (30k cycles) |
| FRD 90% within f/4.0 for f/4.5 input |
| **Input end at focal plane** |
| Output face, flat polished, AR coated (340–1060 nm) <1.5% total loss |
| Ferrule terminated, removable from actuator |
| Ferrule 5 $\mu$m axial position accuracy in actuator |
| Fiber end angle $\pm 0.25^\circ$ |
| **Fiber run** |
| Length <40 m |
| Bulk transmission |
| 340–450 nm $> 50 - 70\%$ |
| 450–550 nm $> 85\%$ |
| 550–1060 nm $> 90\%$ |
| Sub-bundle maximum cross-dimension for focal plane routing 50 mm |
| Bundle performance robust to repeated flexing (30k cycles) |
| Coupling connector |
| >100 fiber per connector |
| <2% loss |
| use in controlled enclosed environment |
| Verified performance life 100 mates |
| **Output end at spectrograph** |
| 500 fibers per slit assembly |
| Slit height 120 mm |
| Slit radius of curvature 330 mm |
| Fiber ends within $\pm 45$ $\mu$m of spectrometer slit radius of curvature |
| Slit made of 5 each blocks with 100 fiber units |
| AR coated (340–1060 nm) <1.5% loss |
| Provision for diffuse back illumination of fiber ends |
| **Environmental** |
| Input end and fiber run operational temp range -10 to $+20^\circ$C |
| Output end operational temp range 15 to $25^\circ$C |

of absorption features that are inherent in high-OH, UV enhanced fibers, although, for reasons which will be covered in the next section, the polyimide buffer is probably the best suited material for this application. The fiber ends will be treated with antireflective coatings so that light loss at each fiber

ends can be reduced from ∼5% to <1.5% each (see Figure 5.20). We will use independent quality control inspection to verify the net transmission of fiber lot bulk transmission and the transmission performance of each fiber.

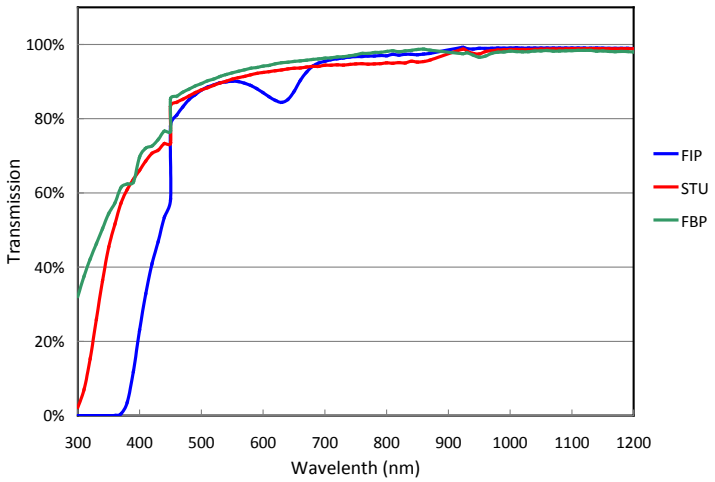


Figure 5.18: Polymicro 30 m length fiber transmission comparison.

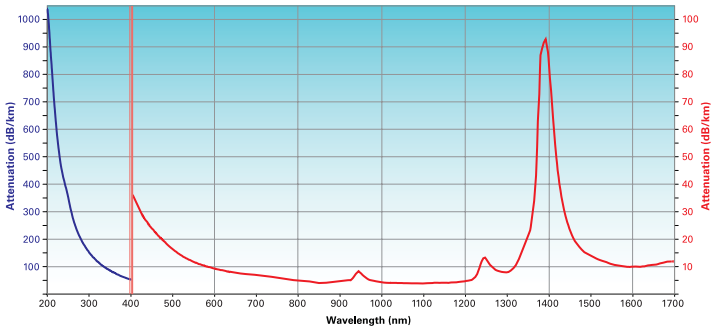


Figure 5.19: Polymicro FPB Low OH fiber attenuation.

Light incident at one angle on a fiber will exit the fiber with a distribution of angles. Consequently, a cone of radiation entering the fiber at a certain focal ratio will exit the fiber spread into a smaller focal ratio, i.e., suffer from focal ratio degradation (FRD). The FRD is caused in part by imperfections in the fiber manufacturing process and by the quality of the fiber-end mechanical treatment, e.g., bonding and polishing stresses induced on the fiber's terminus. Actual measured FRD for a selection of fibers made for BOSS are shown in Figure 5.21. We use achievable values from

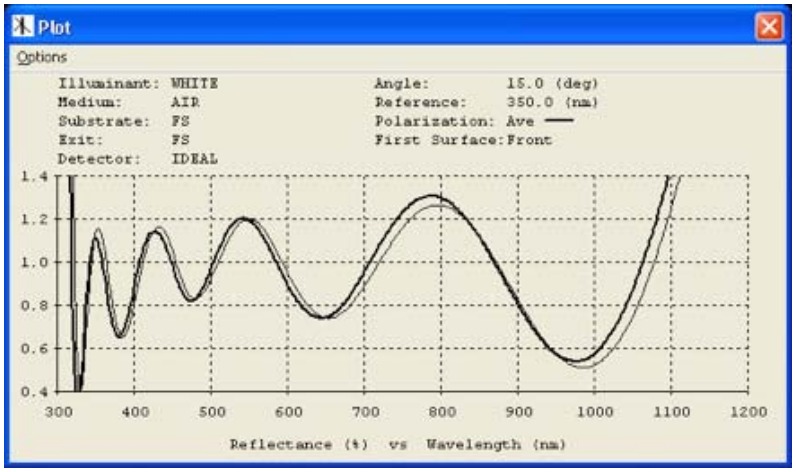


Figure 5.20: Modeled AR coating at 0° and 8°. incidence (by Polymicro on FBP).

this experience in establishing our performance parameters. FRD is exacerbated by stresses, bends and micro-cracks caused by fiber handling and routing. Demonstrated control of FRD is important to achieve the desired throughput because light distributed beyond the acceptance of the spectrograph may be lost or scattered. Quality control inspection will be used to verify the net FRD of performance of each fiber so that an accepted fraction of f/4.5 input flux will be projected within the f/4.0 acceptance of the spectrograph including an allowance for the fiber angular output tolerance. Pupil variations due to FRD, fiber angular output, or fiber modal noise are not critical for this relatively low-resolution spectral application where the spectral resolution requires only a modest sub-aperture of the grating.

We also consider the potential for FRD over the course of the thousands of random motions of the fiber positioner that represent the observation lifetime. Propagation of *ab initio* microcracks as the fiber is flexed during actuator motion may lead to a time dependent degradation of transmission efficiency. Various fiber types differ in their cladding overcoats, which according to vendors can affect flex performance. The Polymicro fibers used for BOSS, a hard clad silica with a single hard polyimide overcoat, have proven FRD robust to hand insertion flexing cycles. CeramOptec makes a fiber construction to minimize internal fiber stresses by using a two-layer clad (hard then soft glass) and a two-layer coat (hard then soft plastic) (see Figure 5.22). We will conduct degradation tests for the different fiber

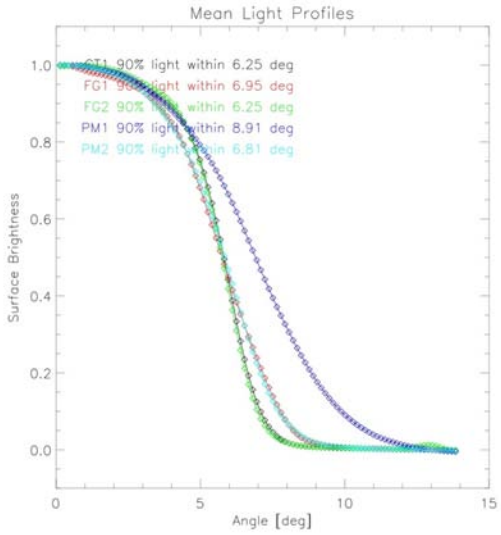


Figure 5.21: FRD of Polymicro FBP 120 $\mu$m core fiber measured for BOSS.

constructions to determine their life FRD properties given the mechanical requirements of the actuator rotation cycles.

The fibers will also be flexed in their bundled run assemblies as the telescope slews over the sky. These repeated motions may also induce worsened FRD. Bundle and sub-bundle bending will be constrained to the rated long-term life radii by using guides belts, rails and soft clamps. Stress propagation to the fiber ends cause by friction induced wind-up over many motion cycles will be mitigated by using low friction sleeves (e.g., Nomex) over the sub-bundles. A fiber bundle assembly mock-up will be exercised over the designed routing system to verify its life performance.

### 5.4.3 Positioner Fiber Termination

At the focal plane, each fiber end is terminated individually to a positioner. The termination will be made by bonding the fiber into a ferrule and then finishing the optical surface (Figure 5.23) with flat polishing. To optimize the light entering the fiber tips at the focal plane an antireflection coating will be applied to the polished fiber ends. Since the coating must be applied to the pre-assembled and polished fiber/ferrule assemblies, a low temperature ion-assisted-deposition IAD coating process is preferred. This avoids the possibility of compromising the epoxy-bonded fiber/ferrule interface. The

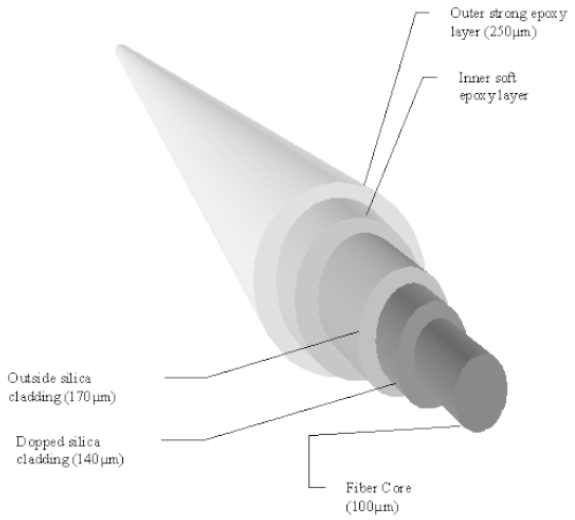


Figure 5.22: CeramOptec fiber with double cladding and double coating layers graded in hardness to minimize fiber stress.

fiber buffer material should be polyimide. This is a relatively hard, thin layer coating that can withstand high temperatures. Its inclusion during the polishing process does not degrade the quality of the polished surface (as can happen with out-gassing from softer acrylate coatings, for example). Polyimide buffers have a higher tolerance on diameter and concentricity, which means that there is no requirement to strip the buffer from the ends of the fibers before assembling into ferrules; a substantial simplification of the construction procedure.

The fiber-end surface stress and damage, and so FRD performance, will be impacted by the choice of the ferrule and adhesive materials as well as the process used for bonding and polishing. Stress can occur during the epoxy curing cycle (some epoxies exhibit greater shrinkage when the cure is thermally accelerated, others behave in the opposite manner). Stress will also occur when coefficient of thermal expansion (CTE) of the fiber and the ferrule are mismatched, and the operating environment is at a different temperature to the ambient temperature at which the assembly was made. Combinations of specific glasses/ceramics/steels with specialized epoxies have proved to be effective solutions for minimizing such effects. There are two routes to achieving a low stress assembly:

a) The CTE of the ferrule and the cured epoxy are matched (approximately) to the fiber. In this case the epoxies used are generally brittle when cured, e.g. Epotek 353-ND. This epoxy stabilises better, with minimal shrinkage, with a thermally accelerated cure. Nevertheless, bulk regions of epoxy surrounding the fiber should be avoided.
b) The CTE of the materials differ but the epoxy retains some elasticity (e.g. Epotek 301-2). The epoxy layer then serves as a cushion, accommodating any differential expansion.

Polishing is relatively straightforward; sub-surface damage is caused to a certain extent by the polishing abrasive. As a rule of thumb, when polishing with progressively finer grades of abrasive the depth of material removed should be at least three times the previous abrasive particle size. So for example a fiber polished with 9 $\mu$m abrasive would typically progress to a 3 $\mu$m abrasive stage. In this case $>27$ $\mu$m of fiber surface should be removed by the 3 $\mu$m abrasive. We plan to verify the fiber termination process and performance over lifetime temperature cycles.

The ferrule will be coupled to the metal actuator arm using a removable interface that provides the required 5 $\mu$m axial precision for matching the focal surface. A dovetailed (or similar) semi-kinematic fitment is anticipated. The fixed, lateral fiber end positioning accuracy with respect to the positioner is not so critical because the fiber tracking camera will calibrate the fiber position. Nonetheless, the lateral position needs to be repeatable and stable between camera calibrations. The ferrule-actuator interface must not induce thermal stress on the fiber tip over the broad thermal range found at prime focus.

Protective sleeving will terminate at each ferrule assembly and will be bonded in place. At the high stress region where the fiber enters the ferrule assembly, the sleeving will serve as reinforcement. The sleeve should be sufficiently flexible to allow unimpeded movement of the actuator. The sleeve should also have a degree of wear resistance, to allow repeated movement within guide channel through the actuator. However it must not be so tough that it causes wear to the actuator channel itself. Candidate sleeving types include precision woven polyimide sleeve (Microlumen Inc.) or closed-wound helical tubing made from PEEK polymer. The jacketed fibers from a localized region of actuators will then be collected into sub-bundles of 100 fibers. The collection ports of the sub-bundles will be suspended from a fiber-harnessing support grid located near the aft of the focal plane's back surface. At the support grid, each sub-bundle will enter a protective sheath to commence the fiber run.

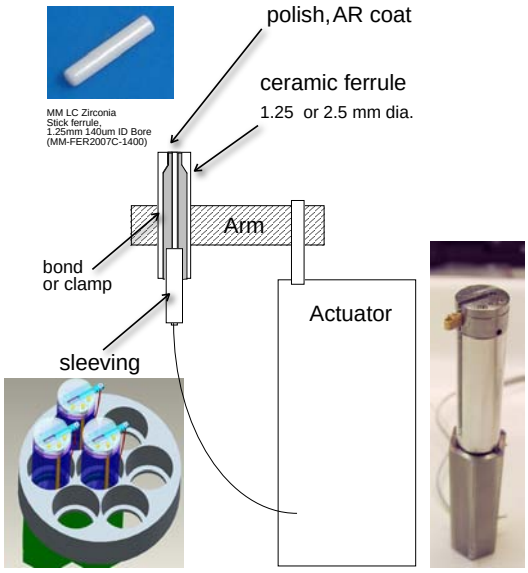


Figure 5.23: An $r$–$\theta$ actuator is shown at the bottom right and a simple array is at the bottom left. The illustration shows a fiber attached to the position arm. The fiber is first glued into a ferule and the tip is then polished and anti-reflective coated.

### 5.4.4 Fiber Run

Fibers and actuator electrical power lines will run in a bundle from the harnessing support grid behind the focal plane, down the telescope structure, across the observatory to the spectrograph room, and then branch out to feed each spectrograph assembly. The fiber run will be harnessed on a traverse down the telescope structure toward the Cassegrain cage and then routed through the elevation mount and polar bearing using spools, guides, and link-belts as required to constrain and limit the bundle motion to limit twists and enforce minimum bend radii.

The cables shall consist of an outer PVC clad ruggedized-steel spiral wrap (ADAPTAFLEX or similar- a standard product for such applications). Within this, the fibers are carried in furcated sub-bundles. MINIFLEX, a segmented polymer tube, is well suited to this application. It exhibits a reasonable flexibility in a relatively tough thick-walled tube, a safe minimum bend radius, low extension under load, and a high crush resistance. The conduits shall in addition each contain an internal Aramid yarn tensile element, to prevent the cables from extending under their own weight over

the length of the drop from the telescope top end ring to the Nasmyth cable wrap. Figure 5.24 shows a cross section through the cable.

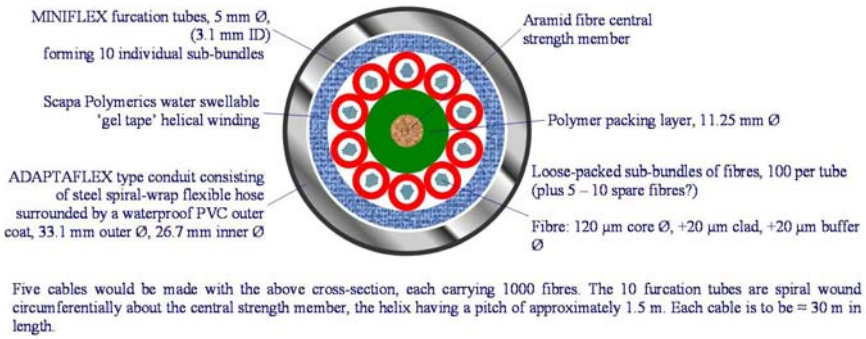


Figure 5.24: Proposed cable cross section.

The furcation tubes carrying the loose fibres are arranged radially around the Aramid tensile element, which is built up with a polymer coating to a diameter around which the tubes pack uniformly. Crucially, the furcation tubes are wound around the core in a spiral pattern. This avoids differential length problems when bending the conduit, where fibers on the outside edge of the bend will require a longer path than those on the inside. The fibers can be considered as a loose coil with a length in excess of the length of the core tensile element, therefore no movement of the cable will generate a cumulative tension in the end terminations. The helical wound cable core is wrapped with a protective ribbon of polymer tape. In typical cable applications this also carries a hygroscopic layer of gel, which ensures a dry and stable environment within the cable volume. Figure 5.25 shows a sample section of cable. Visible in the picture are the outer conduit, polymer tape wrap, tensile element termination hardware, and the spiral wound construction.

There are a range of size options for the fiber cabling, from a large, single conduit carrying all fibers to a set of 10 small conduits, one for each spectrograph. A reasonable solution in terms of size and packaging would consist of five primary cables, each carrying 1000 fibers. This makes use of standard sized 33 mm industrial conduit, each supporting ten regular 5 mm diameter furcation tubes. The fibers would be loose-packed, preferably with a fill-factor of $<80\%$. A schematic sketch of the proposed cable scheme is shown in Figure 5.26.

At the top end ring, the tensile element will terminate at the strain relief boxes (see next section), so the cable diameter reduces; useful for

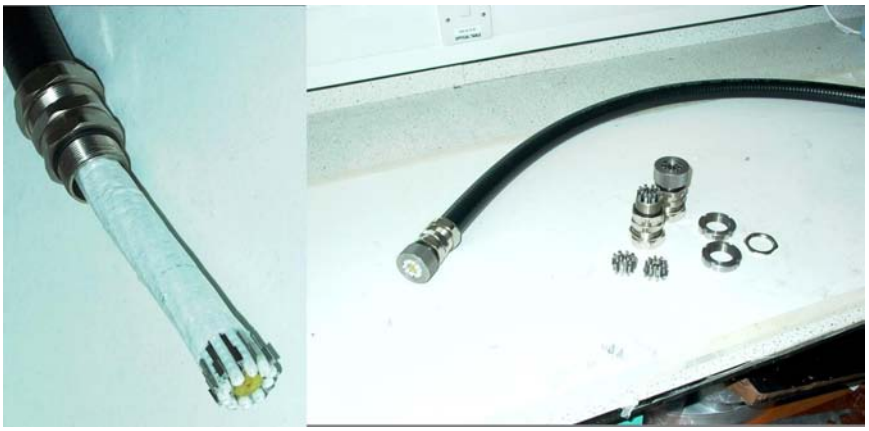

Figure 5.25: Example of fiber cable.

maintaining a low profile where the cabling must cross the incident light-path, in the region from the top-end ring to prime focus. If the original cable size is 33 mm with the tensile element, then the conduit diameter can be reduced to 26 mm without it. It is anticipated that the five cables would be managed between the spider arm structures as a flat ribbon carried on a thin support plate. They could be managed in an IGUS-chain type cable management duct if necessary. A simple sketch illustrating the routing path is shown in Figure 5.27. If a lower profile is required across the spider arm we can double the number of cables from five to ten, and reduce the conduit diameter further. Alternatively, if space is extremely restricted the furcation tubes alone could route across this region, in a simple flat box.

It is assumed that the fiber run will carry some spares (2% - 5%) in case of fiber breakage. These will run from the focal plane where the spare fibers will also be terminated with focal plane buttons, and they will be stowed in the vicinity of the harnessing support grid behind the focal plane. The spare fibers will continue down through the main cable run, but they terminate before the spectrograph slits. The bonded design of the slit unit fiber arrays precludes the option to replace broken fibers within the slit units themselves; the slit units and the fiber run within each spectrograph will therefore carry no spare fibers. This presents a potential problem; swapping a fiber at the top end is of no use if it cannot couple through to the output slit. There are two possible solutions. Either the replacement fibers are spliced into the spectrograph fiber scheme, or connectors with interchangeable fibers are located on the outside of the spectrograph enclosures (see later section).

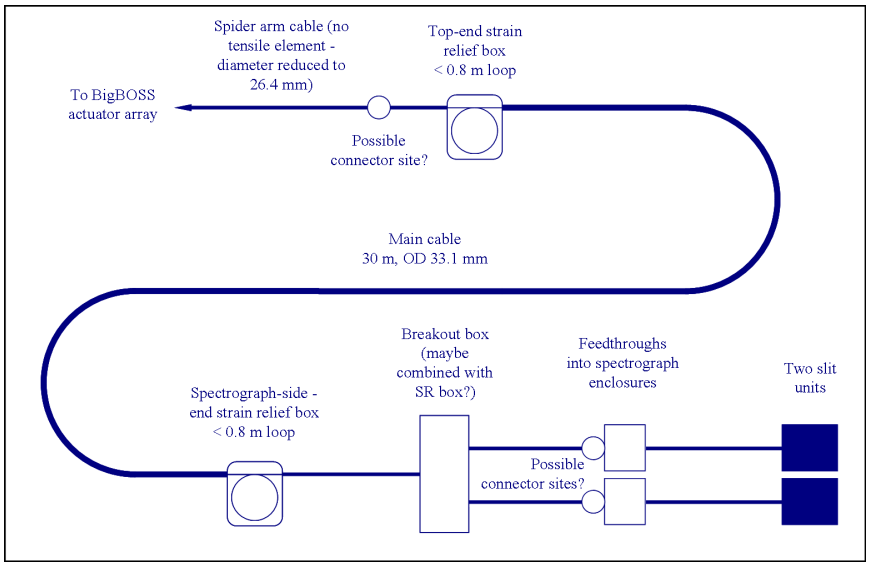


Figure 5.26: Proposed run of fiber cable with strain relief boxes, breakout box and connectors.

### 5.4.5 Strain Relief Boxes and Breakout Boxes

Strain relief boxes are located close to either end of the cabling scheme, and they support free loops of fiber. This permits a degree of movement of the fibers within the main cable, allowing any differential tension to equalize. More importantly, it allows for a reservoir of spare fiber during end termination. By taking up slack within fiber loops, the fiber lengths can be equalized. It is useful should any terminations fail during assembly; the broken termination can be removed and additional fiber can be drawn from the strain relief box to make a replacement. They also provide a barrier, preventing longitudinal fiber movement from passing further down towards the ends of the cable. Should this occur it could lead to tension and therefore stress at any bonded fiber v-groove arrays or ferrules that terminate the fiber system.

The boxes are formed of either aluminum or molded plastic. Within the boxes there are arrays of spacers which manage the bare sub-bundles of fibers in single loops. See Figure 5.28 for a photograph showing strain relief boxes employed on the FMOS fiber system.

The cable divides into two at the spectrographs. This is managed in a breakout box; a simple enclosure that serves as a junction where the cable

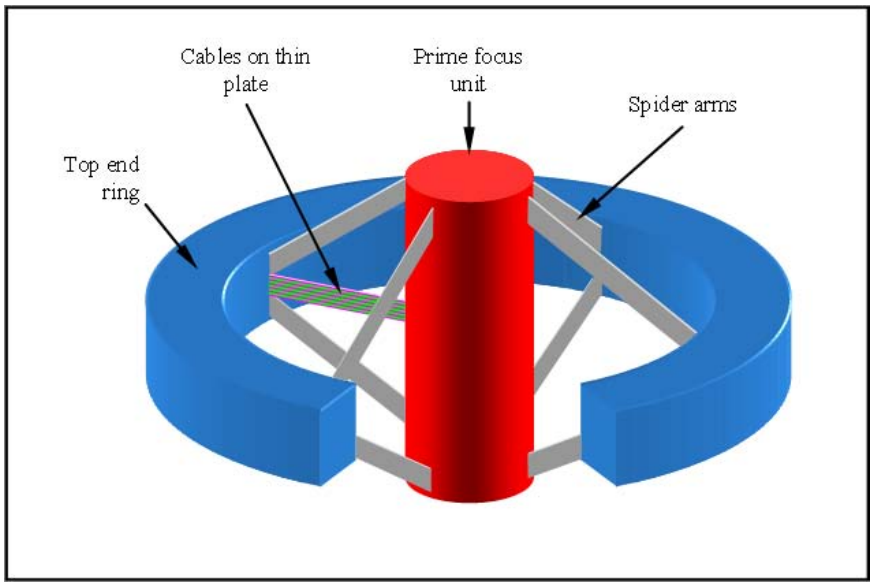


Figure 5.27: Schematic view of the fiber routing at the top end ring of the telescope (near-side shown cut away for clarity).

splits. They are simple aluminum enclosures.

### 5.4.6 Fiber Connectors

We anticipate that an intermediate fiber to fiber connector (or connectors) within the run will ease project fabrication, integration, and schedule demands and will prove essential to facilitate installation. A fiber connector will allow both the focal plane and the spectrograph to be fully and independently assembled and tested off-site. For example, the exit fiber slits can be aligned and tested with their spectrographs in the laboratory, and the fiber input ends can similarly be installed and tested in their actuators at the focal plane. It may therefore be worth considering connectors at both ends of the cable scheme. The use connectors will incur some optical loss, however bare fiber, index-matching gel filled connectors can exhibit losses smaller than 2%. Another option would be to use a lensed connector (using pre-fabricated lenslet arrays or individual elements such as GRIN lenses (high precision but inexpensive). Lensed connectors can additionally be configured to tailor the focal ratio of the light propagating through the fiber train; this is useful if there is a conflict between the focal ratio at the focal plane and the focal ratio for minimum FRD in the fibers and the op-

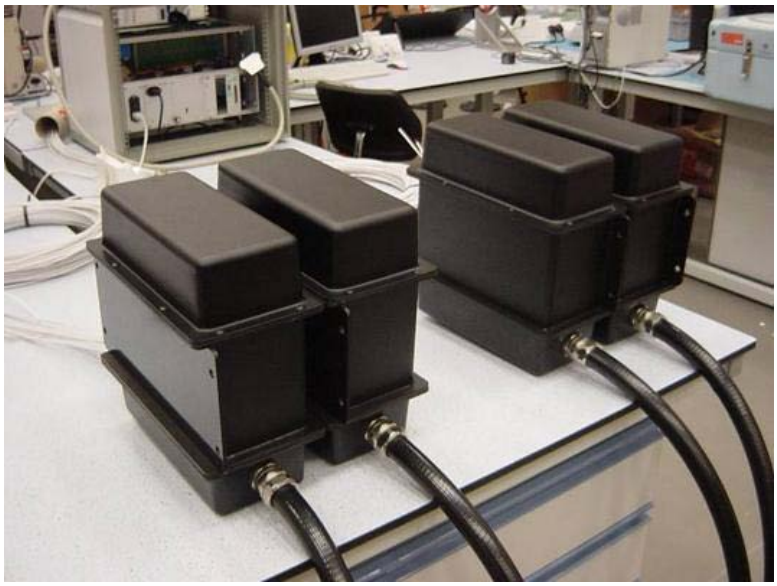

Figure 5.28: Example of strain relief boxes.

timum F number for feeding the spectrographs We propose that the fiber connectors (if they are deployed at the top end) be made with units that couple 1000 fibers, each corresponding to a single routing cable. If connectors are deployed at the spectrographs then it would be logical to have one connector per spectrograph, so each would support 500 fibers. Options for the connectors include adapting commercial devices or constructing custom connector modules from precision 2-D hole arrays. For a bare fiber connector, the design could borrow the high precision technology that has been successfully proven for constructing integral field unit (IFU) inputs. For a lensed connector the fiber pitch would necessarily be larger so the connector heads would be precision CNC machined, or cut using an electric discharge machining (EDM) process. An example of the latter type of connector is shown in Figure 5.29.

The location of the connectors and their enclosure, be it along the telescope structure or on the observatory floor, will be determined following further study of the fiber run installation and routing scheme. These connectors are best used in fairly clean and controlled environments for reliable operation. Therefore we propose to include an environmental enclosure at the junction to limit foreign debris or other environmental intrusions about the connectors. The number of fiber connector couplings over the project life

Figure 5.29: Example of EDM processed fiber connector.

is limited as the coupling will be made for testing the units, the focal plane and spectrograph ends, and for telescope installation or maintenance. We anticipate that a proven lifetime of 100 couplings will suffice for the project.

### 5.4.7 Slit Array

The output end of the fibers are terminated into 10 slit arrays, one per spectrograph assembly. The slit array consists of a group of 500 fibers arranged in a planar arc specified by the spectrograph optical prescription. Fiber ends are directed toward the spectrograph entrance pupil and represent the illumination input, i.e., the spectrograph entrance slit (Figure 5.30). The slit arc is concave toward the spectrograph with a radius of 330 mm to match the pupil. The fiber's center spacing of 240 $\mu$m is established by the spectrograph field size together with the desired dark regions between each fiber's spectral trace on the sensor. Optical tolerances demand a precise location for the fiber tips with respect to focal distance, i.e., the fiber tips must lie within 10 $\mu$m of the desired 330 mm radius input surface. Lateral and fiber center spacings are not demanding.

The slit array is a mechanical assembly that includes five blocks of 100 fibers each which are precisely arranged to a strong-back metal assembly plate. The plate provides the mechanical interface to the spectrograph and is installed using registration pins for accurate location. The assembly plate also supports and constrains each block's fiber bundle and terminates the bundles' protective sheaths. The subset 100-fiber blocks are the basic fabrication unit for the fiber system. The ends of the individual fibers are bonded into V-grooves. The fiber ends are cleaved and then co-polished with the block surface to a 330 mm radius sphere. The V-grooves are EDM machined into a metal planar surface at radial angles that point each fiber toward the

radius of curvature. Fiber jacketing is removed prior to bonding and terminated into a larger V-grooves and the jacketed fiber is supported by adhesive on a free bonding ledge to enforce minimum curvature radii and strain relief the fibers before their entry into bundle sleeving. Following finish polishing, fiber support, and tested for throughput, FRD and alignment, the face of the fiber block will be antireflection coated. The method, materials and process for the block production will be verified through pilot development and test, including the fiber bonding and finish schemes impact on throughput and FRD and the robustness of jacket termination, free fiber support and bundle termination.

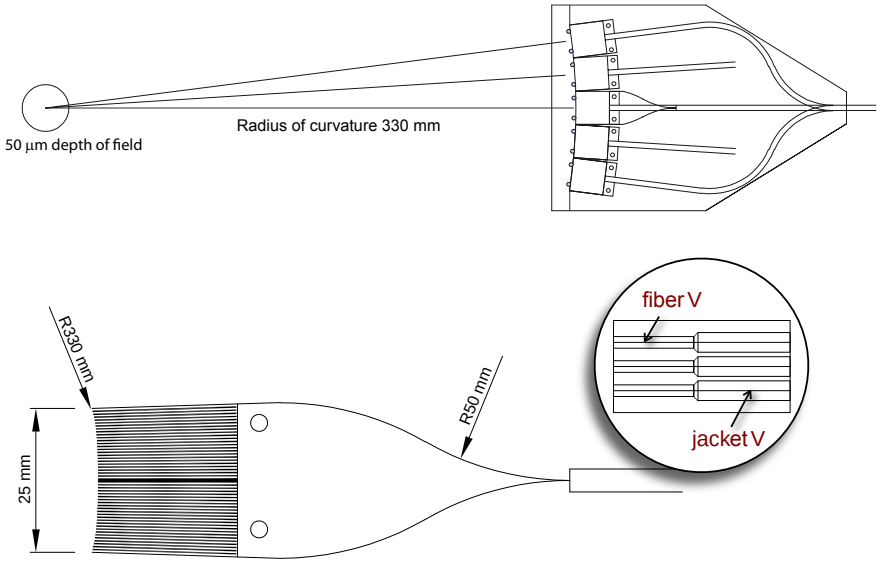


Figure 5.30: At the top is an illustration of 500 fibers focusing on the input of a spectrograph, forming the input slits. Below, a 100 fiber subset is glued in a plane and the fiber tips machined to the focal length of the spectrograph input. The tips require additional polishing and antireflective coating.

### 5.4.8 Calibration and Servicing Provisions

Each slit array assembly also includes a provision to flood the spectrograph focal plane with continuum flux so that a spectral flat field can be obtained. We intend to install a illuminated leaky optical fiber on the slit assembly plate that runs parallel to and nearby the slit. Lamp illumination of the leaky fiber will flood the spectrograph to provide a diffuse field for the de-

tector calibration. An internal shutter in each spectrograph camera can be used to back-reflect this diffuse flux into the fiber ends so that the fiber tracking camera can calibrate the position of the fiber input ends on the focal-plane.

## 5.5 Spectrographs

The list of requirement is derived from the scientific requirements in Table 5.13. These values lead to the optical design. The system is divided into three channels to enhance the throughput and decrease the complexity of each individual one. The overall efficiency is enhanced despite the addition of dichroics by selection of detectors, glasses, AR coatings and gratings optimized for each band. The moderate complexity of each channel allow compact packaging. This optimization will impact dramatically the integration and test and maintenance procedure.

The Figure 5.31 shows the proposed architecture. The full bandpass is divided in three: blue (340–540 nm), visible (500–800 nm) and red (760–1060 nm). This separation is accomplished with dichroics each reflecting the shorter bandwidth and transmitting the longer one. Each channel consists of a two lens collimator, a grism and a six lens camera. A cooled CCD in a dedicated cryostat terminates the optical path. The pupil size is about 85 mm and the lens diameters varying from 80 mm to 120 mm. The lens thicknesses are constraints to be less than 25 mm. This results in small volume lenses, which helps keep the mechanics simple and light.

### 5.5.1 Entrance Slit

The entrance slit of the spectrograph is made by the 500 fibers. They are aligned along a 330 mm radius circle creating a curved slit (Figure 5.32). The pitch of the fibers is 240 $\mu$m while its diameter is 120 $\mu$m. This configuration delivers a 120 mm slit long at the entrance of the spectrograph. Each fiber cone emission is pointed at the center of the slit circle. This configuration mimics a pupil image at this point. The cone of each fiber is a f/4 beam; this leads to a 82.5 mm pupil diameter. Each fiber ends is located within $\pm 45$ $\mu$m to the 330 mm circle in the light beam direction. No specific tolerance on the other direction is given.

### 5.5.2 Dichroics

The dichroics split the fiber light beams into the three bands. The transition between reflection and transmission is set to be at the separation wavelength

Table 5.13: Spectrograph Optical Requirements.

| | | | |
|---|---|---|---|
| **Geometry Specifications** | | | |
| Fiber diameter | | 120 | $\mu$m |
| Detector pixel pitch | | 15 | $\mu$m |
| Spectral detector elements | | 4096 | pixels |
| Spatial detector elements | | 4096 | pixels |
| Minimum resolution elements | | 3 | pixels |
| Demagnification | | 2 | |
| Fiber pitch (detector) | | 8 | pixels |
| Fiber spacing (slit plane) | | 240 | $\mu$m |
| Number of fibers (spatial) | | 500 | |
| Fiber f/# | | 4.5 | |
| Colliminator f/# | | 4 | |
| Spectrograph number | | 3 | |
| **Spectral Specifications** | | | |
| Bandpasses | Blue: | 340–540 | nm |
| | Vis: | 500–800 | nm |
| | Red: | 760–1060 | nm |
| Dispersions | Blue: | 0.488 | Å/pix |
| | Vis: | 0.732 | Å/pix |
| | Red: | 0.732 | Å/pix |
| Resolutions | Blue: | 3004 | |
| | Vis: | 2958 | |
| | Red: | 4142 | |
| **Optical Performance** | | | |
| End-to-end throughput | All | $> 40\%$ | |
| Throughputs w/ dichroics | Blue: | $> 50\%$ | |
| | Vis: | $> 70\%$ | |
| | Red: | $> 70\%$ | |
| Grating throughput at maximum | Blue: | $> 80\%$ | |
| | Vis: | $> 80\%$ | |
| | Red: | $> 80\%$ | |
| Encircled energy | All | $> 85\%$ | In 8 pixels |
| | All | 50% | In $< 3.5$ pixels |
| Scattered light | All | $< 2\%$ | w/o grating |
| Shutter | All | $< 0.1\%$ | Closed |
| | All | $> 99\%$ | Opened |

between two bands. Their transition between reflection to transmission will be smooth enough to permit to cross correlate the two parts of the spectrum. The transition span is 40 nm. Table 5.14 summarizes the specifications of the dichroics and Figure 5.33 shows their configuration.

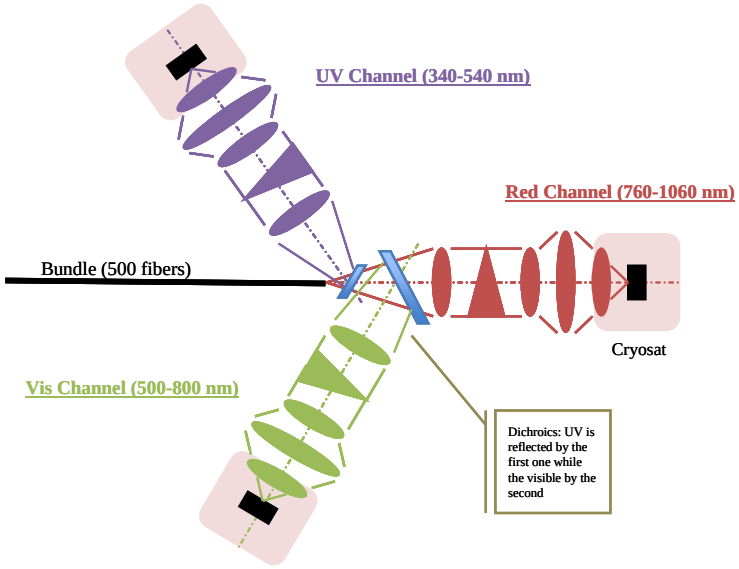


Figure 5.31: Schematic view of the spectrograph channel division.

### 5.5.3 Optical Elements

The collimator is based on a doublet and, as mentioned above, the lenses all have a reasonable diameters. The grating is within a prism. Each face of this prism is perpendicular to the local optical axis, which reduces aberration. The exit face of this prism is powered with a sphere. Three doublets compose the camera. The last one is the entrance window of the detector cryostat. The f/2 beam at the detector favors a short distance between the last lens and the image plane. A flat entrance window for the cryostat would lead to longer distance, a less than optimal design. The current capabilities of the optical manufacturers allows us use a multiple number of aspherical surfaces. In the current process of optimization, we decided to have one aspherical surface per lens. This is not seen as a risk, or even as cost driver, by several vendors. The proposed solution is very compact and elegant. As described further in the description of the structure, the entire spectrograph array will have a volume of about 2 $m^3$, impressive for 30 detectors and 5000 fibers.

### 5.5.4 Gratings and Grisms

The likely grating technology is the volume phase hologram grating (VPHG) to ensure a high throughput. The number of lines is fully compatible with

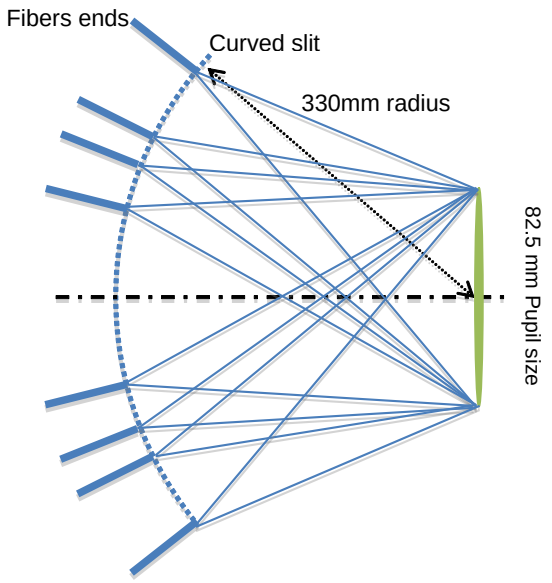


Figure 5.32: Schematic view of the fibers ends configuration (only 8 fibers are represented).

the standard use of VPHG.

### 5.5.5 Optical Performance

The first performance evaluation is the spot diagram. For BigBOSS, diffraction limited performance is not required. The fiber core is to be imaged on 4 pixels while the diffraction limit varies from 1 to 3 $\mu$m. Figure 5.34 shows wavelength versus field position spot diagrams for the three arms.

Next we examine the encircled energy performance. Figure 5.35 shows the 50% and 95% encircled energies for the three arms as a function of wavelength and field of view. The results for both performance metrics are summarized in Table 5.15.

### 5.5.6 Shutter

A shutter will be placed between each spectrograph arm body and its cryostat. Standard shutter will be performing enough for our use. The useful beam will have a diameter of 100 mm. A candidate shutter can be found at http://www.packardshutter.com/

Table 5.14: Dichroics Specifications.

| Item | Value | From | To | Comment |
|---|---|---|---|---|
| **UV Dichroic** | | | | |
| Transition | 520 nm | | | |
| Reflection | $> 98\%$ | 340 nm | 500 nm | TBC |
| Transmission | $> 98\%$ | 540 nm | 1100 nm | TBC |
| Absorption | $< 1\%$ | 340 nm | 1100 nm | TBC |
| Length | 120 mm | | | |
| Width | 30 mm | | | |
| Flatness | $\lambda/4$ PTV | | | Over 30 mm patch |
| Working angle | f/4 | 0° | 13° | |
| Substrate | Silica | | | |
| **Visible Dichroic** | | | | |
| Transition | 780 nm | | | |
| Reflection | $> 98\%$ | 500 nm | 760 nm | TBC |
| Transmission | $> 98\%$ | 800 nm | 1100 nm | TBC |
| Absorption | $< 1\%$ | 500 nm | 1100 nm | TBC |
| Length | 100 mm | | | |
| Width | 80 mm | | | |
| Flatness | $\lambda/4$ PTV | | | Over 30 mm patch |
| Working angle | f/4 | 0° | 13° | |
| Substrate | Silica | | | |

### 5.5.7 Mechanical

**Optical elements support.** The optical elements are grouped in doublets. Each lens will be glued one a side of a doublet barrel. Each doublet will be integrated in the spectrograph body. Mechanical alignment and positioning will be enough to insure the image quality. Since the entire system will be thermalized in the instrument room, the criterion on the differential thermal expansion is not be the driver in terms of image quality. The only time thermal stress of the glass is consideration is for transport and storage.

Table 5.15: Number of CCD pixels containing 50% and 90% encircled energy.

| EE | UV | Visible | Red |
|---|---|---|---|
| 50% | 3.2±0.14 | 3.2±0.16 | 3.1±0.13 |
| 95% | 5.1±0.52 | 5.3±0.70 | 5.1±0.51 |

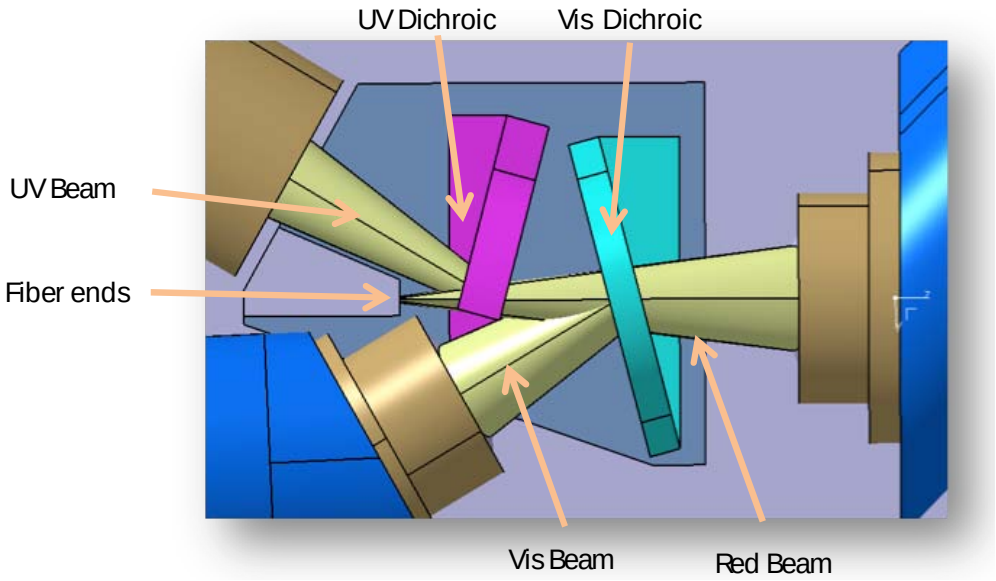


Figure 5.33: Dichroics configuration view.

**Light baffling** The spectrograph body will completely block external light. In the same way, the dichroic support will be a good place to block stray light. The only places were the light could leak into the path are the interface between the fiber and the dichroic body and the dichroic body and the spectrograph body. Interfaces based on light traps will be designed to avoid these.

## 5.6 Cameras

The 30 BigBOSS cameras (10 for each channel of the instrument) are single CCD cameras, each requiring a small cryostat. They will be installed in a stabilized temperature environment adjacent to the telescope.

### 5.6.1 Cryostats

The preliminary requirements for the design of the cryostats are as follows. CCDs are to be cooled down to 160–170K and their temperature must be regulated within 1K. Cryostats include the last two lenses of the spectrographs and must allow CCDs to be aligned within 15 $\mu$m along the optical axis. The design must be simple to give easy access to the instrument, it must require low maintenance and make fast replacements possible (typically, one

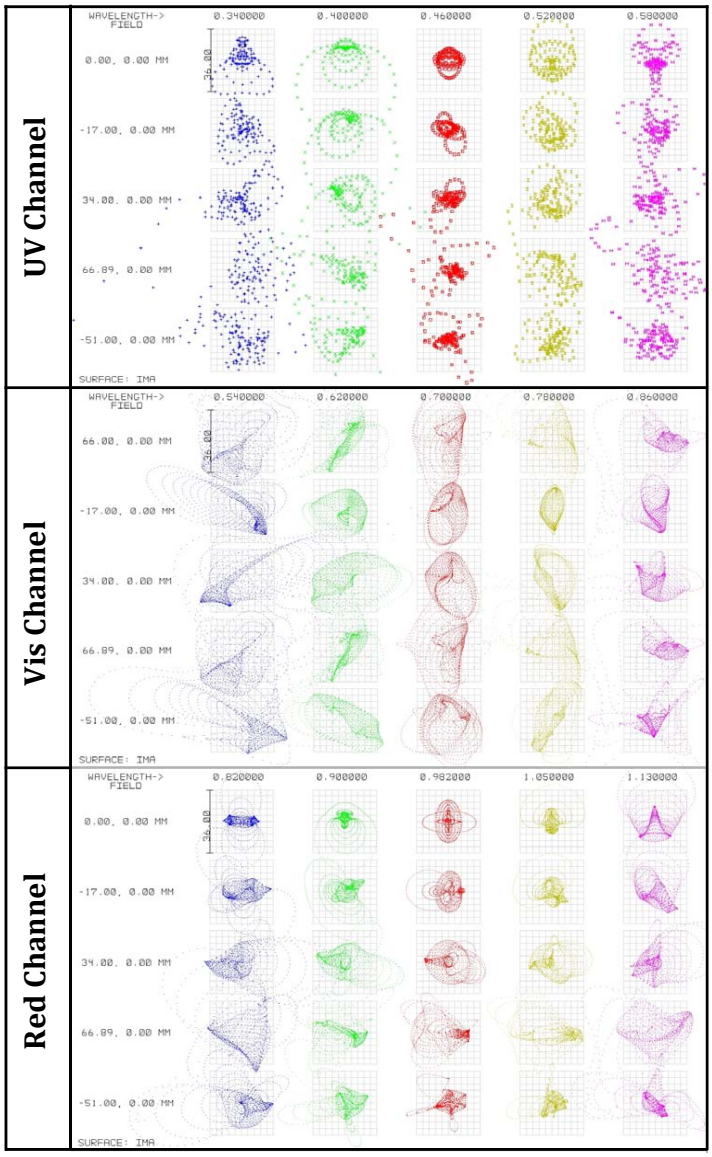


Figure 5.34: Spot diagrams for the three spectrograph arms for five wavelenghts and five field positions.

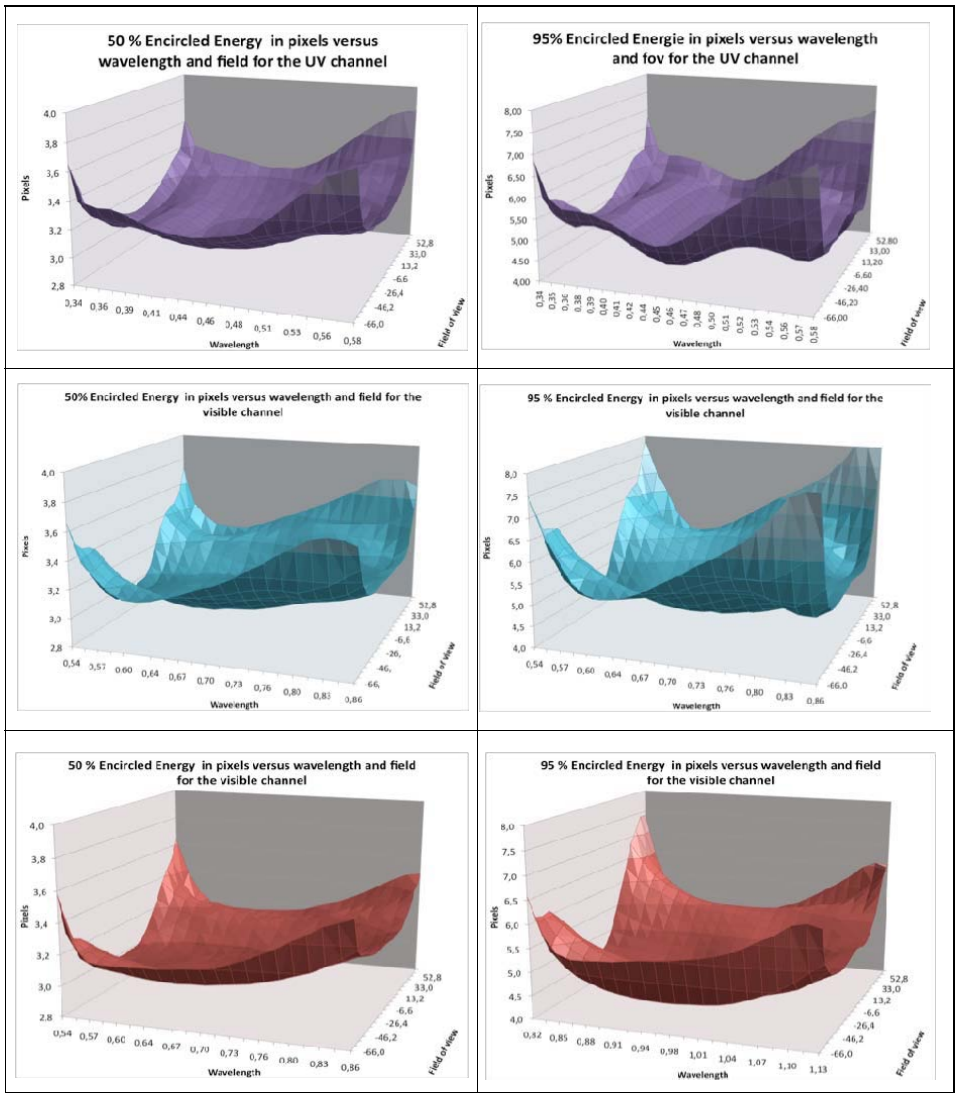


Figure 5.35: Encircled energy contours, 50% on the left and 95% on the right, for the three spectrograph arms as function of wavelength and field of view.

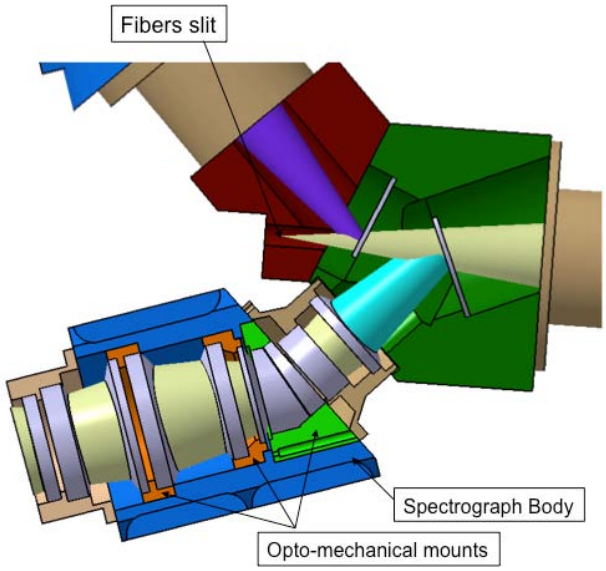


Figure 5.36: Spectrograph mechanics showing the dichroics box (green), visible arm structure housing two lens doublets and the grism (lower blue),and the cryostat with the final lens doublet.

cryostat to be replaced in less than 24 hours by 2 persons). Finally, the system once in operation must be insensitive to electromagnetic discharges.

One of the most important requirements is to have independent units in order to be able to react quickly in case of changes or failures. To produce cooling power for the 30 cameras, we will thus use one closed cycle cryocooler per camera, each with its own CCD temperature monitoring. The above requirement led us to adopt the same mechanical design for all cryostats except for the support of the front optics.

### Focal plane

The focal plane is determined by the optical configuration of the spectrographs and will be slightly different in each channel. The last two lenses of each spectrograph arm have to be integrated in the cryostat due to their short distance to the CCD plane. They will act as the window of the cryostat vessel. These lenses will be aligned (at room temperature) by mechanical construction. Each cryostat has to provide a mechanism to align its CCD under cold conditions. As a reference for the alignment, we use the interface

plane between the last mechanical surface of the spectrograph housing and the front surface of the cryostat (see Figure 5.37).

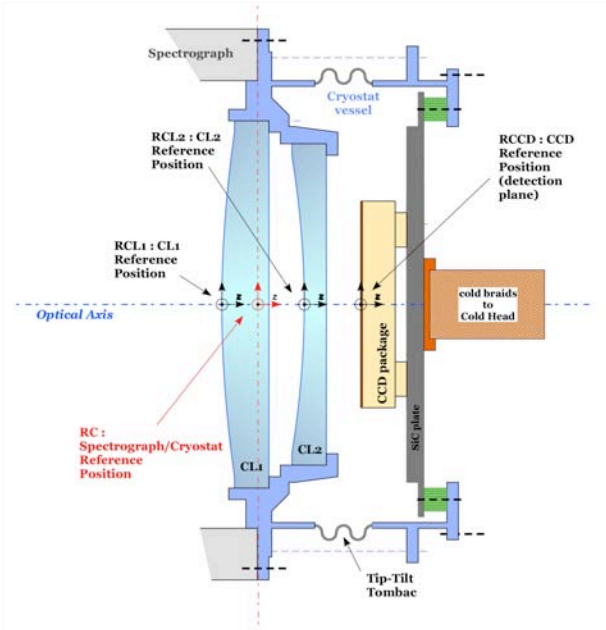


Figure 5.37: Positions and reference (RC) of the last pair of lenses and CCD plane of one spectrograph arm.

The first lens, CL1, will support the pressure difference between ambient conditions and the internal cryostat vacuum, whereas the second one will be in vacuum. The lenses will be assembled in the cryostat front flange and fixed to the spectrograph. The assembly will use specific high precision parts to meet the alignment requirements given in Table 5.16.

Table 5.16: Lenses Positioning Requirements.

| Errors | Cryostat vs Spectrograph | CL1 | CL2 |
|---|---|---|---|
| Along X or Y | $\pm 35$ $\mu$m | $\pm 50$ $\mu$m | $\pm 50$ $\mu$m |
| Along Z | $\pm 15$ $\mu$m | $\pm 40$ $\mu$m | $\pm 35$ $\mu$m |
| Rx or Ry in arcmin | $\pm 1.5$ | $\pm 3$ | $\pm 1.5$ |

The alignment of the cryostat part which supports the CCD will rely on the roll-pitch system developed for MegaCam at CFHT. The system is composed of a pair of outer flanges with 3 micrometric screws positioned

at 120° (see Figure 5.38), inserted between the front flange and the moving part of the cryostat. In order to prevent any lateral displacement, locking will be provided by balls in V-grooves located inside the flanges. Once in position, the balls will be locked by a screw.

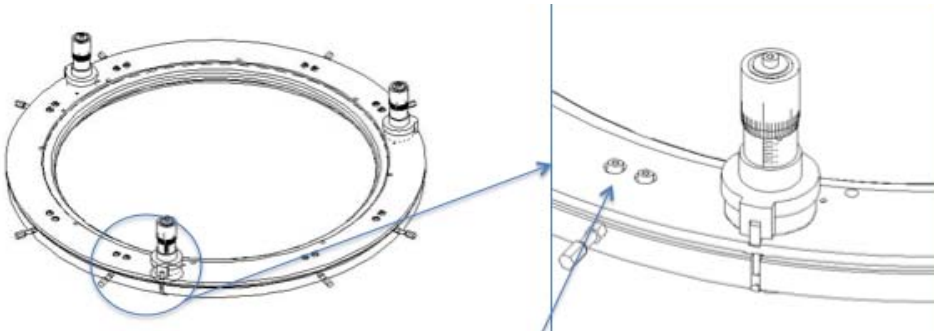

Figure 5.38: Sketch of the tip-tilt system mechanism for fine alignment of the CCD by micrometric screws based on the roll-pitch system developed for MegaCam. The locking system is implemented as stainless steel balls in a grove.

This system should allow us to align the CCD plane within 50 $\mu$m laterally and within 15 $\mu$m along the optical axis. A design study of the mechanical assembly of the lenses and tip-tilt system has been performed with simulations at Irfu. The final validation of the design will require a cryostat prototype to be mounted and tested at Irfu during the R&D phase of the project. Final values of the lens and focal plane positions will be given by the spectrograph design studies.

**Cryostat vessels**

The cryostat vessel ensures the mechanical connection with the spectrograph, the thermal and vacuum conditions for the CCD and the interface with the control system and the CCD electronics.

The cryostat is a metal cylinder that will receive a front flange that integrates the last pair of lenses and the tip-tilt system, and a rear flange to support the cold head. The cylinder sides will be equipped with several connection pipes: one for the vacuum, one for the CCD flex connector and one or two for the electrical connection to the control system.

Figure 5.39 shows cameras assembled on the three arms of a spectrograph, with the CCD electronics (black boxes), the cold heads (dark green),

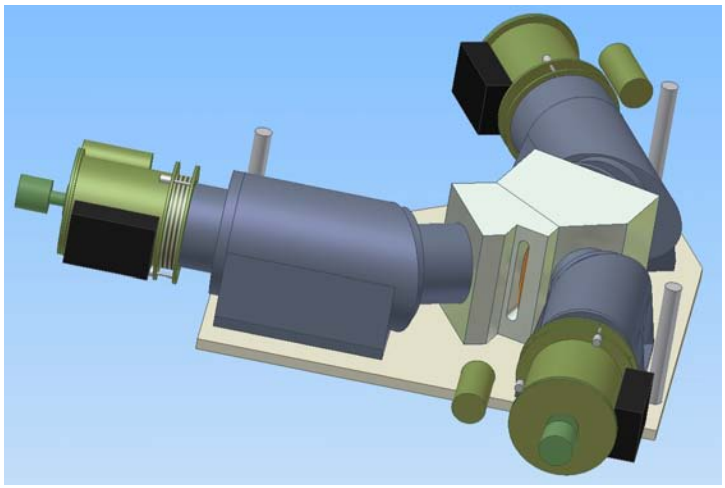

Figure 5.39: 3D model of a complete spectrograph with its 3 cameras.

their compressors (small light green cylinders) and the tip-tilt system (screws in white).

Cooling power is supplied from the cold machine to the CCD through a set of mechanical parts. As shown in Figure 5.40, the CCD, mounted on its SiC package, is followed by a SiC cold plate connected to the Cu cold tip of the cold machine through flexible cryo-braids. The SiC cold plate ensures the mounting of the CCD and supplies cold power with minimal thermal losses. The CCD package and cold plate will be made of the same material to reduce stresses from thermal contraction. The cold plate will be equipped with a Pt100 resistor as a temperature sensor. Braids will be dimensioned to have a thermal capacitance suitable for the CCD temperature regulation, which will be achieved by tuning the electrical power of a resistive heater glued on one side of the tip of the cold machine.

Thermal shielding of the cryostat will be provided in three pieces, one for the vessel sides, one for the rear flange and one for the front lens. The latter will differ for the three arms of the spectrographs, which have lenses of different diameters. The shielding will be provided by polished Al plates or MLI foils. The final choice will be based on the results of the tests with the cryostat prototype.

Finally, the design of the vacuum system takes into account the mechanical assembly of the spectrographs which will be mounted in two towers of five spectrographs each. To allow easy access, each tower will be equipped with three vacuum units. A vacuum unit will be composed of a

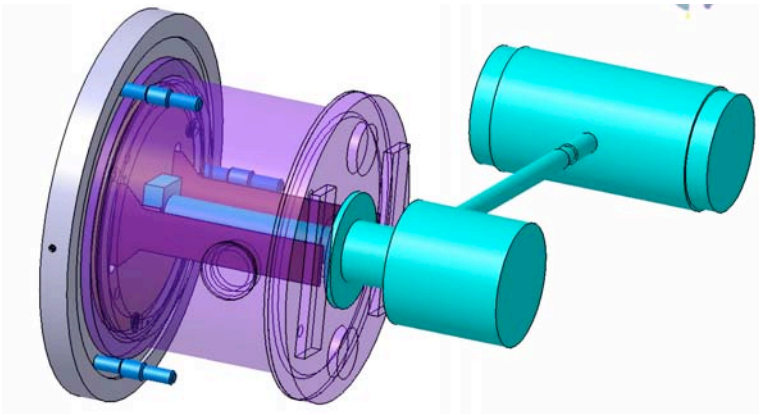

Figure 5.40: Sketch of a cryostat.

primary/secondary pumping machine and a distribution line to five vertically aligned cryostats (see Figure 5.41). Each pipe to a cryostat will be equipped with an isolation valve. One full-range vacuum sensor will allow pressure to be measured. This sensor will be isolated by a manual valve in case of maintenance operation.

We plan to run with static vacuum during the observation periods, cryopumping keeping vacuum conditions inside the cryostats. The procedure of pumping between these periods has to be discussed and defined.

### 5.6.2 Cryogenic System

The cryogenic system uses independent and autonomous cooling machines, based on pulse tube technology, in order to have a simple and robust system for the control of the 30 cameras that also allows easy integration, assembly and maintenance operations.

Linear Pulse Tubes (LPT) were developed by the Service des Basses Temperatures (SBT) from CEA in Grenoble (France). The technology was transferred by CEA/SBT to Thales Cryogenics BV Company which provides several models of LPTs with different power and temperature ranges. To define an appropriate LPT model for BigBOSS cryostats, a preliminary estimate of the power and temperature budget of the different elements of the cameras was done, as shown in Table 5.17. The values are meant for a CCD temperature of 170K and a maximum difference of -20K with respect to the cold finger of the cold head. A 3 W, 150K cold machine appears adequate.

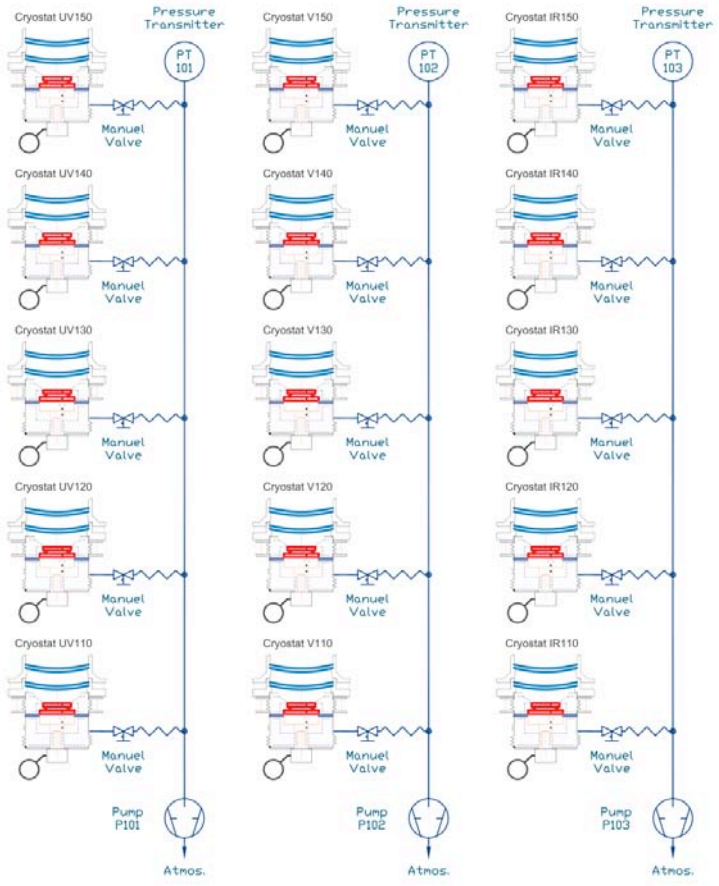


Figure 5.41: Vacuum system for a tower of spectrographs.

### Linear pulse tubes (LPT)

The Linear Pulse Tube (LPT) is a miniature closed-cycle pulse tube cooler, made of a compressor module connected by a metal tube to a pulse tube cold finger (see Figure 5.42). The compressor pistons are driven by integral linear electric motors and are gas-coupled to the pulse tube cold finger. The pulse tube has no mechanical moving parts. This technology, combined with the proven design of the ultra reliable flexure bearing compressors, results in extremely reliable and miniature cryocoolers with a minimum of vibrations. In addition, the compact magnetic circuit is optimized for motor efficiency and reduction of electromagnetic interference.

Table 5.17: Radiative and conductive thermal losses.

| Element | Loss (W) | % of total loss |
|---|---|---|
| Lens (radiative) | 2.0 | 69 |
| CCD dissipation | 0.1 | 3.5 |
| CCD electronic cables | 0.1 | 3.5 |
| Cold plate / vessel (radiative) | 0.2 | 7 |
| Cold plate supports (conductive) | 0.2 | 7 |
| Cold base regulation capacity | 0.3 | 10 |
| TOTAL | 2.9 | 100 |


Figure 5.42: Left: two models of LPT, LPT9510 (in the foreground) and LPT9310, with powers of 1 W and 4 W at 80K, respectively Right: dimensions of the LPT9510 model.

### Device monitoring and temperature regulation

The LPT compressor is powered with an AC voltage signal which sets the cold finger operating point in power and temperature. Changing this voltage allows the thermal performance to be tuned in a given range (see Figure 5.43).

The LPT machine is provided with an electrical interface called CDE (Cooler Drive Electronics) powered by an input DC signal. The CDE converts the input signal from DC to AC and adjusts the output voltage. A pre-tuning is usually done by the manufacturer to meet specific customer requirements.

A CDE with higher functionality is also available. It can be used to drive the LPT in order to achieve extreme temperature stability and provides internal feedback about the thermal control process itself (see Figure 5.44).

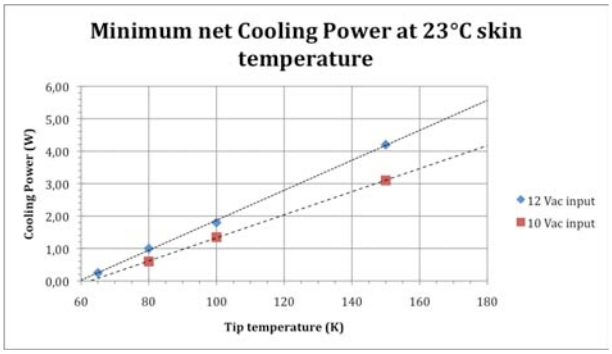


Figure 5.43: Power vs. temperature diagram for the LPT9510.

Combined with the thermal capacitance provided by the cold base and its heater (see Sec.5.6.1), the CDE could offer a second solution to set and regulate the CCD temperatures. The final configuration of the regulation system will be discussed with the LPT manufacturer and will depend on the results of cryogenic tests to be performed during the R&D phase of the project.

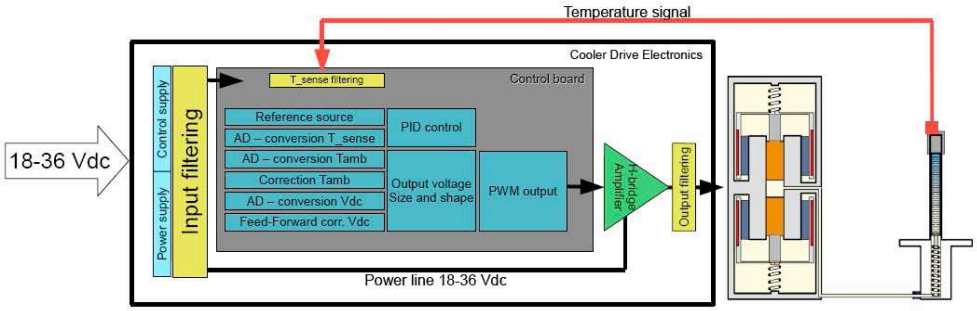


Figure 5.44: Block diagram of a Cooler Drive Electronics.

### 5.6.3 Cryostat Control System

We have adopted a well-tested control system for the 30 CCDs and cryostats that has been working reliably on many projects for several years (MegaCam, Visir/VLT, LHC Atlas and CMS experiments at CERN). The three main components are a programmable logical controller (PLC), measurement sensor modules and a user interface on a PC. The general architecture

of the system is presented in Figure 5.45.

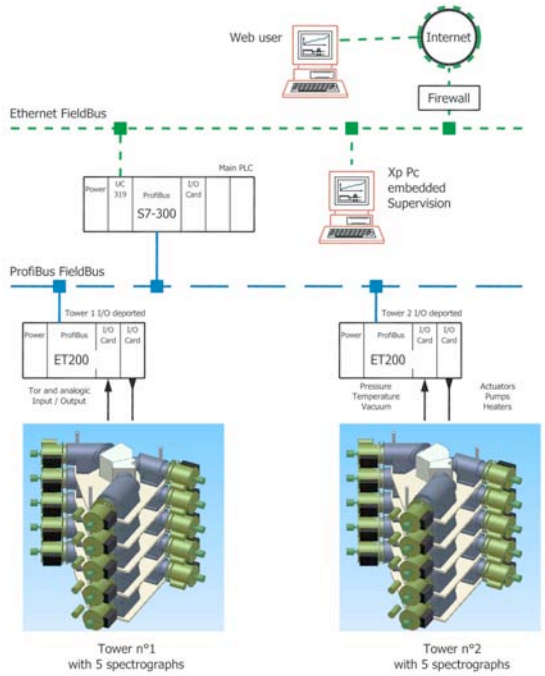


Figure 5.45: Architecture of the BigBOSS cryostat control system.

The PLC is a Simatic S7-300 unit type from Siemens with a system core based on a UC319 mainframe. The program implemented in the PLC will acquire in real time all variables corresponding to the monitoring and control of the instrument: vacuum and temperature monitoring, control of the cold production unit, CCD cooling down and warming up, safety procedures on cryogenics, vacuum and electrical power. Safe operations all systems will be insured. A local network (based on an industrial bus, e.g., ProfiBus or ProfiNet) ensures communication with the remote plug-in I/O modules and with the PLC.

Temperature measurements are provided by Pt100 temperature probes directly connected to the PLC. The other analog sensors (heaters, vacuum gauges) are connected to a 4–20 mA or 0–10 V module. All measurement sensors will be located in two cabinets, each dedicated to one spectrograph tower (see Figure 5.46).

Supervision software (with user interface) is implemented in the industrial PC connected to the PLC via a dedicated Ethernet link. It will ensure

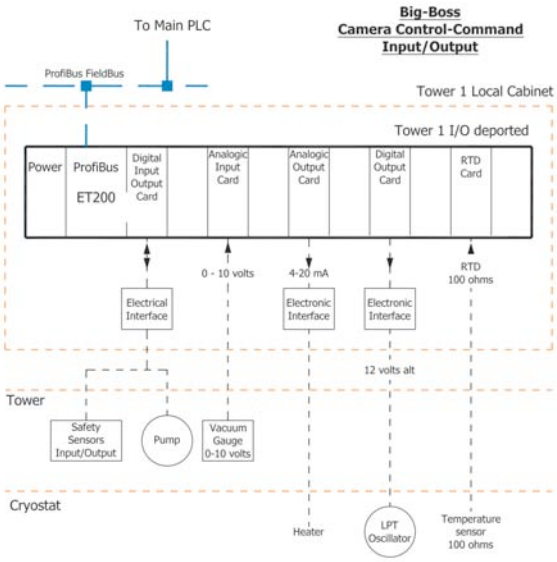


Figure 5.46: Configuration of the control system for one spectrograph tower.

the monitoring and control of all variables, with possibly different levels of user access rights. This system will also allow the set-up to be remotely controlled via the Ethernet network that will be accessible from Internet through a secured interface.

### 5.6.4 Detectors

The three arms of each spectrograph will use 4k×4k, 15 $\mu$m CCDs. For the blue arm we are baselining the e2v CCD231-84 with its good quantum efficiency down to 340 nm. For the visible arm we are baselining the LBNL 4k CCD as used by BOSS. The red arm also uses the BOSS format CCD except that the thickness is ∼650 $\mu$m to achieve usable QE out to 1060 nm. Figure 5.47 show the two types of CCDs. CCD performance characteristics and cosmetics will be the same as established by BOSS. Typical achieved value are shown in Table 5.18.

The quantum efficiency performance of the BOSS e2v and LBNL CCDs is well established and is shown in the two left curves in Figure 5.48. The high-side cutoff of a CCD is determined by its thickness as the absorption length increases rapidly above 900 nm. The absorption is also a function of temperature, decreasing with increasing temperature. To maximize the near infrared reach we propose to use a very thick CCD, 650 $\mu$m to compared to

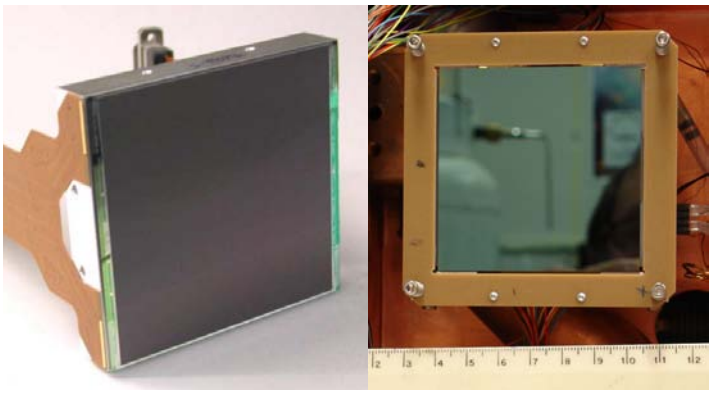

Figure 5.47: 4k×4k, 15 $\mu$m CCDs: left, e2V and right, LBNL. A four-side abuttable package similar to that shown for the e2v device is underdevelopment for the LBNL CCD.

Table 5.18: BOSS achieved CCD performance of detectors proposed for use in BigBOSS. Readnoise is for 70 kpixel/s.

| | | **LBNL** | | **e2v** | |
|---|---|---|---|---|---|
| Parameter | Req. | Red 1 | Red 2 | Blue 1 | Blue 2 |
| Read Noise | Blue: $< 3$ | 2.1 | 2.5 | 1.8 | 1.8 |
| (e-) | Red: $< 5$ | 2.2 | 2.5 | 1.6 | 2.2 |
| | | 2.5 | 2.4 | 1.7 | 1.9 |
| | | 2.1 | 2.4 | 1.8 | 1.8 |
| Dark Current | Blue: $< 4$ | $\sim$1 | $\sim$1 | 1.5 | |
| (e-/pix/hr) | Red: $< 8$ | | | | |
| Cosmetics | $< 15$ | 2 | 0 | 0 | 4 |
| (bad columns) | | | | | |

250 $\mu$m used in BOSS and the visible arm. This will achieve a QE of around 25% QE at 1050 nm at 175K. Measurement of dark current of CCDs of this thickness combined with signal-to-noise simulations for BigBOSS indicate that this temperature can be tolerated. Shown in Figure 5.48 at the left is a simulated QE curve under the these conditions.

An additional concern with the thick CCD is the depth of focus variation that is rapidly changing between 900 nm and 1060 nm. We have simulated this for an f/2 beam focused at the optical surface of a 650 $\mu$m thick CCD. We include the measured effects of lateral charge diffusion. The procedure Monte Carlo procedure is:

- Scan wavelength range.

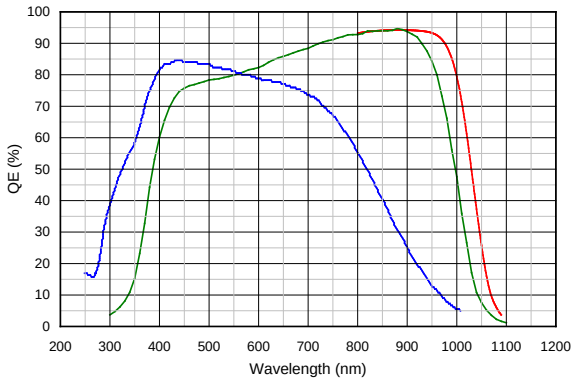


Figure 5.48: Quantum efficiency for the three types of BigBOSS CCDs. Left curve is for e2v CCD231-84, center curve is for LBNL BOSS 250 $\mu$m thick CCD, and the right curve is the simulation for an LBNL 640 $\mu$m BOSS-like CCD.

- Determine absorption depth 1/e parameter based on wavelength.
- Toss incidence angle within the f/2 beam.
- Generate photons and refract into the silicon.
- Propagate the photons to an exponentially sampled conversion depth.
- Add random diffusion-induced lateral offset.
- Project onto pixel plane.

In Figure 5.49 are shown the projected conversion charge distributions at the pixel plane for several wavelengths. The 950 nm photons mostly convert at the surface of the CCD and the distribution is essentially gaussian determined by lateral charge diffusion during the 650 $\mu$m charge drift to the pixel plane. For increasing wavelengths, there is less lateral charge diffusion on average but this is offset by the spread in the conversion area as the f/2 beam diverges in the CCD thickness. We note the relative areas under the curves in the figure are the relative quantum efficiences. Also shown in Figure 5.49 is the PSF of the convolved fiber and spectrograph optics response. Simulations indicate that the contribution from the CCD blurring is not important.

### 5.6.5 Detector Readout Electronics

The electronics for each CCD will be mounted on the warm side of the cryostat wall. This provides easy access for replacement without disturbing

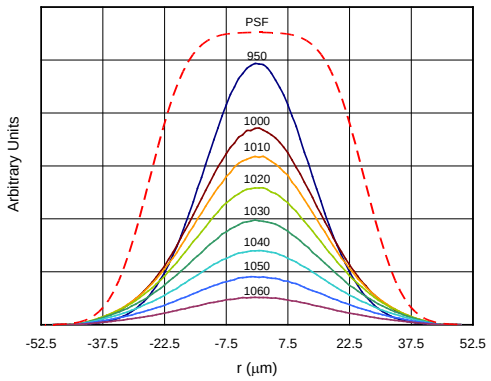


Figure 5.49: Thick CCD PSF for wavelengths near cutoff. The horizontal axis bins correspond to a 15 $\mu$m pixel. The dashed curve is the optical PSF from the fibers and spectrograph optics.

the detector. This will include local power generation from an isolated single input voltage, CCD bias voltages generation, programmable clock levels and pattern, CCD signal processing and digitization, and set voltage readback. Configuration and control of the electronics and delivery of science data will be over Ethernet links, possibly optically isolated. A block diagram is shown in Figure 5.50.

There is a level of complexity introduced into this electronics because the mixture of n-channel (e2v) and p-channel (LBNL) CCDs. The CCD output structures required opposite sign DC biasing voltages and the electron-to-voltage gains are of opposite sign. Common clocking circuitry can work for both, but the e2v devices require four-phase parallel clocking while the LBNL devices require three. In addition, the LBNL devices require a HV depletion supply.

The analog signal processing and digitization can be accomplished with the CRIC ASIC that can accommodate either n- or p-channel devices. CRIC uses a dual-slope integrator correlated double sample. There are four channels per chip, each channel with its own ADC providing 14-bit resolution over a 16-bit dynamic range encode with range bits.

We belive that one configurable board design can service the two types of CCD technologies.

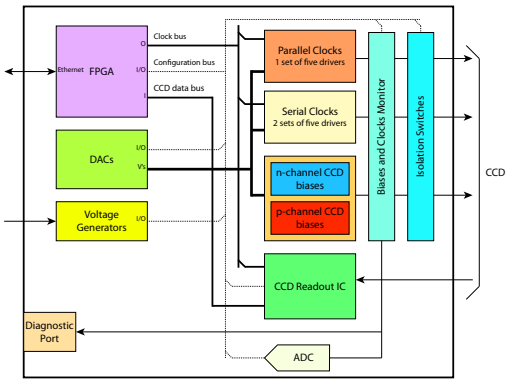


Figure 5.50: CCD frontend electronics module block diagram, which supports both n-channel and p-channel CCDs.

## 5.7 Calibration System

### 5.7.1 Dome Flat Illuminations

Arc lamps and line lamps illuminating the dome flat exercise the entire instrument light path and generate spectra placed on the CCDs as galaxies do. The line lamps are useful for verifying the corrector focus and alignment. The lamps are mounted at the top of the prime focus cage. The dome flat screen is already in place.

### 5.7.2 Spectrograph Slit Illumination

As described earlier, the fiber slit array assemblies will have a lossy fiber that can illuminate the entire spectrograph acceptance with white light or line lamps. This allows the entire CCD area to be illuminated with arc and line lamps. By this means, the four dark pixel rows between spectra can be illuminated.

## 5.8 Instrument Readout and Control System

The BigBOSS data acquisition system (DAQ) is responsible for the transfer of image data from the frontend electronics to a storage device. It has to coordinate the exposure sequence, configure the fiber positioners and it provides the interface between BigBOSS and the Mayall telescope control system. The instrument control system (ICS) is designed to aid in this effort. Every component of the instrument will be monitored and detailed

information about instrument status, operating conditions and performance will be archived in the facilities database. In the following sections we first discuss a typical exposure sequence to introduce some of the requirements for the DAQ and ICS systems. This is followed by a description of the exposure control system which includes the fiber positioners and a section on readout and dataflow. Later sections cover the instrument control system and the interface to the Mayall telescope. We conclude with a discussion of the online software we envision for BigBOSS.

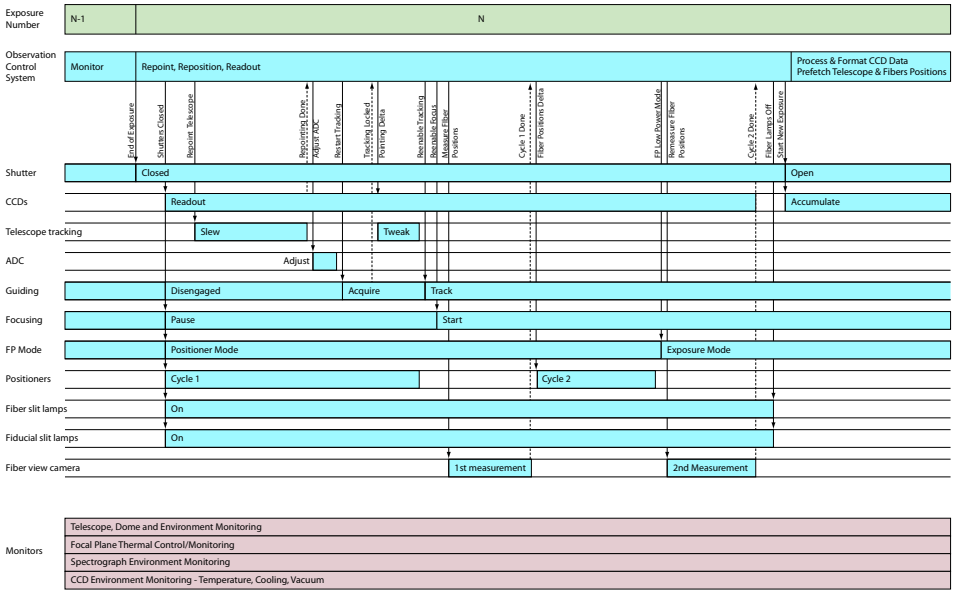


Figure 5.51: An example of a BigBOSS exposure sequence.

### 5.8.1 Exposure Sequence

A typical BigBOSS exposure sequence is shown in Figure 5.51. The observation control system (OCS) is responsible for coordinating the different activities. In order to maximize survey throughput we will set up for the next exposure while the previous image is being digitized and read out.

At the end of the accumulation period of an exposure when the shutters are closed, the OCS instructs the frontend electronics to readout the CCDs. At the same time the guider and focus control loops are paused. Information about the next exposure has already been loaded to the OCS during the previous accumulation phase. Once the shutter is closed the OCS transmits

the new coordinates to the telescope. The focal plane systems are switched to positioner mode and the fiber positioners moved to a new configuration and the first snapshot of actual positions locations is acquired by the fiber view camera. Details of the fiber positioning system will be described in the next section. It will take a second cycle to complete the positioner setup. When the telescope reaches the new target position, the OCS activates the guider to close the tracking feedback loop with the telescope control system. Guider correction signals are sent at a rate of about 1 Hz. Once the telescope is tracking, the OCS re-enables the focus control loop. At the end of the second fiber positioning cycle, the focal plane systems switch back to low power mode. The OCS waits for the CCD readout to complete and for the fiber view camera to signal that the fibers are in position before it signals the shutters to open to start the next accumulation phase. While the spectra are being acquired information about the next exposure including telescope coordinates and target positions is loaded into the OCS.

At a typical pixel clock rate of 100 kHz CCD readout will take approximately 42 seconds. The BigBOSS DAQ system is designed to complete the entire sequence outlined above in a similar amount of time so that the time between exposures will be no longer than 60 seconds.

### 5.8.2 Exposure Control

After a science observation has been made, the spectrograph shutters are closed so the data can be recorded. The telescope and all fibers are now repositioned for the next observation. Both the data readout and the pointing changes must be completed within 60 seconds. Then the star guider system determines the true telescope pointing (and corrects as needed). In parallel, the fibers are moved to the location of their next target. Finally, the fibers are back-lit, positions verified and corrected as needed. The backlights are then extinguished and shutters can reopen. CCD read out occurs concurrently with repositioning of the telescope and fibers.

**Shutter.** Each of the BigBOSS spectrographs will include three shutters, one per CCD camera. Each shutter will be individually controlled by the camera frontend electronics module, or a dedicated system that will control all 30 shutters (TBD). Commercial shutters typically use an opto-isolated TTL signal. The length of the control signal determines how long the shutter is open. We will control exposure times to better than 10 ms precision and keep the jitter in open and close times among the 30 shutters to less than 10 ms. Details of the interface to the shutter will depend on the actual

shutter system selected for the BigBOSS cameras.

**Guidance Sensors.** The guidance sensors will assist in telescope pointing. The fibers will be positioned relative to the pointing direction determined by the star guider system.

**Fiber Positioning.** In parallel with the telescope repointing, the fiber positioners are commanded to their new locations. The fiber view camera and its back-lit fiducial fibers are then used to measure the actual location of the fiber tips to 5 $\mu$m. The fiber positioners are then commanded for small position corrections as required and the fiber view camera documents their final positions. Once the system has determined that all fibers are correctly positioned relative to the determined pointing direction, the shutters are opened and data taking begins.

### 5.8.3 Readout and Dataflow

The BigBOSS instrument consists of ten identical spectrographs each with three cameras covering different wavelength regions. Each camera uses a single 4k×4k CCD with four readout amplifiers that operate in parallel. A default pixel clock of 100 kpixels/s results in a readout time of approximately 42 seconds. The charge contained in each pixel is converted with 16-bit ADCs yielding a data volume of 34 MBytes per camera or about 1 GByte per exposure for the entire instrument. A schematic view of the BigBOSS DAQ system is shown in Figure 5.52. While we are still evaluating different options we are considering a system consisting of 30 identical slices, one for each camera. In the block diagram below data flows from left to right starting with the CCDs and ending with the images stored as FITS files on disk arrays in the computer room. Each CCD is connected to a camera front-end electronics module that will be located directly on the spectrographs. Optical data and control links connect each camera to its data acquisition module which includes a full frame buffer and a microcontroller with a high speed network interface to the online computer system in the control room. Several architecture and technology options are still being investigated at this time. This includes the placement of the Camera DAQ modules. The best location might be close to the frontend electronics near the cameras but because of the data/control link we could also choose a more convenient location in the Mayall dome. We need to determine that the data and control links can be combined and establish the package form factor for the Camera DAQ modules. For the BOSS/SDSS-III data acquisition system we

combined the functionality provided by the DAQ module with the backend of the frontend electronics. We intend to explore this option for BigBOSS as well. Our baseline for the network link on the DAQ module is (optical) Gigabit Ethernet with the assumption that the Camera Controller supports the TCP/IP software protocol. This feature combined with the modular design allows us to operate individual cameras with only a laptop computer, a network cable and of course the online software suite. We expect this to become a very valuable tool, useful during construction, commissioning, for test stands as well as for maintenance during the operations phase.

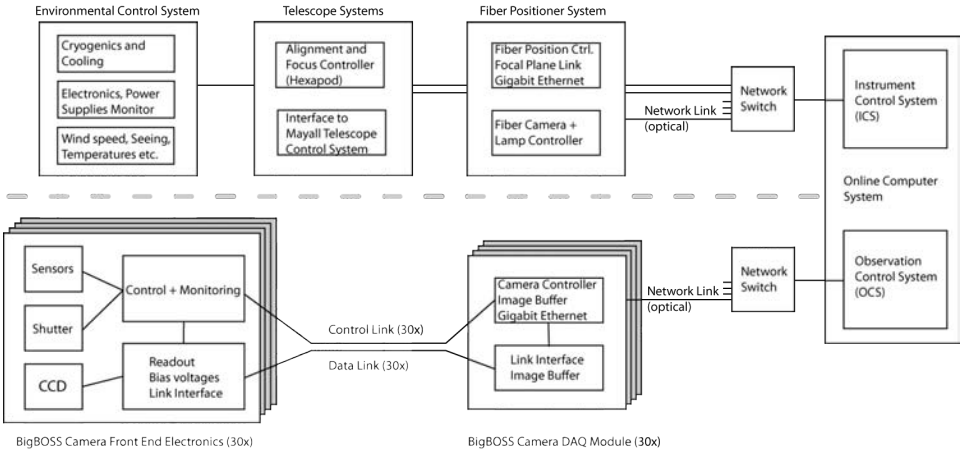


Figure 5.52: Block diagram of the BigBOSS data acquisition system.

Data transfer from the frontend electronics to the Camera DAQ modules will begin shortly after the start of digitization and will proceed concurrently with CCD readout. System throughput will be designed to match the CCD readout time of 42 seconds to avoid additional dead time between exposures. The required bandwidth of approximately 10 Mbits/s is easily achievable with today's technology. A small buffer memory on the frontend electronics module provides a certain level of decoupling between the synchronous CCD readout and the transfer over the data link. The Camera DAQ module will have a full frame buffer. The Camera Controller assembles the pixel data in FITS format and transfers the image over a standard network link to the online computer system in the control room. The BigBOSS online software performs the necessary book keeping to ensure that data from all 30 cameras have been received. Initial quality assurance tests are performed at this stage and additional information received from the telescope control system and other sources is added to the image files. The need for an image

builder stage to create a combined multi-extension FITS file is currently not foreseen. The final image files will be transferred to the BigBOSS processing facility at LBNL NERSC.

### 5.8.4 Instrument Control and Monitoring

Hardware monitoring and control of the BigBOSS instrument is the responsibility of the instrument control system (ICS). Shown schematically in Figure 5.52. we distinguish two sets of ICS applications. Critical systems such as cooling for the CCDs and the monitor system for the frontend electronics have to operate at all times. Fail safe systems and interlocks for critical and/or sensitive components will be implemented in hardware and are the responsibility of the device designer. Control loops and monitor functions for these applications will use PLCs or other programmable automation controllers that can operate stand-alone without requiring the rest of the BigBOSS ICS to be online. Measured quantities, alarms, and error messages produced by these components will be archived in the BigBOSS facility database where they can be accessed for viewing and data mining purposes.

The second set of instrument control applications consists of components that participate more actively in the image acquisition process such as the shutters, the fiber positioning mechanism and the focus and alignment system. The control interface for these devices typically consists of a network enabled microcontroller with firmware written in C. The online system interacts with the hardware controller via a TCP/IP socket connection although other interfaces will be supported if required. We envision that the DAQ group provides the higher level software in the instrument control system while the microcontroller firmware will be developed by the groups responsible for the respective components. Similar to the first set of ICS devices, this group of applications will also use the facility database to archive the instrument status.

BigBOSS controls applications can be categorized by location into spectrograph-based systems, telescope-based system and external systems. Spectrograph-based systems include the fiber slit array lamps, the shutters, electronics monitoring, cryostat thermal and vacuum control and some environmental monitors. The group of telescope-based systems consists of the fiber view camera and fiber view lamps, the hexapod and corrector controllers, the fiber positioner, the focal plane thermal control system as well as additional environmental monitors. Components in both these groups will be integrated with the ICS using the architecture discussed in the previous paragraph.

The third category consists of external instruments such as a seeing monitor, an all sky cloud camera and the dome environmental systems. The interface to these devices will be discussed in the next section.

### 5.8.5 Telescope Operations Interface

The BigBOSS online system has to interface with the existing Mayall telescope control system (TCS) to send new pointing coordinates and correction signals derived from the guider. In return BigBOSS will receive telescope position and status information from the Mayall TCS. Since the dome environmental system and most of the observatory instrumentation for weather and seeing conditions is already connected to the TCS we will not access these devices directly but control and monitor them through the TCS. Similar to the design we developed for the Dark Energy Camera and the Blanco telescope the BigBOSS online system will include a TCS interface process that acts as conduit and protocol translator between the instrument and the telescope control systems.

During an exposure, the BigBOSS guider and the telescope servo systems form a closed feedback loop to allow the telescope to track a fixed position on the sky. For an imaging survey it is sufficient to have a stable position. BigBOSS, however, requires a precise absolute position so that the fibers are correctly positioned on their targets. Given a pointing request, the Mayall slews into position with a typical accuracy of 3 arcsec. Using the guide CCDs in the focal plane we will then locate the current position to 0.03 arcsec accuracy. If the offset between requested and actual position is larger than a certain fraction of the fiber positioner motion we will send a pointing correction to the TCS to adjust the telescope position. Details of this procedure need to be worked out and depend on the pointing precision of the Mayall control system.

### 5.8.6 Observation Control and Online Software

The BigBOSS online software will consist of a set of application processes built upon a layer of infrastructure software that facilitates message passing and information sharing in a distributed environment. The application layer can be divided into several functional units: the image pipeline, the instrument control system including the connection to the Mayall TCS, data quality monitoring and the user interfaces with the observer console. The Observation Control System (OCS) is the central component of the BigBOSS image pipeline coordinating all aspects of the observation sequence.

Connected to the OCS is an application that proposes an optimized sequence of pointings for the telescope based on a number of inputs including survey history, current time and date and the current observing conditions. At the end of an exposure the OCS will initiate readout and digitization and the DAQ system transfers the image data to a disk cache. The OCS notifies the data transfer system developed by NOAO that image data is available to be transferred to the NOAO archive and the BigBOSS image processing center. Continuous monitoring of both the instrument and the image quality is required to control systematic uncertainties to achieve the BigBOSS science goals. Quality assurance processes will analyze every spectrum recorded by the instrument and provide immediate feedback to the observer. Feedback on the performance of BigBOSS is also provided by the instrument control system (ICS) which monitors and archives a large number of environmental and operating parameters such as voltages and temperatures. In addition, the ICS provides the interfaces to the BigBOSS hardware components and the telescope control system as outlined in the previous sections. The BigBOSS user interface architecture will follow the Model-View-Controller (MWC) pattern now in common use for large applications. We intend to evaluate different technologies including the solutions developed for SDSS-III/BOSS and the Dark Energy Survey.

The infrastructure layer of the BigBOSS online software provides common services such as configuration, access to the archive database, alarm handling and processing as well as a standard framework for application development. Due to the distributed architecture of the BigBOSS online software, inter-process communication takes a central place in the design of the infrastructure software. We will evaluate several options including openDDS, an open source implementation of the Data Distribution Service standard used by LSST and the Python-based architecture developed for DES.

## 5.9 Assembly, Integration and Test

### 5.9.1 Integration and Test

Several large subsystems of the BigBOSS will be integrated and tested before delivery to the Mayall. These are the telescope corrector barrel, the focal plane with fiber positioners, fiber slit arrays, the spectrographs and cameras, and the instrument control system. Figure 5.53 pictorially shows the integration flow. Below is a broad brush description of the integration process, which will require much greater elaboration during the conceptual

design phase.

Prior to shipment, the corrector barrel lens elements are aligned and demonstrated to image to specifications. Actuators for the hexapod and the ADC are installed and operational. The fiber view camera mount attachment is verified. A focal plane mock up is test fitted. When delivered to the Mayall, the secondary mirror mount will be verified.

For the systems that contain fibers, we assume that intermediate fiber optic connector blocks will be used between the positioners and the spectrographs. This enables more comprehensive integration and testing before delivery to the Mayall, and makes installation easier.

Prior to delivery to the Mayall, the focal plane will be integrated with the fiber positioners, guider sensors, focus sensors, fiber view camera fiducial fibers, and cable/fiber support trays. The positioners will be installed with their fibers in place, which be terminated in connector blocks. A myriad of tests can be performed by individually stimulating fibers in the connectors. Positioner operation will tested and positioner control address, location and fiber slit array position will be mapped. A fiber view camera emulator can verify the performance of all the positioners.

This focal plane assembly is delivered to the Mayall and fitted to the corrector barrel. An acceptance testing plan will need to be developed that defines when the Mayall top can be disassembled and the BigBOSS prime focus structure installed.

The fiber slit array assembly precision can be measured by stimulating individual fibers in the connector blocks. This will also generate map for slit array position to connector location. This can be repeated with the actual spectrographs after their installation at the Mayall site. The fiber bundles can then be routed to and through the telescope to mate up with the fiber positioner connectors. Support of the fibers will require attachment of several structures to the telescope. The details are yet to be determined.

Spectrographs will be fully assembled and tested prior to shipment. This includes the cameras, cooling and vacuum systems, and the control system. Prior to their delivery, the Mayall FTS room will be reconfigured. The spectrographs and support equipment can be installed during day shifts and tested with the online software system, including acquiring spectra from internal lamps.

The instrument control system will have been developed in parallel with the other systems and will have been used in the commissioning and testing of other assemblies.

In summary, installation activities at the Mayall will entail replacing the existing prime focus structure including the mount ring with the BigBOSS

equivalent. The focal plane will then be mounted and the fiber strung to and from the spectrograph room. In parallel, the spectrographs will installed, plumbed and the fiber slit arrays inserted. Interfacing to the instrument control system and its interface to telescope operations also occurs. Commissioning will then commence.

### 5.9.2 Commissioning

A goal for commissioning is to have equipment delivered to the Mayall and run through preliminary shakedown tests so they are ready for the annual August shutdown. The major disruption to Mayall, the disassembly of the top end occur then. If we take the Dark Energy Survey model, four to six weeks comprise the shakedown period, requiring that the corrector and focal plane arrive in June. DES allocates six weeks for installing and testing the new cage and the f/8 support, a similar activity to that for the BigBOSS corrector and focal plane.

DES uses time over the following 11 weeks to complete on-sky commissioning. For BigBOSS, activities during this time will be demonstrating combined fiber positioning and telescope pointing, achieving and maintaining focus, end-to-end wavelength calibration using dome arc lamps or sky lines, and focusing the f/8 secondary using the corrector internal adjusters.

As described above, the major instrument subsystems will be fully integrated and tested before delivery to the Mayall. The hoped for outcome is that commissioning time will only go into the first-time co-operation of these subsystems.

We note that once the f/8 support and positioning are verified in the telescope, Cassegrain instruments can be once again operated. This, of course, precludes BigBOSS commissioning when in operation.

## 5.10 Facility Modifications

Improvements to the Mayall telescope and its dome are speculative at this time. We describe below potential issues and fixes that have been identified by NOAO and others.

### 5.10.1 Dome Seeing Improvements

There are dome and telescope improvements that can or might improve seeing. These need further study.

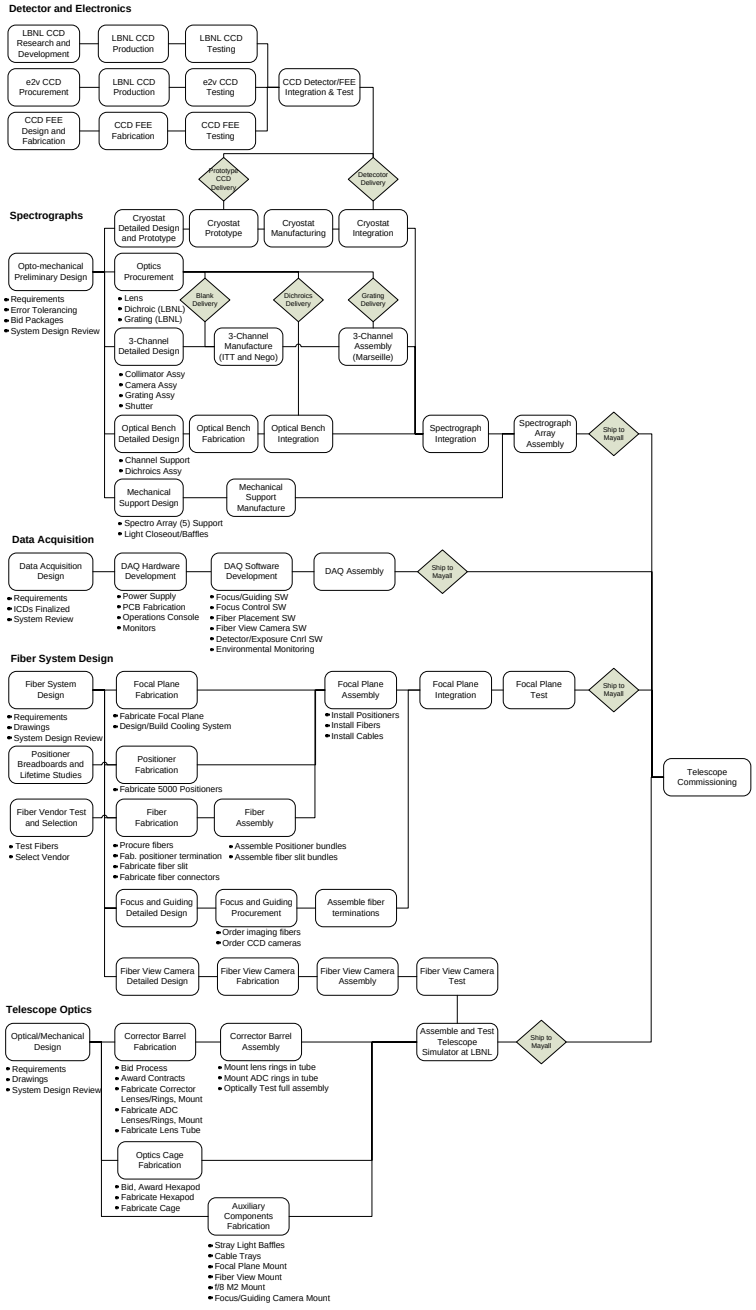


Figure 5.53: Assembly, integration and test flow.

**Stray light**

The Dark Energy Survey did a stray light study of the Blanco telescope. They identified the outer support ring of the primary mirror as the dominant stray light source. This flat annular ring is already painted black at the Mayall, but a conical shape but may be more effective. The Serrurier truss is presently white and there may be a benefit to change this to a matte black. These will be studies with our stray light codes.

**Primary mirror**

The Mayall primary mirror support system is current and no improvements are required. A wavefront map prior to BigBOSS operation should be performed to confirm that it is positioned correctly.

**Thermal sources**

Air currents and heat sources in the dome certainly impact seeing. The telescope control room is presently located on the telescope floor. The room will be relocated to a lower level at the Blanco and a similar solution is being considered in support of BigBOSS. It may be possible to study the impact of the control room in its present position under heated and unheated conditions.

The mass of the primary mirror central baffle impacts its thermalization to ambient temperature. Reconstructing this with a lighter design may be desirable.

A difference between the Blanco and the Mayall is that the former has a two-sheet protective cover for the primary mirror that does not trap air when open. The Mayall has a multi-petal system that partially traps a 1 m column of air above the primary. Again, it is speculative that a redesign of this can improve dome seeing.

### 5.10.2 Telescope Pointing

Historically the Mayall has shown absolute point accuracy of 3 arcsec in both declination and right ascension. More recently, right ascension accuracy is of order 15 arcsec. This will be corrected.

Telescope slew times have been recently measured, <20 sec for moves <5°. Unexpectedly, the primary mirror was observed to take 40–50 sec to settle. This impacts the 60 sec deadtime between exposures that we

have established as a goal. This may be a software issue in the drive of mirror supports. Further study and corrective action, hopefully, should be supported.

### 5.10.3 Remote Control Room

A long term goal of NOAO is to remote the telescope operations to Tucson. A remote instrument control room for BigBOSS is also desirable. The practicality of this and the cost are not yet understood.

### 5.10.4 Secondary Mirror Installation

It is required that BigBOSS provide a mounting mechanism for the existing secondary mirror to support Cassegrain focus instruments. This will require procedures and fixtures to remove the fiber view camera and support and to rig in the secondary. These will have to be jointly developed with NOAO.

### 5.10.5 Spectrograph Environment

A preferred location for the spectrograph system in the FTS room adjacent to the telescope. A large part of this room in on the telescope support pier. The general area is presently partitioned into multiple areas by easily removed walls and will need to be reconfigured for BigBOSS use. There appears to be an air handling in place already, but may require rework to provide a temperature controlled environment at the appropriate level.

## 5.11 R & D Program

Several technology areas of the BigBOSS instrument will benefit from early R&D activities to help insure that the conceptual design is within the bounds of what can be manufactured, costed and scheduled. We discuss several such areas below.

### 5.11.1 Telescope Optics R&D

**Lens design and manufacturability.** We will continue discussion with glass providers and lens makers for the corrector and atmospheric distortion corrector. The lens glass blanks are large and will take some time to produce. Likewise, the grinding and polishing of the lenses will be lengthy and production times need to discussed with vendors. The mounting method

of the lenses needs to be understood early on as this affects both the diameter and shape of the lens elements. This includes the size and optical prescription.

**Anti-reflective coating.** Another area impacted by the large lenses is availability of facilities for AR coating. Once identified, a potential way to verify capabilities is to coat small witness samples over representative areas of actual lenses.

### 5.11.2 Telescope Tracking Performance

To verify that the Mayall can track at the 30 max level, a modest experiment is proposed. A prototype guider system and a small array of fiber positioners and/or imaging fibers will be mounted in the existing prime focus corrector. The guider will be interfaced to the telescope control system and we will measure the tracking performance.

### 5.11.3 Fiber View Camera

A development view camera can be useful for software algorithm development and in support of fiber positioner development. Measuring positioning performance of actuator designs us an obvious early use of a view camera demonstrator.

### 5.11.4 Fiber Optic R&D

**Fiber characterization.** A system to characterize general optical performance of fibers from multiple vendors will be established. Testing includes wavelength dependent transmission losses, flexing dependent transmission losses, and focal ratio degradation.

**Positioner fiber termination.** The fibers are terminated differently at each end. At the positioner, fibers are terminated individually by gluing into a ferule and then finishing the optical surface. Methods for bonding the fiber to the actuator ferrule will be developed and optically tested.

**Spectrograph fiber termination.** At the spectrograph, groups of stripped fibers are terminated in a plane with spacing comparable to the fiber core diameter, for example 120 $\mu$m-core fibers on 240 $\mu$m centers. For an initial BigBOSS spectrograph concept, the fiber tips must lie within 50 $\mu$m of

a circle segment of 330 mm radius.A slit array sub-module containing 100 fibers will be fabricated to test assembly, bonding, and polishing processes. The unit tested for throughput and alignment.

**Fiber antireflection coating.** With appropriate antireflective coatings, light loss at the fiber ends can be reduced to $< 2\%$ each. The challenge here is to work with vendors that can apply AR coatings to individual fibers already mounted in ferules and a linear array of fibers assembled in a slit plane.

**Fiber connectorization.** An intermediate fiber to fiber connector can be useful for fiber slit array assembly verification and for initial installation and maintenance of BigBOSS. The cost is some loss of photons. Test units will be procured from multiple vendors and tested.

### 5.11.5 Fiber Positioners R&D

**Positioner pitch.** Fiber positioners will be developed at Granada, LBNL and University of Science and Technology of China. Positioners supporting 12 and 14 mm fiber pitch have been developed at the latter, with the 12 mm design requiring addition work. Alternative implementation are being looked at. There will be ongoing work to make smaller positioners to support a 10 mm fiber pitch. The motivation is two fold, more fibers on the same diameter focal plane, or a reduced diameter focal plane with a constant fiber count and reduced size corrector optics.

**Positioner performance.** Fiber positioning accuracy and repeatability and positioner lifetime are important characteristics that can distinguish between different designs. We will attach fibers to prototype positioners and, by illuminating the far end of the fiber and imaging the positioner fiber end with a CCD camera, we can measure the positional accuracy and number of iterations required to achieve the required 5 $\mu$m. Exercising positioners over thousands of cycles can expose lifetime issues.

**Position communication.** We envision using ZIGBEE wireless communication to control the fiber positioners. The 2.4 GHz carrier might be of concern to the Kitt Peak NRAO telescope. While ZIGBEE is low power with a $\sim$10-m range and will be confined in a mostly closed structure, we will need to coordinate with NRAO and possibly perform some experiments to check for radio interference.

### 5.11.6 Spectrograph R&D

**Cryostat tip-tilt.** A cryostat will be fabricated to demonstrate the tip-tilt mechanism required to place the CCD optical surface at the spectrograph focus.

**Linear pulse tube.** A linear pulse tube cryocooler will be acquired to measure it performance and understands the interfacing impacts on the cryostat design.

### 5.11.7 CCD R&D

**Blue LBNL CCD.** The baseline detector for the blue arm of the spectrograph is an e2v CCD with a blue enhanced AR coating. A simplification of the cryostat design and the readout electronics is possible if the LBNL CCD can be used here as well as in the other two arms. LBNL has been working with JPL for many years on implementing their delta-doping backside contact on n-type silicon. This has been somewhat successful, but has been limited to processing at the die level (maximum size 2k×4k). The Jet Propulsion Lab is commissioning a new molecular beam epitaxy machine that can perform batch processing at the wafer level. We continue to provide CCDs to JPL to assist in making this a routine processing step. There is a good possibility that we will be able to change the baseline in the next year to use one type of CCD everywhere.

**Red LBNL CCD.** To avoid the introduction of exotic and costly NIR detectors into the reddest spectrograph arm, we have baselined using a very thick version of the standard LBNL 4k x 4k CCD. Simulations indicate that a useable QE out to 1006 nm with acceptable point spread functions can be achieved. We will continue to perform lab measurements to verify the model predictions.

# 6 Survey Operations Plan

## 6.1 Survey Strategy

### 6.1.1 Baseline Survey Plan

The BigBOSS survey will target emission line galaxies, luminous red galaxies, and QSO candidates over a field of view of ≈14,000 deg$^2$. These three sets of primary candidates will be selected using color criteria from broadband imaging from either (or both) the PanSTARRS and Palomar Transit Factory surveys (see Chapter 4 for further details). We anticipate having the imaging data and candidate catalogs in hand one year prior to the start of regular survey operations, in order to enable preparatory studies of the sample definition strategy and to understand the sample selection function(s). In addition, we intend to undertake a short (13 night) Pilot Survey in order to fully characterize the sample selection and refine the color selection criteria. During the course of the regular survey, some of the fields targeted by the Pilot Survey will be repeatedly targeted as calibration fields to track the survey performance.

The survey fields will be selected to include the 10,000 deg$^2$ region covered by the BOSS SDSS-III survey plus an additional 4,000 deg$^2$ which, in our current baseline, covers a strip ∼10−20 deg wide that extends the northern Galactic BOSS region to lower Galactic latitudes. We are exploring other footprints which distribute the additional 4000 deg$^2$ between both spring and fall fields (i.e., northern and southern Galactic regions) and will optimize to cover areas of low Galactic extinction. All of the fields currently chosen are observable at Kitt Peak at airmass less than 2.0 at some point during the year, while the majority have foreground extinction of $E(B-V) < 0.15$ mags. Figure 6.1 shows the footprint of the survey, which includes 9824 pointings.

### 6.1.2 Calibration Fields

In order to properly characterize the BigBOSS survey performance and accurately measure the sampling and completeness functions, we will define 4 to 6 calibration fields, at least two of which can be targeted at any time of the year. These fields will be targeted at least once during each BigBOSS run, and over the period of the survey will build up a total area of ≈30-40 deg$^2$ which is densely sampled with deep spectroscopy. By carefully choosing the calibration fields to lie in regions which have wide-area multi-wavelength and archival spectroscopic coverage (e.g.: selected PS1 calibration fields;

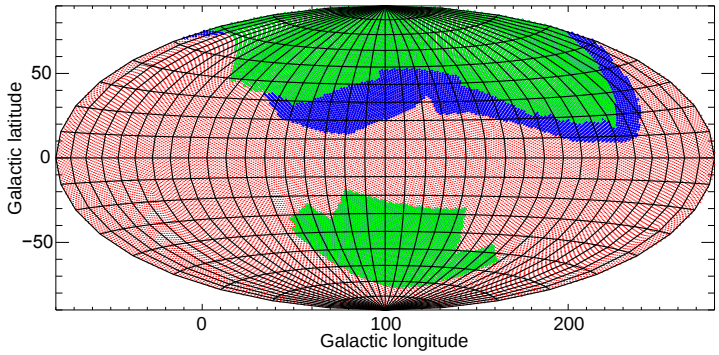


Figure 6.1: Footprint of the survey (in Galactic coordinates), which includes the BOSS LRG Survey currently underway (green) and a 4,000 deg$^2$ strip, chosen here to be at northern Galactic latitudes (blue).

overlapping with M31; the best studied portions of the Sagittarius stream; the 9 deg$^2$ NDWFS Boötes field; the 2 deg$^2$ COSMOS field; the SXDF and UDS fields; etc.), these fields will be invaluable for many ancillary science programs (e.g., galaxy evolution, Galactic structure, etc.) and have high legacy value.

### 6.1.3 Optimizing the Survey Observing Strategy

Kitt Peak observing conditions are strongly affected by the Southwestern monsoon season, which primarily affects the months of July and August (see Figure 6.3). The seeing conditions at the Mayall have not been systematically characterized, but Figure 6.4 shows the measured distribution of $I$-band seeing FWHM measurements from the KPNO 4m Mosaic prime focus camera. In the $I$-band, the median seeing is ≈1.0 arcsec, while the average is ≈1.1 arcsec. The seeing is likely to be largely due to the turbulence around and within the dome, since the mountain seeing is known to be much better (e.g., see http://www.wiyn.org/DIQ.pdf). It is possible that simple modifications to the telescope environment (such as moving the location of the Control Room) can improve the seeing even further; this would translate directly into improved survey performance.

In order to optimize the survey, we modeled the entire BigBOSS Key Science survey in the following manner. Given the 9,824 field positions defined previously, our software calculates arrays of target airmass, moon position and distance from the target field for all times during the year, in one hour intervals. The software then uses these arrays to decide the order in

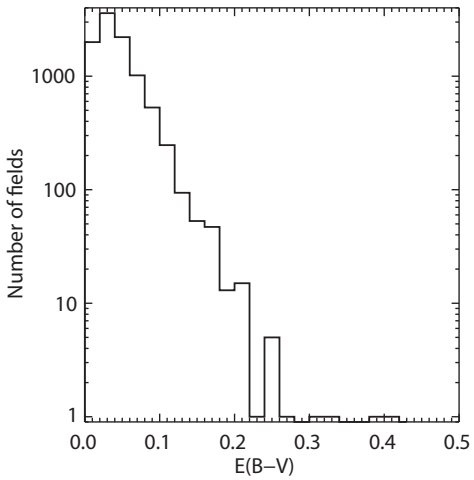


Figure 6.2: Distribution of Galactic extinction for the survey fields in the baseline survey.

which these fields should be observed, calculating the exposure time needed (given the airmass, sky brightness, the desired output signal-to-noise ratio per emission line of 8 for the redshifted [OII] doublet, and an efficiency factor that accounts for the typical clear fraction at the time of the observation) and adding in the relevant overheads (estimated to be a total of 60 seconds per field). For the exposure time calculation, we assumed an average seeing of 1.1 arcsec and an intrinsic target half-light radius of 0.3 arcsec, and calculated fiber losses based on these spatial profiles. The exposure time calculation included all of the efficiency losses identified by the instrument design team in the telescope/instrument system, as well as all of the readily identifiable sources of noise (object photon shot noise, location-dependent sky noise, and detector read noise). We set a minimum exposure time of 1,000 sec, which achieves a S/N>8 for one component of the redshifted [OII] doublet under clear dark-sky conditions at zenith. We constrained the schedule such that no observations were permitted in the three summer months of June, July and August (traditionally summer shutdown for KPNO due to the monsoon) nor during brightest Moon conditions. The night sky brightness was based on a combination of the dark night sky as observed with the VLT/UVES (Hanschik 2003), normalized to a surface brightness of 18.8 $z$ mag arcsec$^{-2}$ and with a dependence on airmass consistent with the airglow arising in a thin layer at 86 km altitude, and a model for the reflected solar spectrum of the moon with a normalization set by the formula of Kriscuinas and Schaefer

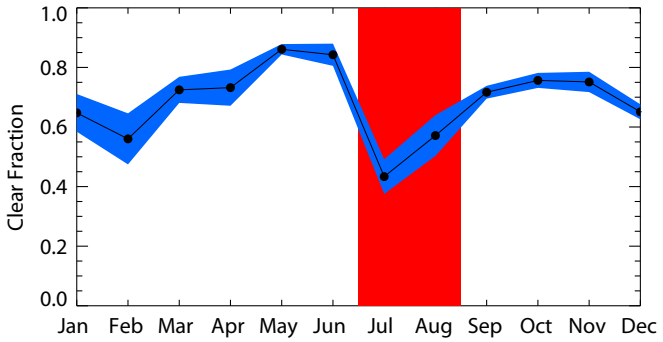


Figure 6.3: Typical fraction of clear conditions at Kitt Peak.

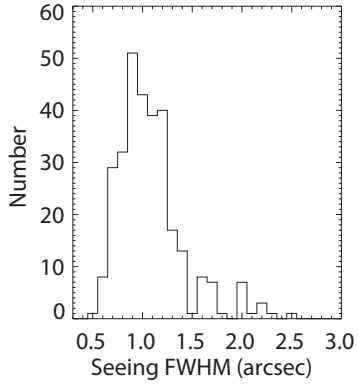


Figure 6.4: Distribution of seeing FWHM measurements from the Mayall prime focus instruments.

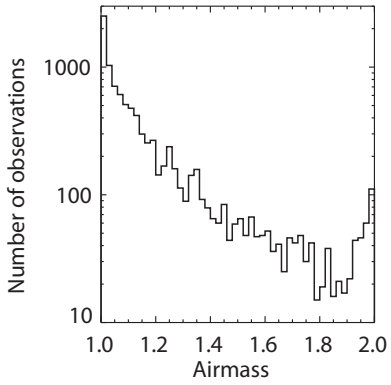


Figure 6.5: Distribution of airmass for the fields observed by the baseline strategy.

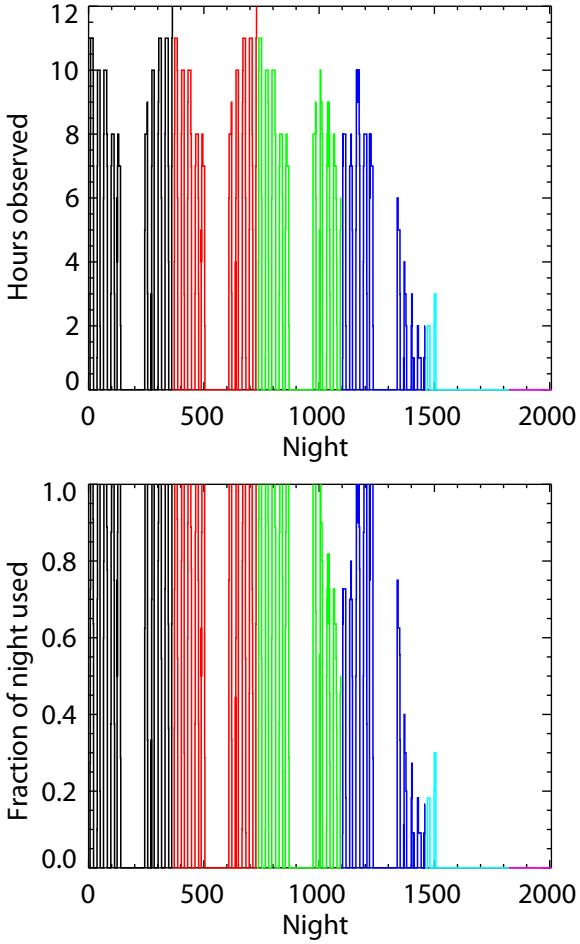


Figure 6.6: Distribution of nights used for the entire BigBOSS Key Science Survey, as computed by our optimization routine. Different colors denote different years. The total time shown here includes the effects of the site seeing and weather conditions.

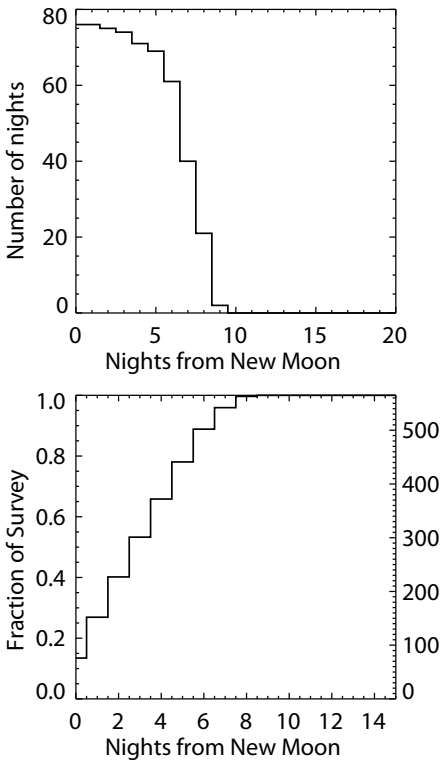


Figure 6.7: *Top:* The distribution of nights on which some data are obtained (i.e., including partial nights) as a function of nights from new moon for the current baseline BigBOSS survey. *Bottom:* The cumulative fraction of nights as a function of days from new moon. The right axis shows the total number of calendar nights used for the survey (includes partial nights).

(1991), which includes dependences on the lunar phase, the Moon position, and the distance between the target field and the moon.

Figure 6.6 and Table 6.1 show the distribution of nights for the optimal survey. Figure 6.8 shows the equatorial projection of the BigBOSS survey footprint, this time color-coded according to the year of observation. We continue to experiment with different models of covering the survey area to determine which approach is optimal, and the current strategy shown may not be the final one.

The total number of scheduled hours used by the survey is 4,265, or ≈450 equivalent 9.5-hour nights. These hours are distributed over 565 calendar nights, a higher number than 450 because it includes partial nights shared

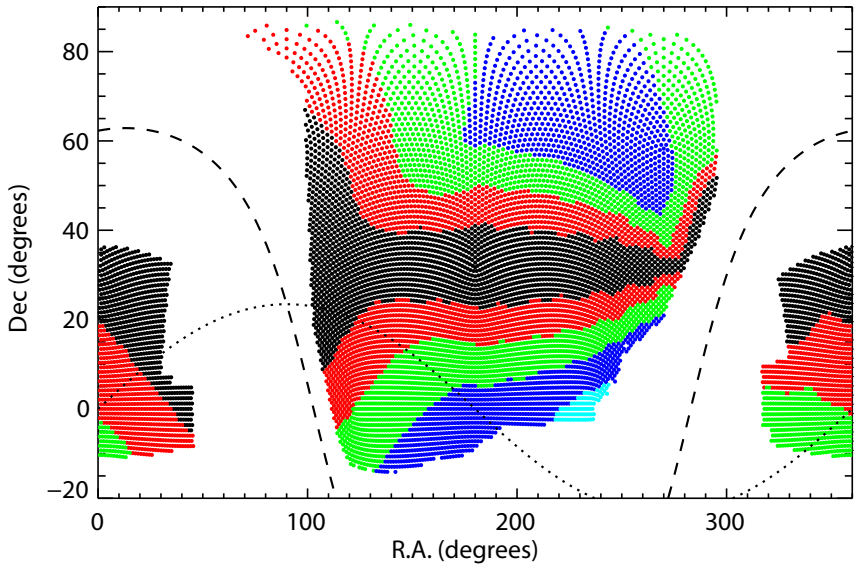


Figure 6.8: Equatorial projection of the field distribution for the BigBOSS baseline survey, color-coded according to the year of completion. The dashed line represents the Galactic plane, and the dotted line the Ecliptic plane. Note that while this footprint depicts the current baseline, it may be reoptimized.

with NOAO users. The baseline plan is to schedule ≈130-140 partial or full nights for the BigBOSS survey during the first four years, and the remaining 20 nights during the last year. A more evenly paced program spread over 5 years can also be accommodated; the exact distribution of nights per year can be negotiated by NOAO. The total survey time presented here does not include the extra overhead that may be required to accommodate any unforeseen issues. Doubling the overhead (from 1 min to 2 min) to account for the current telescope settling time will add an additional 17 equivalent 9.5-hour nights of time to the program; this is still within the 500 night limit.

As shown in Figure 6.7, the current BigBOSS baseline survey mainly uses nights during dark and grey time, no more than $+/-7$ to 8 nights from the new moon. This requirement is driven mainly by the Ly$\alpha$ forest BAO program, which necessitated observing a large number of faint QSOs at blue wavelengths. However, this does not mean that access to dark time will not be available to NOAO users. During the regular survey operations,

up to 20% of the fibers remain unassigned to primary targets and will be available for synchronous observing programs by the NOAO community (see Chapter 3). In addition, the survey makes use of partial nights, especially in the latter years, which can be shared with the community. Finally, we are willing to negotiate the night distribution with NOAO to make some dark nights available every year, especially if the Key Project can use any of the unused fibers on community programs.

Table 6.1: Total Time for the Baseline BigBOSS Survey

| | Calendar Nights | Hours | Effective Nights |
|---|---|---|---|
| Year 1 | 138 | 1211 | 127.5 |
| Year 2 | 139 | 1210 | 127.4 |
| Year 3 | 138 | 1089 | 114.6 |
| Year 4 | 131 | 710 | 74.7 |
| Year 5 | 19 | 45 | 4.7 |
| Total | 565 | 4265 | 449 |

## 6.2 Fiber assignment

In Table 2.2, we quoted a "fiber completeness" for the efficiency to observe our targets of 80%. That is, of all available targets, we can expect to reach the desired exposure times for 80% of them, given the physical constraints of the minimum fiber spacing. In this subsection, we justify this number.

The completeness depends on the density of available targets (discussed and justified in §4) as well as the density of observations in the survey area (discussed and justified in §6.1.1). Given these numbers, we can evaluate the resulting fiber completeness using fiber assignment simulations.

In the simulations used in this model, fibers are assigned randomly to available targets that have not been previously observed. Given a list of targets, we keep track of whether each target has achieved enough effective exposure time. At the time of each observation, each available actuator is assigned randomly to a target in its patrol area (see §5). We step through the actuators in order, and do not allow two actuators to observe the same target in the same exposure. After each exposure the effective exposure associated with each target is evaluated, and if reached, the target is removed from consideration for further observation.

For the default instrument configuration and the baseline survey plan,

we find that the fiber completeness is 80%. Meanwhile, the efficiency (or utilization) of the fibers is also about 80% — in each observation 80% of the fibers are assigned to primary science targets. A greater density of fibers or a greater number of observations would increase the completeness but decrease the efficiency.

In the real observations, a more optimized approach would yield slightly higher completeness than this simple greedy algorithm. Initial work has indicated a gain of about 2% in efficiency by using a more optimal algorithm, or about 600,000 more target total.

### 6.2.1 Fiber Allocation Fractions

To carry out the survey in a manner that achieves the key science goals, BigBOSS must assign each target type (ELG, LRG, or QSO) a fraction of the available fibers. Further, because the LRG and QSO targets require continuum measurements, multiple fiber exposures must be allocated to these objects. We therefore quantify the allocated exposure times per square degree by the *effective* target density, which is the surface density for each target type multiplied by the number of required exposures. Table 6.2 shows the effective target density for the BigBOSS targets and the expected number of exposures per target. These values are also shown in the survey overview Table 2.2.

An additional complication to the survey strategy is the manner in which the QSO targets are confirmed. As discussed in Chapter 4, achieving a highly-complete Ly$\alpha$ quasar sample ing *gri* photometry requires targeting across a large portion of the stellar locus where contamination from objects with similar colors can be high. To weed out the contaminants from the initial target distribution of $\sim$ 250 QSO targets / deg$^{-2}$, BigBOSS will allocate more fibers to the QSO targets in the first tile sweep of the sky. This strategy allows for a confirmation of the Ly$\alpha$ QSOs within the sample before allocating any further exposure time to measure the Ly$\alpha$ forest. While the fraction of ELG targets must decrease in the first tiling to accommodate this strategy, the overall decrease in the number of ELG redshifts is $< 10\%$ while the QSO target completeness increases to $> 80\%$.

BigBOSS will also allocate a fraction of the fiber exposures in each tile to calibration and ancillary targets. The calibration targets include SDSS standard stars and blank sky fibers, while the ancillary targets can be allocated through competitive community access. While specific allocation fractions have not yet been fully developed, we currently allocate 2% of the BigBOSS fibers to these purposes. Further ancillary targets could also be

allocated to the BigBOSS fibers which do not receive a key science target due to the 80% utilization of the focal plane fibers (discussed in the previous section). The remaining 20% of the fibers, $\approx 110$ deg$^{-2}$, will be randomly distributed over the 7 deg$^2$ field of view. Community science projects that could use these unallocated fibers are discussed in Chapter 3.

Table 6.2: Fractional allocation of fibers for the BigBOSS survey.

| | ELGs | LRGs | QSO $0 < z < 2.2$ | QSO $2.2 < z < 3.5$ | Other |
|---|---|---|---|---|---|
| fiber split (tile 1) | 0.41 | 0.2 | 0.28 | 0.09 | 0.02 |
| time split (tile 1) | 1 | 0.5 | 1 | 0.2 | 1 |
| fibers / deg$^2$ | 292.9 | 142.9 | 200 | 64.3 | 14.3 |
| fiber split (tiles 2-5) | 0.69 | 0.2 | 0 | 0.09 | 0.02 |
| time split (tiles 2-5) | 4 | 2 | 0 | 0.8 | 4 |
| fibers / deg$^2$ | 492.9 | 142.9 | 0 | 64.3 | 14.3 |
| Eff. targets / deg$^2$ | 2264.5 | 714.5 | 200 | 257.2 | 71.5 |

## 6.3 Use by External Community

As described in Section 3, we envision that BigBOSS will benefit the NOAO user community in three ways.

First, astronomers will be able to propose for telescope time with the BigBOSS instrument through either the regular or survey Time Allocation Committees run by NOAO. In this instance, the BigBOSS instrument will just be considered a regular facility instrument: full (or partial) nights will be assigned to successful proposals by the NOAO TAC and supported primarily by the NOAO staff. The BigBOSS team will provide the tools required to plan and schedule the observations with the instrument and for basic pipeline reductions. These will be the same tools that will be used for the BigBOSS Key Project, and the BigBOSS collaboration will collaborate with NOAO on a plan on how best to implement and support the use of the instrument.

Second, we also envision that a number of fibers will be made available for use by external users even during time committed to the proposed BigBOSS Key Science Project. Since our proposed survey will be tiling nearly 14,000 deg$^2$ of the northern sky, and because it will not be possible (simply because of the sky distribution of targets) to commit all fibers to primary targets, 10% to 20% (i.e., 500 to 1000!) of the fibers will be available for use by other NOAO users. Spectra (with the standard BigBOSS instrument

configuration) can therefore be obtained, during the course of the regular survey, for potentially large samples of targets sparsely distributed across the sky. Many user programs can be interleaved with the BigBOSS survey operations as long as they can tolerate data obtained on the same cadence as the survey program.

In order to enable such synchronous observations, we envision collaborating with NOAO to set up a mechanism whereby proposals for use of BigBOSS during its regular survey operations are first ranked by the regular NOAO TAC, these targets provided to the BigBOSS collaboration, and included in the targeting lists used by BigBOSS for its survey operations. Observations of these targets will be obtained as part of the regular survey strategy, reduced as part of the standard survey pipeline and made available to the proposers as the reduced data become available. Note that proposals for use of fibers during normal BigBOSS survey operations will be subject to various constraints (e.g., since the survey will be carried out over many years, time critical requests cannot be considered; exposure times will be limited to typical BigBOSS single-pointing integration times; non-standard instrument configurations or reduction and analysis methods cannot be supported, etc.).

Finally, the reduced data from the BigBOSS Key Science Project will be publicly released through NOAO and made available for archival research. This is discussed in more detail in Section 3. We note again the large impact of the archives resulting from the SDSS spectroscopic surveys on astrophysics, and expect that the science yield of the BigBOSS archive will have similarly high legacy value.

As mentioned in section 6.4.3, BigBOSS Key Science Survey observations will be carried out with the help of an Observing Scientist, who will be located in the Mayall control room with the telescope operator. The Observing Scientist will be responsible for the afternoon checks, nightly implementation of the observing plan, monitoring of the instrument and observing, and quality assessment. One possible operational mode would be for this Observing Scientist to be responsible for *all* the observations with the BigBOSS instrument, i.e., by the NOAO community and the BigBOSS team. In this mode of operations, all observations with the BigBOSS instrument would be uniformly obtained by an expert observer (i.e., essentially in a queue mode), and all the data would be reduced by the same pipeline used for the BigBOSS Key Science survey data. In this model, the cost of the Observing Scientist(s) would be proportionately shared between the BigBOSS project and NOAO. The advantages of this operational approach are that NOAO would not have to "start" new observers with this complex

instrument, would not have to maintain a separate (and different) pipeline, and would be able to ensure a smooth transition (through the Observing Scientist(s)) when, at the conclusion of the BigBOSS Survey, responsibility for the maintenance and operation of the instrument is transferred from the BigBOSS team to NOAO.

## 6.4 Day-time Support, Instrument Support and Maintenance Plan

In order to minimize the overheads of switching between instruments and the failure / breakage of any component, we propose that BigBOSS remain permanently mounted at the Prime Focus of the Mayall telescope for the entire duration of its operation at Kitt Peak. This will render the Mayall prime focus unavailable for other instruments during this period. (We note that the only existing prime focus instrument is the $36'$ field-of-view MOSAIC imager, which will be superceded by the WIYN One Degree Imager, and that no other prime focus instruments are currently being planned.) However, as described in Chapter 5, the BigBOSS prime focus assembly will enable the use of the Ritchey-Chretien secondary focus by providing mounting points for the existing Mayall F/8 secondary mirror. We propose to leave the entire fiber train intact and the end-to-end system operational even during periods when the F/8 is being used, so that we can continue to monitor the health of the system and minimize the time used for vetting the instrument during the switch back from F/8 to Prime Focus operations.

BigBOSS is a complex instrument undertaking a complex survey, and proper maintenance and monitoring of the various hardware and software modules will be critical to the success of the survey. In the following subsections, we outline the various tasks that we envision will be required during routine survey operations.

The basic requirement is that there be a sophisticated automated daemon that monitors the instrument status and produces a regular report for the use by the Survey Team. This daemon should schedule tests, analyze the results, and provide regular updates on the status of the different parts of the instrument (e.g., the dewars, vacuum and cooling systems, fiber positioning system, software and hardware supporting the acquisition system, ADC positioning, focus, etc., fiber throughput, etc.). The schedules for testing / monitoring of different systems are likely to be different (for instance, dewar temperatures need to be monitored hourly, whereas CCD gain and noise measurements could be scheduled once every month), and the response times for problems are also likely to be different.

### 6.4.1 Routine Maintenance

- Yearly test of Prime Focus optics (throughput, focus, etc.)
- Yearly test of Fiber Positioning and calibration system
- Yearly test of Spectrograph and CCD system
- Yearly throughput tests of end-to-end system
- Monthly test of vacuum on each of 30 dewars (i.e., two per week-day)
- Monthly test of UPS systems
- Monthly test of calibration sources
- Monthly test of temperature control of spectrograph room

### 6.4.2 Maintenance During BigBOSS Runs

*Tasks Prior to each BigBOSS Run:*

- If an F/8 to Prime Focus swap is required prior to each run, a few-hour on-sky commissioning period may be required at the start of each run
- Test end-to-end installation of instrument (end-to-end system functionality check; elaborate version of the afternoon checkout listed below, but with added rigorous optical quality checks)
- Review survey status and targeting plan for each run (from BigBOSS Team + NOAO PI targets), with weather options

*Day-time Tests and Calibrations:*

- Daily generation of instrument monitoring report and quality assessment of previous nights data / survey status
- Daily test of CCD health (i.e., test exposures to measure read noise, dark current, sensitivity, gain, and exercise readout software and real-time reduction software)
- Daily test of Instrument control software (i.e., test of fibers, alignment camera imaging, measurement of fiducial fiber positions, actuator response, ADC fiducial / motors test, shutter test, etc.)
- Daily spectrograph calibrations (i.e., arc lamps, flat fields, focus check, optical quality check, connectivity to data transfer system, disk space availability, etc.)

- Daily review of targeting and scheduling plan (with options or modifications as needed based on weather predictions and NOAO PI usage)

*Night-time Tasks and Calibrations:*

- Telescope initialization and checkout (verify telescope health and check pointing, focus, tracking, etc.)
- Beginning of night calibrations (twilight observations, standard star / cluster fields to vet end-to-end system and build on-sky throughput history)
- Execution of BigBOSS Key Science observing plan
- Real-time evaluation of observations and strategy (i.e., monitor pointing/airmass/weather/seeing/throughput issues, and reassess plan for night in real time; monitor instrument health; check real time reductions and quality assessment; monitor proper operation of data archiving, etc.)
- End-of-night calibrations (twilight observations, standard star / cluster fields, etc.)
- Telescope shutdown
- Instrument shut-down

### 6.4.3 Staffing During Survey Operations

We assume that NOAO will provide a telescope operator who will be responsible for operating and maintaining the functionality of the telescope during nights assigned to the BigBOSS survey. In addition, the BigBOSS team will provide an Observing Scientist who will be responsible on each night for implementing the schedule, running the instrument, checking / vetting the pointing, acquisition, and fiber alignment, vetting the data and the proper operation of the real-time pipelines. The Observing Scientist should (ideally) be co-located with the telescope operator in the control room. In addition to the on-site Observing Scientist, the BigBOSS Team will provide remote assistance with the day time checkout tasks (described above). The LBNL group will be responsible for running (and maintaining) the pipeline reductions and data quality assessment routines and for preparing a daily report for consideration by the BigBOSS Observing Scientist (and the relevant BigBOSS Team personnel) prior to each night. We anticipate no more

than 3 Observing Scientists employed by the project for the duration of the survey.

### 6.4.4 Plan for Instrument Part Replacement

Detailed maintenance and spares plans will be highly dependent on the components selected during the preliminary design phase and experience gained during development of BigBOSS specific components. Here we describe what we anticipate will be encompassed in the plans. Most failures in the items below will require a day shift to repair.

### 6.4.5 Telescope Systems

**Corrector Motors and Drives.** The corrector barrel is mounted on a hexapod actuator to provide focus and axial alignment with the primary mirror. There are six motors involved and an electronics module to control the motors. When a design is complete and a vendor is selected, we will establish the inspection and maintenance schedule and the parts inventory that needs to stored at the Mayall. The design phase needs to consider *in situ* repair of the hexapod, if possible.

The ADC also has a pair of motors, a mechanical drive system and control electronics. The maintenance and repair issues are the same as those for the hexapod.

**Fiber View Camera.** The fiber view camera is a critical component in the operation of BigBOSS. It is comprised of a CCD and control/readout electronics, probably packaged as a unit. A working spare needs to be available

**Lamps.** Two types are lamp systems exist in the corrector region. One type provides dome flat illumination, both broadband and line lamps. The other type illuminates the fiber view camera fiducial fibers and is probably LED based and built in redundancy is possible. Both systems have a small amount of electronics. Easily accessible locations for these items should make replacement fairly easy with locally stored spare parts.

### 6.4.6 Focal Plane Systems

**Guider and Focus Sensors.** These are critical items to the operation of BigBOSS. Spares of the detectors and their electronics will be maintained at

the telescope. If implemented as CCDs on the focal plane, opposed to being remoted via fiber bundles, repair may be lengthy. In either case, redundancy using multiple sensors can postpone immediate repair.

**Fiber Positioners.** The impact of failed fiber positioners is a complex issue. An individual positioner is not easily accessed, but individual failures are not a serious threat to successful operation. What has not yet been established is the threshold for the total number of failed positioners that would trigger maintenance intervention. It is probably in the low single-digit percent range. Since partial disassembly of focal plane infrastructure will be required for servicing, positioner servicing can only practically be done during summer shutdowns.

### 6.4.7 Spectrographs

**Cryostats and CCDs.** The only component in the cryostats that have any likelihood to fail are the CCD, temperature monitors and heaters. The cryostats are designed for replacement in 24 hours with on-site spares. Since there three CCD types in three cryostat types, one of each needs to be maintained at the telescope.

**CCD Frontend Electronics** The CCD frontend electronics is mounted on the outside of the cryostat. There are two configurations of one board design reflecting the difference between the e2v and LBNL CCDs. Spare will need to maintained at the telescope for daytime replacement.

**Shutters.** Shutter replacement requires removal of a cryostat. Spares will be kept locally.

**Lamps.** The fiber back-illumination lamps are probably LEDs mounted on the dichroic box. They should be inherently reliable and redundancy is easily implemented. The slit array illumination is probably a lossy fiber driven remotely by a fiber bundle itself illuminated by arc lamps. The dome flat lamps are a mixture of arc lamps and halogen lamps. The latter two systems are only used occasionally and are not required for routine operations; repairs can be scheduled with longish lead time.

**Cryocoolers.** The LPTs are given for a MTTF of 40,000 hours and do not require maintenance. The monitoring of their performance during lifetime

could be implemented in the cryostat control system, especially if we use the higher-functionality version of the LPT. In case of one unit failure, the cold machine will be replaced by a spare one belonging to the same series and the faulty unit will be returned to the manufacturer for examination and repair.

**Vacuum System.** Six vacuum pumps are envisioned and are normally valved off. Most likely, one spare will be kept on site.

### 6.4.8 Controls Systems.

The control system and computers are commercial using industry standard interfaces. During the design phase, a list of critical spares will be identified. During the course of BigBOSS operations, we will need to monitor parts becoming obsolete.

While it is desirable to maintain software versions, both our own and operating systems, control system parts replacement may require updates to the software.

## 6.5 Pilot Program

In order to verify the fiber assignment and scheduling algorithms, mitigate the risks associated with the target selection, test the efficiency of various tiling strategies, optimize observing strategies with the aim of minimizing overheads (i.e., resulting from pointing, slewing, fiber positioning, readout, etc.), understand the calibration requirements, and commission the data reduction and archival pipelines, we intend to undertake a short ($\approx$ 13 night) Pilot Survey at the end of the instrument's on-sky commissioning phase. This Pilot Survey will provide an important ground truth which will allow us to finely optimize and finalize our plans for executing the BigBOSS Key Science survey.

We envision this Pilot Survey as targeting 5 fields, three in the north Galactic cap accessible during the spring semester and two in the southern strip accessible during the fall semester. These fields will be targeted to a depth roughly 1 magnitude fainter than the selection depth for the BAO Key Science Survey, and with much higher completeness. In order to reach 95% completeness in our targeting, we expect each field to be targeted by 6 different fiber configurations. Each fiber configuration will be targeted for a total exposure time of 7 times our nominal survey exposure time (i.e., $7 \times$ 15min = 105 min), which will result (with overheads) in roughly 2 hours per

fiber configuration per pointing. This portion of the Pilot Survey requires 6.7 clear nights, or 10 nights (accounting for 65% clear fraction). In addition, we will require an additional 3 nights to experiment with different tiling and calibration strategies and to interface the calibration, reduction and analysis pipeline seamlessly with the survey operations. The Pilot Survey will therefore require a total of 13 nights.

We anticipate requesting this time at the end of the on-sky commissioning phase of the instrument, and note that this time is not considered part of the Key Science survey, since it will be used to verify many aspects of the instrument, pipelines, and survey prior to the start of actual survey operations.

# 7 Data Management Plan

## 7.1 Data-Taking System

### 7.1.1 Operations Database

At the heart of the BigBOSS data-taking system will be an operations database. Currently the SDSS-III data-taking system uses a similar model. A central database logs telescope and instrument status and meta-data. It tracks current observations, priorities, weather, airmass etc. so that observers can make informed decisions about upcoming observations. A web-based interface to this database will provide observers a complete picture of the observation status. This will allow members of the BigBOSS team to remotely monitor observations, which is expected to be especially valuable during commissioning and early operations. This could also allow PIs to monitor their observations during NOAO PI programs.

### 7.1.2 Fiber Location Specification

The fiber location specification will depend on the engineering details of the final system. We propose that the fiber positions will be specified in terms of a radial and angular offset from a central position, that the central positions will be mapped relative to a fixed point on the focal plane and that this fixed point can be mapped to a definite celestial coordinate (Right Ascencion and Declination) during exposures. Thus it is not necessary to track the celestial coordinate of every fiber as long as this mapping exists. Excursions outside of the known mechanical range of motion of the fibers will be flagged. Requests to move fibers to specific positions will be logged in the operations database, as well as the response of the instrument, allowing the request to be verified against fiber camera images.

### 7.1.3 Observation Planning Specification

Targets derived from the target database will be consolidated into a pointing. The constraints of coordinates (airmass), moon, and priority provide a number of days and range of hour angle where each pointing is observable. Scheduling is a difficult, non-linear problem, but our experience with scheduling observations on the Sloan Telescope will form the basis of our observation planning. Observation plans and results will be stored in the operations database.

### 7.1.4 Telescope and Instrument Status

Telescope and instrument status can be monitored in a fashion similar to the current SDSS-III automation on the Sloan Telescope. Various components have "actors" — a cross between a server and a device driver — which accept commands and respond with results in a well-defined way. All requests and results can be logged in the operations database.

### 7.1.5 Raw and Meta-data Structure

Raw spectroscopic data will take the form of FITS images. Meta-data will be stored in FITS headers (as needed) and in a database. It will also be possible for the operations database to generate flat files for the meta-data, which might be needed for downstream processing.

Fiber camera images will be stored as FITS images. Fiber camera meta-data will also be placed in the operations database.

### 7.1.6 Archive: Permission Locks, Backups, Checksums

Raw data will be transferred daily to the central data repository at NERSC. There it will be backed up to the HPSS tape storage system and copied to a mirror facility at the University of Utah. Before transfer, directories containing nightly data will be permission-locked so that no further data can be written. Checksum of files will be computed before transfer to insure data integrity at every stage of transfer and backup. As part of this process, the operations database will also be backed up, both in a flat file form and on a remote clone database.

Failures of the checksums at any point in this chain of steps will trigger human investigation of the problem, and recovery from the original files at KPNO.

## 7.2 Pre-Survey and Target Selection Data Management

During the pre-survey phase of BigBOSS we will assemble a target catalog based on photometric data from PanSTARRS-1, Palomar Transient Factory, and WISE. These will be tied to the astrometric and photometric system of the final SDSS-III/BOSS imaging data, to be publicly released in December 2010. We will store and curate the photometric data files used to construct the targeting catalogs.

The initial target selection will be available approximately 1 year before observations commence. The redshift success rates and redshift distributions

in the Pilot Survey inform any improvements to the targeting algorithms before the Survey proper begins.

## 7.3 Quality Assessment System

We will build on the experience of the BOSS team which has a very good quick reduction pipeline in operation on the Sloan Telescope. The pipeline is a stripped-down version of a full reduction pipeline, replacing the most expensive computational steps with simpler (and in some cases more robust) algorithsm. This system gives an estimate of S/N per exposure as a function of wavelength and object magnitude. This allows a robust, near-real-time decision of whether a tiling on the sky has been observed to completion. The system also flags problems with the telescope or instrument, which has proved valuable at Sloan for quickly identifying problems such as failed shutters or electronics glitches.

The stability of the BigBOSS spectrographs will remove the need to obtain and process quick-look calibrations (arcs and flats) in real time. The computational resources needed for quick extractions will be fairly modest at 1 CPU for each of the 30 CCDs. If the more expensive row-by-row optimal extractions used by full full BOSS reductions were used, the computing requirements would increase by a factor of several but still be very manageable.

## 7.4 Data Processing and Analysis Strategy

### 7.4.1 Extraction Strategy

Extraction is the problem of inferring one-dimensional input astronomical spectra from two-dimensional digital spectrographic images. Since BigBOSS will operate in a very low signal-to-noise regime, it is imperative that our extraction strategy be *statistically* optimal, so that every bit of significant information recorded by the spectrograph CCDs is faithfully propagated into the 1D spectra. Furthermore, we must keep *systematic* extraction errors to an absolute minimum: even small systematic mis-estimates of the night sky spectrum will lead to large non-Gaussian residual errors in the extracted spectra, when considered relative to the flux levels of BigBOSS core science targets.

The "optimal extraction" algorithm described in detail by [Horne, 1986] represents the current standard of quality, and it has many mature implementations including the `idlspec2d` software used for the analysis of SDSS and (currently) BOSS spectroscopic data. However, this algorithm has a

key shortcoming when applied to fiber spectroscopy, in that it treats the spectrograph PSF (i.e., the convolution of the optical fiber image with the spectrograph camera aberrations) as a separable function of $x$ and $y$ coordinates on the CCD detector. Residual coma, astigmatism, and core/wing effects in real spectrographs conspire to falsify this assumption of separability, and thus traditional optimal extraction does not generate a mathematically correct model for the two-dimensional spectrograph data. While this shortcoming can be safely ignored at higher signal-to-noise levels, it must be tackled head-on for BigBOSS.

The BigBOSS extractions will therefore be carried out following the algorithm described by [Bolton & Schlegel, 2010]. This algorithm extracts spectra using a fully correct two-dimensional model to the CCD data. The method accounts for optical heterogeneity among the fibers, and propagates all information and resolution forward to the final extracted spectra. The resolution and statistical covariance of the extracted spectra are accurately characterized, and the extracted samples have (by construction) no covariance from one pixel to the next. This permits straightforward and correct $\chi^2$ comparisons of models against the extracted spectra. The implementation of this method will be carried out initially as part of the ongoing BOSS survey, and we expect to have substantial practical experience and usable code in place by the time that the BigBOSS instrument is commissioned.

One of the greatest challenges to the implementation of the Bolton & Schlegel algorithm is the need for a detailed and accurate representation of the "calibration matrix" that relates input flux as a function of wavelength and fiber number to the response of all CCD pixels. In this regard, the anticipated stability of the bench-mounted and thermally controlled BigBOSS unit spectrographs affords a great advantage. Calibration libraries will be assembled on a monthly or yearly basis using standard arc-lamp and flat-lamp illumination systems, with alternating sparse masking of the input fibers to allow measurement of the fiber PSF wing profiles in the absence of fiber-to-fiber cross-talk. Calibrations may also be obtained using narrowband tunable-laser illumination; several BigBOSS proposal collaborators are actively exploring this method in collaboration with researchers at the National Institute for Standards and Technology, in the context of the BOSS instrument.

Based on a detailed analysis of the computational expense of the Bolton & Schlegel algorithm, we find approximately $4 \times 10^{17}$ operations necessary to extract one frame of 5000 BigBOSS spectra. Clearly this is a very approximate number, and there are many optimizations to be made based upon sparsity and symmetry, but it is expected to require supercomputing hard-

ware. By breaking the analysis up between bundles (with global iterations to solve for scattered light terms), the process is easily parallelizable among multiple supercomputing cluster nodes without the need for shared memory management. We expect to carry out this analysis on cluster computing systems at BigBOSS partner institutions as well as at national facilities (NERSC).

### 7.4.2 Sky Subtraction

Sky subtraction is an important problem for fiber-based spectrographs. In the background-limited faint-galaxy regime in which BigBOSS will operate, it is perhaps *the most* important problem. The most significant challenge is posed by the many OH rotational emission lines that become extremely prominent redward of 7000Å. The resolution of BigBOSS, while not *high resolution*, will be approximately twice as high as that of SDSS-I and BOSS, and thus the wavelength regions strongly affected by these emission features will be cut roughly in half (since the strongest OH lines are already resolved from one another at SDSS-I and BOSS resolution). Nevertheless, optimal handling of the problem of sky subtraction will be crucial to the full scientific success of the BigBOSS instrument and survey program.

Several key strategies for effective sky subtraction have been proven in the SDSS and other surveys already, and we will adopt these strategies in our approach to BigBOSS sky subtraction. Most importantly, the sky must be modeled and subtracted *before any rebinning or combination of the spectra* [Kelson, 2003], so as not to degrade native resolution and introduce ill-characterized correlations. We will also decompose our wavelength solution into *relative* and *absolute* components [Bolton & Burles, 2007]. Relative wavelength calibration is a crucial ingredient to the success of sky subtraction, and it can be determined with much greater accuracy than absolute wavelength calibration. We will also factor our flat-fielding images into pixel-flat and fiber-flat components so as to ensure the most accurate relative calibration between fibers, which will be crucial for the accurate transfer of model sky spectra between fibers. Finally, we will map the large-scale spatial illumination pattern differences between sky and calibration frames using periodically acquired twilight flat frames.

Traditional shortcomings of sky subtraction in multi-fiber spectrographs can be traced to three principal causes: (1) variation of the spectrograph PSF between sky and object fibers (due to fiber non-uniformity and spatially varying camera aberrations); (2) systematic errors due to the use of mathematically inaccurate models in the extraction of 1D spectra from 2D

CCD pixel data; and (3) insufficient spatial sampling of the sky by dedicated background fibers. The extraction algorithm of [Bolton & Schlegel, 2010] will directly remedy the first two problems. By modeling the input night sky spectrum "upstream" from the optical system, and convolving with the varying PSF over the fiber array and camera field of view before computing $\chi^2$ against the data, the algorithm avoids the problem of subtracting spectra with varying extracted line-spread functions between sky and object fibers. In addition, by extracting the raw CCD data using an image-modeling basis composed of *two-dimensional* PSF profiles, the algorithm avoids the systematic shortcomings of the traditional "row-by-row" optimal extraction algorithm [Horne, 1986] that implicitly assumes a separable form for the 2D spectrograph PSF – an assumption that is violated most strongly in the case of narrow emission features such as OH sky lines.

The problem of sufficient spatial sampling will be addressed in two ways. First, a substantial number of blank sky fibers will be allocated in each BigBOSS pointing, to allow a first-pass modeling of the sky spectrum and its variation across the telescope field of view. Second, all faint galaxy targets, once extracted and modeled with a sufficient basis of Eigenspectra, will be subtracted from the data to permit a second-pass modeling of the sky with finer spatial sampling.

Our science goals require the subtraction of night-sky flux to better than 2%. The algorithm of [Bolton & Schlegel, 2010] formally permits "perfect" Poisson-limited sky subtraction, *provided sufficiently accurate system calibration.* We anticipate that our calibration plan, described in the previous subsection, will be sufficient in this regard. Once again, we note that the stability of the bench-mounted BigBOSS spectrographs will make this accurate calibration problem more tractable than for the telescope-mounted SDSS-I and BOSS spectrographs, which experience significant flexure and routine fiber-cartridge changes. To increase the accuracy of BigBOSS sky subtraction, we will investigate the benefits of "tweaking" our high-precision calibration libraries against daily calibrations and individual science frames themselves.

The implementation of all of the above strategies for accurate sky modeling and subtraction (with the exception of tunable laser applications) are included within the Project Execution Plan for the ongoing SDSS-III BOSS project, to be incorporated in the next-generation extraction pipeline for the survey that will be developed and tested over the coming 1 to 3 years. This software will be written within a modular, object-oriented framework so as to allow for maximum generalizability and re-use for future instruments and surveys such as BigBOSS. Hence, we expect to have substantial experience

and code base at the ready for accurate extraction and sky subtraction of BigBOSS first-light data.

### 7.4.3 Redshift Measurement

Redshift measurements from extracted BigBOSS spectra will be made using forward-modeling techniques similar to those that have proven successful in the SDSS and BOSS projects. We will use deep BigBOSS data and (where necessary) spectral models to construct "Eigenspectrum" basis sets for each of a number of object classes: LRGs, ELGs, QSOs, and stars of all spectral types. For each spectrum and each object class, we will: (1) redshift the Eigenspectrum basis to a trial redshift; (2) fit the data with the best error-weighted least-squares linear combination of Eigenspectra at that trial redshift; (3) record the resulting value of $\chi^2$ for that trial redshift; (4) increment the trial redshift value differentially; and (5) repeat from step 1 until the entire plausible range of redshifts for that object class is covered. The classification and measured redshift for the spectrum will then be established by the global minimum reduced $\chi^2$ from this process. We may furthermore place photometric priors on the allowable classes and redshifts of targets, if this strategy is found to objectively improve redshift success metrics. Automated flags for redshift confidence will be set based upon the difference in reduced $\chi^2$ values between the best and next-best classification/redshift for each spectrum, the presence of excessive negative flux in the best-fit template model, reduced $\chi^2$ values that are too large even when minimized, and absence of a sufficient number of good data pixels in the extracted spectra.

The two main target categories for the BigBOSS galaxy BAO survey—LRGs and ELGs—each have characteristic narrow-band features that will make these redshift measurements robust. In the case of LRGs, the strong 4000Å continuum break and prominent Fraunhofer metal absorption lines will provide a clear and unambiguous redshift signal. ELG spectra will be characterized by [O II] 3727 doublet emission, which will be split at BigBOSS resolution and will therefore provide secure emission-line redshifts. For both target categories, the attention to statistical and systematic accuracy in extraction and sky subtraction described in Sections 7.4.1 and 7.4.2 will be of crucial importance to minimize the presence of sky-subtraction residuals that could lead to spurious redshift measurements.

## 7.5 Community Deliverables

### 7.5.1 Database Structure

SDSS has been successful at presenting spectroscopic data in database form. The current SDSS databases include individual spectral parameters and plots of spectra. These have proven to be useful features, and we would use a similar database structure. Since BigBOSS will not have an imaging component, the resulting database will be considerably smaller than the SDSS database. Naturally we will want to connect the spectroscopic database to the target database to enable easy matching to photometric data. We plan to develop the final database structure and interface in the period prior to BigBOSS commissioning. This will allow us to interface with real data via the database immediately.

### 7.5.2 Target Lists and Window Function

Spectroscopic data can be easily matched to photometric data in the targeting database. Information about pointings will also need to be included to compute the window function. SDSS already has considerable experience in constructing database tables and functions to satisfy this need.

### 7.5.3 Spectra

The curated form of the spectroscopic data set will be the FITS images for the raw data, the FITS files for the extracted and calibrated spectra, and the FITS files with the measured parameters. Direct access to these files will be available to the collaboration.

The calibrated spectra will be available as vectors of uncorrelated fluxes with errors. A line spread function (LSF; 1D PSF in the wavelength direction) that is defined at each and every flux value. $\chi^2$ tests of template spectra against these data will procede as projections of those templates using the LSF for each spectrum. We will follow the approach of BOSS, fitting linear combinations of galaxy (or QSO) eigenspectra rather than single templates. Stellar templates will also be fit, although the BigBOSS team will not be developing detailed fits to temperature, abundances, and gravity that would be appropriate for a proper Galactic survey.

The spectroscopic catalog will consist of the best-fit eigenspectra templates to each spectrum, the confidence, redshift error, and object classification.

A more conventional "constant resolution" form of the spectra could easily be provided, although the resulting wavelength-to-wavelength covariances would make that form not usable for the BigBOSS key science program. These spectra, if provided, could be thought of as the constant-resolution spectra that best fits the data. (These have essentially been the data products of the SDSS until now, but something we hope to deprecate by the year 2016.)

In addition to the FITS files, we will enable other "views" of the reduced data products through database tools. These build upon the SDSS "views" of spectroscopic data as tables of reduced parameters, plots of the spectra, and pointers (in the form of URLs) to the spectra in the FITS files.

Photometric information will be available by connecting and matching the spectroscopic database to the target database.

### 7.5.4 Documentation and Web Site

Documentation of the BigBOSS database and algorithms will be provided. We will tailor documentation for both collaborators and for the general research community. Through our collaborators on the PTF and DES, we will have extensive experience in building web portals for accessing and analyzing data. SDSS employs a publicly-available datamodel which describes the format of all flat files used by the project. We will encourage the use of self-documenting code, that is code that contains documentation that can be translated into HTML or other formats.

### 7.5.5 Public Outreach

The BigBOSS team will bring a great deal of experience from SDSS to our public outreach. For example, the SDSS SkyServer[4] provides access to the SDSS data to a wide variety of audiences, from elementary school teachers to research professionals.

### 7.5.6 Software Distribution

Analysis software will be available along with public data. We will release tagged versions of the software used to generate the data in the database. We will provide a complete dependency tree for all software, down to kernel version, so that other researchers can replicate our results. As much

[4] http://cas.sdss.org/dr7/en/

as possible, we will provide test cases with the distributed software. However, to simplify software operations, we will provide a central, cloud-based computing platform with stable, proven software versions to insure that collaborators are all using the same software. NERSC is currently testing this approach.

## 7.6 Computing Requirements

Table 7.1: Summary of BigBOSS computing requirements.

| | |
|---|---|
| Targeting Data Storage (flat files) | 150 TB |
| Targeting Database | 2 TB |
| Telescope and Instrument Control | 10 CPUs |
| Quality Assessment Processing | 30 CPUs |
| On-mountain Storage | 1 TB |
| Raw Data Storage | 4 TB/year |
| Data Reduction | 1000 CPUs |
| Processed Data Storage | 20 TB/year |

We have summarized the computing needs for BigBOSS in Table 7.1. The data storage requirements are relatively modest and can be accommodated by the NERSC Global Filesystem[5]. The on-mountain storage will allow us to store approximately a month worth of data as a contingency against data transfer failures. The data reduction requirements are based on scaling up the existing "riemann" cluster that is used for BOSS data reductions. Data reductions will also take place at NERSC which already has systems that easily meet our CPU requirements.

## 7.7 Risk Assessment

### 7.7.1 Personnel Hiring

The risk profile associated with the data management of BigBOSS has three essential components: personnel, software development, and hardware.

By far the most important of these three is personnel. For the proposed schedule, it is important to move the data management team into place early enough such that survey planning and execution can move forward.

[5]http://www.nersc.gov/nusers/systems/NGF/

This need motivates the hiring of 3 FTEs to assemble the target selection database, increasing to 4 to finalize the target selection, with an additional hire to help with commissioning. Our team is well-placed to address this risk: most notably LBL and NERSC have a proven ability to attract, or already have on staff, personnel with the expertise appropriate to handling massive astronomical data sets. The larger group of partners have expertise with distributing the Sloan Digital Sky Survey data (e.g. New York University).

### 7.7.2 Software Development and Performance

Software development is a second major risk, and breaks down into two parts: sources of delay, and software failures. Delay in target selection software can impede and/or complicate survey execution. Putting the data handling structure and personnel in place early is critical to mitigating this risk. The planned Pre-Survey to acquire spectra of large numbers of our targets is another important way to mitigate this risk (§7.2).

Delay in developing quality assessment software to run at the telescope can complicate commissioning; further, delay on the development of the final pipeline can complicate survey execution. In this case we have the world's experts on major spectroscopic pipelines on our team. They developed real-time quality assessment software and the final spectroscopic pipelines used by the SDSS for the past 10 years. In addition, we will have 2 FTEs, increasing to 3 during commissioning, to focus on this effort. We expect to build on their tools and experience to help address this risk.

Software failures can also put the project at risk. QA software failures can lead to underexposure or overexposure of spectra (the latter putting the overall schedule in jeopardy). Addressing this risk requires significant personnel resources, particularly during commissioning, to be in place to check results visually. In addition, the software tools must be developed to allow easy access to the nightly data to rapidly address any problems that develop. As we outline above, our data management plan includes such tools.

The final pipeline can also fail to sufficiently recover redshifts or calibrate spectra at the level allowed by the data. We mitigate this risk rather simply by saving all metadata and raw data used in reductions, to allow us to improve the software over time. Our planned computing facilities are sufficient for numerous reprocessings of the data set over time.

### 7.7.3 Data Hardware and Connectivity

The last source of risk is hardware inadequacy or failure, which can be either in the data storage or the data transfer. The disk farms used by NERSC are highly reliable systems; however, disk and server failure is a reality in any data facility. This risk motivates the full spinning-disk mirror and tape backups described above.

With about 40 GB of data produced each night, connectivity to the observatory is important. Periodically, as with any network, we will experience a lack of connectivity. The on-mountain computing system described above will be sufficient to store about 20 nights of observing in order to bridge any periods of network failure.

# 8 Project Management Plan

The management organization for BigBOSS construction and operations will have different organizations. The Department of Energy, Office of Science, Office of High Energy Physics (DOE) will be the lead funding agency for BigBOSS construction. While there will be in-kind contributions from non-US partners, the DOE project cost is at a level that requires a management organization compliant with DOE processes.

DOE, the National Optical Astronomy Observatory (NOAO) and non-US partners will fund BigBOSS and Mayall telescope operations. The operations funding is at a level such that a project-investigator-lead organization is sufficient.

## 8.1 BigBOSS Collaboration Organization

Described here is the organization of the BigBOSS collaboration to the extent that is needed to understand its interaction with the construction and operation of the instrument.

### 8.1.1 Collaboration

The collaboration consists of senior scientists from collaborating institutions. The collaboration is lead by the principal investigator (PI). The PI organizes the science goals to be met by the BigBOSS project and leads the collaboration executive board. In addition to collaboration members, there are participants, typically students and post-doctoral scholars from the collaborating institutions who are mentored or sponsored by members.

### 8.1.2 Collaboration Executive Board

The collaboration executive board (CEB) is a small subset of the collaborators designated by the collaboration. The CEB, the PI and the BigBOSS scientist establish scientific goals and objectives of the instrument, data management system and the Mayall facilities improvements. It advises the project manager on all scientific, collaboration and collaborating institution matters of the project. It will develop a policy for membership and will maintain current lists of BigBOSS members, participants and collaborating institutions. The PI is the chair of the CEB.

### 8.1.3 Science Working Groups

The science working groups assist the project scientist and project manager in generating top level science requirements and validating that the flow-down to technical specifications and designs meet these requirements. At later phases of the project they assist construction managers and scientists to verify that as-built systems meet the scientific requirements.

## 8.2 BigBOSS Construction Project Organization

The lead funding agency for BigBOSS construction is the DOE. The lead management institution will be LBNL, which has a long history of successfully managing large DOE scientific projects using earned value management systems and risk-based contingency allocation. Key technical managers will be highly qualified senior individuals drawn from LBNL and across the collaboration.

The BigBOSS project DOE cost is at a level that requires it to be organized and managed according to DOE Order 413.3a[DOE PM, 2000] that defines management activities and methodologies, examples of which are:

- Project budget development.
- Performance baseline.
- Project execution plan.
- Project acquisition plan.
- Critical decision points.
- Configuration management.
- Earned value management.
- Risk management.
- Health and safety plan.

The BigBOSS construction project organization is shown in Figure 8.1. There are three main activity areas: instrument construction and maintenance, data management construction and operation, and improvements to the Mayall facility. This configuration is intended to span research and development activities, construction and operations. The organization should be viewed as dynamic where major activities and emphasis will shift during the course of the project. The management effort, which must be fully costed under DOE rules, has been scaled appropriately to the complexity and cost of BigBOSS

The BigBOSS project includes the instrument and the data management system, each with a project manager. This division of projects recognizes

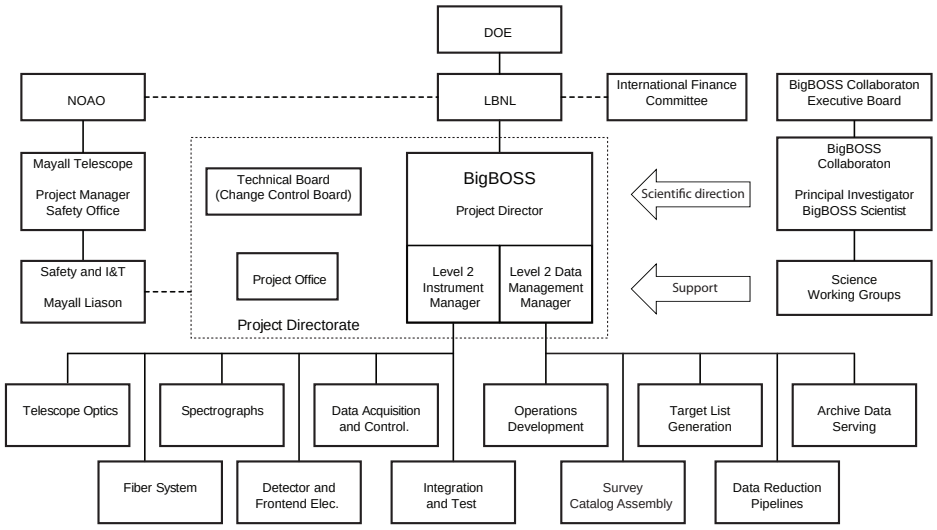


Figure 8.1: BigBOSS construction project organization chart. Interfaces to the funding agencies are simplified, as is the structure of the BigBOSS Collaboration.

that the nature of the work in each is very different and that schedules for the two projects become strongly coupled only near the end of the construction phase.

### 8.2.1 Funding Management

LBNL will manage the funds provided by DOE. In-kind contributions from non-US partners will be managed by MOUs between LBNL laboratory management and the non-US funding agency, or their designate. An international finance committee (IFC) will be established with representatives of each of the U.S. and foreign funding agencies. The role of the IFC is to insure that funding and man power commitments are made available on a timely basis so as not to impact project schedule.

### 8.2.2 Project Directorate

The project directorate consists of the project manager, two level 2 managers, the project office and the technical board.

### Project Manager

The project manager (PM) has overall responsibility for execution of the BigBOSS project. He coordinates the activities and the contributions of the collaboration for the installation, commissioning and operation phases of the survey through MOUs; is the principle point of contact with DOE, Kitt Peak National Observatory (KPNO) and the IFC; is member of the CEB; and chairs the technical board. The PM responsibilities per DOE Order 413 include:

- Plan, implement, and complete a project using a value engineering approach.
- Develop and implement an acquisition strategy and a project execution plan.
- Define project objectives and technical, schedule, and cost scopes.
- Ensure the design, construction, environmental, safety, health, and quality efforts performed by various contractors are in accordance with the contract, public law, regulations, and DOE Executive Orders.
- Ensure timely, reliable, and accurate integration of contractor performance data into project scheduling, accounting, and performance measurement systems.
- Evaluate and verify reported progress; make projections of progress and identify trends.
- Serve as the single point of contact between DOE and the project for all matters relating to the project and its performance.
- Implement a change control process.

The PM works with a KPNO manager to coordinate the work and schedules for the Mayall facilities improvements and for BigBOSS integration and installation at the telescope.

### Level 2 Managers

There is a level 2 manager (L2) for the instrument and for the data management system. Each is responsible to the PM for the execution of their subproject within the schedule, cost and resource constraints available. They work with the project office in preparing and maintaining a full schedule and WBS, including sufficient milestones to allow progress tracking. The milestones will include dates for the reviews of the conceptual design, preliminary design, final design and project completion.

The L2s are responsible for day-to-day management that includes: project status; risk management; documentation; cost and schedule tracking; coordination of team members; and reporting to the PO. The L2s are members of the Technical Board.

### Project Office

The project office (PO) is responsible for supporting the PM in monitoring the technical scope, cost and schedule performance of all portions of the project as per DOE Order 413. The PO maintains the master resource-loaded schedule, linked to a work breakdown structure (WBS), and monitors project progress with an earned value management system. The PO supports the PM in reporting to DOE.

The PO and the L2s assist the PM in developing and maintaining the system hardware and software requirements and specifications. Requirements, specifications, and interface control documents will be maintained in a configuration management system. The PO with insure that all drawings are reviewed prior to release for manufacture or procurement. The PO is informed of all engineering change orders. A designate from the PO is a member of the technical board.

Within the PO is staff responsible for ensuring that all aspects of the project are conducted to the appropriate levels of safety, reliability, and quality required by DOE, LBNL and KPNO. Management methods are: development of a safety implementation plan; documenting all identified hazards to instrumentation and personnel, hazardous procedures, and the methods used to control them; oversight of instrument designs so that appropriate safety features are incorporated. All work will be done in accordance with the requirements of DOE and LBNL Health and Safety standards, and with those of KPNO.

### Technical Board

The technical board (TB) advises the PM to help ensure that all systems of the project are being adequately integrated and executed toward the scientific and technical goals of the project within the constraints of budget and schedule. Its membership consists of the L2s and subsystem L3s. The TB is chaired by the PM and meets on a regular basis to discuss technical, cost and schedule issues. The TB is the change control board.

### Level 3 Leads

There are many major subsystems in the BigBOSS project, each with a subsystem lead (L3). Individual execution responsibilities can be found in the WBS description in Section 9. The L3s report to their respective L2. The L3s are members of the TB.

### Management Processes

#### Science Requirements

The BigBOSS science requirements are presented in Section 2. A top-level project scientific requirements document will be developed during the initial phase of the program by the CEB, PI and PS. Systems requirements and definitions are derived from these by the PM working with the PS. The science requirements will be placed under change control at the completion of preliminary design (DOE CD-2). The science requirements document and a change control process ensure that the scope of the project is controlled at the highest level in the project.

#### Technical Requirements and Specifications

The technical requirements and specifications documents flow from the science requirements and programmatic requirements imposed the telescope environment, the data management environment, and LBNL and KNPO health and safety requirements. The technical requirements in turn define the software and hardware interfaces within the instrument system and data management system, and their interfaces to the telescope and its utilities and environmental control systems.

The PO will lead the definition of lower level system and subsystem requirements using a documented flow down process. All hardware and software elements will be defined in these specifications. At the appropriate point in the program, the specifications will be placed under configuration control with changes made by formally controlled engineering change orders.

#### Systems Engineering

Systems engineering, captured in the PO, views all elements of the BigBOSS project as a single entity and allocates requirements and design ap-

proaches across the entire system. The outcome of this process is definition of interface control documents between subsystems. The PO works continuously with the L2s and L3s to ensure that interfaces are properly defined and that technical issues affecting more than one system are resolved efficiently and effectively.

### Baselines and Change Control

Each major activity will have a set of baselines that will define its technical performance, cost estimate and schedule. Changes to these baselines are inevitable and must be managed. Proposed changes will require different levels of approval based on severity and impact on the project. The PM is informed of all changes at any level.

At the lowest level, involving a relatively small redistribution of funds within a given subsystem, only the appropriate L2 approval is required. The L2 will bring changes in cost and/or schedule to the TB.

Changes impacting scope or scientific goals must be brought to the change control board (the TB) and approved by the PM.

Changes in scientific scope will first be brought to the TB and in turn reported to the CEB by the PM for their concurrence.

### Contingency

Contingency is reserved during cost estimation for the various systems and subsystems based on their perceived risk. During the preliminary phase of the project, a contingency depletion schedule will be established. Schedule and budget depletion will have established time-phased benchmarks. The amount of reserve needed depends on the level of maturity and heritage of the particular item. As a subsystem develops, the reserves may be expended to resolve problems or to meet schedule. Contingency is controlled by the PM and L2s, and any call by a system or subsystem on contingency must be made through the TB. This permits the PM to manage the technical progress, resources and funds by balancing available reserves to preserve performance, budget, and schedule.

### Progress Reports

Monthly financial and project (earned-value) reports will be submitted to the DOE. Technical progress reports will be submitted to summarize

progress, concerns, problems, changes, and plans for the next period. In addition, frequent contact with the DOE technical monitor would be standard practice.

#### Risk Management

The basic approach to risk management is to minimize risks by using proven designs, existing hardware, and conventional fabrication methods to the maximum extent possible. It is not possible, however, that all elements can be based fully developed technology. It is to be anticipated that unexpected events or developments over time will influence the resources, cost and schedule of the final configuration. Nor is it possible at this stage of a project to know all of the risks. Consequently, the allocation of contingency to cover both known and unknown risks is very important.

The first step in the management of risk is its assessment. This is done initially in conjunction with the estimation and determination of the work to be done. Each element used in costing is assessed and scored as to its stage of development and potential impact on the project. Specifically, each element is rated for design/approach maturity, complexity, dependency, technical development, cost uncertainty, and potential schedule variance. Calculations are then done on the assessed risk score to determine an appropriate level of cost and schedule contingency. In parallel, scope contingencies are identified with decision points established where technical trade-off choices must be made.

Once the project is under way, issues identified with risk to the project are monitored and contingency is allocated where necessary. It should be stressed that risk management is not merely the initial allocation of funding contingency to various tasks and subtasks. Complete risk management is an ongoing effort throughout the life of the project and involves the development of not only funding contingency, but schedule and technical contingencies as well.

### 8.2.3 KPNO Interface

Potential improvements to the Mayall facility to improve dome seeing and operational efficiency are described in the Section 5.10. BigBOSS data management needs to be integrated within the NOAO data management system. KPNO will be responsible for these activities and the work will be organized according to KPNO procedures and processes under the direction and oversight of the KPNO Director. An MOU between BigBOSS and KPNO will

the established documenting the expectations and responsibilities of both parties.

We anticipate that KPNO will designate a project manager responsible for preparing and maintaining a full schedule and work breakdown structure for their activities. Sufficient milestones will be identified to allow cross tracking of the BigBOSS and KPNO progress.

KPNO will designate a BigBOSS liaison for coordinating the safety plan implementation, and for integration and test. The liaison will work with staff in the PO and with responsible parties within BigBOSS for integration and test.

The KPNO project manager and liaison are members of the TB.

## 8.3 BigBOSS Operations Management

Once the survey begins, the responsibilities of the instrument team will shift to maintenance and the data management team will be responsible for production data processing and distribution of the data and catalogs, including data quality assurance of the data products. Both teams, in partnership with KPNO operations, will contribute to survey operations. The management structure is shown in Figure 8.2.

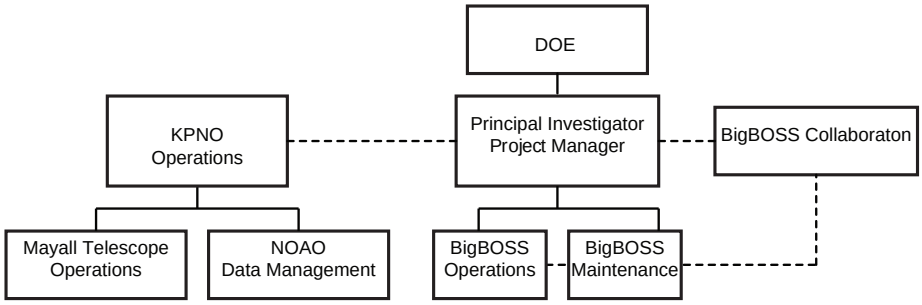


Figure 8.2: BigBOSS operations project organization chart.

NOAO will fund the telescope operations and their data management system. DOE and BigBOSS partners will fund BigBOSS instrument operations, maintenance and data management system. The funding agencies point of contact is the principal investigator (PI). Collaboration membership rules will determine the obligations of collaborators for the operation of BigBOSS. Additionally, MOUs will be established with institutions responsible for hardware and software maintenance. An MOU between KPNO and

the PI will establish their roles and responsibilities for operations and data handling.

A project manager (PM) will oversee day to day activities such as scheduling collaborator observation shifts, ensuring data collection quality, instrument health and equipment spares. The PM will interact with his KPNO Mayall counterpart for observation scheduling and maintenance access.

# 9 Cost Estimate and Funding Strategy

## 9.1 System Cost and Cost Breakdown by WBS

## 9.2 Schedule

## 9.3 Funding Plan

## 9.4 Partners

# A Exposure Time Calculator

In order to estimate the exposure time requirements and planned survey length, BigBOSS has developed two exposure time calculators (ETCs). The first of these calculators is in the form of a simple spreadsheet where all calculations are open to scrutiny with minimal effort. The second calculator is written in IDL and is based on the spreadsheet but extended to incorporate an entire 2D simulation of the measured spectrum. The full wavelength-dependent simulation, called *bbspecsim*, uses existing measurements of sky brightness, sky transparency, and instrumental throughputs in all possible cases. The results of these exposure time calculators provide a transparent way to forecast the BigBOSS survey requirements.

In the following discussion, the ETCs are described in the context of acquiring sufficient S/N on the [OII] emission line of ELG targets to make a detection and redshift measurement. This criterion results in a *minimum* exposure time for each tile of the survey, and therefore generally governs the speed at which the survey can be performed.

**Sky Properties** The measured signal in the vast majority of the BigBOSS galaxy spectra will be limited by background sky emission. The BigBOSS spectra will be at sufficient resolution to separate most of the sky emission lines, and therefore, the majority of the ELG [OII] line detections will occur over the background continuum between the sky lines. Historically, this background sky continuum level has been uncertain due to instrumental limiting conditions (such as scattered light) and site variations. Noxon (1978) found the continuum to be 130 photons $s^{-1}$ $m^{-2}$ $arcsec^{-2}$ $\mu m^{-1}$ at 8500Å during dark time. DEEP2 measurements from the Keck DEIMOS spectrograph give a similar value of 133 photons $s^{-1}$ $m^{-2}$ $arcsec^{-2}$ $\mu m^{-1}$, but the SDSS spectrograph measurement is $\sim$ 180 photons $s^{-1}$ $m^{-2}$ $arcsec^{-2}$ $\mu m^{-1}$. Since BigBOSS will be closer in design to that of the SDSS spectrograph, we assume the conservative value of 180.

Figure A.1 shows the sky emission spectrum measured from the BOSS spectrographs during dark time near zenith out to 10300Å. This spectrum is at the BOSS resolution (R$\sim$ 3000), so the sky lines do not fully represent what would be achieved in the BigBOSS spectrographs (R$\sim$ 4500). Beyond 10300Å, the spectrum is supplemented with the higher resolution Gemini emission spectrum. This portion of the spectrum is scaled to match the BOSS continuum and emission line peak level in a small overlap region. Note that wavelengths >10300Å correspond to [OII] at a $z > 1.75$ and therefore are not critical to the survey. The current sky emission reflects

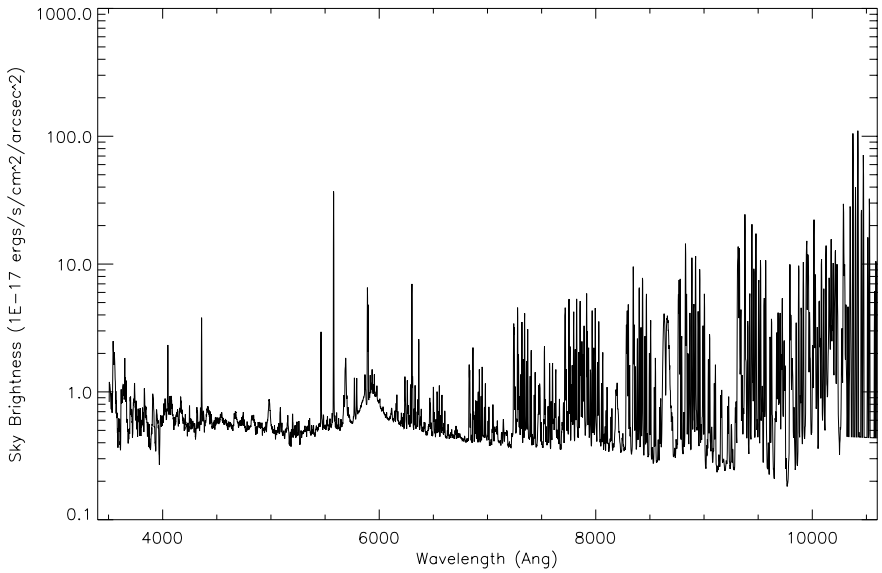


Figure A.1: Sky emission spectrum used in the calculation of exposure times for BigBOSS. The data for $\lambda < 10300$Å is from the BOSS spectrographs and was taken during during dark time near zenith. Data beyond $\lambda > 10300$Å is taken from the Gemini model sky spectrum and scaled to match the BOSS resolution and sky continuum level.

that observed at APO (at a lower resolution than BigBOSS) and not KPNO. This spectrum should conservatively estimate the sky conditions at KPNO.

The sky extinction for KPNO is derived from kpnoextinct.dat, a widely used extinction curve for Kitt Peak which extends from 3400Å to 9000Å. Beyond 9000Å, we have supplemented the extinction curve with simulated HITRAN data. This calculation was originally performed for Palomar observatory with 3mm of water vapor at 1700m. The HITRAN data is at a very high resolution which we downsample to the resolution of BigBOSS (see Figure A.2). The combined extinction curve is computed for zenith angle.

The final atmospheric input terms are the airmass, $X$, and Gaussian RMS variation, $\sigma_s$, of the observation. The current ETC uses default values of 1.25 airmass and 1.1″ FWHM seeing for the baseline calculations. The average airmass term is calculated from the mean of all tiled observations simulated in the survey lifetime (see Section 6). The seeing value is taken from the most recent average seeing measured from the MOSAIC camera mounted at prime focus on the Mayall telescope. The ETC also scales the

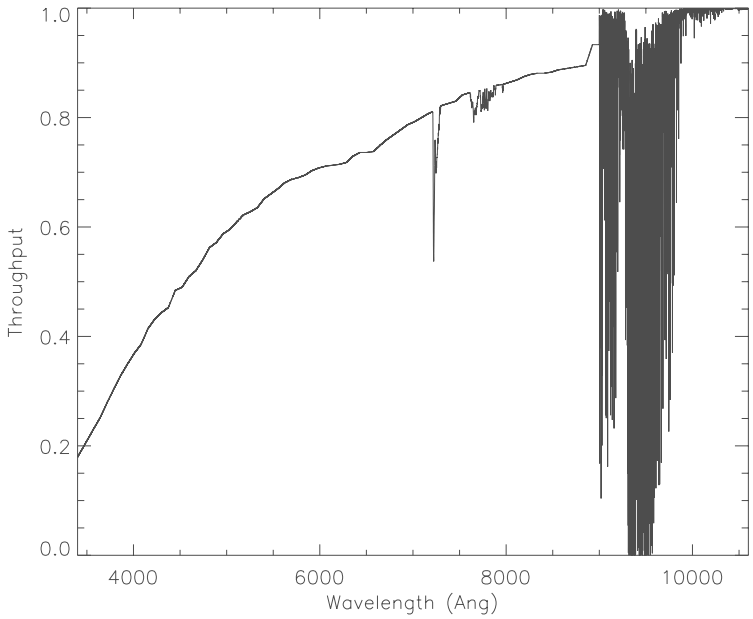


Figure A.2: The transmission of the sky used in the calculation of exposure times for BigBOSS. The data for $\lambda < 9000$Å is from low resolution KPNO observations. Data beyond $\lambda > 9000$Å is simulated from HITRAN for the Palomar observatory with 3mm atmospheric water vapor and rescaled to match the KPNO data at 9000Å. The HITRAN data is sampled every 0.1Å, and therefore the absorptions seen here must be convolved with the object and sky background spectrum before being downsampled to the BigBOSS resolution.

sky brightness and seeing as a function of the airmass. The sky brightness scales as $X^1$ since the column density through the OH sky emission is linear with airmass. Imaging data from the MOSAIC camera indicates that the seeing is not airmass dependent in the $i$-band for $X < 2$, indicating that dome seeing is dominating the delivered point spread function (see Figure 6.4). We therefore currently adopt airmass independent seeing for the Mayall. The ETC does not currently handle effects like differential atmospheric dispersion, although we expect to use an Atmospheric Dispersion Corrector.

**Telescope and Corrector Throughput** The telescope collecting area is defined by the primary mirror diameter and reduced by the obscuration

of the secondary support structure. We compute this area as the geometric throughput of the telescope relative to the full collecting area. For a primary mirror of 3.797m and secondary diameter of 1.8m, BigBOSS will have a geometric throughput of 0.775, and therefore the collecting area of the telescope is 8.72m$^2$. The reflectivity of the telescope is taken from the witness sample measurements during re-aluminization of the Sloan 2.5m primary mirror at Kitt Peak. The average value is $\sim 90\%$. The corrector is currently designed to have 12 optical interfaces and glued prisms in the ADC. Detailed ZEMAX calculations of the glass component thickness and applied anti-reflection coatings result in an average throughput of 0.78. The full wavelength dependent throughput for both the telescope and corrector is shown in Figure A.4.

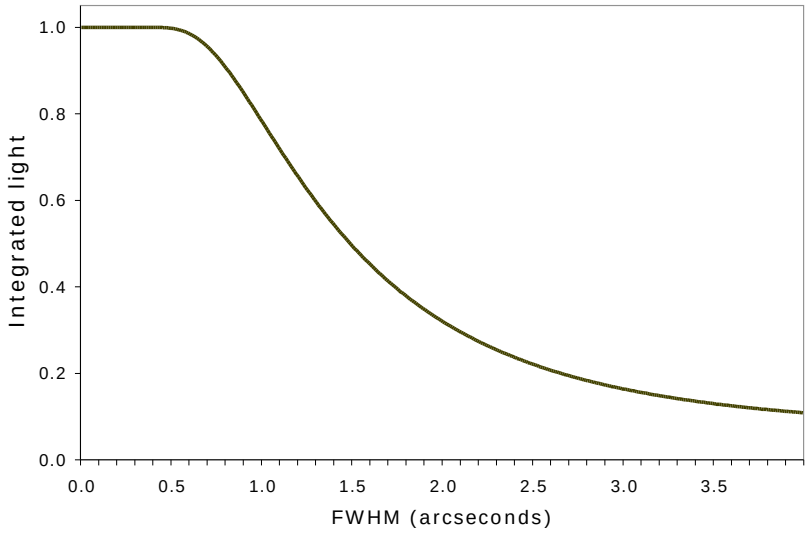


Figure A.3: The integrated fraction of light received by a 1.5″ diameter fiber for values of Gaussian FWHM. This calculation assumes a perfect centering of the Gaussian profile on the fiber.

**Fiber Properties** The BigBOSS baseline design calls for 1.5″ diameter fibers. The amount of light from the source that enters the fiber will depend on several factors, including (but not limited to) atmospheric seeing, source size, and telescope pointing. Assuming that the seeing and source size are the dominant terms for galaxy observations in the BigBOSS survey, we calculate the size of a Gaussian spot convolved with an exponential galaxy

profile, which can be expressed analytically as

$$\sigma_{psf}^2 = 2\left(\frac{h_l}{1.68}\right)^2 + \sigma_s^2 \tag{A.1}$$

where $\sigma_s$ is the seeing RMS and $h_l$ is the galaxy half light radius. We use the measured seeing from the MOSAIC camera ($1.1''$) as our baseline value and note that the measurement *includes* sub-dominant blur contributions from the camera corrector optics and guiding system (see Jacoby et al. [1998] for details). We anticipate similar, if not better, optical and guiding performance for the BigBOSS focal plane. Using high-resolution imaging from the COSMOS field with HST [Leauthaud et al., 2007], we estimate that the mean $h_l$ size of ELGs between $0.5 < z < 1.5$ will be $0.3''$, and therefore the nominal FWHM of the PSF will be $1.25''$ for 1 airmass. We compute a lookup table for the fractional loss of light within a $1.5''$ fiber circle for a given Gaussian spot with $\sigma_{psf}$ and perfectly centered on the fiber. The amount of light captured by the fiber as a function of the spot FWHM is shown in Figure A.3.

For the focal plane plate scale of 82.64$\mu$m arcsec$^{-1}$, BigBOSS will require 120$\mu$m core fibers. We assume that BigBOSS will use the Polymicro FBP fibers which have low water absorption and have broad applications in astronomy. For wavelengths of 8000-10000Å, the attenuation can be as low as 3db/km. For a typical fiber run length of 30m, this would translate to 98% transmission. However, all silica fibers have heavier attenuation for bluer wavelengths and can have ∼60% transmission at 4000Å. The full wavelength dependent throughput for the Polymicro fibers are shown in Figure A.4.

**Spectrograph Properties** The BigBOSS spectrograph design calls for 3 pixel FWHM sampling of a monochromatic spot. In the red arm of the spectrograph, this sampling corresponds to a 2.2Å resolution at a dispersion of 0.732Å/pixel. To first order, the BigBOSS spectrograph will image the 120$\mu$m core fiber end onto the BigBOSS detectors with a 2.67 demagnification, producing a circular image with a 45$\mu$m diameter. In the full spectral simulation, the ETC uses monochromatic, photon-level 2D images produced by a ZEMAX monte carlo simulation. These spots are generated over the entire spatial reach of each spectrograph arm and therefore include more subtle effects such as distortion and coma produced by the spectrograph optics (see Figure A.5). The simulation linearly interpolate between these monochromatic images in the dispersion direction to generate a full spectral image.

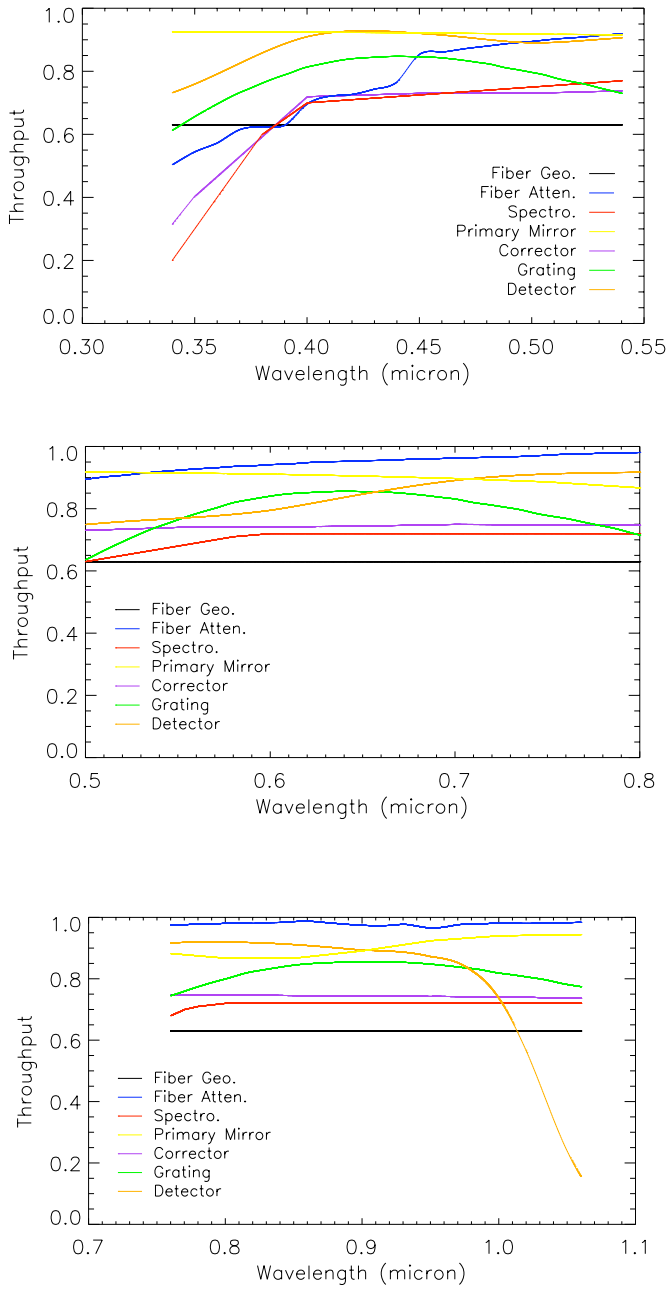


Figure A.4: The assumed throughputs for various instrument components in the blue (top), visible (middle), and red (bottom) BigBOSS optical paths.

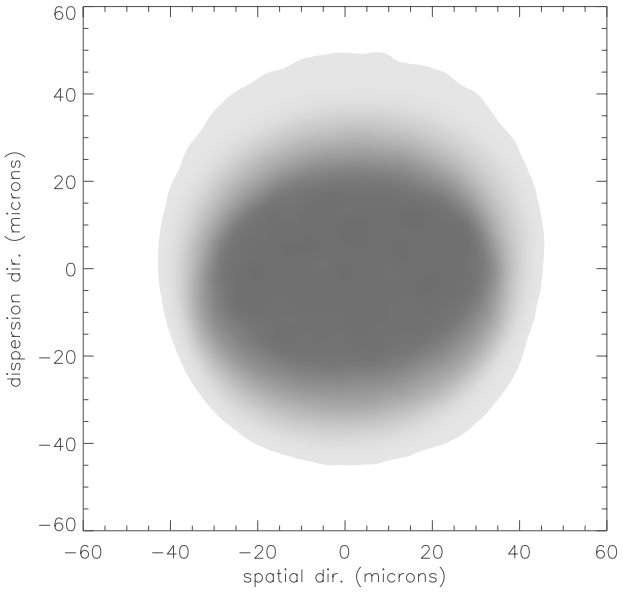


Figure A.5: A 2-dimensional monochromatic spot image generated by ZEMAX from the BigBOSS spectrograph optics. This particular image is near the center of the CCD in the red spectrograph and has been stretched to show the behavior of the PSF wings. The pixel sampling is 1 micron.

Along with optical images, the ZEMAX model of each spectrograph arm also generates a wavelength-dependent throughput that takes into account the effects of all the glass materials needed to construct the image. The throughputs are currently $> 50\%$ in the blue arm for wavelengths $> 4000$Å and $> 70\%$ in both the visible and red arms of the spectrograph. These throughputs do not take into account the transmission from the VPH gratings required to achieve spectral dispersion in each arm. The throughput of the gratings is scaled from the measured VPH designs used in the BOSS spectrographs by moving the blaze wavelength to the central wavelength in each BigBOSS arm. This simple scaling represents what is reasonably achievable given current technology and may be improved upon in the final BigBOSS design. The throughputs for both the spectrograph optics and VPH gratings is plotted in Figure A.4.

**Detector Properties** Similar to the BOSS instrumentation, each arm of the BigBOSS spectrographs will hold a single 4kx4k CCD detector with 15$\mu$m pixel size provided by either e2v (blue arm) or LBNL (visible and

red arms). The critical properties of these devices are the read noise and the quantum efficiency (QE) as a function of wavelength. We nominally assume the read noise, $\sigma_{read}$, is 3.0 electrons pixel$^{-1}$, consistent with the experience of BOSS. The QE for these devices are also available from the BOSS experiment and the wavelength curves are provided along with all other instrumental thoughputs in Figure A.4.

**Sky Subtraction** As seen in Figure A.1, the emission from the sky background introduces a complex wavelength-dependent signal that can both mask the detection of [OII] emission lines and degrades the signal from the astronomical source. The signal from the sky background must therefore be removed from each object spectrum and done so carefully to avoid false detections and obtain optimal use of the instrumentation. Current algorithms used in BOSS achieve near Poisson-limited sky subtraction of the sky background emission, but in a few cases, non-Poisson errors remain from minor variations in the the OH emission lines. A new analysis of the multi-object fiber spectral data using the modeled PSF of the spectrographs and decomposed templates for the sky spectrum have produced evidence for achieving the Poisson limit in sky foreground subtraction [Bolton & Schlegel, 2010].

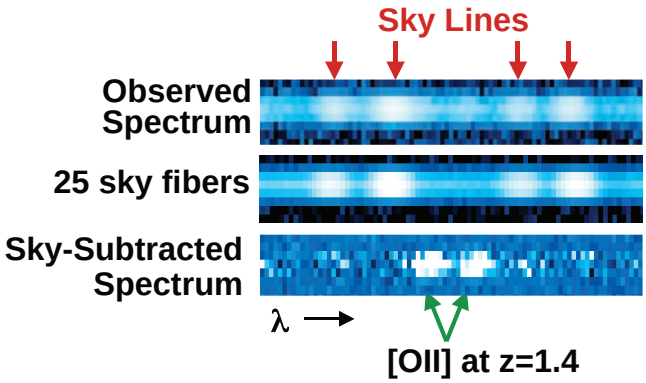


Figure A.6: A graphical representation of the subtraction of sky emission from simulated $z = 1.4$ ELG spectrum in BigBOSS. The top panel is the observed spectral image, the middle panel is the averaged sky spectrum formed from 25 sky fibers, and the bottom panel shows the sky-subtracted spectrum with prominent [OII] doublet signal.

For the purposes of a quick estimation of the noise contributed from the sky subtraction process, we presently skip the details of the "perfect"

sky-subtraction process (involving sparse matrix inversion of multi-object spectra) and assume that the sky measured from each exposure is the mean value of $n_{sky}$ co-added sky-only fiber spectra. Therefore, the residual error of the sky subtraction, $\sigma_{skysub}$, is proportional to $\sqrt{n_{sky}}$ and is added in quadrature to the noise from the sky-subtracted object spectrum. Given that all ELG object spectra ($\approx 300 - 500$ targets deg$^{-2}$) will contain sky emission with little to no contamination from the galaxy continuum, we should expect to construct a mean sky spectrum with $n_{sky} = 25$ and easily resolve field-dependent variations in the sky emission background. This process represents a conservative estimate of Poisson noise contributed from the sky-subtraction process while non-Poisson errors should be avoided with the "perfect" sky subtraction technique. Figure A.6 shows a graphical representation of the sky subtraction process for a [OII] emission line doublet at $z = 1.4$ and where each line of the doublet has a S/N=8.

**Signal to Noise Calculation** The single-pixel signal-to-noise per exposure is performed using the following equation:

$$(S/N)_{pix} = \frac{S_{obj}}{\sqrt{(S_{obj} + S_{sky}) + \sigma^2_{skysub} + \sigma^2_{read}}} \tag{A.2}$$

where $S_{obj}$ and $S_{sky}$ are the photon signals from the object and sky. All terms are computed on a per pixel basis as subtended by the monochromatic spot with 1 unit of dispersion (i.e. 0.732Å for the red arm). To compute the S/N for a single line of the [OII] doublet, we simply multiply $(S/N)_{pix}$ by $\sqrt{n_{pix}}$, where $n_{pix}$ is the effective number of pixels used in the optimal extraction of the emission line, or

$$n_{pix} = 4\pi(\sigma^2_{psf} + \sigma^2_{line}), \tag{A.3}$$

where both $\sigma_{psf}$ and $\sigma_{line}$ are in units of pixels. In our baseline calculations, we assume the emission line has a velocity dispersion of 70km s$^{-1}$.

Tables A.1 and A.2 shows the S/N and exposure time values based on the above instrumental parameters at 10300Å ($z = 1.75$). Specifically, Table A.1 calculates exposure times for a constant S/N=8 of half the [OII] doublet given various values of [OII] line flux and seeing. We find in this simple calculation that the requirement of S/N=8 for a line flux of $0.9 \times 10^{-16}$ ergs s$^{-1}$ cm$^{-2}$ is achieved in $\sim$ 1000 seconds. Table A.2 uses the same values of line flux and seeing but computes the line S/N for a fixed 1000 second exposure. In general, $(S/N) \propto t^2$ and depends linearly on the line flux

signal. Therefore a 10% difference in time or even line flux will only have a marginal impact on the line S/N. However, the S/N degrades rapidly with seeing as signal is lost outside the fiber but the sky brightness remains fixed.

For the full spectral simulation, we compute $(S/N)_{pix}$ for each spectral pixel (spaxel) in each spectrograph arm. The simulation uses the ZEMAX 2D images of the fiber spot and convolves all throughputs, sky, and object spectra with sub-pixel sampling. The 2D spectrum is then reduced to a 1D spectrum by linearly fitting the signal in each spaxel with the spatial profile generated by the simulated PSF collapsed along the spectral dimension and weighted by the spaxel variance. Figure A.7 shows the S/N of a $z = 1.4$ [OII] emission line doublet at $0.9 \times 10^{-16}$ ergs s$^{-1}$ cm$^{-2}$ line flux and a 1000 second exposure. The S/N produced by one half of the [OII] doublet is consistent with the simple single-wavelength calculation. Computing the variance per pixel also allows us to apply random variation from a normal distribution and therefore produce realistic monte carlo spectra. Such spectra will aid development of software that optimizes [OII] line detection and redshift measurement.

Table A.1: Calculated exposure times for a fixed S/N=8 for one line of the [OII] doublet.**PLACEHOLDERS**

| **[OII] Flux** | **Seeing FWHM** | | |
|---|---|---|---|
| **(ergs s$^{-1}$ cm$^{-2}$)** | **0.9″** | **1.1″** | **1.3″** |
| $1.0 \times 10^{-16}$ | 645 | 874 | 1186 |
| $0.9 \times 10^{-16}$ | 758 | 1031 | 1402 |
| $0.8 \times 10^{-16}$ | 911 | 1241 | 1694 |

Table A.2: Calculated S/N values for one line of the [OII] doublet in a fixed 1000 second exposure.**PLACEHOLDERS**

| **[OII] Flux** | **Seeing FWHM** | | |
|---|---|---|---|
| **(ergs s$^{-1}$ cm$^{-2}$)** | **0.9″** | **1.1″** | **1.3″** |
| $1.0 \times 10^{-16}$ | 10.1 | 8.7 | 7.5 |
| $0.9 \times 10^{-16}$ | 9.3 | 8.0 | 6.9 |
| $0.8 \times 10^{-16}$ | 8.5 | 7.3 | 6.2 |

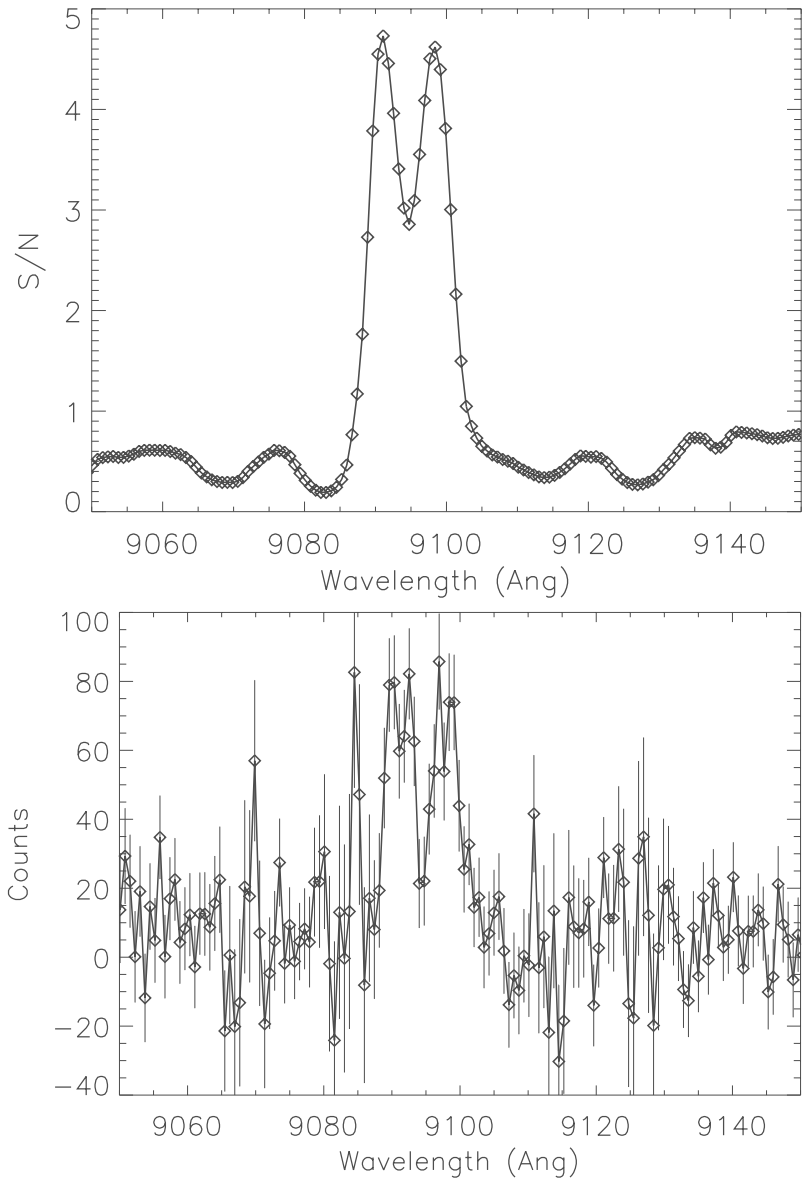


Figure A.7: Extracted 1D spectra for simulated $z = 1.4$ [OII] emission line with $0.9 \times 10^{-16}$ ergs s$^{-1}$ cm$^{-2}$ in a 1000 second exposure at the BigBOSS red spectrograph resolution. The top figure shows the direct S/N for the simulated emission line, where one line of the double achieves S/N=8. The bottom figure is the same simulated spectrum with errors applied from a normal distribution.

# B Letters of Support

## References

Abell, A. A., et al., 2009, LSST Science Book, arXiv:0912.0201v1

Abazajian, K. N., et al. 2009, Astrophys. J. Supp., 182, 543.

Abbott, T., et al. 2005, arXiv:astro-ph/0510346v1

Albrecht, A., et al., 2006, Report of the Dark Energy Task Force, arXiv:astro-ph/0609591.

Albrecht, A., et al., 2009, Findings of the Joint Dark Energy Mission Figure of Merit Science Working Group, arXiv:0901.0721.

Alcock, C. & Paczinsky, B. 1979, Nature, 281, 358.

Amanullah, R., et al. 2010, Astrophys. J., 716, 712.

Ashby, M. L. N., et al. 2009, Astrophys. J., 701,428.

Baldwin, J. A., Phillips, M. M. & Terlevich, R. 1981, Proc. Astron. Soc. Pacific, 93, 5.

Barmby, P., et al. 2008, Astrophys. J. Supp., 177, 431.

Battaglia, G., et al. 2005, Mon. Not. R. Astron. Soc., 364, 433

Bauer, A., Baltay, C., Coppi, P., Ellman, N., Jerke, J., Rabinowitz, D., & Scalzo, R. 2009, Astrophys. J., 696, 1241

Beers, T. C., Preston, G. W., & Shectman, S. A. 1985, Astron. J., 90, 2089

Begelman, M. C., Blandford, R. D. & Rees, M. J. 1980, Nature, 287, 307.

Belokurov, V., et al. 2006, Astrophys. J. Lett., 642, L137

Bianchi, S., Chiaberge, M., Piconcelli, E., Guainazzi, M. & Matt, G. 2008, Mon. Not. R. Astron. Soc., 386, 105.

Blanton, M. R., Eisenstein, D., Hogg, D. W., Schlegel, D. J. & Brinkmann, J. 2005, Astrophys. J., 629, 143.

Bolton, A. S., Burles, S., Koopmans, L. V. E., Treu, T. & Moustakas, L. A. 2006, Astrophys. J., 638, 703.

Bolton, A. S., & Burles, S. 2007, New Journal of Physics, 9, 443.

Bolton, A. S., Burles, S., Koopmans, L. V. E., Treu, T., Gavazzi, R., Moustakas, L. A., Wayth, R. & Schlegel, D. J. 2008a, Astrophys. J., 682, 964.

Bolton, A. S., Treu, T., Koopmans, L. V. E., Gavazzi, R., Moustakas, L. A., Burles, S., Schlegel, D. J. & Wayth, R. 2008b, Astrophys. J., 684, 24.

Bolton, A. S. & Schlegel, D. J. 2010, Proc. Astron. Soc. Pacific, 122, 248.

Bonoli, S., Marulli, F., Springel, V., White, S. D. M., Branchini, E., & Moscardini, L. 2009, Mon. Not. R. Astron. Soc., 396, 423

Booth, C. M., & Schaye, J. 2009, Mon. Not. R. Astron. Soc., 398, 53

Bower, R. G., Benson, A. J., Malbon, R., Helly, J. C., Frenk, C. S., Baugh, C. M., Cole, S., & Lacey, C. G. 2006, Mon. Not. R. Astron. Soc., 370, 645

Brown, M. J. I., Dey, A., Jannuzi, B. T., Brand, K., Benson, A. J., Brodwin, M., Croton, D. J. & Eisenhardt, P. R. 2007, Astrophys. J., 654, 858.

Bruzual, G. & Charlot, S. 2003, Mon. Not. R. Astron. Soc., 344, 1000.

Calzetti, D., Kinney, A.L., & Storchi-Bergmann, T. 1994, Astrophys. J., 429, 582

Cannon, R., et al. 2006, Mon. Not. R. Astron. Soc., 372, 425.

Cappellari, M., et al. 2006, Mon. Not. R. Astron. Soc., 366, 1126.

Chamballu, A., Bartlett, J. G., & Melin, J. -. 2010, arXiv:1007.3193

Christlieb, N., Wisotzki, L., Reimers, D., Homeier, D., Koester, D., & Heber, U. 2001, Astron. Astrophys., 366, 898

Cimatti, A., et al. 2008, Astron. Astrophys., 482, 21.

Clewley, L., Warren, S. J., Hewett, P. C., Norris, J. E., & Evans, N. W. 2004, Mon. Not. R. Astron. Soc., 352, 285

Cole, S., et al. 2005, Mon. Not. R. Astron. Soc., 362, 505.

Coleman, G. D., Wu, C. C. & Weedman, D. W. 1980, Astrophys. J. Supp., 43, 393.

Comerford, J. M., et al. 2009, Astrophys. J., 698, 956.

Comerford, J. M., et al. 2010, Astrophys. J., in preparation.

Coil, A. L., Newman, J. A., Croton, D., et al. 2008, Astrophys. J., 672, 153.

Cooper, M. C., et al. 2006, Mon. Not. R. Astron. Soc., 370, 198.

Cooper, M. C., et al. 2008, Mon. Not. R. Astron. Soc., 383, 1058

Cooray, A., Sarkar, D. & Serra, P. 2008, Phys. Rev. D, 77, 123006.

Cresswell, J. G. & Percival, W. 2009, Mon. Not. R. Astron. Soc., 392, 682.

Croom, S. M., et al. 2004, Mon. Not. R. Astron. Soc., 349, 1397.

Croom, S. M., et al. 2005, Mon. Not. R. Astron. Soc., 356, 415

Croom, S. M., et al. 2009, Mon. Not. R. Astron. Soc., 392, 19

Croom, S. M., et al. 2009, Mon. Not. R. Astron. Soc., 399, 1755.

Croton, D. J., et al. 2006, Mon. Not. R. Astron. Soc., 365, 11

Croton, D. J. 2009, Mon. Not. R. Astron. Soc., 394, 1109

Daddi, E., et al. 2005, Astrophys. J., 626, 680.

Dalal, N., Doré, O., Huterer, D. & Shirokov, A. 2008, Phys. Rev. D, 77, 123514.

Daniel, S. F., et al. 2010, Phys. Rev. D, 81, 123508.

Daniel, S. F. & Linder, E. V. 2010, arXiv:1008.0397.

Davis, M., et al. 2003, Proc. of SPIE, 4834, 161.

Davis, M., et al. 2007, Astrophys. J. Lett., 660, 1.

De Lucia, G., & Blaizot, J. 2007, Mon. Not. R. Astron. Soc., 375, 2

Desjacques, V., Seljak, U. & Iliev, I. 2009, Mon. Not. R. Astron. Soc., 396, 85.

http://management.energy.gov/policy_guidance/project_management.htm.

Dressler, A. 1980, Astrophys. J., 236, 351.

Eisenhardt, P. R. M., et al. 2008, Astrophys. J., 684, 905

Eisenstein, D. J. & Hu, W. 1998, Astrophys. J., 496, 605.

Eisenstein, D. J., et al. 2001, Astron. J., 122, 2267.

Eisenstein, D. J., et al. 2003, Astrophys. J., 585, 694.

Eisenstein, D. J., et al. 2005, Astrophys. J., 633, 560.

Eisenstein, D. J., et al. 2006, Astrophys. J. Supp., 167, 40

Eisenstein, D. J., Seo, H.-J. & White, M. 2007, Astrophys. J., 664, 660.

Eisenstein, D. J., Seo, H.-J., Sirko, E. & Spergel, D. 2007, Astrophys. J., 664, 675.

Emsellem, E., et al. 2004, Mon. Not. R. Astron. Soc., 352, 721.

Eracleous, M., Halpern, J. P., Gilbert, A. M., Newman, J. A. & Filippenko, A. V. 1997, Astrophys. J., 490, 216.

Faber, S. M., et al. 2007, Astrophys. J., 665, 265.

Feldman, H., Kaiser, N. & Peacock, J. 1994, Astrophys. J., 426, 23.

Ferguson, A. M. N., Irwin, M. J., Ibata, R. A., Lewis, G. F., & Tanvir, N. R. 2002, Astron. J., 124, 1452

Franx, M., et al. 2003, Astrophys. J. Lett., 587, L79

Gates, E., et al. 2004, Astrophys. J. Lett., 612, L129

Gavazzi, R., Treu, T., Koopmans, L. V. E., Bolton, A. S., Moustakas, L. A., Burles, S. & Marshall, P. J. 2008, Astrophys. J., 677, 1046.

Gerke, B. F., et al. 2007, Astrophys. J. Lett., 660, L23.

Gilks, W. R., Richardson, S. R. & Spiegelhalter, D. J., "Markov chain Monte Carlo in practice", Chapman & Hall (Florida, 1996).

Glazebrook, K., et al. 2007, Proceedings of the Durham "Cosmic Frontiers" ASP conference eds. Metcalfe & Shanks.

Glazebrook, K., et al. 2005, White paper submitted to the Dark Energy Task Force, arXiv:astro-ph/0507457v2.

Guhathakurta, P., Ostheimer, J. C., Gilbert, K. M., Rich, R. M., Majewski, S. R., Kalirai, J. S., Reitzel, D. B., & Patterson, R. J. 2005, arXiv:astro-ph/0502366

Guzzo, L., et al. 2008, Nature, 451, 541.

Gwyn, S. D. J. 2008, Proc. Astron. Soc. Pacific, 120, 212.

Haiman, Z., & Hui, L. 2001, Astrophys. J., 547, 27

Hamilton, A. J. S. 1998, in "The Evolving Universe. Selected Topics on Large-Scale Structure and on the Properties of Galaxies" Kluwer Academic Publishers, v. 231, p. 185, ISBN: 079235074X.

Harris, H. C., et al. 2006, Astron. J., 131, 571

Hildebrandt, H., van Waerbeke, L. & Erben, T. 2009, Astron. Astrophys., 507, 683.

Hill, G. J., Gebhardt, K., Komatsu, E. & MacQueen, P. J. 2004, Mitchell Symposium, AIP Conf. Proc. 743, 224.

Ho, S., Lin, Y., Spergel, D. & Hirata, C. M. 2009, Astrophys. J., 697, 1358.

Holland, S. E., Bebek, C. J., Dawson, K. S., Emes, J. H., Fabricius, M. H., Fairfield, J. A., Groom, D. E., Karcher, A., Kolbe, W. F., Palaio, N. P., Roe, N. A. & Wang, G. 2006, "High-voltage compatable, fully depleted CCDs," SPIE 6068-12.

Hopkins, A. M. & Beacom, J. F. 2006, Astrophys. J., 651, 142.

Hopkins, P. F., et al. 2006, Astrophys. J. Supp., 163, 1

Hopkins, P. F., Richards, G. T., & Hernquist, L., 2007b, Astrophys. J., 654, 731.

Horne, K. 1986, Proc. Astron. Soc. Pacific, 98, 609.

Hu, W. 1999, Astrophys. J., 522, 21.

Ilbert, O., et al. 2009, Astrophys. J., 690, 1236.

Ivezic, Z., et al., for the LSST collaboration, arXiv:0805.2366v1

Jacoby, G. H., Liang, M., Vaughnn, D., Reed, R., & Armandroff, T., 1998, Proc. of SPIE, 3355, 721

John, T. L. 1988, å, 193, 189.

Jiang, L., et al., 2006, Astron. J., 131, 2788.

Kaiser, N. 1987, Mon. Not. R. Astron. Soc., 227, 1.

Kazin, E., et al. 2010, Astrophys. J., 710, 1444.

Kelson, D. D. 2003, Proc. Astron. Soc. Pacific, 115, 688.

Kennicutt, Jr., R. C. 1998, Annu. Rev. Astron. Astrophys., 36, 189.

Kewley, L. J., Geller, M. J. & Jansen, R. A. 2004, Astron. J., 127, 2002.

Kewley, L. J., Groves, B., Kauffmann, G. & Heckman, T. 2006, Mon. Not. R. Astron. Soc., 372, 961.

Kewley, L. J. & Ellison, S. L. 2008, Astrophys. J., 681, 1183.

Kilic, M., et al. 2006, Astron. J., 131, 582

Kochanek, C., et al. 2004, Bulletin of the AAS, 36, 1495.

Komatsu, E., et al. arXiv:1001.4538.

Komossa, S., Burwitz, V., Hasinger, G., Predehl, P., Kaastra, J. S. & Ikebe, Y. 2003, Astrophys. J. Lett., 582, L15.

Koopmans, L. V. E., Treu, T., Bolton, A. S., Burles, S. & Moustakas, L. A. 2006, Astrophys. J., 649, 599.

Kowalski, M., et al. 2008, Astrophys. J., 686, 749.

Kubo, J. M., Allam, S. S., Annis, J., Buckley-Geer, E. J., Diehl, H. T., Kubik, D., Lin, H., & Tucker, D. 2009, Astrophys. J. Lett., 696, L61

Lauer, T. R., et al. 2007, Astrophys. J., 662, 808.

Law, N. M., et al. 2009, Proc. Astron. Soc. Pacific, 121, 1395.

Le Févre, O., Vettolani, G., Paltani, S., et al. 2005, å, 439, 845.

Leauthaud, A., et al. 2007, Astrophys. J. Supp., 172, 219

Linder, E. V. 2005, Phys. Rev. D, 72, 043529.

Linder, E. V. & Cahn, R. N. 2007, Astropart. Phys., 28, 481.

Linder, E. V. 2008, Astropart. Phys., 29, 336.

Liu, X., Shen, Y., Strauss, M. A. & Greene, J. E. 2010, Astrophys. J., 708, 427.

López-Corredoira, M. 2010, Astron. J., 139, 540.

Ly, C., et al. 2007, Astrophys. J., 657, 738.

Majewski, S. R., Skrutskie, M. F., Weinberg, M. D., & Ostheimer, J. C. 2003, Astrophys. J., 599, 1082

Marchesini, D., et al. 2007, Astrophys. J., 656, 42

Marinoni, C., et al. 2005, Astron. Astrophys., 442, 801.

Martin, C. L., & Sawicki, M. 2004, Astrophys. J., 603, 414.

Martinez-Delgado, D., et al. 2010, arXiv:1003.4860

Martini, P., & Weinberg, D. H. 2001, Astrophys. J., 547, 12

McDonald, P., et al. 2005, Astrophys. J., 635, 761.

McDonald, P. & Seljak, U. 2009, J. Cosmology Astropart. Phys., 10, 007.

McDonald, P. 2008, Phys. Rev. D, 78, 123519.

Milosavljević, M. & Merritt, D. 2001, Astrophys. J., 563, 34.

Milosavljević, M., Merritt, D., Rest, A. & van den Bosch, F. C. 2002, Mon. Not. R. Astron. Soc., 331, L51.

Montero-Dorta, A. D., et al. 2009, Mon. Not. R. Astron. Soc., 392, 125.

Morrison, H. L., Olszewski, E. W., Mateo, M., Norris, J. E., Harding, P., Dohm-Palmer, R. C., & Freeman, K. C. 2001, Astron. J., 121, 283

Moustakas, J., Kennicutt, Jr., R. C. & Tremonti, C. A. 2006, Astrophys. J., 642, 775.

Mukadam, A. S., et al. 2004, Astrophys. J., 607, 982

Myers, A. D., Brunner, R. J., Richards, G. T., Nichol, R. C., Schneider, D. P., & Bahcall, N. A. 2007, Astrophys. J., 658, 99

Newman, J. A. 2008, Astrophys. J., 684, 88

Nilson, P. 1973, Acta Universitatis Upsaliensis. Nova Acta Regiae Societatis Scientiarum Upsaliensis - Uppsala Astronomiska Observatoriums Annaler, Uppsala: Astronomiska Observatorium.

Padmanabhan, N., et al. 2007, Mon. Not. R. Astron. Soc., 378, 852.

Padmanabhan, N., et al. 2008, Astrophys. J., 674, 1217.

Padmanabhan, N. & White, M. 2009, Phys. Rev. D, 80, 063508.

Palanque-Delabrouille et al. 2010, in preparation

Pan-STARRS Survey Website 2010, http://pan-starrs.ifa.hawaii.edu/public.

Papovich, C., Rudnick, G., Rigby, J. R., Willmer, C. N. A., Smith, J.-D. T., Finkelstein, S. L., Egami, E., & Rieke, M. 2009, Astrophys. J., 704, 1506

Parkinson, D., et al. 2010, Mon. Not. R. Astron. Soc., 401, 2169.

Pasquali, A., van den Bosch, F. C., Mo, H. J., Yang, X., & Somerville, R. 2009, Mon. Not. R. Astron. Soc., 394, 38

Peebles, P. J. E. 1980, The large scale structure of galaxies, Princeton University Press.

Pen, U. 2004, Mon. Not. R. Astron. Soc., 350, 1445.

Percival, W. J., et al. 2010, Mon. Not. R. Astron. Soc., 401, 2148.

Perlmutter, S., et al. 1999, Astrophys. J., 517, 565.

Pettini, M., Steidel, C. C., Adelberger, K. L., Dickinson, M. & Giavalisco, M. 2000, Astrophys. J., 528, 96.

Pradhan, A. K., et al. 2006, Mon. Not. R. Astron. Soc., 366, L6.

Rengstorf, A. W., et al. 2004, Astrophys. J., 617,184

Reyes, R., Mandelbaum, R., Seljak, U., Baldauf, T., Gunn, J., Lombriser, L. & Smith, R. 2010, Nature 464, 256.

Richards, G. T., et al. 2006, Astron. J., 131, 2766.

Richards, G. T., et al. 2009, Astrophys. J. Supp., 180, 67.

Riess, A. G., et al. 1998, Astron. J., 116, 1009.

Rodriguez, C., Taylor, G. B., Zavala, R. T., Peck, A. B., Pollack, L. K. & Romani, R. W. 2006, Astrophys. J., 646, 49.

Ross, N. P., et al. 2009, Astrophys. J., 697, 1634.

Rubin, V. C., Ford, W. K. J. & Thonnard, N. 1980, Astrophys. J., 238, 471.

Sawicki, M. 2002, Astron. J., 124, 3050.

Schiavon, R. P., et al. 2006, Astrophys. J. Lett., 651, L93.

See, for example, D. Schlegel, M. White, and D. Eisenstein, arXiv:0902:4680.

Schmidt, G. D., et al. 2003, Astrophys. J., 595, 1101

Schmidt, K. B., et al. 2010, Astrophys. J., 714,1194.

Schneider, D. P., et al. 2010, Astron. J., 139, 2360.

Schulz, A. & White, M. 2006, Astropart. Phys., 25, 172.

Scoccimarro, R. 2004, Phys. Rev. D, 70, 083007.

Seljak, U., et al. 2005, Phys. Rev. D, 71, 3515.

Seljak, U., Hamaus, N. & Desjacques, V. 2009, Phys. Rev. Lett., 103, 091303.

Seljak, U. 2009, Phys. Rev. Lett., 102, 021302.

Seo, H.-J. & Eisenstein, D. J. 2007, Astrophys. J., 664, 675.

Senatore, L., Smith, K. M. & Zaldarriaga, M. 2010, J. Cosmology Astropart. Phys., 01, 028.

South Galactic Cap U-Band Sky Survey, 2010, http://batc.bao.ac.cn/Uband

Shankar, F., Weinberg, D. H., & Shen, Y. 2010, Mon. Not. R. Astron. Soc., 406, 1959

Shen, Y., et al. 2007, Astron. J., 133, 2222

Shen, Y., et al. 2009, Astrophys. J., 697, 1656

Shen, Y. 2009, Astrophys. J., 704, 89

Silvestri, N. M., et al. 2006, Astron. J., 131, 1674

Slosar, A., Hirata, C., Seljak, U., Ho, S. & Padmanabhan, N. 2008, J. Cosmology Astropart. Phys., 08, 031.

Smith, K. L., Shields, G. A., Bonning, E. W., McMullen, C. C., Rosario, D. J. & Salviander, S. 2010, Astrophys. J., 716, 866.

Song, Y.-S. & Percival, W. J. 2009, J. Cosmology Astropart. Phys., 10, 004.

Springel, V., Di Matteo, T. & Hernquist, L. 2005, Mon. Not. R. Astron. Soc., 361, 776.

Stern, D., et al. 2005, Astrophys. J., 631, 163.

Stril, A., Cahn, R. N. & Linder, E. V. 2010, Mon. Not. R. Astron. Soc., 404, 239.

Sumiyoshi, M., et al. 2009, arXiv:0902.2064.

Takahashi, M. I., et al. 2007, Astrophys. J. Supp., 172, 456.

Tegmark, M., et al. 2006, Phys. Rev. D, 74, 123507.

van Dokkum, P. G., et al. 2009, Proc. Astron. Soc. Pacific, 121, 2

van Waerbeke, L., White, M., Hoekstra, H. & Heymans, C. 2006, Astropart. Phys., 26, 91.

Verde, L., et al. 2002, Mon. Not. R. Astron. Soc., 335, 432.

Wang, Y. 2008, J. Cosmology Astropart. Phys., 05, 021.

Wang, J., Chen, Y., Hu, C., Mao, W., Zhang, S. & Bian, W. 2009, Astrophys. J. Lett., 705, L76.

Weiner, B. J., et al. 2005, Astrophys. J., 620, 595.

White, M. 2005, Astropart. Phys., 24, 334.

White, M., et al. 2009, Mon. Not. R. Astron. Soc., 397, 1348.

Wright, E. L., et al. 2010, arXiv:1008.0031v1

Xue, X. X., et al. 2008, Astrophys. J., 684, 1143

Yan, R., Newman, J. A., Faber, S. M., Konidaris, N., Koo, D., & Davis, M. 2006, Astrophys. J., 648, 281

Yang, X., Mo, H. J., van den Bosch, F. C., Pasquali, A., Li, C., & Barden, M. 2007, Astrophys. J., 671, 153

Yanny, B., et al. 2009, Astrophys. J., 700, 1282

Yanny, B., et al. 2009, Astron. J., 137, 4377

Yee, H. K. C., Ellingson, E., Bechtold, J., Carlberg, R. G. & Cuillandre, J.-C. 1996, Astron. J., 111, 1783.

Yee, H. K. C., Gladders, M. D., Gilbank, D. G., Majumdar, S., Hoekstra, H. & Ellingson, E. 2007, Cosmic Frontiers, 379, 103.

Yeche, Ch., et al. 2010, submitted to å, arXiv:0910.3770v1

Zhang, P., et al. 2007, Phys. Rev. Lett., 99, 141302.

Zhu, G., Moustakas, J. & Blanton, M. R. 2009, Astrophys. J., 701, 86.

Zwicky, F. 1933, Helvetica Physica Acta, 6, 110.